DEVELOPMENT OF A SAPOSIN A BASED NATIVE-LIKE PHOSPHOLIPID BILAYER SYSTEM FOR NMR STUDIES

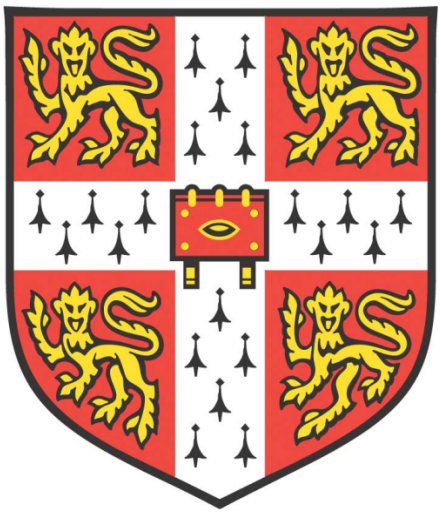

Chih-Ta Chien

Clare Hall

Department of Biochemistry

University of Cambridge

September 2018

This dissertation is submitted for the degree of Doctor of Philosophy

ABSTRACT

Membrane proteins are important targets that represent more than 50% of current drug targets. However, characterisation of membrane proteins falls behind compared to their soluble counterparts. The most challenging part of membrane protein research is finding a suitable membrane mimetic that stabilises them in solution and maintains their native structure and function. The recently developed saposin-A (SapA) based lipid nanoparticle system seems to be advantageous over existing membrane mimetic system. It provides a native-like lipid bilayer, high incorporation yield and more importantly size adaptability. SapA lipid nanoparticles have been applied to structural studies and two high-resolution structures of membrane proteins were previously obtained using cryo-electron microscopy. This thesis aimed to study small-to-medium sized membrane proteins in SapA lipid nanoparticles using NMR spectroscopy.

We first explore the mechanism of SapA lipid nanoparticle formation for the purpose of establishing an incorporation protocol that can be applied to most membrane proteins. The effect of pH and the presence of detergents on the opening of SapA was investigated in Chapter 2. A proposed energy diagram describing the mechanism of SapA opening is reported with which we were able to develop a protocol that can generate different sizes of SapA-1,2-dimyristoyl-sn-glycero-3-phosphocholine (DMPC) nanoparticles. In addition, we also showed that SapA can form lipid nanoparticles with various lipid compositions, showing the versatility of the system.

In Chapter 3, we validated the ability of SapA lipid nanoparticles to be used as a membrane mimetic. A β-barrel model protein, bacterial outer membrane protein X (OmpX), was incorporated into SapA-DMPC nanoparticles and a 2D ^{15}N-^{1}H correlation NMR spectrum was recorded. Our result was compared to the NMR parameters of the same protein in MSP nanodiscs from the literature, and it was concluded that SapA lipid nanoparticles indeed provide a lipid bilayer environment similar to MSP nanodiscs. Because of high incorporation yield, we were able to incorporate OmpX into different lipid compositions to investigate the effect of lipid head groups and aliphatic chains on the membrane protein's chemical environment.

Next, the applicability of SapA lipid nanoparticles was expanded to α-helical transmembrane proteins in Chapter 4. Two microbial rhodopsins, *Anabaena* sensory rhodopsin (ASR) and *Natronomonas pharaonis* sensory rhodopsin II (pSRII), were

tested. The parameters for expression and purification of ASR were first screened for the optimal yield. Although incorporation of ASR resulted in inhomogeneous particles due to imperfect experimental procedure, pSRII in SapA-DMPC nanoparticles showed high sample quality. The 2D NMR spectrum of pSRII in SapA-DMPC nanoparticles shows distinct differences to pSRII in detergent micelles, suggesting substantial effects from the membrane mimetic on the conformation of the membrane protein. Despite the good NMR spectral quality considering the large particle size, perdeuteration of pSRII and the lipids will be necessary for further investigation.

With the SapA lipid nanoparticles established, we aimed to use it for the study of a biologically important G protein-coupled receptor, β_1-adrenergic receptor (β_1AR), discussed in Chapter 5. The possibility of expressing β_1AR using a cell-free expression system was explored first. Although a good amount of the protein was obtained, only a fraction of it was functional. Therefore, a conventional baculovirus-insect cell expression system was used to produce selective isotope labelled β_1AR for NMR studies. NMR spectra of β_1AR in SapA-DMPC nanoparticles with activating ligands and an intracellular binding partner were recorded and compared to the spectra of the same protein in detergents. This revealed a more active-like conformation of ligand-bound β_1AR in the lipid bilayer, suggesting that certain parts of the protein are sensitive to the membrane mimetic used. This emphasises the importance of using a native-like membrane mimetic to capture the full properties of membrane proteins.

In conclusion, I demonstrate in this thesis that SapA lipid nanoparticles are a versatile membrane mimetic system that can accommodate membrane proteins with different sizes and folds. This system is also compatible with solution NMR spectroscopy enabling structure and dynamics studies of biologically important membrane proteins. We believe SapA lipid nanoparticles will have a significant impact on membrane protein research in the future.

ACKNOWLEDGEMENTS

First of all, I would like to thank my PhD supervisor, Daniel Nietlispach for his guidance and support along this incredible journey. I really appreciate the freedom of developing my own project. I also learnt from Daniel his attitude of doing science that is to get to the bottom of any problems.

I would also like to thank Mark Bostock for proofreading my manuscript and this PhD thesis. Mark also shares with me papers which he found interesting or might be useful to me. I still remember he sent this Salipro paper to me in March 2016, and that was the moment the direction of my PhD project changed completely. Andras Solt, Niclas Frei, Yilei Tan, and I joined the group at the same time. We had a great time working together, and I enjoyed discussing exciting findings or experimental issues with them.

I am grateful for all the support from the past members in Nietlispach group including Sandra Berndt, Duncan Crick, Yvonne Yu, Prashant Kumar, and Teyam Peryie. Many thanks to Rowina Westermeier for showing me how to set up cell-free expression in my first year. Two part-II students that I supervised, Lukas Helfinger and Daniel Gentle, contributed some of the work in this thesis. I have learnt a lot from supervising them and the results we obtained together were very helpful. Fortnightly NMR journal club gave me the opportunity to learn the background knowledge of biomolecular NMR. I would like to thank everyone in Helen Mott's group, Bill Broadhurst's group, Katherine Stott's group who participated in the NMR journal club. I have learnt a lot from them.

First three years of my PhD were funded by Cambridge Trust. The fourth year was funded together by Cambridge Trust, Philosophical Society, and Clare Hall. I would also like to thank Clare Hall for providing me funding to go to scientific conferences and short-term research visit.

Finally, I would like to thank my family for their unconditional support. My girlfriend Chih-Yi Lin spent two years here in Cambridge with me. She witnessed the highs and lows of my PhD. I really appreciate her support.

I believe obtaining a PhD degree needs a combination of hard working, a bit of luck, and most importantly the help from other people. I thank everyone I met in this four years' time. This thesis would not be possible without your help.

CONTENTS

LIST OF TABLES

LIST OF FIGURES

LIST OF ABBREVIATIONS AND ACRONYMS

β_1AR	β_1-adrenergic receptor
β_2AR	β_2-adrenergic receptor
βAR	β-adrenergic receptor
A8-35	Amphipol A8-35
AEX	Anion-Exchange chromatography
ASR	*Anabaena* sensory rhodopsin
ASRT	*Anabaena* sensory rhodopsin transducer
C6-DHPC	Dihexanoyl-*sn*-glycero-3-phophatidylcholine
C7-DHPC	Diheptanoyl-*sn*-glycero-3-phophatidylcholine
CD	Circular dichroism
CHAPS	3-[(3-Cholamidopropyl)dimethylammonio]-1-propanesulfonate
CV	Column volumes
D-CF	Detergent-based cell-free expression
DDM	n-Dodecyl β-D-maltoside
DLS	Dynamic light scattering
DM	n-Decyl-β-D-maltoside
DMPC	1,2-dimyristoyl-*sn*-glycero-3-phosphocholine
DMPG	1,2-dimyristoyl-*sn*-glycero-3-phospho-(1'-rac-glycerol)
DPC	Dodecylphosphocholine
DPPC	1,2-dipalmitoyl-*sn*-glycero-3-phosphocholine
ESI-MS	Electrospray ionisation mass spectrometry
FM	Feeding mixture
GFP	Green fluorescence protein
GPCR	G protein-coupled receptor
GRK	G protein-coupled receptor kinase

HEGA-10	Decanoyl-N-hydroxyethylglucamide
HMQC	Heteronuclear multiple quantum coherence
HSQC	Heteronuclear single quantum coherence
HtrII	Haloarchaeal transducer II
ICL	Intracellular loop
IPTG	Isopropyl β-D-1-thiogalactopyranoside
L-CF	Lipid-based cell-free expression
LB	Lysogeny broth
LDAO	Lauryldimethylamine N-oxide
LMNG	2,2-didecylpropane-1,3-bis-β-D-maltopyranoside
MALDI-TOF	Matrix-assisted laser desorption ionization time of flight
Nb6B9	G protein-mimicking nanobody 6B9
Nb80	G protein-mimicking nanobody 80
Ni-NTA	Nickel-nitrilotriacetic acid
NMR	Nuclear magnetic resonance
NOE	Nuclear Overhauser effect
OG	n-octyl β-D-glucoside
OmpX	Bacterial outer membrane protein X
P-CF	Precipitate-based cell-free expression
PC	Phosphatidylcholine
PDB	Protein data bank
PFG	Pulsed field gradient
PG	Phosphatidylglycerol
POPC	1-palmitoyl-2-oleoyl-*sn*-glycero-3-phosphocholine
POPG	1-palmitoyl-2-oleoyl-*sn*-glycero-3-phospho-(1'-rac-glycerol)
pSRI	*Natronomonas pharaonis* sensory rhodopsin I
pSRII	*Natronomonas pharaonis* sensory rhodopsin II

RM	Reaction mixture
SapA	Saposin A
SDS	Sodium dodecyl sulphate
SDS-PAGE	Sodium dodecyl sulphate polyacrylamide gel electrophoresis
SEC	Size-exclusion chromatography
SOFAST	Band-selective optimized flip-angle short-transient
T7RNAP	T7 RNA polymerase
T_m	Melting temperature
TM	Transmembrane helix
TROSY	Transverse relaxation-optimised spectroscopy

1 INTRODUCTION

1.1 Transmembrane proteins

An integral membrane protein is a type of protein that permanently locates in the biological membrane. Integral membrane proteins can be further divided into two categories: integral monotopic proteins that attach to one side of the membrane and transmembrane proteins, also called integral polytopic proteins, that span the entire membrane.[1] Transmembrane proteins, with an arrangement that connects two sides of the membrane, often function as a bridge between the intra- and extracellular environments across the hydrophobic lipid bilayer. They frequently undergo large conformational changes in order to perform their function in transport or signal transduction across the membrane.

1.1.1 Biological functions of transmembrane proteins

Transmembrane proteins carry out many biological functions such as signal transduction, bioenergetics, transporting substances, cell adhesion, enzymatic reactions, cellular structure and support. More than 60% of the human membrane protein family belong to three major functional groups: membrane receptors, membrane transport proteins, and membrane enzymes.[2]

Membrane receptors function as signal transducers transferring a signal across the membrane to mediate a cellular response to external stimuli e.g. upon ligand binding. G protein-coupled receptors (GPCRs) are the largest member in this category, as about 800 human genes are predicted to be GPCRs.[2] Their mechanism often involves a large conformational change of the receptor induced by binding extracellular ligands which can be hormones, neurotransmitters, cytokines, or growth factors. The conformational

change in the receptor induces the recognition of effector proteins on the intracellular side, thus passing the signal to its destination.

Membrane transport proteins move substances such as ions, small molecules, or macromolecules across the membrane. They can be further categorized into three major classes: ATP-powered pumps, channel proteins, and transporters.[3] ATP-powered pumps use the energy of ATP hydrolysis to transport ions or small molecules across the membrane against a concentration gradient or electric potential. This process is referred to as active transport. In contrast, channel proteins move water or ions down their concentration gradient or electric potential, a spontaneous reaction that does not need an energy input, hence it is referred to as passive transport. When the channel protein is open, multiple molecules can travel across the channel protein simultaneously with a rate of up to 10^8 per second.[3] Transporters, on the other hand, bind only one substrate molecule at a time and undergo a significant conformational change such that the bound substrate is transported across the membrane. Because of this, the whole process is much slower than that of channel proteins with a rate of 10^2–10^4 molecules per second.[3]

Membrane enzymes are membrane proteins with the ability to catalyse a specific chemical reaction. Six types of reaction were found that are performed by human membrane enzymes: oxidoreductases, transferases, hydrolases, lyases, isomerases, and ligases.[2]

1.1.2 Structures of transmembrane proteins

Transmembrane proteins can be classified into two types based on their structures, α-helical and β-barrel transmembrane proteins.[4]

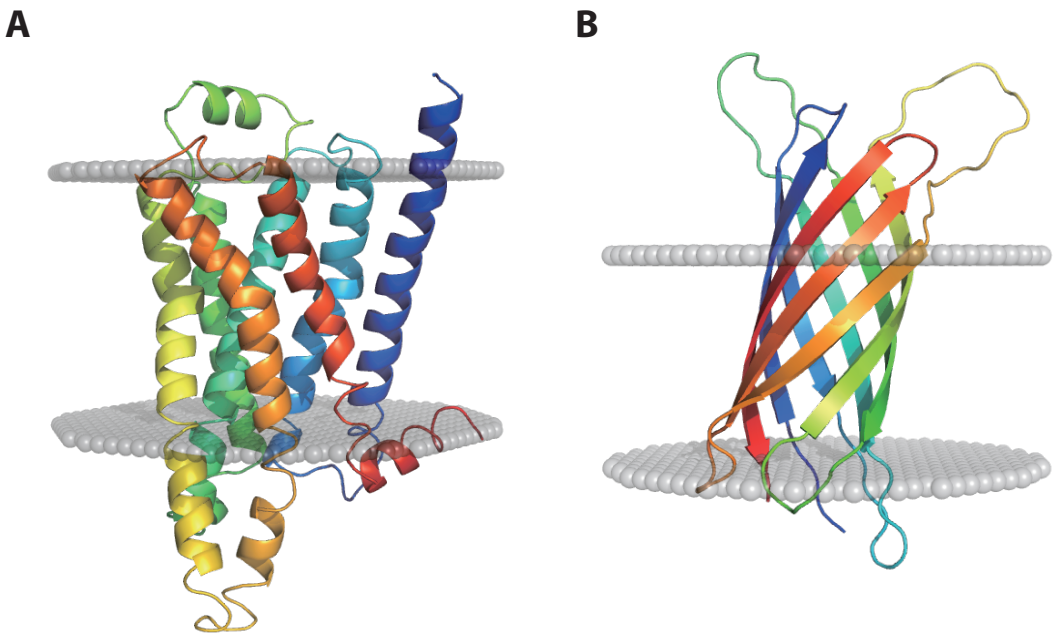

Figure 1-1: Two types of transmembrane proteins.

Examples of A) α-helical transmembrane protein (PDB code: 2CYW) and B) β-barrel transmembrane protein (PDB code: 2M06). Lipid bilayer regions are predicted by a computational approach[5] and are shown in grey spheres.

α-helical transmembrane proteins are the major category of transmembrane proteins that can be found in the inner membrane of bacterial cells or the plasma membrane of eukaryotes. It has been predicted that 27% of all human proteins are α-helical transmembrane proteins.[2] α-helical transmembrane proteins contain one or more membrane-spanning helices, which consist mostly of hydrophobic amino acids (Figure 1-1 A).[6] Individual helices are formed by hydrogen bonds between the amide group of an amino acid and the carbonyl group of the amino acid four residues earlier in the sequence. The typically hydrophobic side chains of the amino acids are exposed to the lipid bilayer hydrocarbon core in order to stabilise the protein in a membrane environment. The individual helices are in general very stable on their own in a hydrophobic environment, therefore it is unclear what is the main driving force for the formation of helical bundles. Since hydrophobic interactions, which drive the folding of soluble proteins, cannot account for the folding of transmembrane proteins, it is thought that Van der Waals interactions between specific side chain pairs are important for α-helical transmembrane proteins to pack to their functional structure.[7] Much efforts has been devoted to the prediction of transmembrane helix region from amino acid sequence information. A simple rule that searches for ~20 continuous hydrophobic amino acids

was used to predict transmembrane helices 35 years ago.[8] Since then, the prediction has been further improved by combining information from solved high-resolution membrane protein structures. There are more than 12 programs available to predict the presence of transmembrane helices from a protein sequence.[9]

β-barrel membrane proteins, also known as outer membrane proteins (OMPs) are found only in the outer membrane of gram-negative bacteria, mitochondria, and chloroplasts, as well as the cell wall of gram-positive bacteria.[10] There are around 100 non-homologous structures of OMPs in the PDB showing the fundamental design of OMPs.[11] β-barrel strands are amphipathic and are generally oriented in an antiparallel fashion (Figure 1-1 B). The strands are held together by hydrogen bonds between backbone amide groups, causing the side chains to alternate in direction between the hydrophilic side chains pointing inward to the pore and the hydrophobic side chains pointing outward to the membrane.[11] The number of strands ranges from 8 to 24, and almost all OMPs contain an even number of strands except VDAC-1.[10] Despite adopting the same β-barrel fold, OMPs are involved in a variety of biological functions including transporting substances across membranes,[12] signaling,[13] and membrane biogenesis.[14] There is growing interest in OMPs because of their role in antibiotic resistance and their location which makes them accessible for drug targeting.[11]

1.2 Structural studies of transmembrane proteins

Obtaining a molecular structure is essential to understand the function and detailed mechanism of a protein. The structural elucidation of membrane proteins has proven to be difficult. This can be clearly seen in that less than 3% of all PDB structures are for membrane proteins[15] even though 20–30% of all genes are predicted to be membrane proteins.[16] There are currently 2619 PDB coordinates of membrane protein structures of which 817 are unique structures, excluding mutants, different bound substrates, or different sample conditions (September 2018, http://blanco.biomol.uci.edu/mpstruc/). Nevertheless, the number of membrane protein structures is increasing dramatically; 74 unique membrane protein structures had been determined by September in 2018 whereas only about 30 structures per year were deposited ten years ago. This increase is due to the recent technological developments in the three main techniques used for structure determination, X-ray crystallography, nuclear magnetic resonance (NMR) spectroscopy, and cryo-electron microscopy (cryo-EM), which I will discuss in more detail in the following sections.

1.2.1 X-ray crystallography

X-ray crystallography remains the most frequently used technique for membrane protein structure determination as more than 85% of all membrane protein structures in the PDB were solved by X-ray crystallography.[15] The most difficult part of this technique is obtaining a protein crystal that diffracts well. Protein crystallization is often a trial-and-error and iterative process that involves construct design, protein production, and screening for the optimal conditions to produce quality crystals.[17] Crystallization of membrane proteins is even more difficult because the hydrophobic molecules such as detergents or lipids, which are necessary to keep the membrane proteins in solution, might make the formation of crystal contacts between two membrane proteins more complicated. Several strategies can be used to stabilise membrane proteins in a particular conformation including stabilisation by antibodies or nanobodies,[18] insertion of a fusion protein to increase crystal contacts,[19] and thermostabilisation by mutagenesis and the truncation of flexible regions.[20] These strategies have allowed several membrane protein structures including some of the difficult GPCR targets to be determined. Two approaches are currently used to crystalize membrane proteins.[21] The *in surfo* approach generates crystals of a protein-detergent complex in which crystal contacts form only between hydrophilic parts of the protein.[22] Alternatively, the *in meso* approach incorporates the membrane protein in a lipidic mesophase such as lipidic cubic phase,[23] lipidic sponge phase,[24] connected-bilayer gel,[25] etc. The *in meso* approach in general leads to better ordered crystals and higher resolution diffraction compared to the *in surfo* approach. X-ray crystallography in general produces molecular structures with the highest resolution compared to other techniques used to investigate protein structures. However, the whole protein crystallisation process is rather unpredictable.

1.2.2 NMR spectroscopy

Characterising the structure and function of membrane proteins by solution and solid-state NMR bypasses the need for obtaining a good quality protein crystal, but the technique has its own challenges as well. Solution NMR can only applied to small to medium sized macromolecules that tumble fast with correlation times smaller than 100 ns.[26] Slow tumbling increases the transverse relaxation rate leading to reduced signal-to-noise ratios. This would make the interpretation and analysis of the NMR spectra extremely difficult. Many efforts have been made to tackle this problem, and the most revolutionary development was transverse relaxation optimized spectroscopy (TROSY).

TROSY is an NMR experiment that was designed for studying large molecules such as biomolecules.[27] In a conventional 2D-HSQC spectrum without decoupling, peaks appear as multiplets because of scalar *J*-coupling (Figure 1-2 A). Each of the multiplet components shows dramatically different linewidths because of constructive or destructive interaction between two dominant relaxation mechanisms; the dipole-dipole mechanism and the chemical shift anisotropy mechanism. To reduce spectral complexity, decoupling is normally employed in 2D-HSQC experiments to produce a single peak with averaged linewidths (Figure 1-2 B). The TROSY experiment is designed to select the sharpest component (Figure 1-2 C) for which the two relaxation mechanisms almost cancel each other, increasing the spectral resolution and sensitivity. The dipole-dipole mechanism is a result of interaction between two nuclear spins, therefore it is field-independent. On the other hand, chemical shift anisotropy is a result of an anisotropic electronic environment, meaning the chemical shift depends on the orientation of a molecule with respect to the external magnetic field, therefore it is field-dependent. Therefore, there is an optimal field strength at which the cancellation between the two relaxation mechanisms is maximal. For example, an external magnetic field of around 1 GHz produces the maximal TROSY effect for $^{15}N/^{1}H$ correlation.[27,28] Since the dipole-dipole mechanism and chemical shift anisotropy mechanism are the two most dominant factors in transverse relaxation for large proteins, the TROSY effect becomes advantageous in studying large proteins and significantly increases the size limit of NMR spectroscopy.

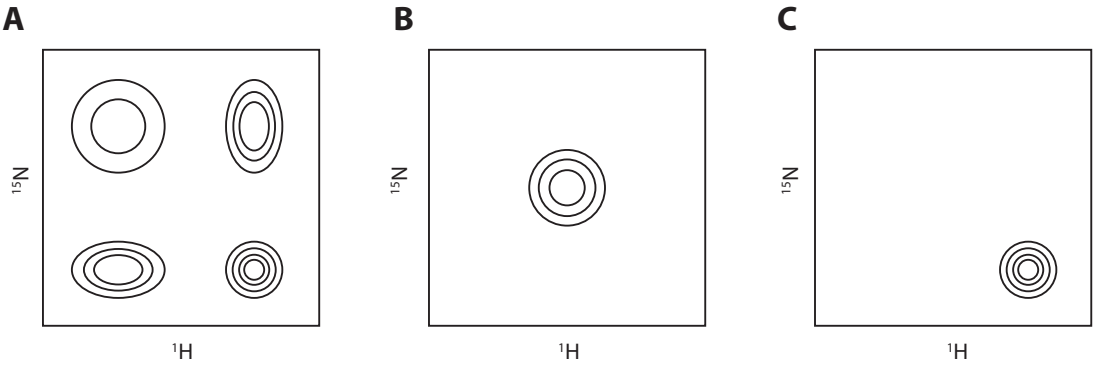

Figure 1-2: Schematic representation of 2D ^{1}H, ^{15}N correlation HSQC.

Demonstration of the effect of a TROSY experiment. A) HSQC spectrum without decoupling. B) HSQC spectrum with decoupling. C) TROSY experiment.

With the development of TROSY and advances in NMR instrumentation, small membrane proteins are feasible targets for solution NMR studies, including structure determination, using similar methods as for soluble proteins. Uniformly [^{2}H, ^{13}C, ^{15}N]-labelled membrane proteins are often used for the best spectral quality. The first membrane protein backbone structure solved by solution NMR was bacterial outer membrane protein A, a 19 kDa β-barrel protein.[29] Since then, several strategies have been developed to improve the determination of membrane protein structures. For example, selectively methyl-protonated labelling of isoleucine, leucine and valine in a perdeuterated background allows 140 out of 141 methyl side chains to be assigned and the identification of a large number of nuclear Overhauser effect (NOE) distances, leading to structure determination of a seven-transmembrane helical protein.[30] Paramagnetic relaxation enhancement (PRE),[31] residual dipolar couplings (RDC),[32] and pseudocontact shifts (PCS)[33] were employed in several solution NMR studies for further improvements in membrane protein structure determination. Because of the size limitation of solution NMR, most of the studies used detergent micelles for membrane protein stabilisation to reduce the overall particle sizes. Nanodiscs are well-defined particles with lipid bilayer environments which have been used in several solution NMR studies and will be discussed in more detail in Chapter 3.

The transverse relaxation that causes the size limitation of solution NMR is not an issue in solid-state NMR because of magic angle spinning. By mechanically spinning the sample at a high speed, the three main transverse relaxation mechanisms, namely dipolar, chemical shift anisotropy, and quadrupolar interactions, are averaged out. This produces narrower line shapes and higher resolution spectra. Nevertheless, solid-state NMR spectra of uniformly labelled protein samples are in general complex and have a large number of overlapped peaks. As a result, selectively labelled samples are necessary.[34] Magic angle spinning solid-state NMR has been shown to be useful for determination of membrane protein structures in a native lipid environment. An atomic-resolution structure of the sensory rhodopsin from the cyanobacterium *Anabaena* was obtained by combining torsional and internuclear distance restraints with PRE constraints.[35] The structure of the transmembrane domain of the *Yersinia enterocolitica* adhesin A was determined using a single uniformly [^{13}C,^{15}N]-labelled microcrystal that diffracts poorly.[36] Recently, the same strategy was used to solve the structure of the 14-strand outer membrane protein G from *Escherichia coli* in a lipid bilayer.[37]

1.2.3 Cryo-EM

Cryo-EM has become very popular recently for structure determination with many advantages over conventional techniques. This is because of recent technical advances and the development of image-processing software. The first breakthrough was the development of a sample preparation method that prevents water-soluble samples from drying out in the vacuum. A protein solution is flash-frozen using liquid ethane quick enough that water molecules, instead of forming ice, remain in a vitreous state.[38] Secondly, a methodology that aligns experimental images of biological samples with low signal-to-noise ratio produces higher quality averaged images, which greatly improves the results of structure reconstruction.[39] Lastly, development of a direct electron detector enables high data-throughput and corrections of beam-induced particle movement.[40] The advantage of using cryo-EM is that large quantities and a high level of homogeneity of the protein sample are not necessary, unlike NMR or X-ray crystallography. Only μg amounts of sample are needed for grid preparation and small amounts of inhomogeneous particles or impurities can be excluded during particle picking. This is particularly useful in membrane protein studies because it is even more difficult, compared to soluble proteins, to express and purify membrane proteins to meet the high standards that NMR and X-ray crystallography require.

With all the technical advancements described above, the structure of the TRPV1 ion channel, a medium sized membrane protein, was solved to a resolution of 3.4 Å.[41] Since then, many other membrane proteins have been determined using cryo-EM including the protease γ-secretase at 3.4 Å resolution,[42] Slo2.2 potassium channel at 4.5 Å resolution,[43] and recently several GPCR-G-protein complex structures were solved at close to 4 Å resolution.[44–47] Although the resolution is in general not as good as that of X-ray crystallography, cryo-EM certainly opens a way to investigate membrane proteins that are difficult to crystallise.

1.3 G protein-coupled receptors

GPCRs are seven-transmembrane proteins which can be activated by interacting with a wide range of extracellular signalling molecules including hormones, neurotransmitters, peptides. Activated GPCRs initiate signalling through classical heterotrimeric G proteins, as well as through G protein-independent pathways by interactions with G protein-coupled receptor kinases (GRKs) and β-arrestins.[48] The human genome encodes nearly 800 GPCRs,[49] and they can be classified into four groups on the basis of

sequence and structural similarity, A: Rhodopsin family, B: Secretin family, C: Glutamate family, and F: Frizzled family.[50] All four groups share the same seven-transmembrane helical architecture. Class B, C, and F have large extracellular N-terminal domains which the class A receptors do not have.[51–53]

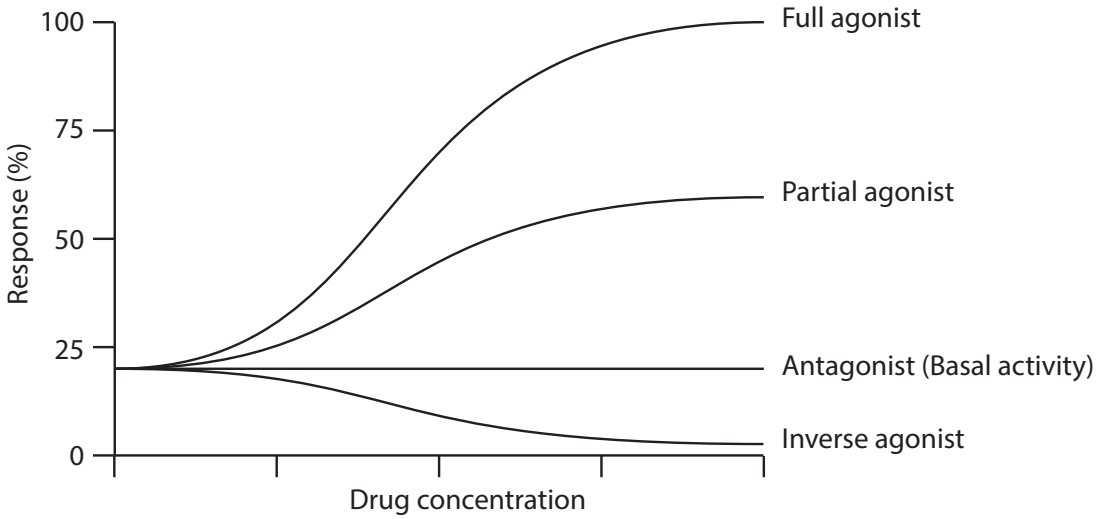

Figure 1-3: Ligand induced biological activity of a GPCR.

GPCRs are involved in a wide range of biological functions including vision, taste, smell, mood regulation, and nervous system transmission. Because of their critical role in physiological functions and high druggability as cell surface exposed membrane proteins, GPCRs represent the target of approximately 34% of all modern drugs.[54] Many GPCRs show basal activity which can be modulated by endogenous ligands or synthetic drugs. For example, β-blockers are synthetic drugs developed to inhibit β-adrenergic receptors for the treatment of arrhythmia, hypertension, and cardiac dysfunction.[55] All the agonists are classified as full agonists, partial agonists, antagonists, and inverse agonists depending on the cellular response (Figure 1-3). By binding to antagonists, the activity of GPCRs remain at the basal level, the same as in the absence of ligand. Antagonists block the binding site and prevent further activation from other ligands. Full agonists activate GPCRs to the maximal signalling response, while partial agonists only partially induce GPCRs. In contrast, inverse agonists reduce the activity of GPCRs below the basal level.

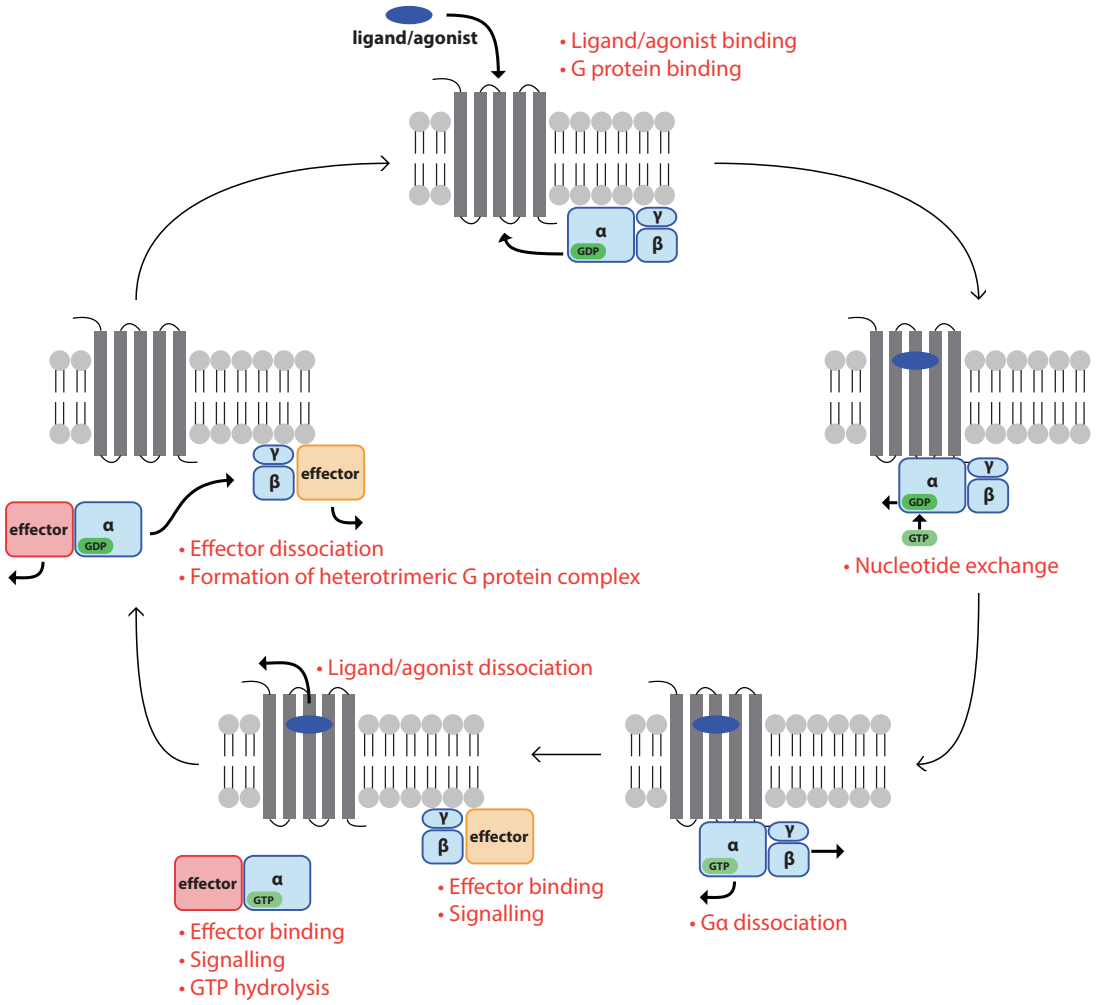

Figure 1-4: Schematic representation of classical GPCR signalling.

Agonist binding to a GPCR leads to G protein binding to GPCR on the intracellular side which induces nucleotide exchange. The GTP bound G_{α} dissociates from $G_{\beta\gamma}$ dimer and both of them can bind to effector proteins for further signalling. Hydrolysis of GTP in the G_{α} subunit leads to reformation of the heterotrimeric G protein complex.

1.3.1 G protein-mediated signalling

The classical GPCR signal transduction pathway involves activation of a heterotrimeric G protein complex. In contrast to the wide variety of GPCRs in the human genome, there are only four G protein families, G_s, $G_{i/o}$, $G_{q/11}$, $G_{12/13}$, identified based on sequence homology.[56] The observation that a limited number of G proteins can be activated by a large number of GPCRs suggests a conserved activation mechanism. G protein-mediated GPCR signalling is outlined in Figure 1-4. The activation process is initiated either by light or binding to activating ligands or agonists, outside the cell

membrane. Upon binding of activating ligands, the receptor undergoes a large conformational change on the intracellular side that enables the GPCR to bind to a heterotrimeric G protein complex (G_α, G_β, G_γ subunits) inside the cell. The GPCR then activates the bound G protein by exchanging the GDP on the G_α subunit for GTP and this exchange triggers the dissociation of the heterotrimeric G protein into its G_α subunit and $G_{\beta\gamma}$ dimer, both of which can interact with other intracellular effector proteins and ultimately modulate cellular responses through secondary messenger downstream signalling. Effector binding may result in hydrolysis of GTP on the G_α via an effector's GAP (GTPase activating protein) activity which allows the reformation of the heterotrimeric G protein complex and completes the signalling cycle.

1.3.2 Structural studies of β_2-adrenergic receptors

So far, a total of 52 unique GPCR structures have been published, 45 of which are class A GPCRs (September 2018, http://gpcrdb.org/structure/statistics). These structures reveal a common seven-transmembrane helical bundle architecture connected by three extracellular loops (ECL 1-3) and three intracellular loops (ICL 1-3) in GPCR family. The N-terminus and the ECLs are responsible for agonist binding whereas the intracellular side and the ICLs recognise G proteins, β-arrestins, and GRKs for downstream signalling. Based on the structures of active and inactive GPCRs, a detailed structural change is observed upon receptor activation. The most common feature of receptor activation is a significant conformational reorganisation on the intracellular side, where a large outward movement of transmembrane helix 6 (TM6) and rearrangements of other helices open a cavity for recognition of G proteins, GRKs, or β-arrestins.

The β_2-adrenergic receptor (β_2AR), a member of β-adrenergic receptor (βAR) family, is a class A GPCR which can activate intracellular heterotrimeric G proteins upon binding to adrenaline or noradrenaline to modulate heart muscle contraction and smooth muscle relaxation. β_2AR is also one of the most structurally characterised GPCRs in the literature, representing 21 out of total 270 available GPCR structures. The crystal structure of human β_2AR was determined more than a decade ago using an engineered β_2AR-T4 lysozyme fusion construct, in which the ICL3 of β_2AR was also removed (Figure 1-5 A, yellow).[57] Fusion with T4 lysozyme increases the hydrophilic surface for more crystal contacts while the removal of ICL3 reduces the flexibility of the protein.

Since then, several crystal structures of β_2AR bound to different antagonists or inverse agonists have been solved.[18,58] However, the crystallisation of full agonist-bound β_2AR was difficult due to the rapid off-rate of the agonist and perhaps the highly dynamic nature of the complex.[59] This difficulty was overcome by using a covalently bound full agonist, which shows the capability of activating a heterotrimeric G protein. The crystal structure of the covalent β_2AR-full agonist complex was solved (Figure 1-5 A, pink),[59] but the structure does not show fully activated states, and in particular, lacks the characteristic outward movement of TM6 that was previously observed in activated rhodopsin.[60,61] Instead, the structures of β_2AR bound to full agonist, antagonist, and inverse agonist overlaid very well and all show the inactive structure (Figure 1-5 A). It was realised that binding to both the extracellular ligand and intracellular binding partner are required to stabilise the active conformation for crystallisation.[59,62] A camelid antibody fragment (nanobody Nb80) was generated to the β_2AR that binds to the intracellular side of β_2AR and shows G protein-like binding behaviour.[62] The structure of the agonist bound, β_2AR-nanobody complex (Figure 1-5 B) shows an 11 Å outward movement of the cytoplasmic end of TM6 that is similar to those observed in rhodopsin activation.[62] Finally, the structure of the full agonist-β_2AR-G_s protein complex (where the G_α subunit is trapped in a non-exchangeable nanobody-bound (Nb35) form that mimics the GDP bound state) was eventually solved, showing an even more significant conformational change, a 14 Å outward movement of TM6 (Figure 1-5 C).[63]

Figure 1-5 (*opposite*): Crystal structures of β_2AR.

A) Overlay of the crystal structures of inverse agonist bound β_2AR (green) (PDB ID: 3NY8), antagonist bound β_2AR (yellow) (PDB ID: 2RH1), and irreversible agonist bound β_2AR (pink) (PDB ID: 3PDS). B) Overlay of the crystal structures of irreversible agonist bound β_2AR (pink) (PDB ID: 3PDS) and full agonist and G protein mimicking nanobody (Nb80) bound β_2AR (blue) (PDB ID: 3P0G). C) Crystal structure of β_2AR (green) in complex with G_s protein (PDB ID: 3SN6). All the components in the complex are coloured and indicated.

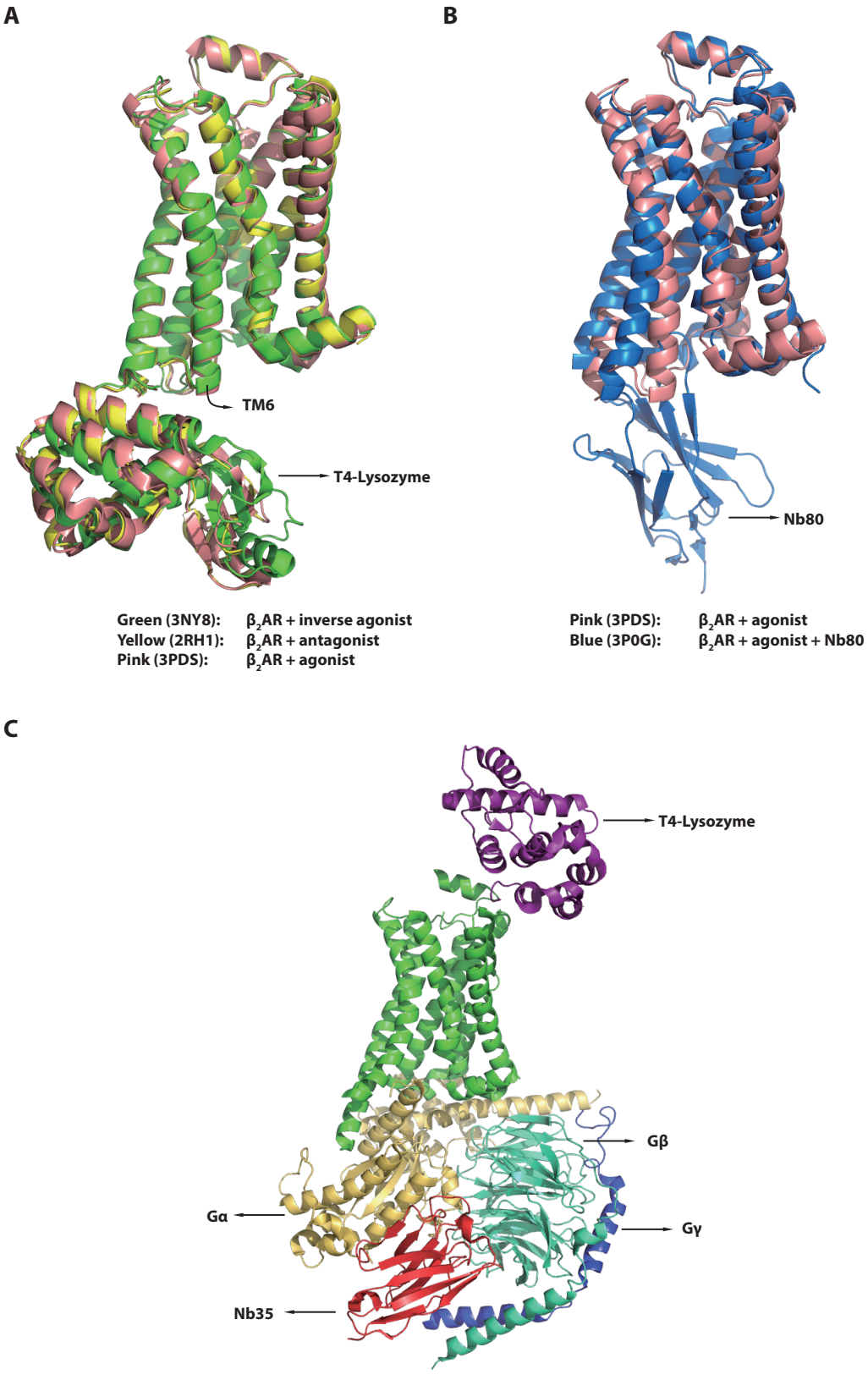

Although crystal structures provide atomic resolution information that helps us understand the inter- and intramolecular interactions in each state, there are still

limitations of this method, e.g. flexible states are invisible in the crystals and only the conformation of the lowest energy state will be revealed. Crystal structures of β_2AR bound to agonist and antagonist show similar conformations which is counter-intuitive. One possible explanation is that X-ray crystallography can only provide snapshots of the most stable state, i.e. the inactive conformation, but not of any conformational ensemble present during the activation. There is no information on the presence of alternative conformations that are energetically less favourable but nevertheless might be substantially populated. Further, detailed mechanistic insight for the activation process of β_2AR between extracellular agonist binding and cytoplasmic G protein recognition has still not yet been obtained.

Nuclear magnetic resonance (NMR) spectroscopy provides a powerful technique to study the dynamics of biological macromolecules over a wide range of timescales from picosecond to days, potentially providing more knowledge about this important question.[64] ^{15}N T_1, T_2 and heteronuclear NOE relaxation experiments are commonly used to investigate protein motion on the ps-ns timescale, with the relaxation rates determined by the internal motions of the amide bonds and the overall tumbling rate of the protein.[64] However, the investigation of GPCR activation using NMR spectroscopy is limited by the large apparent molecular size in the micelle environment making samples prone to signal broadening due to slow overall tumbling. Moreover, GPCRs are α-helical transmembrane proteins, so the amide resonances tend to appear in a relatively narrow chemical shift window. As a result, peak overlap becomes a difficulty in analysing NMR spectra of GPCRs. Also, conventional uniform labelling is only possible and not prohibitively expensive in *E. coli* and yeast protein expression systems which normally are not able to produce functional GPCRs. Selective labelling strategies, instead of uniform labelling, offer one possible solution that can decrease the complexity of the NMR spectrum. In this strategy, only residues of interest are labelled with NMR active isotopes, e.g. ^{13}C, ^{15}N; thus the number of the peaks in the spectrum is considerably reduced.[65]

Several NMR studies of β_2AR using selective isotope labelling strategies have been reported, all aiming to decipher the activation mechanism of the receptor and to observe the activated state that is invisible in crystallography. By monitoring the NMR signals of residue M82 from methionine-labelled β_2AR, a conformational equilibrium between the antagonist-bound and the full agonist-bound states is observed, and the population

of the latter is proposed to reflect the efficacy of the ligand.[66,67] The same model was supported by another ^{19}F NMR study of β_2AR, in which the residue C265 located at the cytoplasmic end of TM6 was labelled with a trifluoroacetanilide probe.[68] Selectively ^{13}C labelled lysine side chains have also been employed to monitor extracellular surface conformations of β_2AR in different states.[69]

1.4 Membrane mimetics

The biggest challenge for *in vitro* studies of membrane proteins is finding a suitable mimic of the native lipid membrane bilayer. The ideal membrane mimetic should be sufficiently stabilising for structural studies and also maintain the protein's biological function and ability for interaction with ligands and other protein partners.[70] Detergents are generally the first choice because they are the most straightforward systems. However, several other mimetics that have a lipid bilayer structure are becoming more popular due to technological advances. Membrane mimetics that are often used in membrane protein studies, namely detergent micelles, amphipols, bicelles, SMALPs, MSP nanodiscs and SapA nanoparticles, are reviewed in the following sections (Figure 1-6).

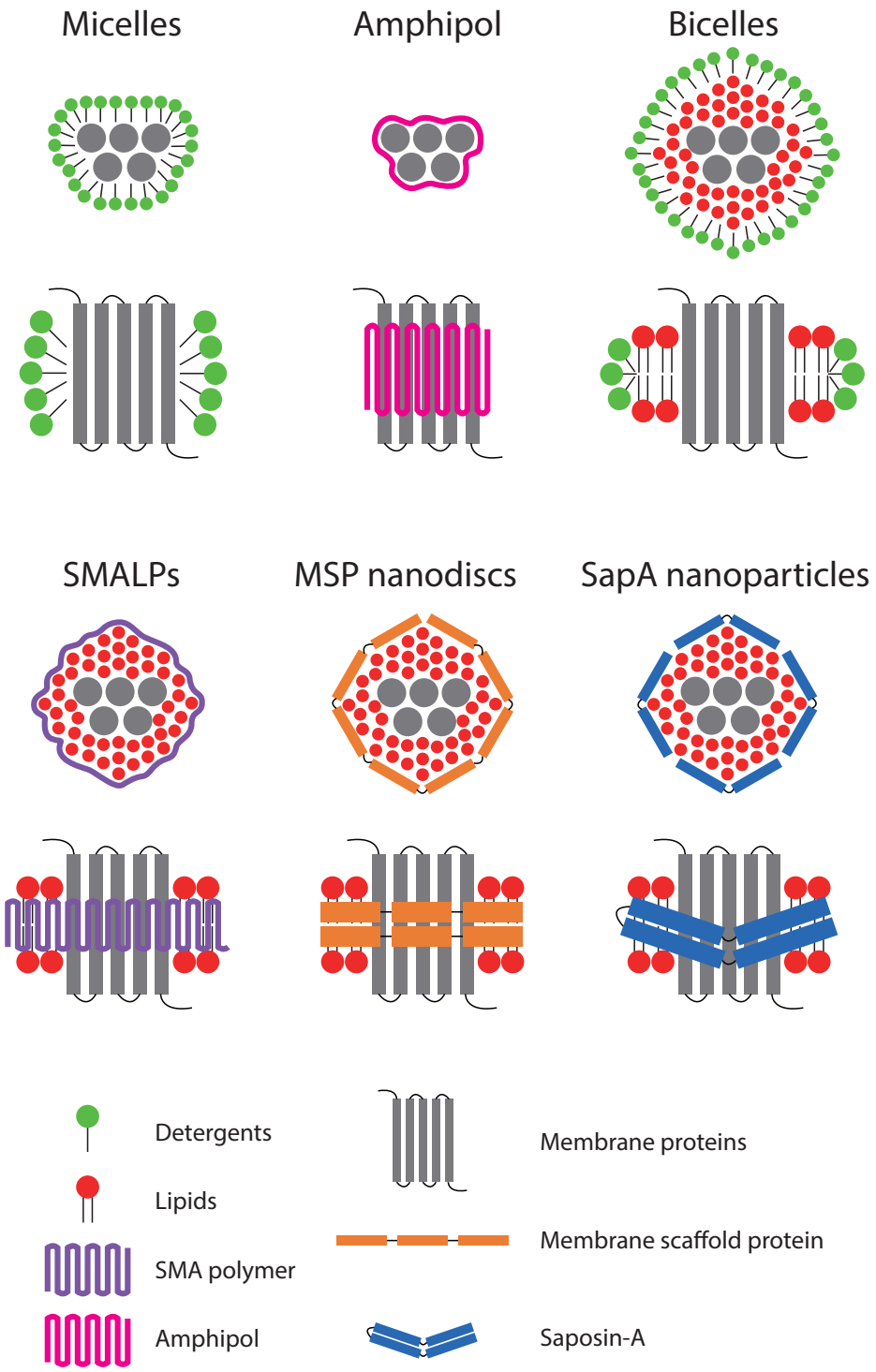

Figure 1-6: Schematic representation of six membrane mimetic systems.

Micelles, amphipols, bicelles, SMALPs, MSP nanodiscs, and SapA nanoparticles are shown in cartoon representation. Top view and side view for each system are shown. Legends for each component are shown at the bottom.

1.4.1 Detergent micelles

Detergents are the most commonly used membrane mimetic for MP characterisation due to the range available, their simplicity of use, and for NMR spectroscopy, the relatively small size of the resulting protein-detergent complex (Figure 1-6).[71,72] Although the use of detergents has contributed a lot to our understanding of membrane proteins' structure and function, there are some drawbacks of using detergents as a membrane mimetic. First, there is no universal rule that can predict which detergent provides the best stabilising environment for a membrane protein that has not been characterised. It requires an extensive and empirical screening process to find a suitable detergent, if any, for each membrane protein of interest. Second, detergents may exhibit denaturing properties and remove native lipid molecules that might be important to a membrane protein's functionality. Therefore, using detergents may interfere with ligand binding and down-stream functional assays,[73] disrupt protein-protein interactions,[74] lack crucial protein-lipid contacts,[75] interfere with protein dynamics,[76,77] and may denature soluble binding partners[78] making it difficult to study signalling across the membrane such as GPCR signalling. Third, detergent micelles are not a very good membrane mimetic either geometrically or physicochemically. Detergent molecules with a single hydrophobic chain form spherical micelles with high curvature which is very different from the native lipid bilayer. In addition, detergent molecules exchange rapidly between micellar and monomeric states, which may produce unfavourable dynamics very different from the native environment.

1.4.2 Amphipols

Amphipols are another membrane mimetic, a class of short amphiphilic polymers developed to keep membrane proteins in the solution without the need for detergents. Amphipols carry a large number of hydrophobic chains that bind strongly to the membrane protein of interest and never dissociate (Figure 1-6). This desirable characteristic allows one to handle membrane proteins without detergent and without free amphipols.[79] Another advantage of using amphipols is the presence of a variety of functional groups on the sidechains which can be utilised for chemical modification or labelling.[80] One of the first amphipols developed, called A8-35,[81] has become the most often used amphipol. A8-35 has a relatively short polyacrylate chain with around 35 acrylate residues. Some of the carboxylates on the acrylate residues are randomly replaced by octylamine (25%) or isopropylamine (40%) making the average molecular

weight of A8-35 around 4.3 kDa. The ~12 remaining acid groups on the acrylate residues remain charged and therefore make the polymer highly soluble in water while the octylamine groups provide a hydrophobic moiety to interact with membrane proteins.

1.4.3 Bicelles

Bicelles are composed of a planar lipid bilayer and detergent molecules to cover the edge of the bilayer (Figure 1-6). The membrane protein of interest would be incorporated into the centre of the bicelles which provides a native-like lipid bilayer environment; therefore bicelles are considered to be a good membrane mimetic. The size of the bicelles is determined by the lipid:detergent ratio (q-ratio). Too low a q-ratio would result in forming a mixed micelle instead of a bicelle, thus losing the desired bilayer structure. A higher q-ratio generates larger bicelles that better mimic the native cell membrane. However, large particle size is not compatible with solution NMR studies because of unfavourable transverse relaxation. In general, q-values of 0.5–0.8 provide a good balance between solution NMR spectral quality and membrane mimicking ability.[82,83] Bicelles are also compatible with X-ray crystallography with q-values in a range 2.2–2.8 commonly used.[84] Many of these structures have been determined to high resolution with an average resolution of 2.5 Å.[84] Despite the promising characteristics of the bicelle system, small amounts of detergent remain in the sample, including free (non-bicelle bound) detergent, which might have the same negative effect as detergent micelles.

1.4.4 Styrene-maleic acid copolymer-lipid particles (SMALPs)

Styrene-maleic acid copolymer (SMA) is amphipathic because it is composed of two components: hydrophobic styrene and charged, hydrophilic maleic acid.[85] There are different ratios of SMA polymers available, and both 2:1 and 3:1 styrene:maleic acid ratios have been successfully used in membrane protein studies.[85] The polymer spontaneously forms discoidal particles with synthetic lipids or biological lipid extracts with a diameter of ~10 nm (Figure 1-6), named Styrene-maleic acid copolymer-lipid particles (SMALPs).[86] The most novel feature of SMALPs is the possibility to directly extract the membrane protein of interest and its associated lipids from a native biological membrane. The proteins in SMALPs can be purified using conventional chromatography without any other additives. This means membrane proteins can be

extracted and purified without ever leaving their original lipid environment. Similar to amphipols, SMA is used for the initial solubilisation step and is not required in the buffers for the remaining purification steps. SMALPs have been proven to be compatible with structural tools including X-ray crystallography,[87] Cryo-electron microscopy,[88,89] and solid-state NMR spectroscopy.[90] Despite the success in many structural studies of membrane proteins using, intolerance of low pH and divalent metal ions significantly limits the applicability of SMALPs. With pK_as of ~6 and ~10 for the two carboxyl groups of maleic acid,[91] SMA is neutralised at low pH, losing its hydrophilic property, and therefore precipitates out of solution. A similar principle is that the carboxyl groups interact with divalent cations through electrostatic interactions, which also causes SMA precipitation.[86] This limits the application of SMALPs in membrane proteins that require cofactor ions such as Mg^{2+}. As solution NMR spectroscopy prefers a low pH due to backbone amide proton exchange, using SMALPs in NMR studies needs to be performed within a narrow pH range of 6.8–7.5.[92] Several researchers are developing alternative copolymers that have the same ability as SMA but with improved buffer compatibility.[93–96]

1.4.5 MSP nanodiscs

The nanodisc system was developed recently by Sligar and co-workers.[97] These disc-like particles consist of a small patch of phospholipid bilayer enclosed by two belt-like membrane-scaffold proteins (MSPs),[97] with the MP of interest incorporated into the centre of the discs, making it a native-like lipid bilayer suitable for MP characterisation (Figure 1-6).[98] MSPs are engineered amphipathic helical proteins derived from human apolipoprotein A-I which originally has a specific function in lipid metabolism.[97] The first version of MSP was called MSP1, with the N-terminal globular domain of apolipoprotein A-I truncated.[97] MSP1 nanodiscs are about 9.7 nm in diameter. Several extended or truncated MSP constructs were designed by changing the length of the amphipathic helical part of the MSP.[99] One, two, or three additional 22-amino acid amphipathic helices were inserted into MSP1, creating MSP1E1, MSP1E2, and MSP1E3 proteins respectively, resulting in nanodiscs with a diameter of 10.4 nm, 11.1 nm, and 12.0 nm respectively.[99] MSP1D1, with the first 11 amino acids of MSP1 deleted, generates nanodiscs with a diameter of 9.5 nm.[99] In order to make even smaller nanodiscs for solution NMR studies, further truncations were designed including MSP1D1ΔH5 (9.2 nm), MSP1D1ΔH4 (9.1 nm) and MSP1D1ΔH4H5 (7.8 nm), without

MSP1D1 helix 5 and/or 4 respectively.[77] With all these MSP variants developed, the MSP nanodisc system has become a complete tool set for studying different sizes of membrane proteins.

Nanodiscs seem to be generally applicable regardless of the type of protein and are widely used as a detergent-free environment; more than 800 papers using the key-words "Nanodisc-membrane protein" were returned in a literature search.[100] The broad range of applications involves structural studies, analytical and functional studies, biotechnology and medical applications.[98] The suitability of the MSP nanodisc system for solution NMR has been demonstrated,[101,102] along with the functional relevance of lipid bilayer mimetics demonstrated for conformational equilibria of receptors and ion channels.[103–105] More detailed developments and applications of the nanodisc technology for NMR studies will be reviewed in Chapter 3.

1.4.6 Saposin A lipid nanoparticles

There are other apolipoproteins or peptides available that can be used as scaffold proteins to form disc-like lipid particles.[106–108] Among all the reported scaffold proteins, saposin A (SapA) is arguably the most promising system because of its size adaptability. Instead of a belt-like arrangement of MSPs, multiple SapA molecules interact with the exposed hydrophobic surface of the lipid bilayer (Figure 1-6), therefore the size of the resulting particles is determined by the number of SapA molecules surrounding them. This characteristic makes SapA an attractive tool that could potentially be a universal system which is able to accommodate different sizes of membrane proteins.

The idea of using SapA as an alternative membrane scaffold protein was first realised in a cryo-EM study where an archaeal mechanosensitive channel T2 (32.9 kDa), which is a putative homopentamer, and a bacterial homotetramer peptide transporter $PepT_{So2}$ (56 kDa) were both incorporated into SapA lipid nanoparticles at pH 7.4.[109] In the case of the $PepT_{So2}$, it was significantly more stable in the SapA lipid nanoparticles than when in nonyl-β-D-maltopyranoside detergent micelles, resulting in a 29 ºC increase in melting temperature. This study yielded a single-particle cryo-EM structure of $PepT_{So2}$ with a resolution of 6.5 Å. The crystal structure of the transporter $PepT_{So2}$ could be docked into the EM density. However, the electron density of four SapA molecules could only be observed at a lower isosurface level probably due to their high flexibility. This study demonstrated that SapA lipid nanoparticles can be used as a membrane mimetic to study 150–200 kDa membrane proteins with cryo-EM, providing a

stabilising, native-like lipid bilayer in a detergent-free environment. This study also demonstrated direct solubilisation of HIV-1 spike protein from the membrane of virus-like particles using SapA. Another detailed protocol for reconstitution of sarco-endoplasmic reticulum calcium ATPase into SapA lipid nanoparticles was reported.[110]

It was also reported in the literature that SapA is the least lipid specific of the four human saposins.[111] This makes SapA lipid nanoparticles the perfect membrane mimetic because it can be used to study membrane proteins in various lipid compositions. Four membrane proteins containing 14 to 56 transmembrane α helices were successfully reconstituted in to SapA lipid nanoparticles and studied using small angle X-ray scattering.[111] Overall, SapA lipid nanoparticles seem to be a versatile tool for membrane protein studies.

1.5 Aims

Solution NMR spectroscopy is a powerful tool which provides valuable information about the conformation and dynamics of membrane proteins. In addition, it is clear that the lipid bilayer environment is important for membrane protein structure and functions. Therefore a membrane mimetic system that faithfully mimics the native membrane and is compatible with solution NMR spectroscopy is needed in the membrane protein field. The MSP nanodisc system, well established and verified in many NMR studies, fits the criteria. However, the incorporation procedure in MSP nanodiscs needs intensive screening for the optimal condition and the yield is generally low. An alternative bilayer membrane mimetic that overcomes these barriers would be welcome. The newly developed SapA lipid nanoparticle system seems very promising with several advantages over conventional MSP nanodiscs. The promising size flexibility of this system enables us to study membrane proteins with different sizes using the same SapA scaffold protein and should be applicable to a wide range of membrane proteins. Despite its promising properties, this is a relatively new approach and its applicability to other structural tools such as NMR spectroscopy still remains unclear. We hoped to expand the applicability of SapA lipid nanoparticles to investigate small-to-medium sizes of membrane proteins using NMR spectroscopy. Therefore, my PhD thesis focuses on the application of the SapA system in membrane protein studies using NMR spectroscopy.

In order to design a protocol that can be used to incorporate membrane proteins into SapA lipid nanoparticles, we must first understand the formation mechanism. This will be discussed in Chapter 2. With the knowledge of how these particles are formed in

hand, the suitability of using SapA lipid nanoparticles as a membrane mimetic will be explored in Chapter 3. A β-barrel model protein is used to confirm that SapA lipid nanoparticles really provide a lipid bilayer environment. Next, α-helical membrane proteins in SapA lipid nanoparticles will be explored in Chapter 4 using microbial rhodopsins. Finally, the ultimate goal is to combine the SapA system with NMR spectroscopy to study biologically important membrane proteins. In Chapter 5, the β_1-adrenergic receptor, a GPCR, will be incorporated into SapA lipid nanoparticles and conformational changes in the receptor will be monitored using NMR spectroscopy.

2 MECHANISM OF SAPOSIN A LIPID NANOPARTICLE FORMATION

2.1 Introduction

2.1.1 Biological function of sphingolipid activator proteins

SapA is a member of the family of sphingolipid activator proteins (SAPs) which are non-enzymatic proteins participating in the breakdown of certain sphingolipids in the lysosome.[112] Five SAPs are found in human lysosomes: GM2 activator and saposins A, B, C, D.[113] The four saposins are proteolytic cleavage products from a single precursor molecule prosaposin.[114] In the absence of saposins, lipid degradation is completely disrupted.[115] The function of the four saposins is different as they interact with a specific hydrolase and cannot compensate for the loss of other saposins,[116,117] therefore causing different diseases. Accumulation of galactosylceramide was found in saposin A (SapA) mutated mice.[118] Loss of functional SapA in humans results in Krabbe disease, a rare and fatal disease which progressively damages the nervous system.[119] Loss of saposin C (SapC) causes Gaucher disease, a rare autosomal recessive lysosomal storage disorder.[120]

It has been proposed that saposins act as a 'solubiliser' that completely extracts lipids out of the membrane and presents them to glycosyl hydrolases.[121] For example, the crystal structure of SapA and the β-galactocerebrosidase heterotetramer shows how a soluble hydrolase can cleave the polar glycosyl headgroups from their hydrophobic tails

with the help of SapA.[121] On the contrary, other saposin-like proteins function in a 'liftase' model that improves lipid accessibility by membrane distortion, destabilisation or localised remodelling for degradation to take place on the membrane. Acid sphingomyelinase (ASM) is believed to be in this category.[122–124] It is composed of a N-terminal saposin domain, a proline-rich linker, and a catalytic domain. In acidic conditions, ASM is positively charged and subsequently binds to negatively charged membranes which contain bis(monoacylglycerol)phosphate. The saposin domain could open up and expose its hydrophobic surface to the membrane. This would cause a local disruption of lipid packing and allow the substrate headgroup to enter the enzyme active site.[124]

2.1.2 The structure of SapA and its interaction with lipids

The crystal structure of SapA, a 9.2 kDa protein, in its apo form was solved to a 2.0 Å resolution,[125] revealing a general saposin fold that comprises three pairs of disulphide bonds holding four amphipathic α-helices together (Figure 2-1 A).[125] Helices 2 and 3 are disulphide linked to form the first segment, a helical hairpin, whereas two disulphide bonds hold helices 1 and 4 together to form the second segment. The conserved hydrophobic residues point inward holding the two segments together, while the non-conserved charged residues are located on the surface. This typical saposin fold is shared with all the other saposin-like proteins. This is later defined as the closed conformation.[126]

SapA has been observed to form 35–45 kDa particles, hereafter called SapA lipid nanoparticles, in the presence of liposomes of varying lipid composition or several non-denaturing detergents at pH 4.8.[126] Although the crystallisation of SapA with lipids was not successful, a crystal of detergent Lauryldimethylamine-N-Oxide (LDAO)-bound SapA was obtained and the model was refined to 1.9 Å resolution.[126] The structure revealed an open form, in which the two segments of SapA open up into a V shape with an angle of 115º (Figure 2-1 B,C). Two open SapA molecules hold the LDAO minibilayer, composed of 40 LDAO molecules, in the middle.[126] Notably, the two V-shaped SapA are in an asymmetric manner in which the first segment of one SapA is close to the second segment of the other one, hence a head-to-tail arrangement. Moreover, no saposin-saposin contacts were observed in the crystal structure, indicating the particle is held together entirely by the hydrophobic interaction between detergents and SapA. With these characteristics, unlike the continuous belt-like MSP nanodiscs

that were discussed in Chapter 1, SapA has the potential to form lipid nanoparticles of various sizes by altering the number of SapA molecules per nanoparticle. Compositions of SapA lipid nanoparticles at different pH values have been explored using electrospray ionization mass spectroscopy and multiangle laser light scattering.[127] SapA-POPC nanoparticles were predominantly $SapA_2$-$POPC_{23-29}$ at pH 4.8, but were $SapA_4$-$POPC_{37-60}$ at pH 6.8. However, $SapA_4$-$POPC_{37-60}$ species at pH 6.8 were found to be unstable and converted to $SapA_3$-$POPC_{29-36}$ over a period of hours.

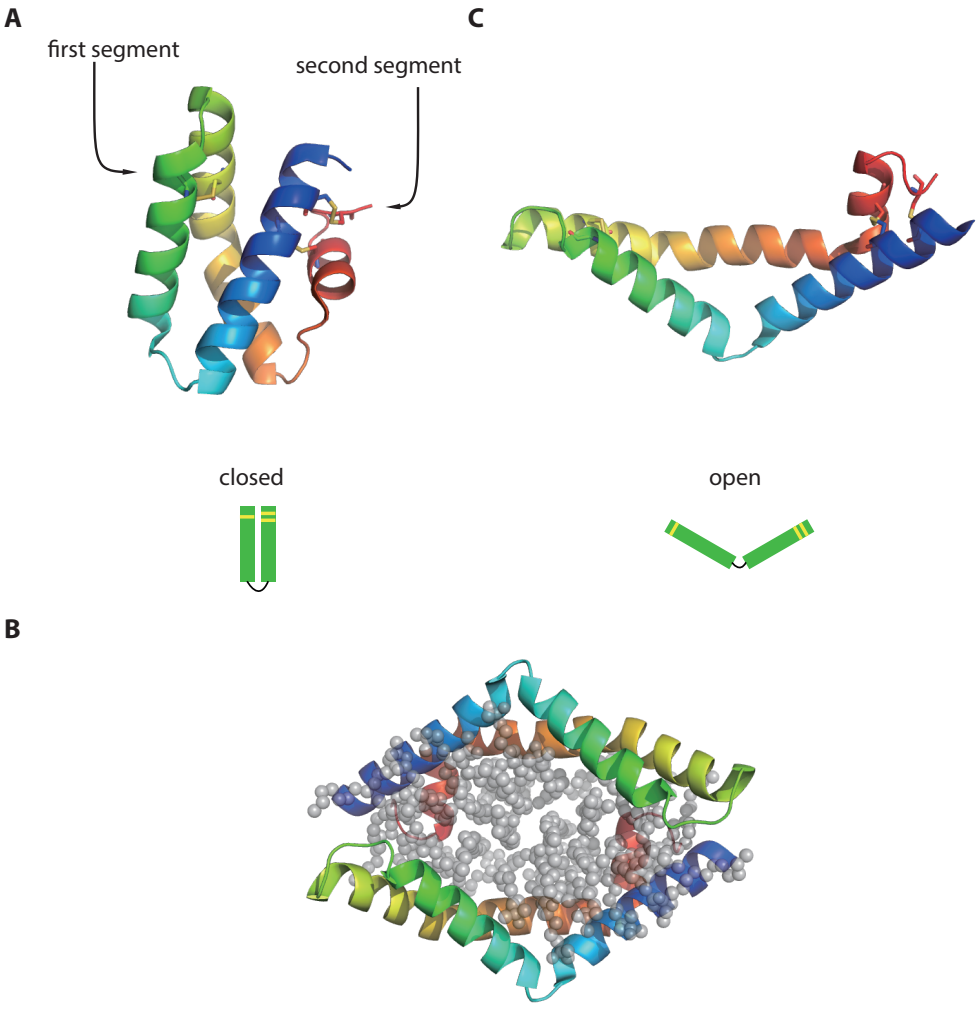

Figure 2-1: Crystal structures of SapA.

SapA in A) closed form (PDB: 2DOB) and in B) open form (PDB: 4DDJ) when bound to detergent LDAO shown in grey spheres. C) The monomer SapA in open form extracted from the aforementioned PDB structure in B) for comparison with the closed form. The disulphide bonds are shown in yellow sticks. The cartoon representations are shown at the bottom.

The size flexibility of SapA lipid nanoparticles is a very attractive characteristic for a membrane mimetic system. Membrane proteins with different sizes could be incorporated into SapA lipid nanoparticles using a single scaffold protein, SapA. This would be advantageous over the conventional MSP nanodisc system, because it would no longer be necessary to screen multiple scaffold protein constructs. However, the requirement of low pH significantly limits the potential of SapA because most membrane proteins would not be stable in this extreme environment. This limitation was overcome later.[109] It was shown that SapA lipid nanoparticles can be generated at physiological pH 7.4 using DDM-solubilised lipids.[109] Although the role of DDM in SapA lipid nanoparticle formation at neutral pH was not explored in this paper, it significantly extended the applicability of the SapA lipid nanoparticles in the membrane protein field.

2.1.3 Aims

Using SapA lipid nanoparticles as a membrane mimetic system was discussed in section 1.4.6. This approach has the advantage of size adaptability that can accommodate 150–200 kDa proteins and has resulted in cryo-EM structures of membrane transporters.[109] Inspired by this previous work, we hoped to use SapA to stabilise small to medium size membrane proteins in solution for NMR studies. Preliminary investigations demonstrated that using DDM solubilised lipids can bypass the low pH requirement for SapA opening,[109] enabling a wider application as a membrane mimetic. However, the detailed mechanism of how DDM promotes SapA lipid nanoparticle formation at neutral pH remains unexplored. In order to fully utilise the potential of this system, we aimed to further understand the mechanism of SapA opening at different pH values. Therefore we explored the relationship between SapA, lipids, and DDM in various conditions, with the intention of establishing a defined protocol for making SapA lipid nanoparticles. The size flexibility and the ability of SapA to interact with various lipid compositions are also investigated in this chapter. The work presented in this chapter lays a foundation for further development of the incorporation of a membrane protein of interest in later chapters.

2.2 Results and discussion

2.2.1 Expression and purification of SapA

In order to maximise the yield of SapA production, expression conditions and the purification protocol were screened and optimised. Since SapA contains three pairs of disulphide bonds, a SHuffle® T7 competent cell (New England Biolabs; a kind gift from the Hyvönen group, University of Cambridge, Biochemistry Department) was used for protein expression. This strain is a derivative of *E. coli* K12 cells, engineered to promote disulphide bond formation in the cytoplasm. We tested two temperatures (37 ºC and 30 ºC) for growing SHuffle® T7 cells and two for protein expression after IPTG induction (30 ºC and 16 ºC). The cells were lysed using BugBuster® (Merck) and the SapA expression level was checked by SDS-PAGE (Figure 2-2). The result showed that 30 ºC in the cell-growing phase slightly increased the SapA yield when compared to that at 37 ºC, while low temperature during the protein production phase seemed to be essential for optimising the yield. Therefore, initial cell growth at 30 ºC followed by growth at 16 ºC after induction was chosen for the final protocol.

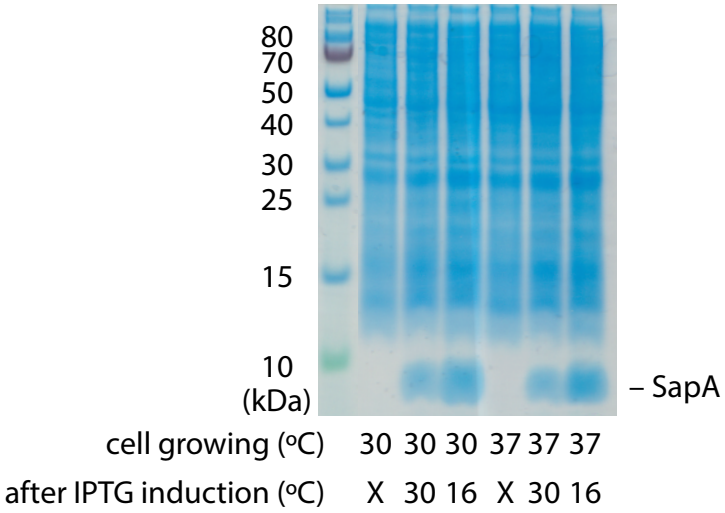

Figure 2-2: Screening optimal condition for SapA expression.

SHuffle® T7 cells containing SapA plasmid were grown in one mL LB culture at the indicated temperature for four hours before the addition of 1 mM IPTG and incubation at the indicated temperature for another two hours. Cells were lysed using BugBuster® (Merck) and checked by SDS-PAGE.

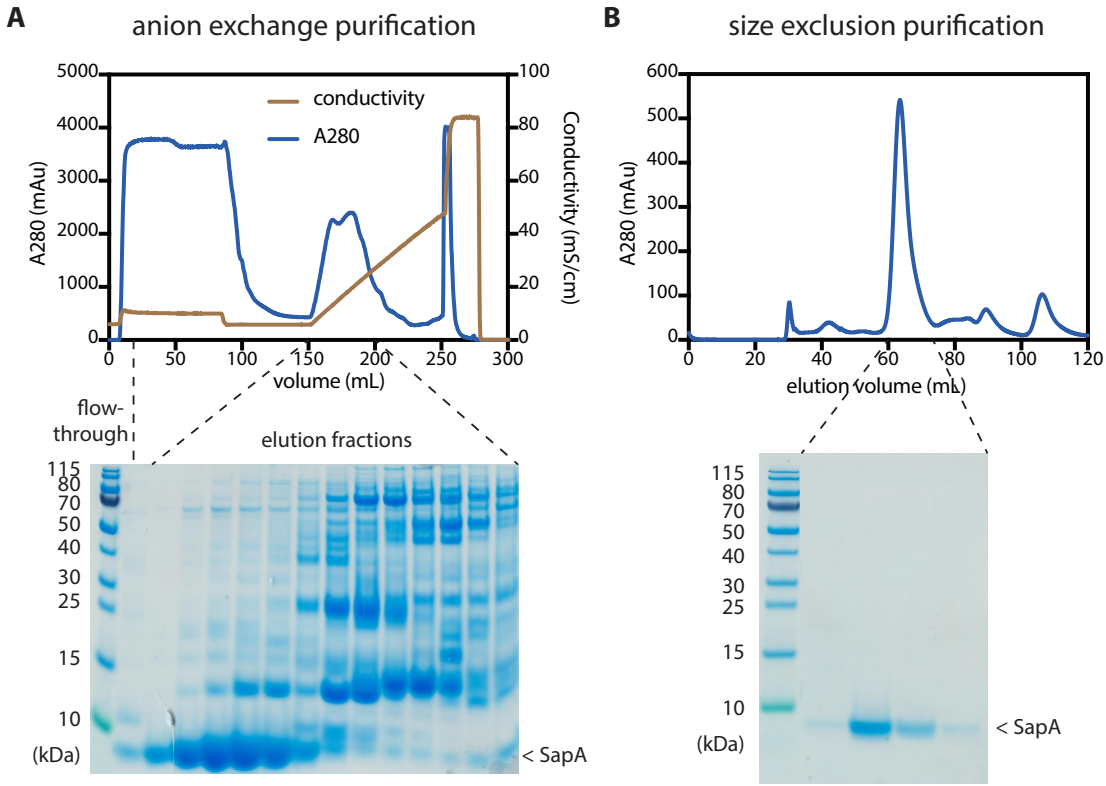

Figure 2-3: Chromatography purification of SapA.

Cell lysate containing expressed SapA was purified by A) anion exchange chromatography followed by B) size-exclusion chromatography. SDS-PAGE analysis of the corresponding fractions is shown at the bottom.

In order to purify SapA, we adopted a protocol reported previously (discussed in more detail below).[128] The SapA construct we used did not contain a purification tag because a heating step, an anion exchange (AEX) chromatography, and a size-exclusion chromatography (SEC) were sufficient to produce pure SapA. In addition, we preferred to use scaffold proteins that did not possess an affinity purification tag so that membrane protein incorporated in the lipid nanoparticles could be separated from empty lipid nanoparticles using an affinity tag on the target membrane protein. The first purification step after cell lysis was a 85 ºC incubation to precipitate out most of other proteins. This was only possible because SapA, with three pairs of disulphide bonds, is a very stable protein. This step produced a lysate that was sufficiently clean for further purification. The next step involved AEX chromatography (Figure 2-3 A). SapA, with a pI of 4.2, is negatively charged therefore should bind to an AEX column. It is worth mentioning that the capacity of a 5 mL HiTrap QSepharose column (GE Healthcare) was only able to purify lysate from 3 L culture at most. It can be clearly observed from SDS-PAGE analysis that there was still SapA in the flow-through fractions when lysate

from 6 L culture was loaded on the column (Figure 2-3 A). This was probably due to all the other impurities and residual DNA fragments that were able to bind to the AEX column competing with SapA, as suggested by the many other protein bands in the SDS-PAGE gel. The elution fractions from the AEX column were checked by SDS-PAGE, and the fractions containing SapA were pooled and concentrated down to 1 mL, followed by a SEC purification step using a HiPrep Sephacryl S-200 column (GE Healthcare) (Figure 2-3 B). The final sample purity was higher than 95% judging from SDS-PAGE and the yield was approximately 10 mg/L culture in general.

2.2.2 Mechanism of SapA lipid nanoparticle formation

It has been shown that SapA can interact with liposomes at pH 4.8 to form disc-like particles,[126] but n-Dodecyl β-D-maltoside (DDM) is required to achieve the same at pH 7.4.[109] However, the role of DDM in SapA lipid nanoparticle formation remains elusive. If the presence of DDM is solely to increase the solubility of the lipid, this would not explain why it is not necessary at lower pH. Therefore, we hypothesised that the pH can regulate the interaction between SapA and lipid molecules and the presence of DDM effectively achieves the same as acidic pH. In order to reduce the variables in the system, we designed experiments to look at only two parameters at a time. We first investigated the interactions between SapA and DMPC, a model lipid often used in nanodisc systems, at various pH values. We also performed experiments to confirm the potential interactions between SapA and DDM at neutral pH.

We first characterised SapA in its apo form at pH 7.4 using analytical SEC. The peak eluted at 17.5 mL corresponding to 17 kDa (Figure 2-4 A, red). This species was probably dimeric, as monomeric SapA has a molecular weight of 9.2 kDa, and in closed form based on the available structural information for SapA.[126] Next, SapA was incubated with DMPC solution, which remained cloudy due to low solubility without detergents, in different pH buffers at 37 ºC for 10 min and the resulting particles were analysed by size-exclusion chromatography (Figure 2-4 A). Most of the SapA at pH 6 and pH 7.4 remained the same size as in the apo form, indicating that SapA remained in a closed conformation under these conditions and was not able to recruit DMPC to form nanoparticles (Figure 2-4 A, green and blue). On the contrary, SapA-DMPC nanoparticles with a molecular weight of 37 kDa, consistent with the value reported previously,[126] were observed at pH 4.8 (Figure 2-4 A, purple). Interestingly, a negative control experiment that included apo SapA at pH 4.8 showed that SapA crashed out of

solution in the absence of DMPC (Figure 2-4 A, inset). This data suggests that acidic pH values destabilise SapA and the presence of DMPC compensates for this destabilisation by forming SapA-DMPC nanoparticles.

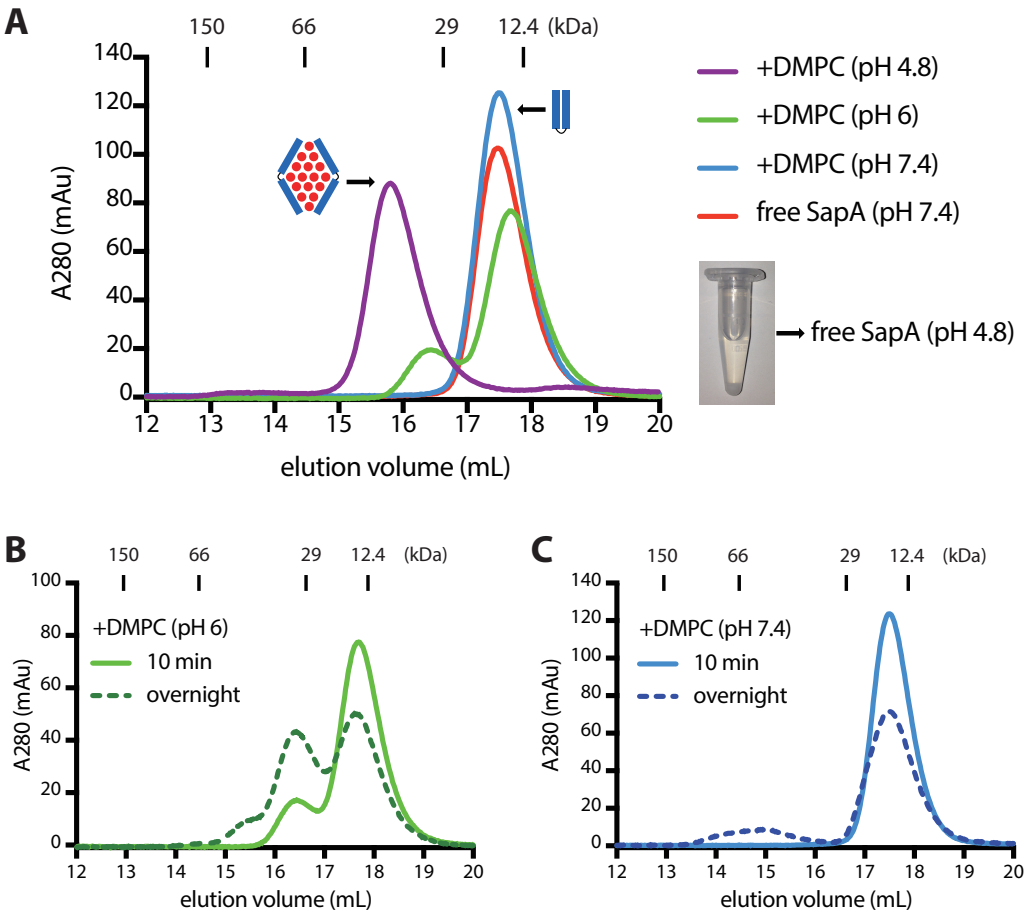

Figure 2-4: SEC of SapA and the mixture of SapA and DMPC at various pH.

A) Free SapA in the absence of DMPC at pH 7.4 (red), after incubation with a 10-fold molar ratio of DMPC at pH 7.4 (blue), pH 6 (green), and pH 4.8 (purple). Molecular weight standards are indicated above in kilodaltons. The proposed SapA conformation is indicated next to the peak. Precipitated SapA at pH 4.8 is shown in the inset photograph. Incubation time of 10 min (solid line) and overnight (dashed line) are compared for B) pH 6 and C) pH 7.4.

Although SapA at pH 6 and pH 7.4 seemed unable to form SapA-DMPC nanoparticles, we found that the process was actually time-dependent. If the samples were incubated at 37 ºC overnight, instead of 10 min, more nanoparticles were observed as the peak at around 16.5 mL for pH 6 and a broad peak at 15 mL for pH 7.4 increased with longer incubation time (Figure 2-4 B,C). This result indicates that the presence of a kinetic

barrier makes the formation of SapA lipid nanoparticles extremely slow, and therefore SapA lipid nanoparticles cannot be observed in a reaction time as short as 10 min. This also shows that the SapA lipid nanoparticle state remains energetically favourable as it still formed spontaneously over time.

With all the data together, we hypothesised that there is a kinetic barrier prevents the formation of SapA-DMPC nanoparticles. Low pH environments destabilise the closed form, possibly by opening up SapA, causing either recruitment of DMPC to form SapA-DMPC nanoparticles or insolubility, due to intermolecular interactions, in the absence of lipids.

Next, we investigated the interaction of SapA with DDM at pH 7.4. The idea was to check if DDM, which, unlike lipids, is soluble in water, could encourage the opening of SapA at pH 7.4. We observed a significant peak shift in size-exclusion chromatography indicating the formation of a stable SapA-DDM complex with a molecular weight of 30 kDa (Figure 2-5 A). The introduction of DDM induces a different conformation of SapA which forms a particle larger than the closed conformation (17 kDa) and smaller than the fully open conformation observed in SapA-DMPC nanoparticles at pH 4.8 (37 kDa).

The SapA-DDM sample together with the SapA-DMPC nanoparticles at pH 4.8 and the apo SapA sample were further characterised using intrinsic fluorescence (Figure 2-5 B) and 1D proton NMR (Figure 2-5 C). A significant blue-shift and increased intensity in intrinsic fluorescence for SapA lipid nanoparticles can be observed (Figure 2-5 B) and this is consistent with previous observations in the literature.[126] Based on the crystal structure of the closed and open forms of SapA in the literature (Figure 2-5 D), the only tryptophan in SapA should be completely solvent exposed in the closed form, but buried in the lipid bilayer in the open form. Therefore, any observed changes in intrinsic fluorescence should correlate with the opening of SapA. Interestingly, SapA-DDM (Figure 2-5 B, green) showed a characteristic fluorescence signal in between those of closed SapA and SapA-DMPC nanoparticles. We propose that SapA adopts an open-like conformation in complex with DDM at pH 7.4. This suggestion is supported by 1D ^{1}H NMR spectra, which show a trend of downfield shift of the tryptophan side-chain signal indicated by * in Figure 2-5 C from apo SapA to SapA-DDM to SapA-DMPC. This downfield shift is probably due to movement into a more hydrophobic environment, consistent with the observation in the intrinsic fluorescence data (Figure

2-5 B). There are two tryptophan side-chain peaks in the SapA-DDM spectrum and both of them shift downfield compared to the spectrum for apo SapA. It is unlikely that one of them corresponds to apo SapA because the peak position and the peak width are very different from that in the apo SapA spectrum. Therefore, these results suggest that the tryptophan residue exchanges slowly between two conformations in the SapA-DDM complex. The broader linewidth of the Trp signal observed in the SapA-DDM complex is in line with the generally broader lines of signals from the amide backbone as would be expected due to the increased molecular weight of the detergent bound protein. We also observed different 1D NMR profiles in the amide region (6–10 ppm) in all three samples indicating different conformations of SapA in these conditions. Peaks became broader following the trend of apo SapA, SapA-DDM, and SapA-DMPC due to a larger particle size, which is consistent with the SEC data. Overall, all our data suggests that SapA is able to form an open-like conformation in complex with DDM at neutral pH.

Figure 2-5 (*opposite*): Biophysical characterisation of free SapA, SapA-DDM, and SapA-DMPC nanoparticles.

Free SapA (blue), SapA-DDM (green), and SapA-DMPC nanoparticles (red) were analysed using A) analytical size-exclusion chromatography, B) intrinsic fluorescence spectroscopy using an excitation wavelength of 280 nm, and C) 1D ^{1}H NMR spectroscopy. Tryptophan indole proton signals are indicated by *. D) Crystal structures of SapA in apo form (PDB: 2DOB) and LDAO-bound form (PDB: 4DDJ). Tryptophan residues are shown in spheres.

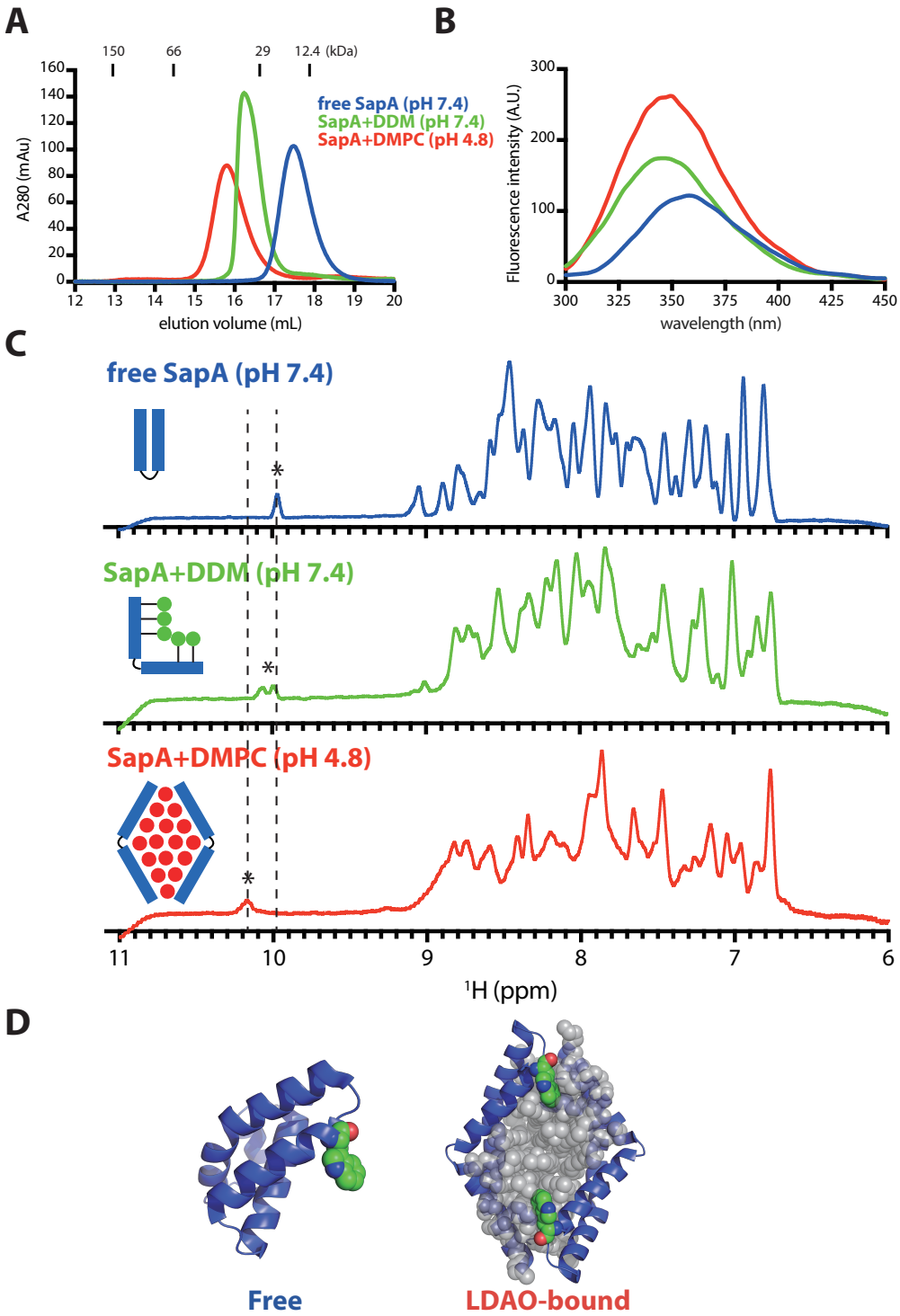

Figure 2-6 A shows an illustrative free energy diagram to summarise our observations. A high free energy barrier separates the closed form of SapA from the transition state, the open form of SapA at pH 7.4, which slows down the formation of SapA lipid nanoparticles dramatically (Figure 2-6 A, blue). When SapA is in an acidic environment, the closed conformation of SapA is destabilised (Figure 2-6 A, red). This effectively removes the energy barrier, thus SapA interacts with lipids and forms nanoparticles

spontaneously in a short period of time. We think that the open form of SapA is a transition state that is not stable without other hydrophobic molecules. This model also explains the observation of SapA precipitating when incubated with pH 4.8 buffer. The acidic pH forces SapA to open, exposing the hydrophobic surface, therefore SapA aggregates and precipitates. On the other hand, SapA spontaneously interacts with DDM and forms a stable open-like conformation as an intermediate state (Figure 2-6 B green). This effectively lowers the energy barrier at neutral pH, allowing efficient formation of SapA-DMPC nanoparticles. However, detergent removal becomes important if this route is used to generate SapA-DMPC nanoparticles because there would be a mixture of side products such as open-like SapA, mixed micelles, and potentially nanoparticles with mixed DMPC and DDM.

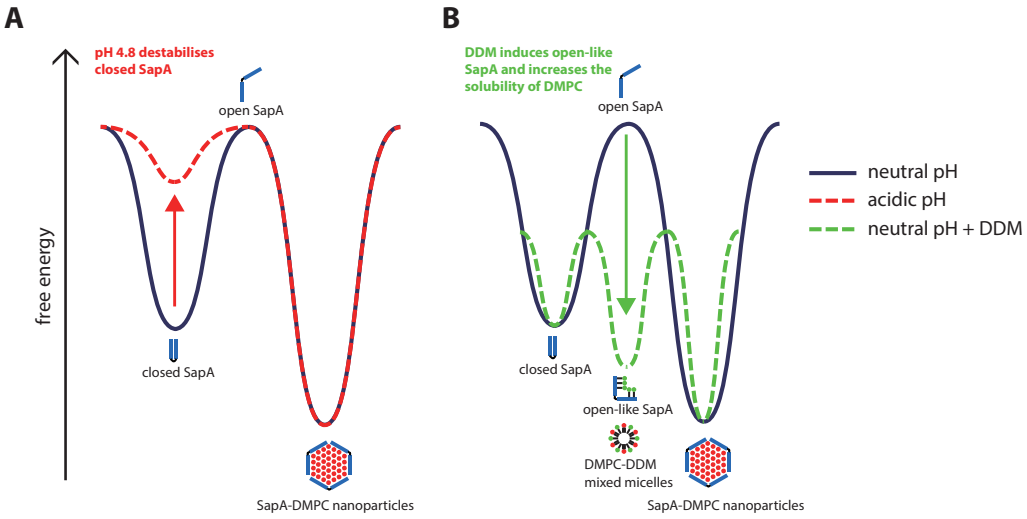

Figure 2-6: Proposed free energy diagram of SapA-DMPC nanoparticle formation.

The reaction at neutral pH (dark blue) shows two stable states: closed SapA and SapA-DMPC nanoparticles. A) Acidic pH destabilises the closed form. B) DDM induces a stable intermediate state containing open-like SapA and DMPC-DDM mixed micelles.

During the preparation and characterisation of free SapA without detergents and lipids, we found that sequential size-exclusion chromatograms of the same apo SapA sample showed different profiles. We observed not only the usual apo SapA peak at around 17.5 mL but also a larger particle, which eluted at around 16 mL. However, the second peak decreased when we ran the same sample again and almost disappeared in the third run (Figure 2-7). This irreproducibility indicates that the results, instead of showing the properties of the sample, were affected by the variables introduced during the

experiments. This phenomenon was only observed after the column was used by other group member using a buffer that contained detergent. Therefore, we think the peak at around 16 mL must correspond to SapA in complex with the residual detergent molecules left in the column, which essentially are 'cleaned' from the column after two SapA runs. This data shows that even when the column was washed and equilibrated with large volumes of water and buffer, detergent molecules can still remain in the column. It also demonstrates that the interactions between SapA and detergents are strong.

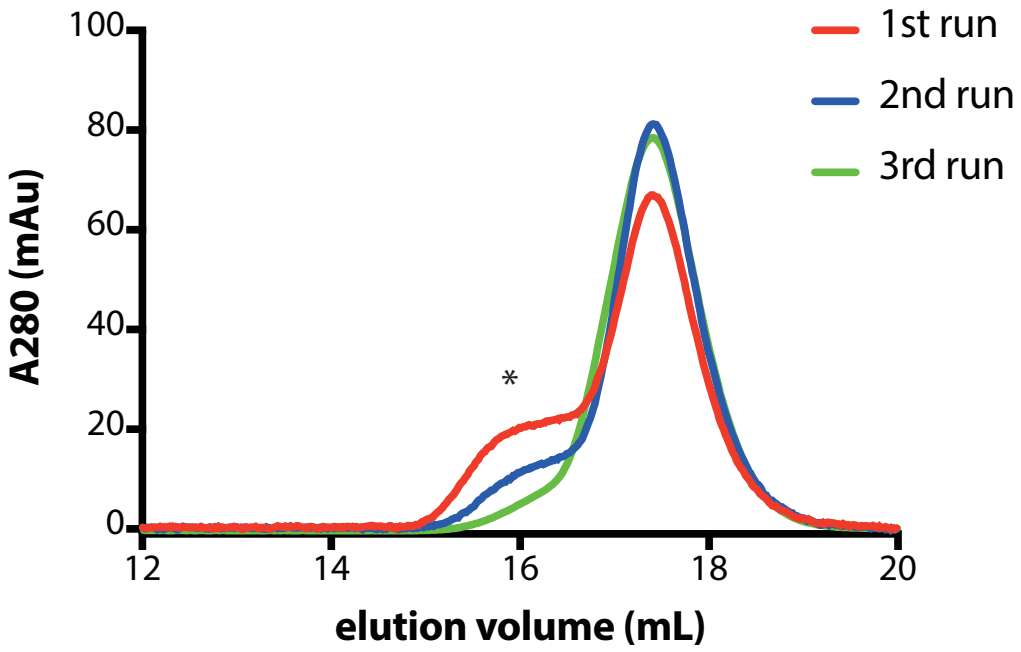

Figure 2-7: Sequential SEC of the same SapA sample.

Same SapA samples with 120 μM concentration were loaded to the S200 10/300 column that was previously used with a detergent buffer. The putative SapA-detergent complex is indicated by *.

2.2.3 Detergent removal by Amberlite XAD2 beads

We have established that DDM is required for making SapA lipid nanoparticles at non-acidic pH. However, the detergents must be removed completely during the formation of SapA lipid nanoparticles to rule out the formation of mixed detergent-lipid nanoparticles. We also observed strong binding of detergents to SapA, indicating that even a small amount of residual detergent can be picked up by SapA (Figure 1-7). With these data, we suspected it would be difficult to remove detergents using passive

methods such as dialysis or dilution and concentration. A proactive detergent binding method that could compete with SapA would therefore be necessary to remove detergents efficiently. We decided to test a detergent absorbent widely known as Bio-beads, which are frequently used in the well-established nanodisc technology.[129]

We used Amberlite XAD2 beads (Merck) as the detergent absorbent. In order to confirm the performance of this material before applying it to our system, the efficiency of DDM and LMNG removal by Amberlite XAD2 beads was investigated. We focused on these two detergents because they are most frequently used in our laboratory for membrane extraction and purification of membrane proteins and also because they both have sugar-based head groups. The advantage of the sugar head group is that the amount of the detergent can be quantified using a 2,6-dimethylphenol assay.[130,131] This is an improved version of phenol-sulfuric acid methods for carbohydrate quantification.[132] In this method, concentrated sulfuric acid breaks down polysaccharides to dehydrated monosaccharides which then react with 2,6-dimethylphenol to produce an orange color. The color can be quantified by UV absorbance at 510 nm. A standard curve for each detergent was generated by applying the assay to samples with known concentration (Figure 2-8). Each sample was tested in triplicate for accuracy. The UV absorbance at 510 nm was plotted against detergent concentration and fitted by linear regression. The fitting quality for both was good, $R^2 > 0.98$, therefore the resulting formulae were used to determine the detergent concentration of unknown samples. It is noteworthy to mention that the slope in the formula we obtained for LMNG is approximately two times that for DDM. This is because LMNG has double the number of the sugar head groups compared to DDM.

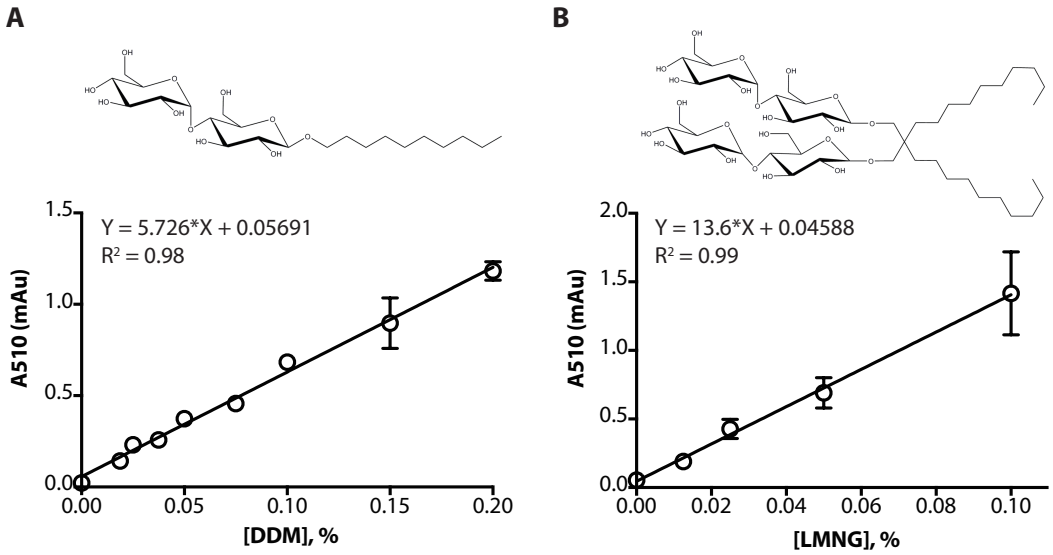

Figure 2-8: Standard curve for detergent quantification.

A) DDM and B) LMNG samples with known concentration were quantified using 2,6-dimethylphenol assay. The fitting results and the quality of the fit are shown. The chemical structure of the corresponding detergents are shown above.

With a validated assay that can accurately determine detergent concentration, we investigated the performance of Amberlite XAD2 beads. In the literature, the proportion of detergent removal beads required membrane protein incorporation into the MSP nanodisc system is within the range of 50%–100% (w/v).[129] Therefore, we decided to test the detergent removal rate using 80% beads. Detergent samples with various starting concentrations were mixed with the beads and incubated at 25 ºC with gentle agitation. Samples were taken every 30 min for determination of detergent concentration using the 2,6-dimethylphenol assay. The result for DDM shows that initial concentrations of up to 0.2% detergent can be completely removed in 2 h. With higher initial concentrations, 1% and 0.5%, less than 10% of the original concentration was detected after incubation with Amberlite XAD2 beads. A single exponential decay was fitted to the data, resulting in a rate constant of approximately 0.02 min^{-1}. In contrast, LMNG was much more difficult to remove, with a rate constant of approximately 0.003 min^{-1}, taking 22 hr to remove 0.01% LMNG. The very low critical micelle concentration of LMNG (0.001%) should significantly reduce the population of single detergent molecules in solution, thus leading to a very slow detergent removal rate. This may also be the reason for the inconsistent readout from the assay for high concentrations of LMNG. LMNG in micelle form may not be able to react with the 2,6-

dimethylphenol completely, so the phenomenon becomes obvious when using a high concentration of LMNG.

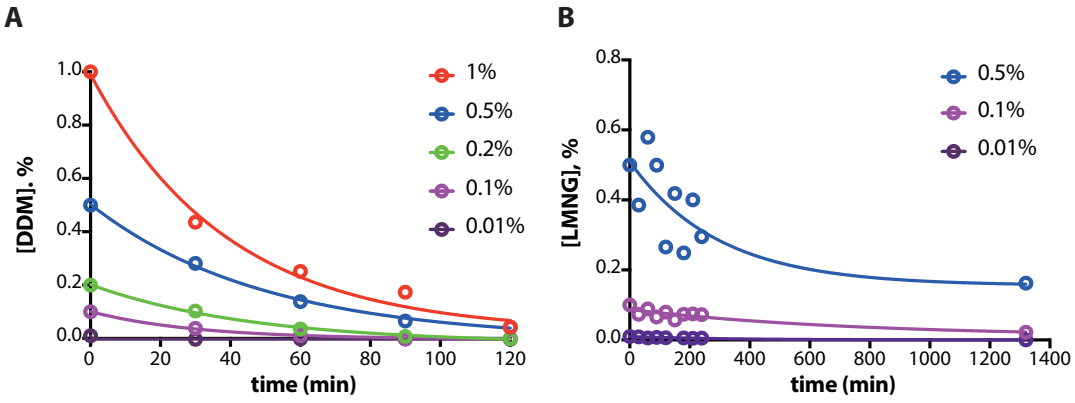

Figure 2-9: Detergent removal by 80% w/v Amberlite XAD2 beads.

The concentration of A) DDM and B) LMNG was measured by 2,6-dimethylphenol assay.

The results above show that DDM is much easier to remove. Thus, it is the preferred detergent for membrane protein purification for the purpose of incorporation into MSP nanodiscs or SapA nanoparticles. Calculation of removal rates gives us information about the interaction of the beads for a specific detergent which is useful to design the protocol for incorporation for different membrane proteins into SapA nanoparticles.

2.2.4 Size-tuneable characteristic of SapA lipid nanoparticle

Based on our knowledge of SapA lipid nanoparticle formation, we attempted to make SapA-DMPC nanoparticles using the procedure described below and illustrated in Figure 2-10. Calculated amounts of SapA and DMPC depending on the testing ratio were mixed in a 1.5 mL eppendorf. In order to assist SapA-DMPC nanoparticle formation, 0.2% DDM was included in the assembly mixture. The buffer with the desired pH was then added to the mixture to a final volume of 500 µL. Table 2-1 shows the detailed composition of the mixture. The assembly mixture was incubated at 37 ºC for 10 min before the removal of DDM using 80% w/v Amberlite XAD2 beads, equivalent to 400 mg in 500 µL sample. Complete detergent removal was confirmed by 2,6-dimethylphenol assay. The size of the resulting particles was measured by analytical SEC.

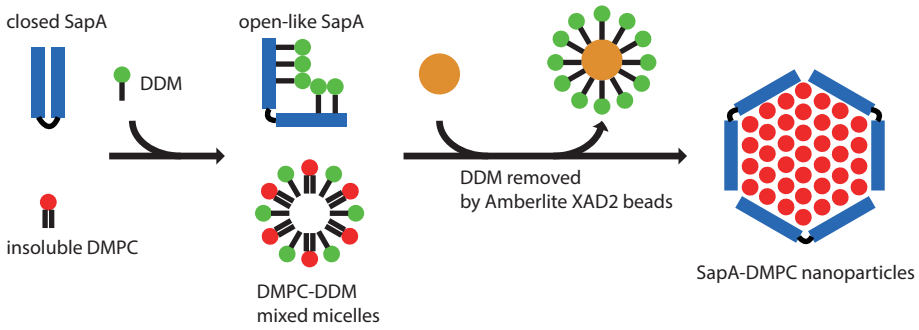

Figure 2-10: Illustration of the SapA-DMPC nanoparticle formation.

Table 2-1: Composition of a SapA-DMPC (1:10) assembly mixture.

	Volume	Final concentration
SapA (3 mM)	20 µL	120 µM
DMPC (10 mM)	60 µL	1.2 mM†
DDM (10%)	10 µL	0.2%
Buffer‡	410 µL	
Total volume	500 µL	

‡ The buffer used in the assembly mixture depends on the desired pH for the experiments. Three buffers were used in this section: 50 mM sodium acetate (pH 4.8), 50 mM sodium acetate (pH 6), and 50 mM Tris-HCl (pH 7.4), all with 150 mM NaCl.

† The final concentration of DMPC depends on the ratio used in the experiments. This table shows a SapA:DMPC molar ratio of 1:10 as an example.

Different SapA:DMPC ratios, namely 1:0, 1:5, 1:10, 1:20, and 1:30, were screened to see if the particle size increased with more DMPC in the initial assembly mixture. The data revealed the formation of two sizes of SapA-DMPC nanoparticles when different SapA:DMPC ratios were screened at pH 4.8, pH 6, and pH 7.4 (Figure 2-11). The 1:0 ratio at pH 4.8 did not show any absorbance at 280 nm (Figure 2-11 A, black) because all SapA precipitated as described previously (2.2.2), consistent with the model for SapA opening (Figure 2-6). A 1:5 ratio converted all the SapA to SapA-DMPC nanoparticles with a molecular weight of 37 kDa (Figure 2-11 A, red), determined by molecular weight markers for the size-exclusion column. As the DMPC ratio increased, a second size of SapA-DMPC nanoparticles appeared at around 135 kDa (Figure 2-11 A, purple). The behaviour for pH 6 and pH 7.4 was quite different from that for pH 4.8. An additional peak at 17.5 mL which corresponds to free SapA could be observed (Figure 2-11 B,C, black), whereas the 37 kDa nanoparticles disappeared. As for pH 6, a

1:10 ratio converted approximately 80% of SapA to SapA-DMPC nanoparticles with a molecular weight of about 70 kDa (Figure 2-11 B, blue). We observed a large overlap of two peaks in 1:20 and 1:30 ratio at pH 6 (Figure 2-11 B, green and purple), which prevented accurate determination of the peak position. In the case of pH 7.4, the elution profile was mostly similar to that at pH 6 with the exception of a little shoulder at 15 mL in the 1:5 and 1:10 ratio profiles (Figure 2-11 C, red and blue). This peak was not stable as we only observed the free SapA at 17.5 mL when we reran the fractions. Therefore, we suspect it was some residual detergent on the column that interacted and broke down the SapA-DMPC nanoparticles into smaller particles. Overall, the results show that SapA is only able to form the 37 kDa SapA-DMPC nanoparticles at acidic pH. In all cases, SapA and DMPC assembled into nanoparticles of fixed sizes. In the pH 7.4 case, for example, SapA-DMPC nanoparticles with 73 kDa or 135 kDa sizes were observed. With increasing amounts of DMPC, the population shifted from 73 kDa size to 135 kDa size instead of forming a SapA-DMPC nanoparticle with a size in between 73 kDa and 135 kDa. This indicates that SapA-DMPC nanoparticles have defined compositions that are determined by the number of SapA molecules per nanoparticle. Our results also show that we can tune the size of SapA-DMPC nanoparticles by altering the SapA:DMPC ratio in the initial mixture. If the mixing ratio is exactly correct, uniformly sized SapA-DMPC nanoparticles are generated. Otherwise, a mixture of two particle sizes was observed. Therefore, we sought to find the optimal ratio that generates only one size of SapA-DMPC nanoparticle, which would allow us to characterise them further.

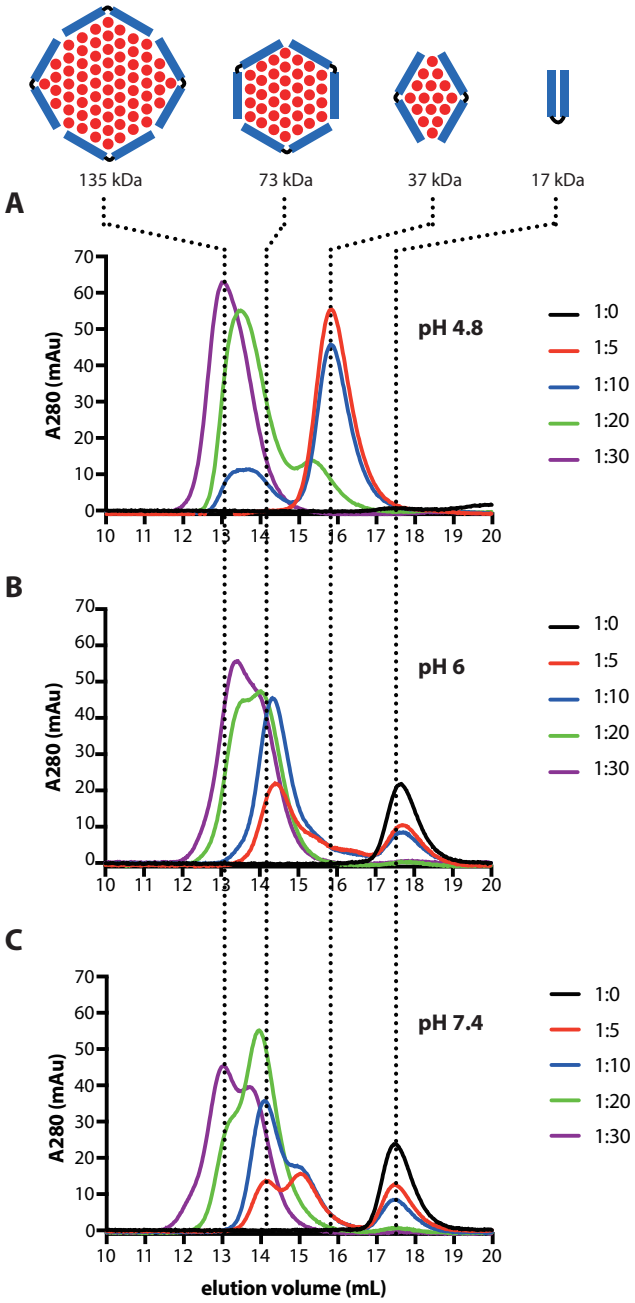

Figure 2-11: Analytical SEC of SapA-DMPC nanoparticles with different ratio.

Assembly particle sizes were assessed at A) pH 4.8, B) pH 6, and C) pH 7.4. The proposed SapA arrangements of each species are shown in cartoon representation.

We aimed to generate a uniform size of SapA-DMPC nanoparticles with an optimal assembly ratio at pH 6. Previous results (Figure 2-11 B) revealed that the 1:10 ratio sample still contained apo SapA, whereas the 1:20 sample already contained larger nanoparticles, indicating that the optimal ratio must lie between these two boundaries. Indeed, we found that a ratio of 1:15 generated a single peak in SEC with a molecular weight of about 64 kDa (Figure 2-12 A, blue; Table 2-2). The optimal ratio for larger

nanoparticles was also screened, showing a homogeneous single peak at a ratio of 1:45 with a molecular weight of about 170 kDa (Figure 2-12 A, red; Table 2-2). Although these two optimal initial mixture ratios of 1:15 and 1:45 generated nanoparticles of a single size, the SapA:DMPC ratio in the final nanoparticles was not defined by these experiments. A molybdate assay, often used for phospholipid quantification,[131] was performed to quantify the amount of DMPC in the fractions from SEC (Figure 2-12 A, open circle). In combination with the absorbance at 280 nm, a measurement of SapA concentration, the SapA:DMPC ratio could be determined experimentally for the final product. The results showed ratios of 1:14 and 1:45 respectively, very close to the ratio provided in the initial mixtures, 1:15 and 1:45. By considering the ratios and the apparent molecular weights of the two particles, we propose that the 1:14 ratio generated nanoparticles consisting of three SapA and 42 DMPC, hereafter called $SapA_3$-DMPC, and the 1:45 ratio species comprised four SapA and 180 DMPC, termed $SapA_4$-DMPC.

The expected disc-like shapes were confirmed by negative-stain electron microscopy for both $SapA_3$-DMPC and $SapA_4$-DMPC. A side view of $SapA_3$-DMPC nanoparticles stacked together can be seen (Figure 2-12 B, red arrow), as well as a top view of single nanoparticles (Figure 2-12 B, blue arrow). Stacking is likely to be an artefact during grid preparation and is also often observed in EM images of MSP nanodiscs.[133,134] A similar artefact was observed in images of $SapA_4$-DMPC nanoparticles (Figure 2-12 C). The larger particle size of $SapA_4$-DMPC allows us to pick out some representative top-down views showing the uniform size.

The same SapA:DMPC ratio of 1:15 also generated a single size of SapA-DMPC nanoparticles at pH 7.4, showing as a single peak in the SEC elution profile (Figure 2-13, dark blue; Table 2-2). We did not measure the final SapA:DMPC ratio by the molybdate assay, which we used for characterisation of SapA-DMPC at pH 6, because the assay was not yet established at the time this experiment was performed. However, the corresponding molecular weight was about 100 kDa, 50% larger than the particles generated at pH 6 (64 kDa). This suggests that the optimal ratio leading to a single particle is pH independent, but the size of the resulting particle is pH dependent. It is highly likely that the lipid bilayer packed much more loosely at pH 7.4. The reason for this behaviour is unclear. SapA at pH 7.4 might have a more flexible opening hinge, i.e. a wider range of inter-helical angles may be available, potentially leading to a more

dynamic bilayer in the middle and hence a larger particle size. However, this theory will need further experiments to be confirmed.

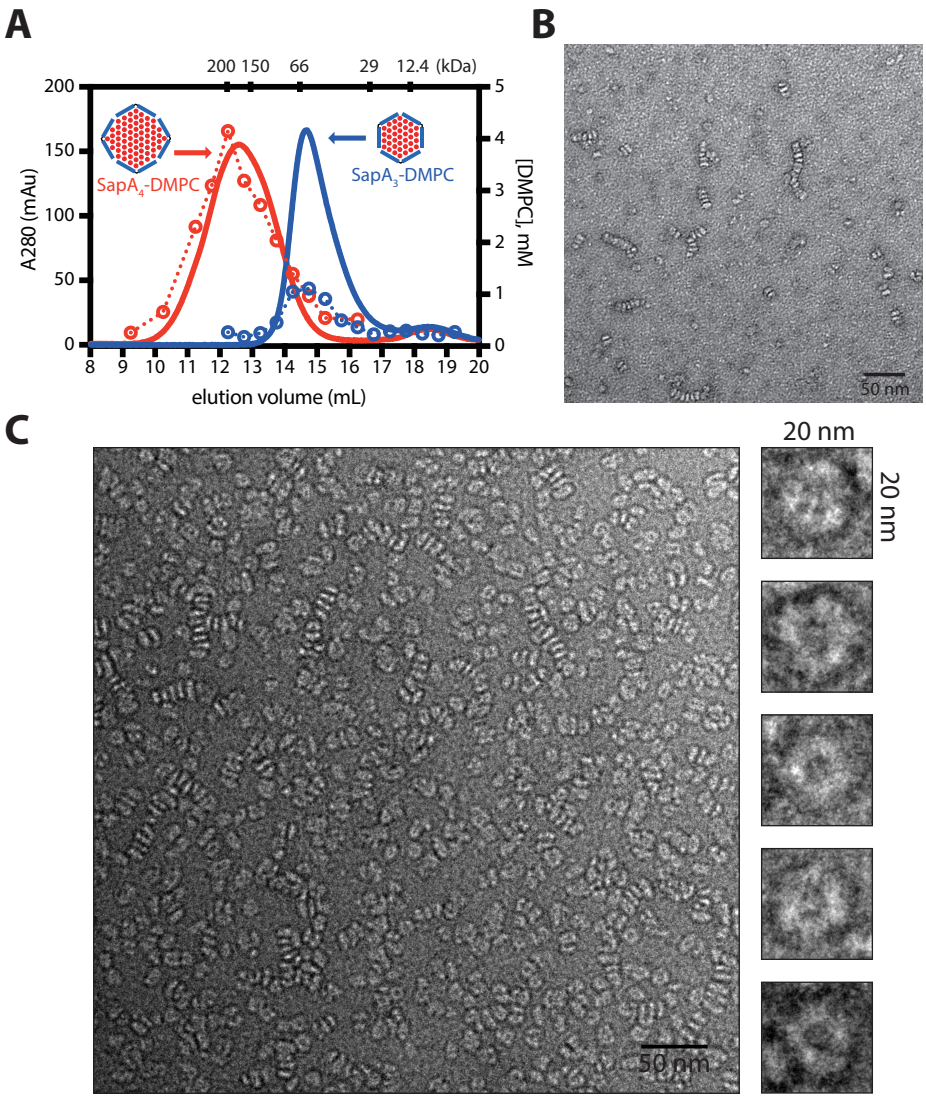

Figure 2-12: Characterisation of SapA-DMPC nanoparticles at pH 6.

A) Size-exclusion chromatography of SapA-DMPC with the SapA:DMPC ratio of 1:15 (blue) and 1:45 (red). DMPC was quantified by the molybdate assay (open circle). The proposed compositions and the arrangement of the SapA-DMPC particles are indicated. B) Negative-stain images of $SapA_3$-DMPC. Scale bar, 50 nm. C) Negative-stain images of $SapA_4$-DMPC. Scale bar, 50 nm. The insets show top-down views of representative $SapA_4$-DMPC nanoparticle images in a 20 nm box.

It has been shown recently that SapA has a low lipid specificity for nanoparticle formation, meaning that SapA can interact with a wide range of lipids to form SapA lipid nanoparticles.[111] This could be an advantage for further studies on the impact of lipid composition on the structure and dynamics of membrane proteins. Using the same SapA:lipid ratio of 1:15 at pH 7.4, we tested several lipid mixtures other than DMPC that were previously used in MSP nanodiscs including DMPC:DMPG (3:1) and POPC:POPG (2:1).[77,105,135] The SEC elution profiles show that homogeneous particle sizes were formed with all the lipid mixtures tested (Figure 2-13). Interestingly, doping with lipids that possess phosphatidylglycerol (PG) headgroups results in smaller particles. This can be observed by comparing the profiles for DMPC (102 kDa) and DMPC:DMPG (3:1) (93 kDa) and the profile of POPC (77 kDa) and POPC:POPG (2:1) (70 kDa). In addition, doping with 10% cholesteryl hemisuccinate (CHS), a soluble homologue of cholesterol, generates larger particles. It is possible that these added lipid molecules can change the liquidity of the bilayer, therefore affecting the size of the lipid nanoparticles.

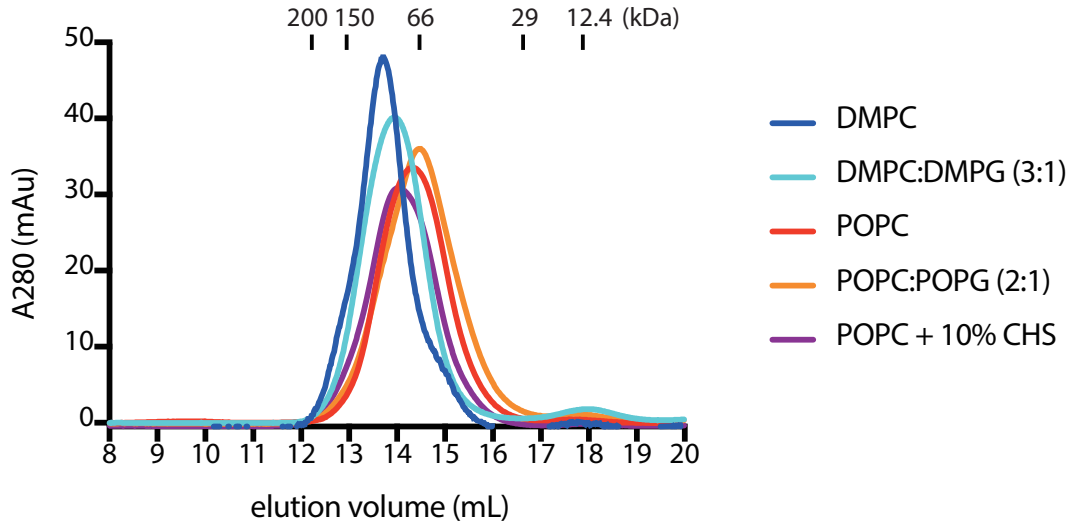

Figure 2-13: SEC of SapA-lipid mixture nanoparticles.

Sample was prepared by mixing SapA, lipid mixture, and DDM at pH 7.4 followed by detergent removal step. Different lipid mixtures were used; DMPC (blue), DMPC:DMPG (3:1) (cyan), POPC (red), POPC:POPG (2:1) (orange), and POPC with 10% CHS (purple).

Table 2-2: Size determination of SapA lipid nanoparticles.

	Mixing SapA:lipid ratio	Determined SapA:lipid ratio[‡]	SEC[†]		Translational diffusion[#]		Proposed compositions	Calc. MW (kDa)[§]
			V_e (mL)	MW (kDa)	D_t *10^{-10} (m^2/s)	MW (kDa)		
$SapA_3$-DMPC (pH6)	1:15	1:14	14.7	64	1.05	57	3xSapA + 42xDMPC	56
$SapA_4$-DMPC (pH6)	1:45	1:45	12.6	170	0.75	165	4xSapA + 180xDMPC	159
SapA-DMPC (pH7.4)	1:15	-	13.7	102	-	-	-	-
SapA-DMPC/DMPG (pH7.4)	1:15	-	13.9	93	-	-	-	-
SapA-POPC (pH7.4)	1:15	-	14.3	77	-	-	-	-
SapA-POPC/POPG (pH7.4)	1:15	-	14.5	70	-	-	-	-
SapA-POPC/CHS (pH7.4)	1:15	-	14	88	-	-	-	-

[†] V_e = elution volume. The molecular weights were calculated based on the calibration curve obtained from protein standards. Details and the formula can be found in section 7.2.3.

[‡] SapA:lipid ratio was experimentally determined by UV absorbance at 280 nm and molybdate assay.

[#] Translational diffusion coefficients (D_t) were measured by PFG NMR spectroscopy at 318 K and were corrected for viscosity changes. Details can be found in section 7.6.2.

[§] The molecular weights were calculated based on the proposed compositions with 9.2 kDa for SapA and 677.5 Da for DMPC.

2.3 Conclusions

We proposed in this chapter a mechanism for the formation of SapA lipid nanoparticles. SapA can spontaneously open up to interact with lipids and subsequently form nanoparticles in acidic environments, whereas detergents are needed to facilitate SapA opening at neutral pH. Moreover, we found that SapA can form a stable complex with DDM in an open-like conformation. In order to completely remove DDM during SapA lipid nanoparticle formation, Amberlite XAD2 beads were used to actively remove detergents from the assembly mixture. A 2,6-dimethylphenol assay was used to quantify DDM left in the sample through a time course and eventually to confirm that the detergent had been completely removed. Based on our proposed mechanism for SapA opening, we established a protocol for making SapA-DMPC nanoparticles over a range of pH values. Variation in the ratio of SapA to DMPC present in the initial mixture was used to make different sizes of SapA-DMPC nanoparticles, showing the size-flexibility of this system. At pH 6, optimal ratios of 1:15 and 1:45 generate SapA-DMPC nanoparticles with molecular weights of 64 kDa and 170 kDa, respectively. The compositions of the two sizes of SapA-DMPC nanoparticles were confirmed using A_{280} and a molybdate assay, and the disc-like shapes were observed in negative-stain EM images. We also tested the ability of SapA to form lipid nanoparticles with various lipid compositions. With the same 1:15 ratio of SapA to the total amount of lipid, particles using DMPC, DMPC/DMPG, POPC, POPC/POPG and POPC/CHS, respectively, showed as single homogeneous species but varied in their molecular sizes, according to their SEC elution profiles. While the exact reason for this size variation has not yet been established, there is a possibility that lipid composition may affect the compactness of the SapA lipid nanoparticles hence leading to assemblies with different apparent molecular weights. In summary, SapA lipid nanoparticles appear to be highly versatile and size-adaptable small lipid rafts. In the next chapters their properties as lipid membrane mimetics are used to investigate membrane proteins embedded in a native-like lipid bilayer environment.

3 USING SAPA LIPID NANOPARTICLES AS A MEMBRANE MIMETIC FOR NMR SPECTROSCOPY: A CASE STUDY OF BACTERIAL OUTER MEMBRANE PROTEIN X

3.1 Introduction

3.1.1 Application of MSP nanodiscs in solution NMR studies

It is important to study membrane proteins in a membrane mimetic system that suitably imitates their natural environment. However, it is very difficult to find a membrane mimetic that at the same time stabilises a membrane protein sufficiently, has native-like membrane properties, and is compatible with a range of analytical tools. Solution NMR spectroscopy is a very powerful tool that can provide structure and dynamics information about proteins, however, its size limitation puts considerable limitations on the suitability of many membrane mimetic systems. As discussed in Chapter 1, MSP nanodiscs among others show the most promising properties in view of NMR

compatibility. In this section, I review some of the solution NMR studies of membrane proteins using MSP nanodiscs including several modifications to the system that greatly improve its NMR compatibility. A detailed experimental procedure for membrane protein incorporation is included. Finally, I discuss some of the issues with MSP nanodiscs that are still in need of improvement.

MSP nanodiscs consist of a small patch of phospholipid bilayer surrounded by two units of the engineered apolipoprotein A-I (ApoA-I), also known as membrane scaffold protein, creating a well-defined, membrane-like particle. A membrane protein of interest can be reconstituted into the lipid patch of an MSP nanodisc, which emulates the native membrane environment. This technology has been widely employed for membrane protein studies using various biological assays and biophysical tools including solution NMR spectroscopy.[98] Several membrane proteins were successfully incorporated into the first version of MSP nanodiscs, MSP1D1 nanodiscs, for 2D heteronuclear NMR measurements, such as VDAC-1,[101] VDAC-2,[136] CD4mut,[137] Aam-I,[138] KvAP.[138] However, the large particle size of MSP nanodiscs, about 120 kDa, severely limits their applicability and also makes multidimensional NMR data, which is required for peak assignment and structure determination, extremely difficult to obtain. To improve the suitability of MSP nanodiscs for NMR studies further, Hagn et al. developed a set of truncated MSP constructs that resulted in a reduced nanodisc molecular weight as discussed in Chapter 1.[77] This enabled the 3D backbone resonance assignment and structure determination of an integral membrane protein.[77] The development of these shorter MSP constructs also facilitated many NMR studies of other small-to-medium sized membrane proteins.[139–141] Moreover, the availability of the truncated MSP construct also prompted a solution structure determination of the scaffold proteins in an MSP nanodisc, showing the detailed antiparallel arrangement of the double belt scaffold proteins.[134] Further improvements have been achieved through the introduction of covalently circularised nanodiscs, which result in a well-defined particle size rather than a broad distribution in sizes that require additional separation through multiple chromatographic methods.[142] These developments undoubtedly expanded the application of nanodiscs in the field of NMR studies of membrane proteins.

A detailed protocol was published recently describing all the critical points that have to be considered when optimising nanodisc preparations for NMR spectroscopy.[129] The general procedure involves mixing MSP, lipids solubilised in cholate buffer and

detergent-micelles containing the membrane protein in a ratio that needs to be empirically optimized. The assembly mixture is then incubated for 1-2 h followed by a detergent-removal step either using detergent absorbent beads or dialysis. The self-assembly of membrane protein embedded nanodiscs is thought to be initiated by removing the detergent. The incubation temperature used in this step is also important, with the nanodiscs forming most efficiently near the phase-transition temperature of the lipids being used. The reason for this temperature requirement is still not clear but it may be explained by an effect of the phase behaviour of the phospholipid on the organisation of the phospholipid/detergent micelle during nanodisc formation.[143] Presumably, being close to the phase transition temperature allows lipid molecules to exchange between the liquid and gel phase, so small patches of lipid bilayer can associate or dissociate until a well-defined structure becomes encircled by scaffold proteins. After nanodisc assembly, an optional affinity column can be applied to remove any empty discs provided there is an affinity tag on the embedded membrane protein, while the scaffold protein is typically free of tag. Finally, the size of the assembled particles can be checked, and their homogeneity improved by size-exclusion chromatography.

Despite this well-established procedure for MSP nanodisc assembly and membrane protein incorporation, there are several screening steps required that are time-consuming and costly. One example is the need to screen for suitable MSP constructs: there are currently six MSP constructs of different lengths and which one gives the most desirable properties, in terms of NMR spectral quality, needs to be screened for every membrane protein of interest. Using a construct that is too long will result in particles with a molecular weight that is too high, making them incompatible with NMR studies, whereas using a construct that is too short will result in insufficient lipid molecules to stabilise the membrane protein or to represent a native lipid environment. The MSP-to-lipid ratio also needs to be optimised for every study. Although the ratio for empty nanodiscs is defined by the size of the MSP construct, the number of lipid molecules that incorporated membrane protein will replace needs to be determined. Provided a structure of the target protein is known, the likely ratio can be approximated based on geometrical arguments,[129] otherwise, the ratio needs to be determined empirically by a series of small-scale tests. Using an incorrect ratio can generate inhomogeneous particles or aggregates. This also means it is difficult to incorporate lipid extract from natural sources such as brain lipid extract or *E. coli* lipid extract, as the molar

concentration of the lipid mixture is either unknown or likely to be inaccurate. Due to these reasons, incorporation of membrane proteins into MSP nanodiscs is still a laborious process that may take months for full optimization, and often needs multiple SEC steps to result in homogeneous samples. The latter can substantially reduce the yield of incorporation, as 10% is typically lost in each size-exclusion run at our hands.

3.1.2 Using SapA as an alternative scaffold protein for NMR studies

We have shown the size flexibility of SapA phospholipid nanoparticles by altering the SapA:lipid ratio in Chapter 2. This adaptability makes SapA an attractive system because a single scaffold protein should be able to accommodate a wide range of membrane proteins of different molecular sizes, removing the need to screen for the optimal MSP construct. Chapter 2 also elaborated that although SapA lipid nanoparticles have size flexibility, all the particles formed are disc-shaped and homogeneous. Accordingly, this means that it is not necessary to maintain an accurate SapA:lipid ratio during the assembly process, unlike with MSP nanodiscs. A slight deviation of the SapA:lipid ratio from the ideal will generate a second size of nanoparticle without compromising the homogeneity of the primary, desired species. As such, the SapA system should be capable of assembling lipid nanoparticles without the need for a time-consuming screening process. We have also shown in Chapter 2 that $SapA_3$-DMPC nanoparticles possess an apparent molecular weight of about 70 kDa. This is smaller than the particles formed by the most commonly used MSP construct in NMR studies, MSP1D1ΔH5 at 107 kDa. In view of its size the SapA system could potentially be competitive, assuming that there is an approximate inverse correlation between spectral quality and size of the overall particle into which the membrane protein is embedded.

3.1.3 Structure, function and related NMR studies of OmpX

Gram-negative bacteria are surrounded by two layers of membrane, the cytoplasmic membrane and the outer membrane.[144] The outer membrane protects the bacterial cell from the outside environment. About 50% of the outer membrane mass consists of membrane proteins, either integral membrane proteins or membrane associated proteins.[144] These proteins carry out essential cellular functions such as nutrient uptake, cell adhesion, cell signalling and waste export.[145] Many of these outer membrane proteins are also characterised as virulence factors for nutrient scavenging and evasion

of the host defence system, including OmpX.[146] The molecular structure of OmpX was first determined at 1.9 Å resolution by X-ray crystallography (Figure 3-1 A).[147] The structure shows an eight-stranded antiparallel β-barrel with a barrel height of approximately 32 Å.[147] The four β-strands found protruding at the extracellular side were proposed to function as a 'fishing rod' to form hydrogen bonds with binding partners, therefore being responsible for cell adhesion and invasion.

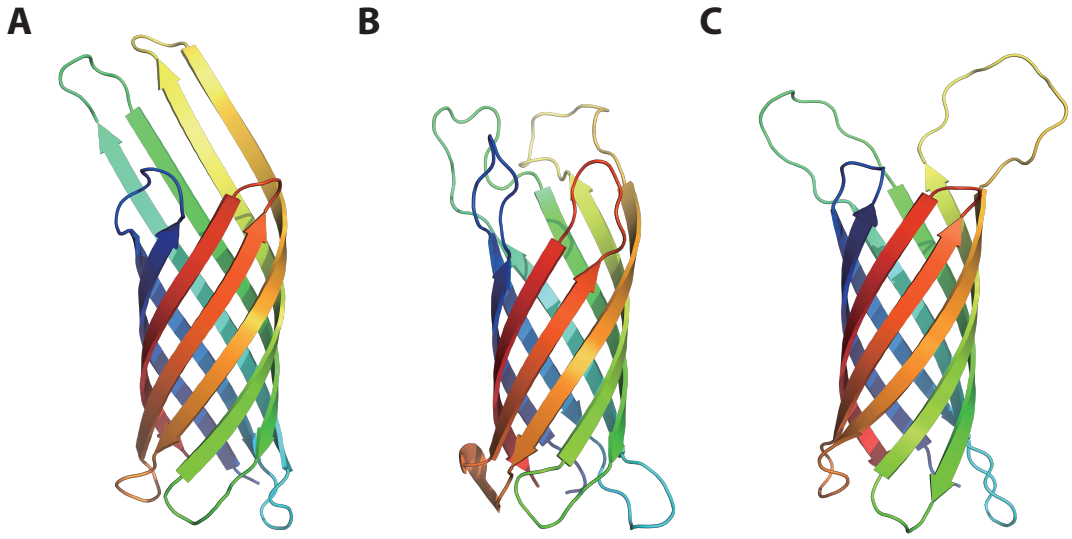

Figure 3-1: Molecular structure of OmpX.

A) Structure of OmpX in n-octyltetraoxyethylene determined by X-ray crystallography (PDB ID: 1QJ8[147]). B) Solution structure of OmpX in dodecylphosphocholine (DPC) determined by NMR spectroscopy (PDB ID: 2M07[77]). C) Solution structure of OmpX in MSP1D1ΔH5-DMPC/DMPG nanodiscs (PDB: 2M06[77]).

NMR studies of OmpX became reachable due to the development of transverse relaxation-optimized spectroscopy (TROSY) experiments.[27] The solution NMR structure of OmpX in detergent micelles was solved, revealing the same fold as in the crystal structure (Figure 3-1 B).[148,149] Comparing the results of the two methods, it is clear that the crystal structure shows the extracellular regions as extended β-sheets, while the solution NMR structure reports them as random coil. The extended β-sheets are probably artefacts due to crystal packing.

Several desirable characteristics make OmpX a good model system for NMR studies, such as its small size (15 kDa), its high expressability in *E. coli* and its high thermal

stability. Not surprisingly, OmpX was used as a model protein for the development of shorter MSP constructs.[77] Using the shorter construct MSP1D1ΔH5 (ΔH5) the solution structure of lipid-nanodisc embedded deuterated OmpX was determined by NMR spectroscopy (Figure 3-1 C).[77] No protruding β-strands, as seen in the crystal structure (Figure 3-1 A), were found in this structure. The β-barrel assembly is composed of longer β-strands with shorter extracellular and intracellular loops, compared to the structure in detergent (Figure 3-1 C). In addition, the ^{15}N heteronuclear NOE data suggests increased dynamics of the loop regions in the nanodisc structure.[77] In another NMR study, OmpX was used to demonstrate the effect of membrane mimetics, namely micelles, bicelles, and nanodiscs, on backbone dynamics.[76] The relaxation data suggests that the inherent flexibility of this β-barrel membrane protein is largely compromised in the detergent micelles.[76] These studies emphasise the importance of choosing a native-like membrane environment when conducting structural studies.

In view of the considerable amounts of NMR data that are available for OmpX in many different environments, it is convenient to use this protein as a model system to investigate the performance of SapA lipid nanoparticles as a native-like membrane mimetic.

3.1.4 Aims

The existing MSP nanodisc technology in combination with solution NMR spectroscopy has been very powerful and has made several important breakthroughs in the membrane protein field. However, there are still some difficulties in using MSP nanodiscs including the long screening process and the low incorporation yield. Therefore, an alternative system would be welcome. SapA lipid nanoparticles have been used as a new membrane mimetic system in cryo-EM studies.[109,110] Inspired by this cryo-EM study, we hoped to extend the application of the SapA system to study small-to-medium size membrane proteins of less than 50 kDa using solution NMR spectroscopy.

In Chapter 2, we showed that our established protocol can generate SapA lipid nanoparticles with the desired size-flexibility characteristic. In order to use SapA lipid nanoparticles for studying biologically important proteins, we have to validate the ability of SapA to be used as an alternative membrane scaffold protein. OmpX seems to be a good candidate as a model protein for validation because OmpX in MSP nanodiscs

has been previously studied extensively by solution NMR spectroscopy, providing a good point of comparison.[76,77,150] The 2D NMR spectra of OmpX in detergent and in MSP nanodiscs are very different in terms of the peak positions because the two chemical environments are distinctly different. Therefore, we hypothesised that if SapA lipid nanoparticles can provide a similar lipid bilayer environment to MSP nanodiscs then their 2D NMR spectra should look very similar. A comparison should therefore allow us to validate the suitability of using SapA lipid nanoparticles as a native-like membrane mimetic for NMR studies.

SapA has been shown to be able to bind a variety of lipids,[111] making the SapA lipid nanoparticle a versatile platform to study the effect of lipid composition on membrane proteins. Consequently, we sought to incorporate OmpX into various lipid compositions and investigate the effect of the lipid headgroup, the length of the aliphatic chain, and the degree of unsaturation on the incorporated membrane protein. 2D NMR experiments were then used to report on the structure and dynamics of OmpX in different lipid environments with atomic resolution. We expected the outcome of these proof-of-concept investigations to facilitate further applications to biologically relevant molecules.

3.2 Results and discussion

3.2.1 Incorporation of OmpX into SapA-DMPC nanoparticles

In Chapter 2, we proposed the mechanism for the formation of SapA lipid nanoparticles in which DDM is required in the process. We also showed the existence of a stable SapA-DDM complex, and that detergent absorbent beads must be included in the incorporation procedure to proactively remove detergents. Here, we demonstrate the incorporation of OmpX using our developed protocol to show that SapA lipid nanoparticles can be used as a membrane mimetic for NMR studies.

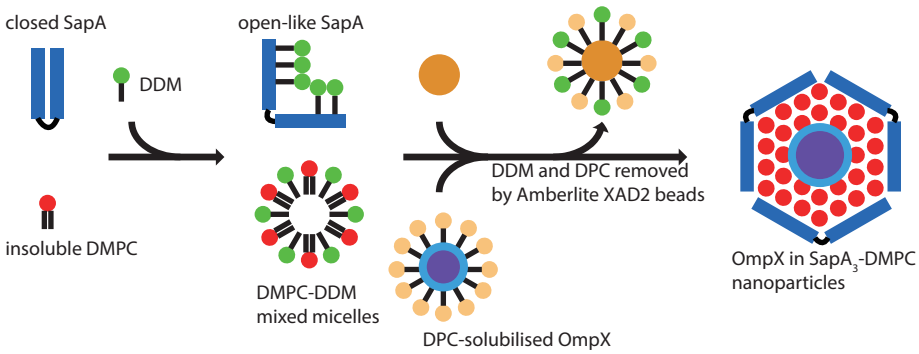

Figure 3-2: Illustration of OmpX incorporation into SapA-DMPC nanoparticles.

The procedure for OmpX incorporation is illustrated in Figure 3-2. OmpX was originally solubilised in the detergent DPC. As DDM is the only detergent we ever tested to promote the open conformation of SapA, it was not clear if other detergents such as DPC would have the same ability. Consequently, we always supplemented 0.2% DDM, the same amount used in making SapA-DMPC nanoparticles, in the initial mixture for OmpX incorporation. The initial mixture consisted of SapA, DMPC and OmpX at a ratio of 10:50:1 at pH 6 in the presence of 0.2% DDM (Table 3-1). A ten-fold excess of SapA over OmpX was chosen to increase the rate of protein incorporation. In comparison, an excess amount of MSP is often used for the same reason during nanodisc assembly, next to decreasing the incorporation of more than one protein per nanodisc.[129] The 1:5 ratio of SapA:DMPC was the result of a rough initial estimate. Accordingly, as shown in Chapter 2, the composition of empty $SapA_3$-DMPC nanoparticles was three SapA and 42 DMPC molecules. In the literature it has been shown that OmpX displaces about 20 DMPC molecules.[77] Therefore, we estimated that the composition of OmpX containing $SapA_3$-DMPC nanoparticles would be one OmpX, three SapA, and 22 DMPC, leading to a SapA:DMPC ratio of 1:7. Our first experimental attempts used a 1:5 ratio, which gave excellent results. Due to the size-adaptability of SapA lipid nanoparticles we did not have to carefully screen for the optimal ratio, unlike with MSP nanodiscs.

Table 3-1: Composition of an OmpX incorporation assembly mixture.

	Volume	Final concentration
SapA (3 mM)	20 µL	120 µM
DMPC (10 mM)	30 µL	600 µM
OmpX (1 mM)	6 µL	12 µM
DDM (10%)	10 µL	0.2%
Buffer‡	434 µL	
Total volume	500 µL	

‡ The buffer used in the OmpX incorporation is 50 mM sodium acetate (pH 6), 150 mM NaCl.

After mixing all the components, the mixture was incubated at 37 ºC for 10 min. At this point the cloudy sample converted into a clear solution. The sample was then subjected to a detergent removal step through incubation with 80% w/v Amberlite XAD2 beads at 25 ºC for 2 h. Although efficient detergent removal was expected, at this stage of the nanoparticle formation procedure we were not able to estimate the DPC concentration as the 2,6-dimethylphenol assay only responds to sugar-based detergents.[130] 1D proton NMR was ambiguous in this case because both DPC and DMPC yield signals from choline protons that we usually use for detecting the phosphatidylcholine (PC) headgroup. However, in one experiment which is discussed in section 3.2.4, OmpX was incorporated into DMPG nanoparticles and the corresponding 1D proton NMR showed negligible PC signal indicating almost quantitative removal of DPC by the established protocol.

Nevertheless, after final detergent removal, OmpX remained in solution and showed a symmetrical elution peak at 14.1 mL (84 kDa) by SEC (Figure 3-3 A), which appeared to be significantly larger than OmpX in DPC micelles (15.5 mL; 44 kDa). The SDS-PAGE gel of the corresponding fractions from the SEC confirmed the presence of both OmpX and SapA in the major peak (Figure 3-3 B). It was likely that OmpX had been successfully incorporated into $SapA_3$-DMPC nanoparticles based on the molecular weight (Table 3-2).

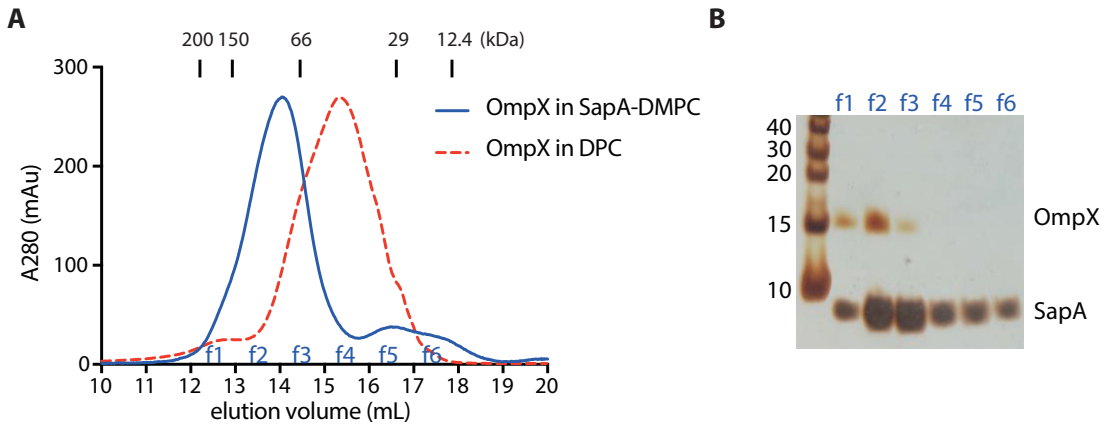

Figure 3-3: Incorporation of OmpX into SapA-DMPC nanoparticles.

A) SEC of OmpX in SapA-DMPC nanoparticles (solid blue) and in detergent DPC micelles (red dotted). B) The fractions from OmpX in SapA-DMPC indicated by f1–f6 were analysed by SDS-PAGE (bottom) showing the presence of both OmpX and SapA in the main elution peak. The fractions containing OmpX (f1–f3) were pooled and concentrated for further investigation.

The incorporation yield was generally higher than 80% judging by the OmpX band in the SDS-PAGE analysis. Moreover, the resulting particle size of 84 kDa was smaller than for OmpX in MSP1D1ΔH5 (ΔH5) nanodiscs (107 kDa).[77] Guided by these observations, it seemed reasonable to expect that 2D [^{1}H,^{15}N] TROSY NMR experiments could be collected without the need to produce highly deuterated, ^{15}N-labelled OmpX.

3.2.2 NMR studies of OmpX in SapA-DMPC nanoparticles

A 2D [^{1}H,^{15}N]-SOFAST-TROSY spectrum was recorded using non-deuterated ^{15}N labelled OmpX to assess its structural integrity in SapA$_3$-DMPC nanoparticles (Figure 3-4 A). The resulting spectrum was of good quality even without deuteration, indicative of the sample being homogeneous. Clearly the quality of the spectrum of the ΔH5-DMPC/DMPG nanodiscs in the literature[150] is superior due to the use of deuterated OmpX. However, rotational correlation time measurements using 1D ^{15}N TRACT[151] indicated that SapA nanoparticle embedded OmpX was smaller in size (τ_c = 28 ns, calculated MW of 87 kDa) compared to that in ΔH5 nanodiscs (τ_c = 34 ns, calculated MW of 107 kDa). Accordingly, using deuterated protein should result in further improvements, and based on the quality of the spectrum shown in Figure 3-4 A one

would anticipate high-quality data for OmpX in SapA nanoparticles. Nevertheless, 121 out of 131 backbone assignments from the literature[150] could be transferred unambiguously to our spectrum based on peak proximity, allowing us to investigate the chemical environment of OmpX without the need for a complete reassignment.

Table 3-2: Proposed compositions of OmpX in SapA-DMPC nanoparticles.

	SEC†		Rotational diffusion		Proposed compositions	Calc. MW (kDa)§
	V_e (mL)	MW (kDa)	τ_c (ns)#	MW (kDa)		
OmpX in DPC	15.5	44	-	-	-	-
OmpX in $SapA_3$-DMPC	14.1	84	28	87	3xSapA + 42xDMPC + 1xOmpX	71
OmpX in ΔH5-DMPC/DMPG (3:1)‡	-	-	34	107	2xΔH5 + 60xDMPC + 20xDMPG + 1xOmpX	115

† V_e = elution volume. The molecular weights were calculated based on the calibration curve obtained from protein standards. Details and the formula can be found in section 6.2.3.

Correlation time (τ_c) was measured by 1D ^{15}N TRACT[151] at 318 K.

§ The molecular weights were calculated based on the proposed compositions with 9.2 kDa for SapA, 677.5 Da for DMPC, 15 kDa for OmpX, 22.1 kDa for ΔH5, and 0.688 kDa for DMPG.

‡ Data was obtained from the literature.[77]

Chemical shifts are very sensitive to the chemical environment of the molecules under investigation. Similarities in chemical shift should indicate similar membrane protein environments. The chemical shift assignment datasets of both OmpX in detergent DPC (BMRB: 18797) and OmpX in ΔH5-DMPC/DMPG nanodiscs (BMRB: 18796) are available.[150] Therefore, we compared our spectrum, OmpX in $SapA_3$-DMPC, to these two chemical shift assignments to confirm the chemical environment of OmpX in our sample. Although the lipid composition used was not exactly the same, pure DMPC in our sample and DMPC/DMPG (3:1) in the ΔH5 nanodiscs,[150] the TROSY spectrum of OmpX in SapA-DMPC nanoparticles shares strong similarities with that recorded in ΔH5-DMPC/DMPG nanodiscs (BMRB: 18796)[150]. In contrast, considerable differences exist throughout when compared against the spectrum obtained in DPC micelles (BMRB: 18797)[150]. This can be clearly observed for some peaks, e.g. G64, R29, I65, V5, by zooming in to some well resolved regions (Figure 3-4 B–D). These results

confirm that OmpX was surrounded by the DMPC lipid bilayer offered by SapA-DMPC nanoparticles and was no longer in the DPC detergent micelles, which were removed during the protein incorporation and nanoparticle assembly process.

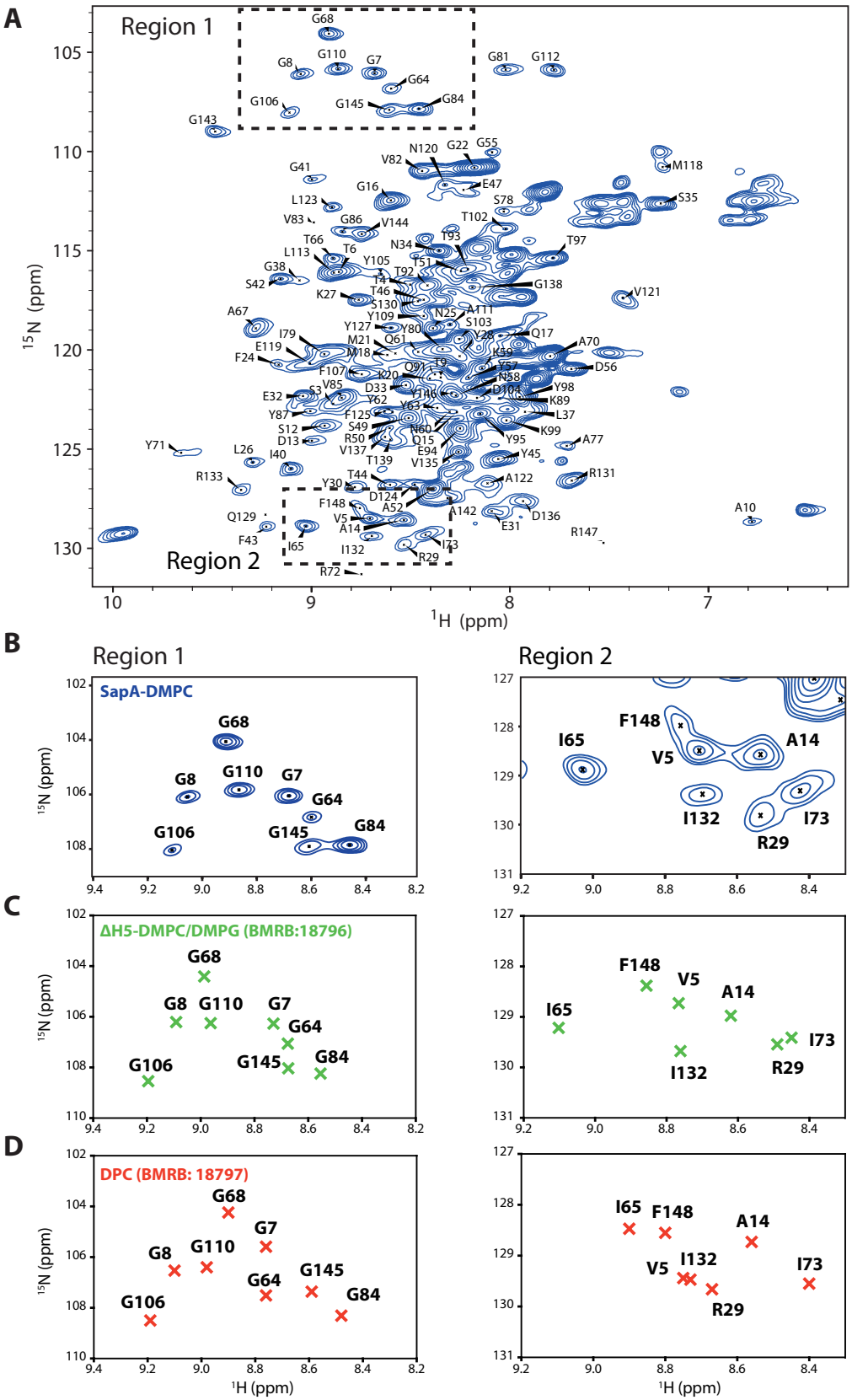

Figure 3-4 (*opposite*): NMR spectrum of OmpX in SapA-DMPC nanoparticles.

A) 2D [^{1}H,^{15}N]-SOFAST-TROSY spectrum of non-deuterated ^{15}N-labelled OmpX in SapA$_3$-DMPC nanoparticles. The spectrum was recorded at 318 K on a Bruker Avance AVIII 800 spectrometer (^{1}H frequency of 800 MHz) equipped with a 5 mm TXI HCN/z cryoprobe. The experiment was recorded with 3,078 scans, resulting in an experiment time of 36 h. Selected Region 1 and Region 2 are indicted in dashed box. B) Enlarged Region 1 (left) and Region 2 (right). Region 1 and Region 2 of previously reported NMR peak assignments of OmpX in C) ΔH5-DMPC/DMPG nanodiscs (BMRB: 18796) and D) in DPC micelles (BMRB: 18797).[150]

For a better comparison, another sample with the exact same lipid composition, DMPC/DMPG (3:1), was prepared. The experimental data including the size exclusion chromatogram (Figure 3-10 A) and the corresponding TROSY spectrum (Figure 3-11 blue) are discussed in section 3.2.4. All the assignments from the SapA-DMPC spectrum could be transferred onto the SapA-DMPC/DMPG (3:1) spectrum. In order to provide a more quantitative comparison, weighted chemical shift perturbations (CSP) were calculated for every residue between OmpX in SapA and ΔH5 and between OmpX in SapA and DPC using the formula:

$$\Delta\delta_{\mathrm{H,N}} = \sqrt{(\Delta\delta_{\mathrm{H}})^2 + 0.13 \times (\Delta\delta_{\mathrm{N}})^2}$$

where $\Delta\delta_{\mathrm{H,N}}$ is the CSP, and $\Delta\delta_{\mathrm{H}}$ and $\Delta\delta_{\mathrm{N}}$ are the chemical shift differences along the proton and nitrogen dimensions, respectively. All the CSPs are plotted as scatter plots in Figure 3-5. The results show a smaller and more uniform CSP between the SapA-DMPC/DMPG and ΔH5-DMPC/DMPG spectra, with a mean value of 0.13 ± 0.08 ppm. A much wider distribution with a mean value of 0.21 ± 0.18 ppm is observed in the comparison of SapA nanoparticles with DPC micelles. These results show that the spectrum of OmpX in SapA-DMPC/DMPG is more similar to the spectrum of OmpX in ΔH5-DMPC/DMPG. This again is supportive of a proper incorporation of the protein into the DMPC/DMPG bilayer provided by SapA-DMPC/DMPG nanoparticles.

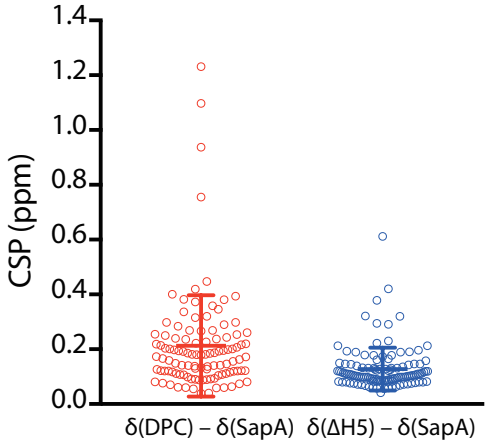

Figure 3-5: Spectral similarities of OmpX in different membrane mimetics.

Comparison of backbone amide chemical shifts of OmpX in SapA-DMPC/DMPG nanoparticles with OmpX solubilized in DPC micelles (red) or MSP1D1ΔH5-DMPC/DMPG nanodiscs (blue).[77] Weighted chemical shift perturbations (CSPs) were calculated for all the assigned residues and plotted as scatter plot. The mean value and the standard deviation are indicated.

This section has confirmed the suitability of SapA lipid nanoparticles for solution NMR studies and their ability to provide high resolution membrane protein NMR spectra. The comparison of protein occupied $SapA_3$-DMPC nanoparticles and ΔH5-DMPC nanodiscs revealed that OmpX was in a similar chemical environment, consisting of a DMPC lipid bilayer. In the case of OmpX, comparable nanoparticles were smaller than their typically used nanodisc counterparts

3.2.3 Influence of the phospholipid aliphatic chain on OmpX

Following the successful incorporation of OmpX into $SapA_3$-DMPC nanoparticles we started to investigate the influence of phospholipid side-chain length and side-chain saturation level on OmpX. Expanding on the results obtained using DMPC, we decided to test DPPC and POPC, both of which contain the same PC headgroup, to assess the influence of aliphatic chain length and the degree of unsaturation. The molecular structures of DMPC, DPPC, and POPC are depicted in Figure 3-6 A-C at the same overall scale. A comparison between DMPC and DPPC shows an increase in the length of the side chain through the introduction of an additional ethyl group, while a

comparison of DPPC and POPC shows the effect of an additional double bond in the aliphatic side-chain at position nine.

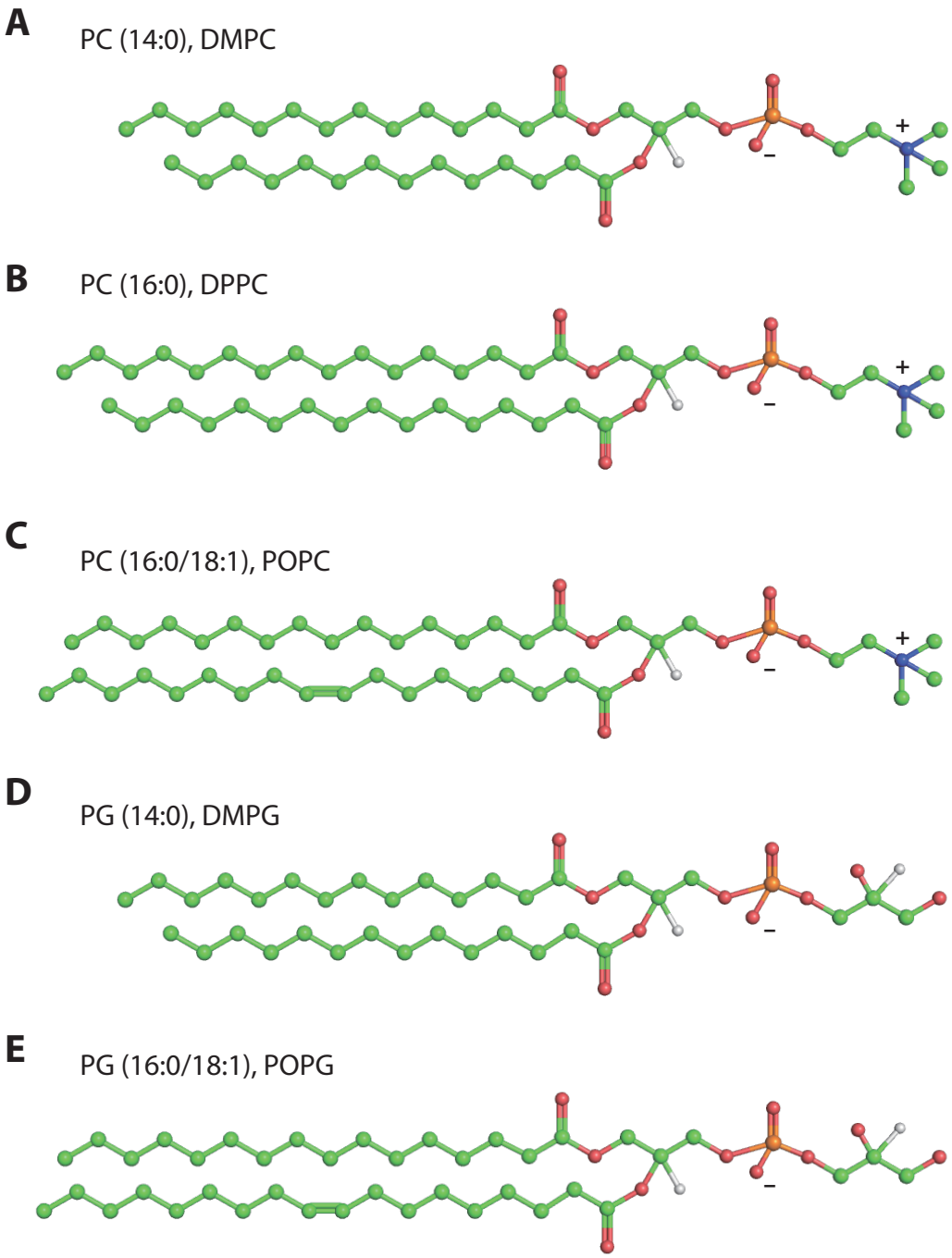

Figure 3-6: The structure of the lipids used in this study.

A) DMPC, B) DPPC, C) POPC, D) DMPG, and E) POPG. Carbon (green), oxygen (red), phosphorus (orange), nitrogen (blue), and hydrogen (white) are shown in sphere representation.

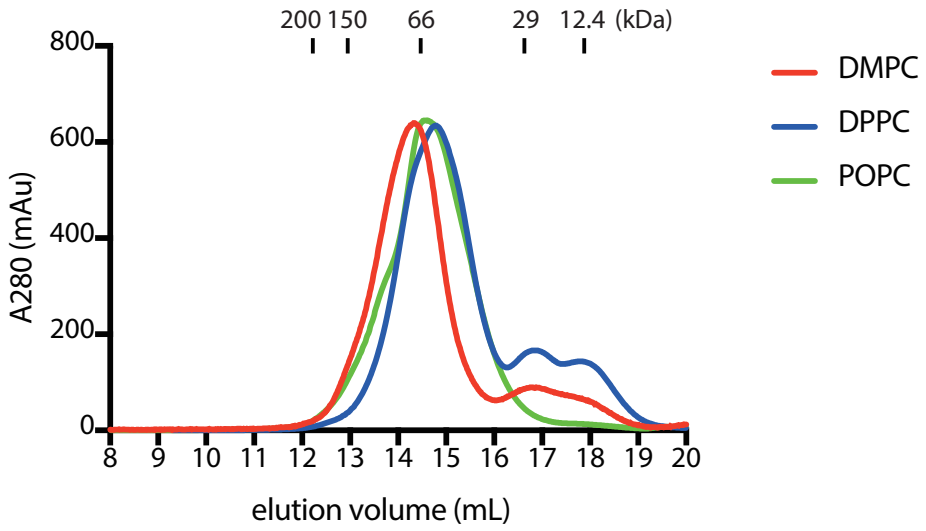

Figure 3-7: SEC of OmpX in different phosphocholine lipids.

The SEC profile of OmpX in SapA-DMPC (red), SapA-DPPC (blue), and SapA-POPC (green) are overlaid. The profile of OmpX in SapA-DMPC (red) is the same one as in Figure 3-3 A with A280 values scaled up 2.3 times for easier comparison in this figure.

OmpX was incorporated into SapA-DPPC nanoparticles and SapA-POPC nanoparticles using the same protocol and same SapA:lipid:OmpX ratio as that used for SapA-DMPC nanoparticles. SEC showed similar elution profiles with a little variation in the peak position (Figure 3-7). The exact reason for this variation is unclear. It could be that the longer aliphatic chain, which should produce a lower transition temperature would generate a less dynamic, more ordered and compact bilayer, leading to slightly smaller SapA lipid nanoparticles. Nevertheless, the sizes of the OmpX embedded nanoparticles are all in the same region, so it is clear that OmpX is in $SapA_3$ lipid nanoparticles regardless of the lipids used for incorporation. Elution fractions 13–16 mL were collected and concentrated for NMR experiments.

Figure 3-8 (*opposite*): NMR spectra of OmpX in DPPC and POPC.

2D [^{1}H,^{15}N]-SOFAST-TROSY spectra of non-deuterated ^{15}N-labelled OmpX in A) SapA-DPPC nanoparticles and B) SapA-POPC nanoparticles. The spectra were recorded at 318 K on a Bruker Avance AVIII 800 spectrometer (^{1}H frequency of 800 MHz) equipped with a 5 mm TXI HCN/z cryoprobe. The experiments were recorded with 3,078 scans, resulting in an experiment time of 36 h.

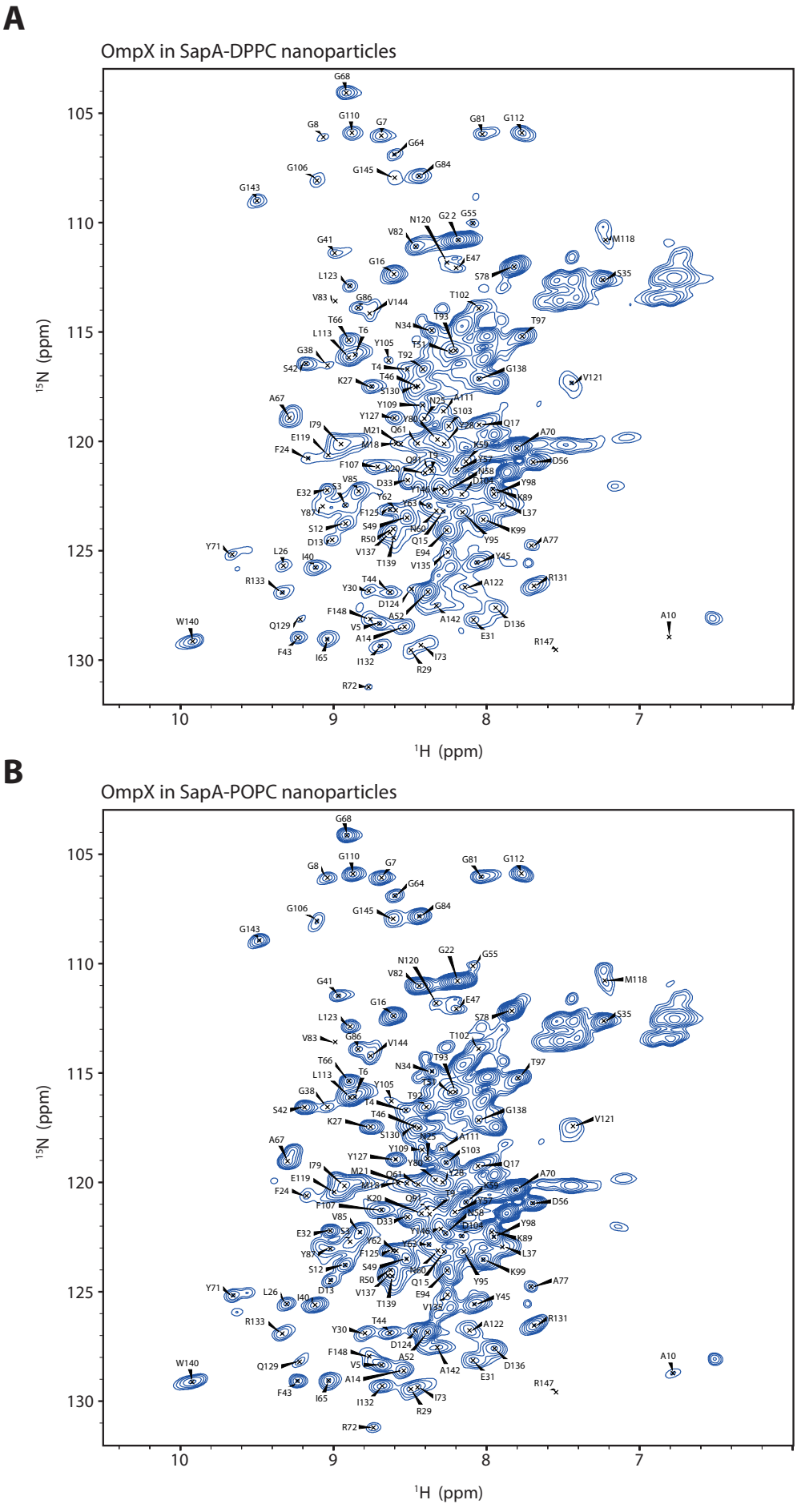
A
OmpX in SapA-DPPC nanoparticles
B
OmpX in SapA-POPC nanoparticles
^{15}N (ppm)
^{1}H (ppm)
105
110
115
120
125
130
10
9
8
7

A 2D [^{1}H,^{15}N]-SOFAST-TROSY spectrum was recorded for each nanoparticle sample containing OmpX embedded in either DPPC or POPC (Figure 3-8). Because the spectra of OmpX in DPPC and POPC are very similar to that in DMPC, the original 121 OmpX backbone assignments from the DMPC spectrum (Figure 3-4 A) could all be transferred unambiguously onto the new spectra based on peak position similarity. The weighted chemical shift perturbations were then calculated for each residue to report on the influence of the lipid side chain on the OmpX structure.

Firstly, the TROSY spectrum of OmpX in DPPC was examined. The resulting spectrum was very similar in terms of the peak position to that for DMPC, allowing all the assignments to be transferred unambiguously. The weighted chemical shift perturbations relative to the DMPC spectrum are shown in Figure 3-9 A. Based on these chemical shift differences, the chemical environment that DPPC provides is overall very similar to that of DMPC, with only approximately 2% of the peaks shifting by more than 0.1 ppm. This indicates that within the small range explored in this work, aliphatic chain length has only a minor effect on the structure of OmpX. In a situation of hydrophobic mismatch,[152] i.e. where the thickness of the hydrophobic transmembrane region of the protein is larger or smaller than the hydrophobic part of the lipid bilayer, there are several possible adaptations that the protein or membrane bilayer can make in order to avoid the unfavourable exposure of hydrophobic regions to water. The lipid bilayer has the ability to adjust itself by stretching, squashing, and/or tilting of the lipid chains to match the hydrophobic surface of the membrane protein.[153,154] Membrane proteins, on the other hand, can tilt with respect to the membrane bilayer to reduce effective hydrophobic thickness, or their hydrophilic and hydrophobic side-chains near the membrane-water interface can adopt different conformations. Alternatively, membrane proteins can aggregate if the hydrophobic mismatch cannot be compensated. However, previous studies on bacteriorhodopsin showed that this protein is rather tolerant to changes in membrane thickness and that within a range of 4 Å thicker and 10 Å thinner than the estimated thickness of the protein there was no sign of aggregation.[155] It is not surprising therefore that the chemical environment of OmpX, with a thickness of 23.6 ± 2.8 Å estimated by the OPM database,[156] remained similar in DMPC with a bilayer thickness of 25.4 Å[157] and DPPC with a bilayer thickness of 28.4 Å.[157]

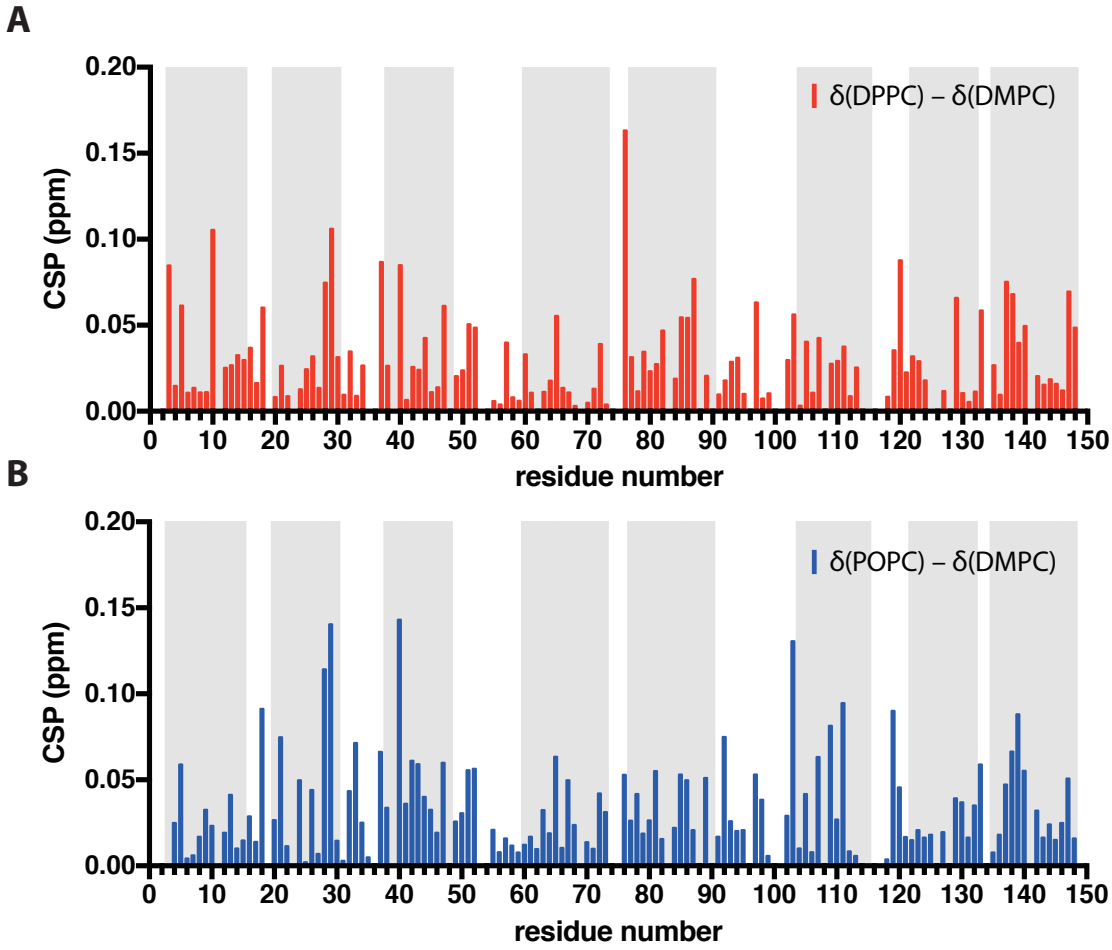

Figure 3-9: The effect of lipid aliphatic chain on the chemical environment of OmpX.

Weighted chemical shift perturbation between A) OmpX in DPPC and in DMPC and B) OmpX in POPC and in DMPC. Secondary structure is shown with grey bars indicating the β-sheet regions.

A similar type of analysis was repeated for OmpX in POPC. The results of the chemical shift perturbation calculation are shown in Figure 3-9 B, revealing that changes against DMPC were again only minor. However, larger perturbations were observed for some regions, i.e. residues 40–48, 102–111, 129–131, when compared to the effects of DPPC. The thickness of the POPC bilayer is reported to be 27.2 Å, in between that of DMPC and DPPC,[157] hence, these larger chemical shift perturbations are unlikely to be the result of differences in membrane thickness. It has been shown previously that introducing a double bond into the lipid acyl chain can not only result in a decrease in membrane thickness but also an increase in surface area per lipid, a decrease in direct head group interactions, and an increase in membrane fluidity.[158] It is possible that the

larger differences observed result from a change in membrane fluidity and the transient interaction between the double bond and the membrane protein. However, it is not clear how the concept of membrane fluidity can be transferred onto small lipid rafts such as nanoparticles. In addition, it has to be assumed that the fast exchange of lipid molecules within the bilayer would average out such effects and lead to only subtle chemical shift changes, unless some very specific interactions were involved that would lead to long lipid residence times. It is quite possible that OmpX, as a β-barrel protein, has a sufficiently large number of hydrogen bonds that hold the backbone of the protein together and thus limit the amount of adaptability of the protein within the transmembrane region. Therefore, this stably assembled β-barrel protein might be less sensitive to the effects of lipids with different aliphatic chain lengths. In contrast, helical membrane proteins are likely to be more dynamic, with individual helices packing against each other through weaker side-chain hydrogen bonds and hydrophobic interactions. This implies that changes in the lipid bilayer that result from variations in aliphatic side chain length would affect helical membrane proteins more dramatically by altering weak inter-helix contacts or through changes in membrane fluidity. However, these conclusions will need further experimental data to support.

3.2.4 Influence of anionic lipids on OmpX

It is becoming increasingly clear that lipids, especially charged ones, in many cases not only provide a lipid bilayer environment to accommodate membrane proteins but also participate in modulating the structure and function of embedded proteins. For example, it was shown in a crystallography study that binding to the negatively charged phosphatidylinositol 4,5-bisphosphate (PIP2) induces a large conformational change of the cytoplasmic domain of the Kir2.2 channel, which translates into a 6 Å domain movement.[159] PIP2 also binds to the intracellular side of the β_1-adrenergic receptor to stabilise its active conformation and enhance selective binding to G_s over binding to other G proteins.[160] It has also been reported that the β_2-adrenergic receptor in PG lipid nanodiscs markedly favoured agonist binding and that the negatively charged lipid promoted receptor activation, whereas phosphatidylethanolamine favoured antagonist binding and stabilised the inactive conformation.[161] Despite a large number of molecular dynamics (MD) simulation studies that are investigated the ability of charged lipids to modulate the structure and function of membrane proteins,[162] direct

experimental evidence is still scarce and the underlying molecular basis of these lipid-induced effects are not clear.

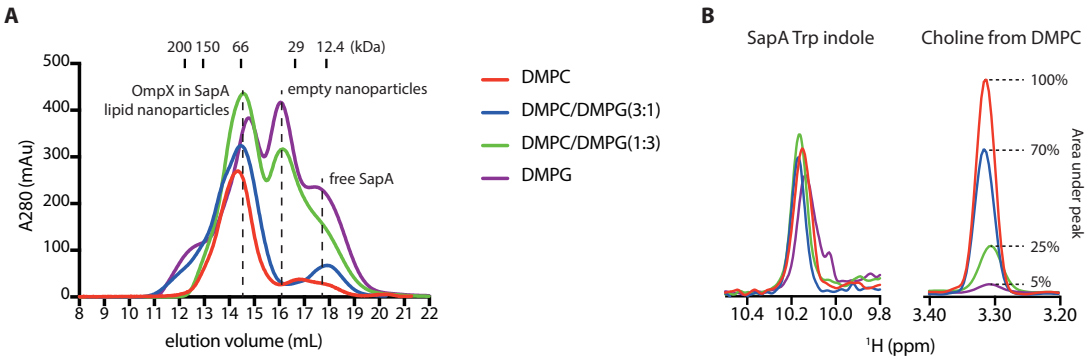

Figure 3-10: Characterisation of OmpX in SapA-DMPC/DMPG nanoparticles.

A) SEC of OmpX in SapA-DMPC (red), SapA-DMPC/DMPG (3:1) (blue), SapA-DMPC/DMPG (1:3) (green), and SapA-DMPG (purple). The peaks corresponding to empty nanoparticles and free SapA are indicated. The main peaks eluted at 13–15 mL are OmpX in SapA lipid nanoparticles. B) 1D proton NMR shows the SapA Trp indole signal and the choline proton signal originating from DMPC. The spectra are normalised based on the SapA Trp indole signals so a quantitative analysis of DMPC can be performed. Colour code is the same as A).

Here, we investigated the effect of introducing lipids with a negatively charged headgroup by comparing NMR spectra of OmpX in nanoparticles with anionic DMPG with those containing zwitterionic DMPC. As the only difference between these two lipids is their headgroup, PG for DMPG and PC for DMPC, any spectral changes observed should relate to variation in the headgroups and in particular their differing charges.

OmpX was incorporated into SapA lipid nanoparticles using the same protocol as before. Four samples were prepared with different lipid compositions: DMPC, DMPC/DMPG (3:1), DMPC/DMPG (1:3) and DMPG. Their resulting particle sizes were similar, as determined by size-exclusion chromatography (Figure 3-10 A). The overall incorporation yield was similar across the four tested lipid compositions. There were much more empty nanoparticles and free SapA in SapA-DMPC/DMPG (1:3) and SapA-DMPG due to an experimental error. These two samples contained an unintentionally higher ratio of SapA in the initial mixture because of an overestimation in the concentration of the SapA stock solution. Nevertheless, this error did not affect

the incorporation of OmpX and still produced a similar amount of sample. Size-exclusion fractions between 13 mL and 15 mL were collected and concentrated for NMR measurements. NMR samples with about 200 μM OmpX were obtained in all four conditions. The samples were first checked using 1D ^{1}H NMR. The quantity of DMPC in the sample could be compared using the peak corresponding to choline protons at around 3.3 ppm (Figure 3-10 B). The four spectra were scaled according to the SapA tryptophan indole proton signal (Figure 3-10 B, left), normalizing the effect of sample concentration, so the choline signal should reflect the amount of DMPC per particle. As expected, the choline proton signal of DMPC decreased as the DMPC ratio in the sample was reduced. The area under the choline peaks was calculated and normalized against the result from the pure DMPC spectrum. The results showed 100%, 70%, 25%, and 5%, respectively, which are close to what we would expect from the mixing ratio. There was still a small signal (5%) in the purple DMPC spectrum probably due to a tiny amount of detergent DPC, which also contains choline protons, remaining in the sample.

For each of the samples a 2D [^{1}H, ^{15}N]-SOFAST-TROSY spectrum was also recorded (Figure 3-11 A). A gradual shift of peak positions upon an increase in the DMPG contribution could be observed as shown in full and selected regions of an overlay of the four spectra (Figure 3-11). This suggests that the observed changes correlate with changing amounts of DMPG in the lipid bilayer. With the gradual peak shift, we could carefully follow the peak movement and transfer all the peak assignments from the DMPC spectrum. This allowed us to investigate in more detail which parts of OmpX were affected by switching from DMPC to DMPG. Interestingly, the two residues F24 and Y87, which showed the largest chemical shift perturbations seemed to be strongly broadened in the spectra with the larger DMPC content (pure DMPC and DMPC/DMPG 3:1), indicating a chemical exchange process on a slow-to-intermediate timescale (Figure 3-11 B). In contrast, these residues were much sharper in environments with higher DMPG content (DMPC/DMPG 1:3 and pure DMPG). This suggests that changes in the lipid composition also affect the dynamics of embedded membrane proteins. It could be that in a DMPC bilayer F24 and Y87 exchange between multiple conformations, and that increasing amounts of negatively charged DMPG stabilise a single conformation resulting in single sharp peaks. In contrast, the W140 indole sidechain signal showed a linear shift without changing its peak intensity. This

means that increasing the amount of DMPG changes the chemical environment around W140 sidechain as one might expect, but does not perturb the energy landscape of the W140 residue.

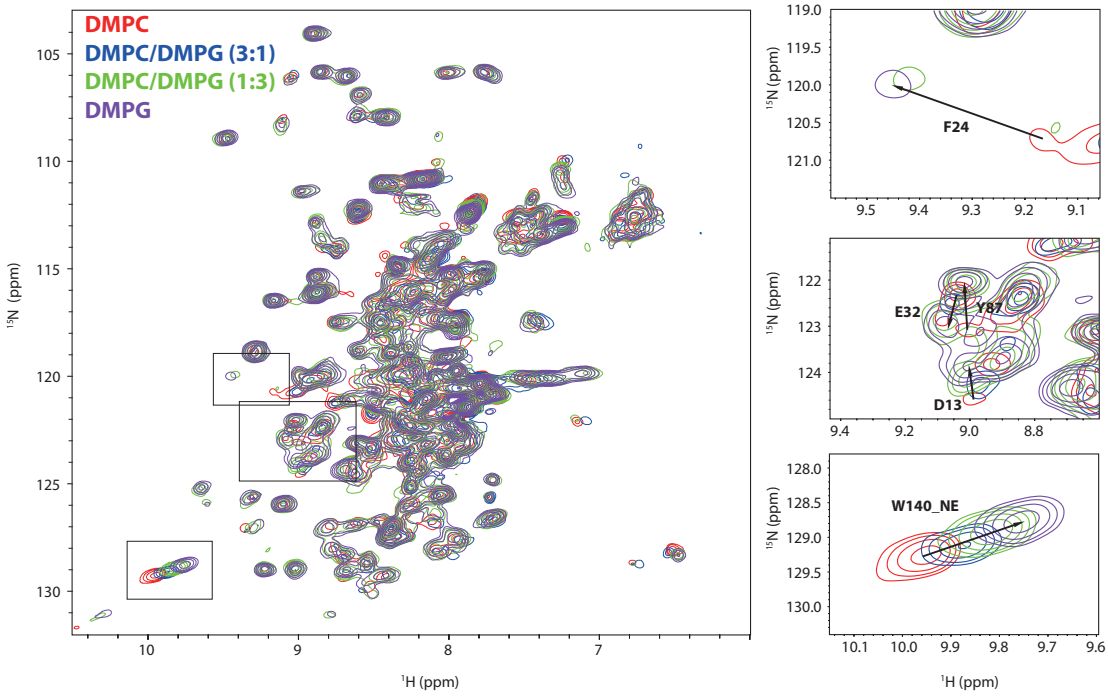

Figure 3-11: Comparison of the chemical environment of OmpX in SapA-DMPC/DMPG nanoparticles.

Overlays of 2D [^{1}H, ^{15}N]-SOFAST-TROSY experiments of OmpX in SapA-DMPC (red), SapA-DMPC/DMPG (3:1) (blue), SapA-DMPC/DMPG (1:3) (green), and SapA-DMPG (purple). Selected regions are indicated and zoomed in on the right panels. Some of the residues that are significantly affected by the changes in the composition of the lipid bilayer are highlighted in the zoomed in spectra.

The weighted chemical shift perturbations between the pure DMPG and pure DMPC samples were calculated and plotted against residue number (Figure 3-12 A). The result shows over 20% of the peaks shifting by more than 0.1 ppm. This is clearly much more than the 2% observed when comparing the influence of the side chains between DPPC and POPC (3.2.3). This means the chemical environment of OmpX is much more sensitive to the headgroup charge than to lipid side chain composition. We also calculated the standard deviation of all the chemical shift perturbations and defined significantly perturbed residues as those with perturbations greater than two standard deviations away from the mean value. We mapped the chemical shift perturbations onto

the structure with significantly perturbed residues shown in spheres (Figure 3-12 B). Several hydrophobic residues (F24, W76, Y87, and W140) located at the membrane-water interface show significant shifts. It has been proposed that aromatic amino acids especially tryptophan and tyrosine with amphipathic characteristics are enriched in interfacial regions of membrane proteins,[163] where they are thought to help anchor proteins at the bilayer-water interface.[164,165] Because these residues are close in space to lipid headgroups, their chemical shifts are very sensitive to changes in lipid headgroups especially from a zwitterionic to an anionic headgroup. It is also possible that DMPG with its negatively charged headgroup can affect the orientation of the protein in the lipid bilayer, leading to significant chemical shift perturbations for these aromatic residues. There are also several residues located on the solvent exposed loops, which are strongly affected by DMPG. Some negatively charged residues in the intracellular side (E32, D33, E119) show significant perturbations probably due to electrostatic repulsion with the negatively charged membrane surface. Some polar residues on the extracellular loop (T51, Q91, T92, S103) are affected probably due to interactions with the hydroxyl group on the PG.

Figure 3-12 (*opposite*): The effect of DMPG on the chemical environment of OmpX.

A) Weighted chemical shift perturbation between OmpX in SapA-DMPG nanoparticles and OmpX in SapA-DMPC nanoparticles were calculated and plotted against the residue number. The secondary structure of OmpX is shown with grey bars. A standard deviation of all the chemical shift perturbations was calculated and the value two times the standard deviation is indicated by the red dotted line. B) The chemical shift perturbations, δ(DMPG) – δ(DMPC), are mapped onto the structure with increasing changes coloured gradually from blue to red. The significantly perturbed residues with chemical shift changes larger than two standard deviations are shown in spheres.

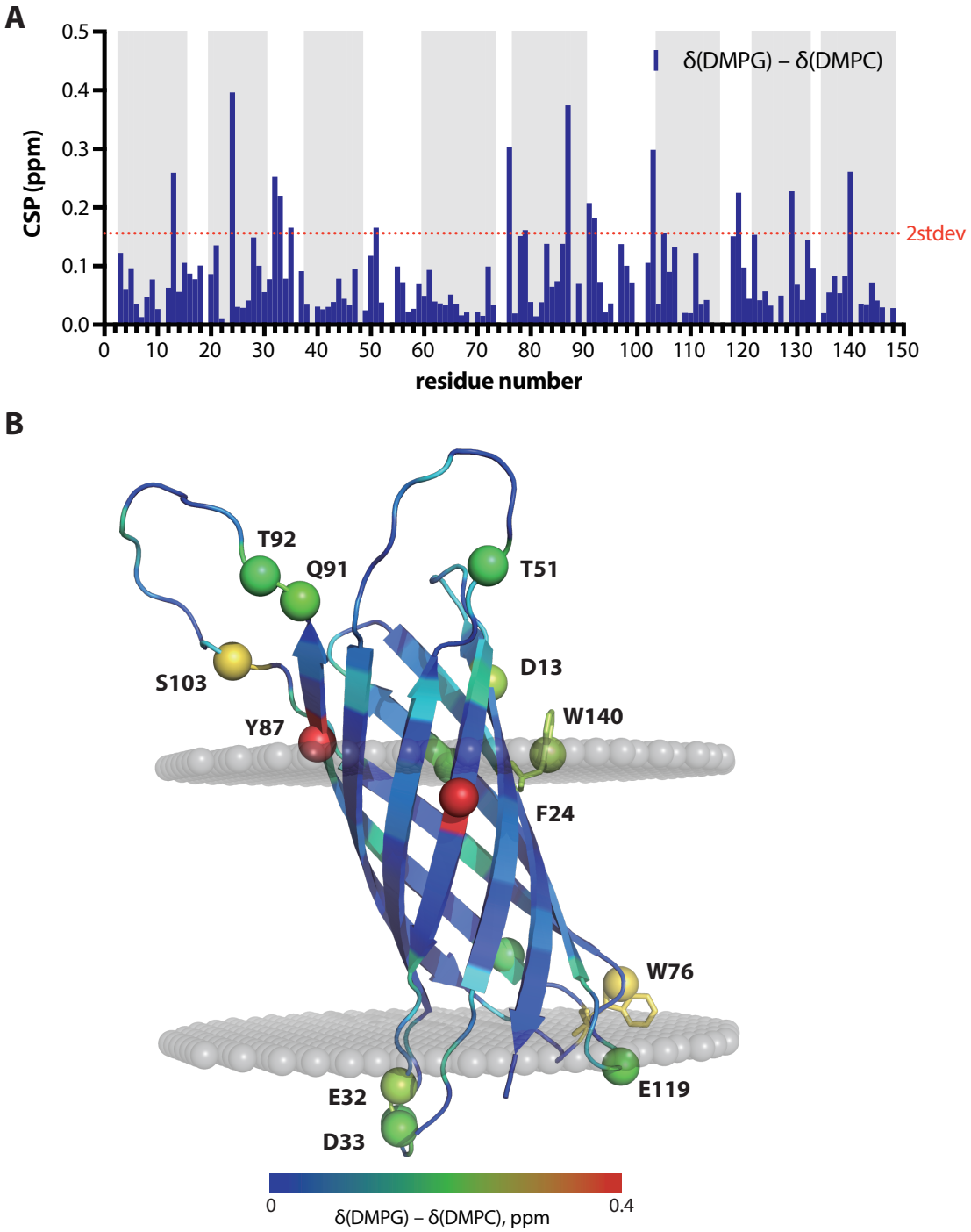

Additional experiments were performed in order to confirm the observed effect of the PG head group on the structure of OmpX. OmpX was incorporated into SapA$_3$-POPG nanoparticles using the same protocol and assembly ratio and then a 2D TROSY spectrum was recorded. This data in comparison with the SapA$_3$-POPC spectrum in section 3.2.3 was expected to confirm again the effect of the PG head group. The weighted chemical shift perturbations between POPG and POPC were calculated and plotted together with those between DMPG and DMPC (Figure 3-13). The results show

a very similar pattern, suggesting that the effect of the lipid headgroup is dominant and independent from the aliphatic chain length or the saturation degree of the lipids.

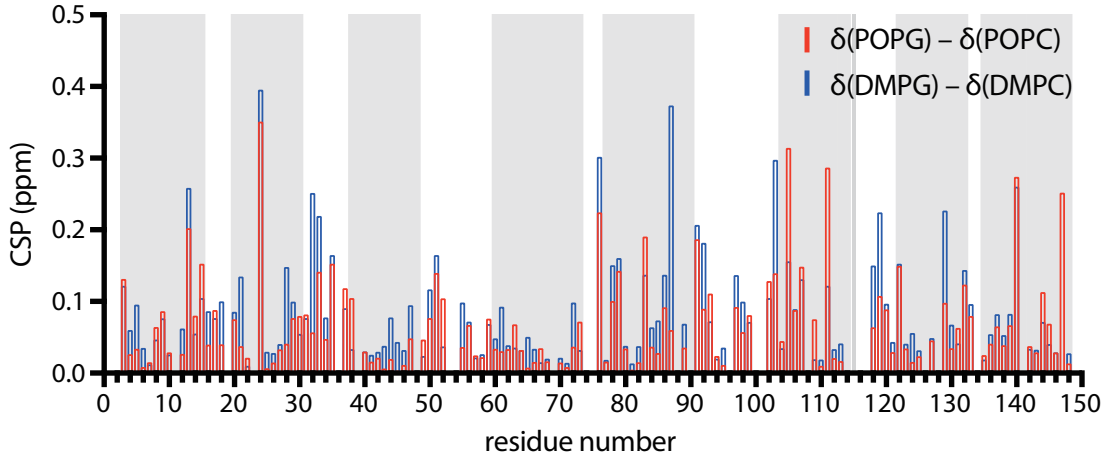

Figure 3-13: The effect of anionic lipid head group on OmpX.

Weighted chemical shift perturbation of OmpX in SapA$_3$-POPG nanoparticles compared to that in POPC (red) are plotted against residue number and overlaid with the chemical shift perturbation between DMPG and DMPC (blue).

3.2.5 Attempt to include lipopolysaccharides into SapA-DMPC nanoparticles

In its natural environment, OmpX is found in the bacterial outer membrane which is rich in lipopolysaccharides (LPS). LPS, also known as endotoxins, are molecules consisting of a lipid A, a core oligosaccharide, and an O-polysaccharide joined by covalent bonds (Figure 3-14). LPS provides structural integrity for the bacteria and protects the membrane from certain chemicals that are harmful to bacteria.[166] LPS is essential for many Gram-negative bacteria, which cannot survive without it.[167] It has been proposed that LPS interacts directly with OprH, an outer membrane protein of *Pseudomonas aeruginosa*, showing predominantly electrostatic interactions with charged residues near the membrane-water interface and loops on the extracellular region to be important.[168,169] Based on the significant perturbations caused by the PG headgroup observed in section 3.2.4, we hypothesised that the extracellular loops of OmpX may have specific interactions with LPS, similar to OprH, that might be important to its function. Therefore, we aimed to incorporate OmpX into SapA-DMPC/LPS nanoparticles to see if this would lead to significant differences in the 2D NMR spectrum of OmpX.

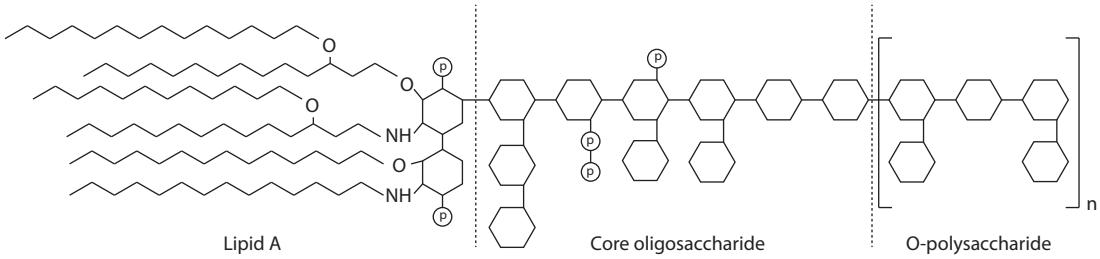

Figure 3-14: Schematic structure of LPS.

Three main components of LPS, lipid A, Core oligosaccharide, and O-polysaccharide, are shown in a schematic representation. Carbohydrates are simplified to hexagons and phosphate groups are shown in circles annotated by p.

Together with a Part II student, Daniel Gentle, we first tried to generate SapA-DMPC/LPS nanoparticles. SapA and DMPC were mixed at a ratio of 1:15, the same as previously used in Chapter 2, as this combination was known to generate $SapA_3$-DMPC nanoparticles, and were supplemented with 1 mg/mL LPS. The molarity of LPS could not be determined accurately as the material used was an extract from *E. coli* (L8274, Sigma) which is a mixture of LPS with different length of O-polysaccharides. DDM (0.2%) was added to the mixture before incubation with Amberlite beads. The SapA-DMPC/LPS sample was then analysed by a SEC experiment (Figure 3-15 A). Surprisingly, the sample appeared to be similar in size to $SapA_3$-DMPC nanoparticles (Figure 2-12). One would expect a much larger particle size because contributions from the extended O-polysaccharides. The SEC fractions were checked using silver stained SDS-PAGE, in which an additional band at around 10 kDa was visible. A similar band appeared in a lane loaded with the original LPS stock solution, therefore we hypothesised that this band corresponds to LPS molecules. Next, we used different amounts of LPS in the assembly mixture and performed the same experimental procedure. The final SEC fractions showed higher LPS band intensity with increasing amounts of LPS in the initial mixture (Figure 3-15 B). However, surprisingly the particle size did not change with more LPS in the SapA-DMPC nanoparticle mixture. We also attempted to generate larger SapA-DMPC nanoparticles, $SapA_4$-DMPC, with 1 mg/mL LPS, and indeed the silver-stained gel showed LPS bands in the main peak, eluting earlier than that of $SapA_3$-DMPC (Figure 3-15 C).

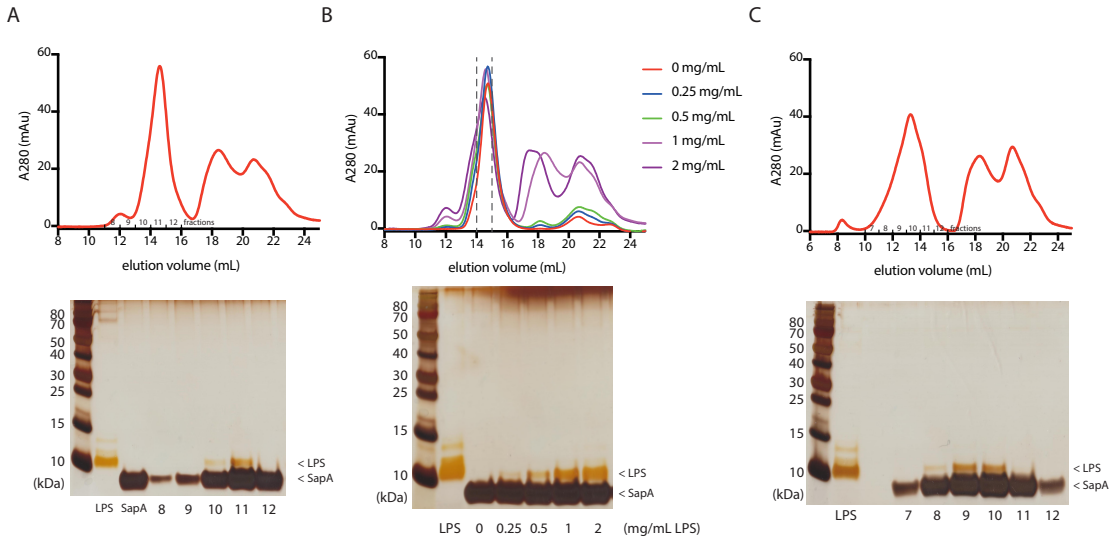

Figure 3-15: Incorporation of LPS into SapA-DMPC nanoparticles.

A) SEC of 1 mg/mL LPS in SapA$_3$-DMPC nanoparticles. B) SEC of SapA$_3$-DMPC nanoparticles prepared in the presence of varying amounts of LPS (0–2 mg/mL). The SEC fraction collected between the two dashed lines is analysed by silver-stained SDS-PAGE. C) SEC of LPS in SapA$_4$-DMPC nanoparticles. SEC trace with corresponding silver-stained SDS-PAGE shown below. The bands corresponding to LPS and SapA are indicated.

Although the SDS-PAGE showed that LPS bands always appeared in the same fractions as SapA-DMPC and the band intensity was proportional to the amount of LPS used in the assembly mixture, we wanted to confirm the presence of LPS by other analytical tools such as 1D ^{1}H NMR spectroscopy or electrospray ionisation mass spectrometry (ESI-MS). Two samples were examined, SapA-DMPC and SapA-DMPC/LPS. By carefully comparing NMR spectra and ESI-MS spectra, however, we were not able to observe any differences between these two samples (Figure 3-16). We concluded that LPS could not be detected either by NMR spectroscopy or ESI-MS.

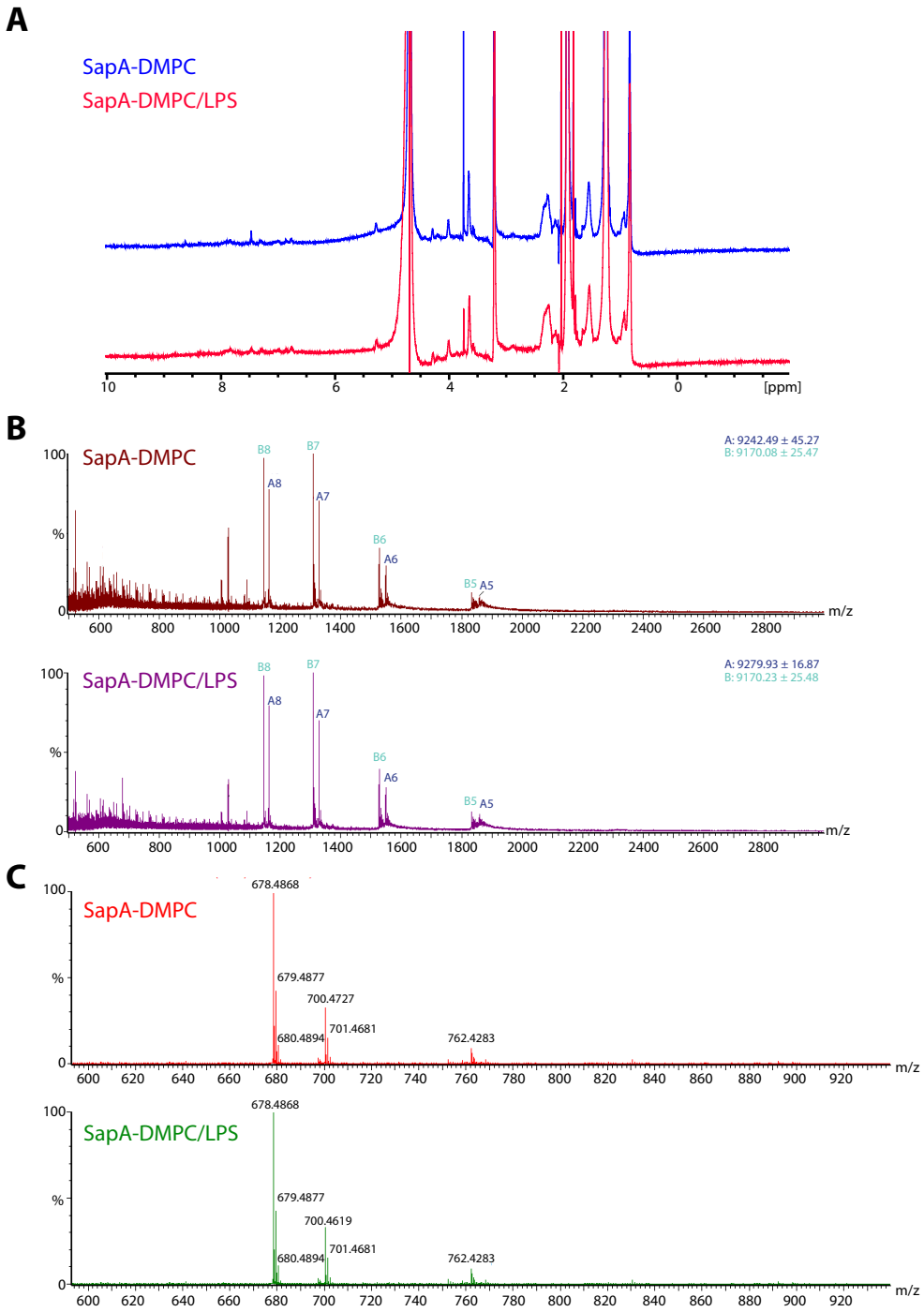

Figure 3-16: Attempts to identify LPS using analytical tools.

A) 1D proton NMR spectrum of SapA-DMPC and SapA-DMPC/LPS. ESI-MS spectrum of SapA-DMPC and SapA-DMPC/LPS in B) protein region and C) lipid region. SapA with the molecular weight of 9.2 kDa and DMPC with the theoretical molecular weight of 677.5 Da were identified in both samples. Both NMR and mass did not indicate any differences between these two samples.

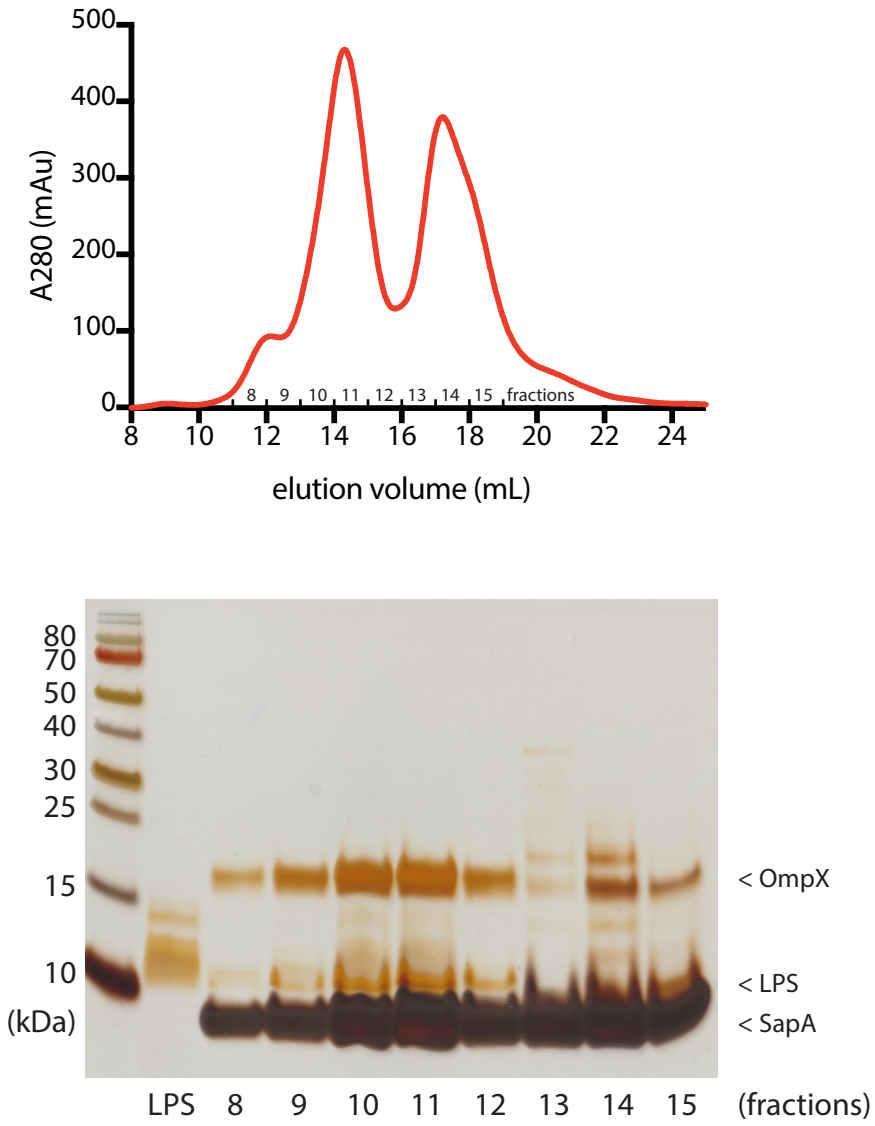

Figure 3-17: SEC of OmpX in SapA$_3$-DMPC/LPS nanoparticles.

OmpX was incorporated into SapA$_3$-DMPC in the presence of 1 mg/mL LPS in the initial mixture. The resulting sample was checked by SEC shown in the top panel. Silver-stained SDS-PAGE of the corresponding SEC fractions are shown at the bottom. The bands that correspond to OmpX, LPS, and SapA are indicated.

Even though two analytical tools did not show the presence of LPS, it is possible that the intrinsic limitations of the techniques prevented the detection of LPS. We decided to take one step further to incorporate ^{15}N-labelled OmpX into SapA-DMPC/LPS nanoparticles and record a 2D NMR spectrum to see if any conformational changes of OmpX could be observed. The assembly ratio was 10:50:1 (SapA:DMPC:OmpX), the same as in section 3.2.1, with an addition of 1 mg/mL LPS in the mixture. The SEC

profile showed a main peak at elution volume 14.3 mL (Figure 3-17), slightly smaller than OmpX in $SapA_3$-DMPC (14.1 mL, Figure 3-3 A). The same observation was made in Figure 3-15 B where the alleged incorporation of LPS hardly changed the particle size. A silver-stained SDS-PAGE gel (Figure 3-17) showed the presence of OmpX, SapA and LPS in the main peak, suggesting that OmpX had been successfully incorporated into SapA-DMPC-LPS nanoparticles. Fractions 14 and 15 contained mainly free SapA and the impurities carried from the SapA stock solution. A small amount of OmpX was also observed in these fractions which was probably denatured OmpX nonspecifically interacting with SapA. We then pooled fractions 9–12 and concentrated them to 400 µL for 2D NMR experiments.

The TROSY spectrum of OmpX in SapA-DMPC/LPS nanoparticles was as good in quality as that obtained in SapA-DMPC (Figure 3-18 A). All the assignments could be transferred for CSP analysis and the spectra superimposed very well. The chemical shift perturbations of the sample that was intended to contain LPS showed only minor differences with an average of 0.038 ppm (Figure 3-18 B). This was surprising because the effect of LPS appeared to be much smaller than the effect of the PG head group. Based on the resulting TROSY spectrum, 1D ^{1}H NMR spectra, mass spectra, and SEC analysis, we concluded that LPS was not incorporated into SapA-DMPC nanoparticles. We have to assume that the 10 kDa band observed in the silver-stained SDS-PAGE gel was something else. It could be nucleotides or proteins carried from the LPS stock solution which interact with SapA-DMPC nanoparticles and hence elute together in SEC. However, we also could not identify this substance by NMR spectroscopy or mass spectrometry.

Currently, we have only limited information on the composition of the LPS extract from Sigma, e.g. O-polysaccharide length and purity, making the interpretation of our data difficult. We suspect that the long polysaccharide head group makes LPS highly soluble, which removes the driving force that promotes bilayer formation. In the case of SapA-DMPC nanoparticles, DMPC was solubilised in DDM at the beginning. When DDM was removed by Amberlite beads, DMPC molecules were forced to form a bilayer surrounded by SapA molecules because of low solubility on their own. LPS in contrast is highly soluble in water and can form micelles. Accordingly, it will have a very low propensity to form a pure LPS bilayer and hence is unlikely to form lipid nanoparticles with SapA. If bilayer formation could be achieved this would require dramatic changes to the incorporation protocol as detergent removal does not trigger LPS bilayer

incorporation. Therefore, we hypothesised that using a less soluble version of an LPS with reduced polysaccharide content, e.g. lipid A or lipid A with core oligosaccharides, might increase the possibility of incorporation. These experiments will be conducted in the future. In summary, further experiments are necessary to investigate the interactions between OmpX and LPS.

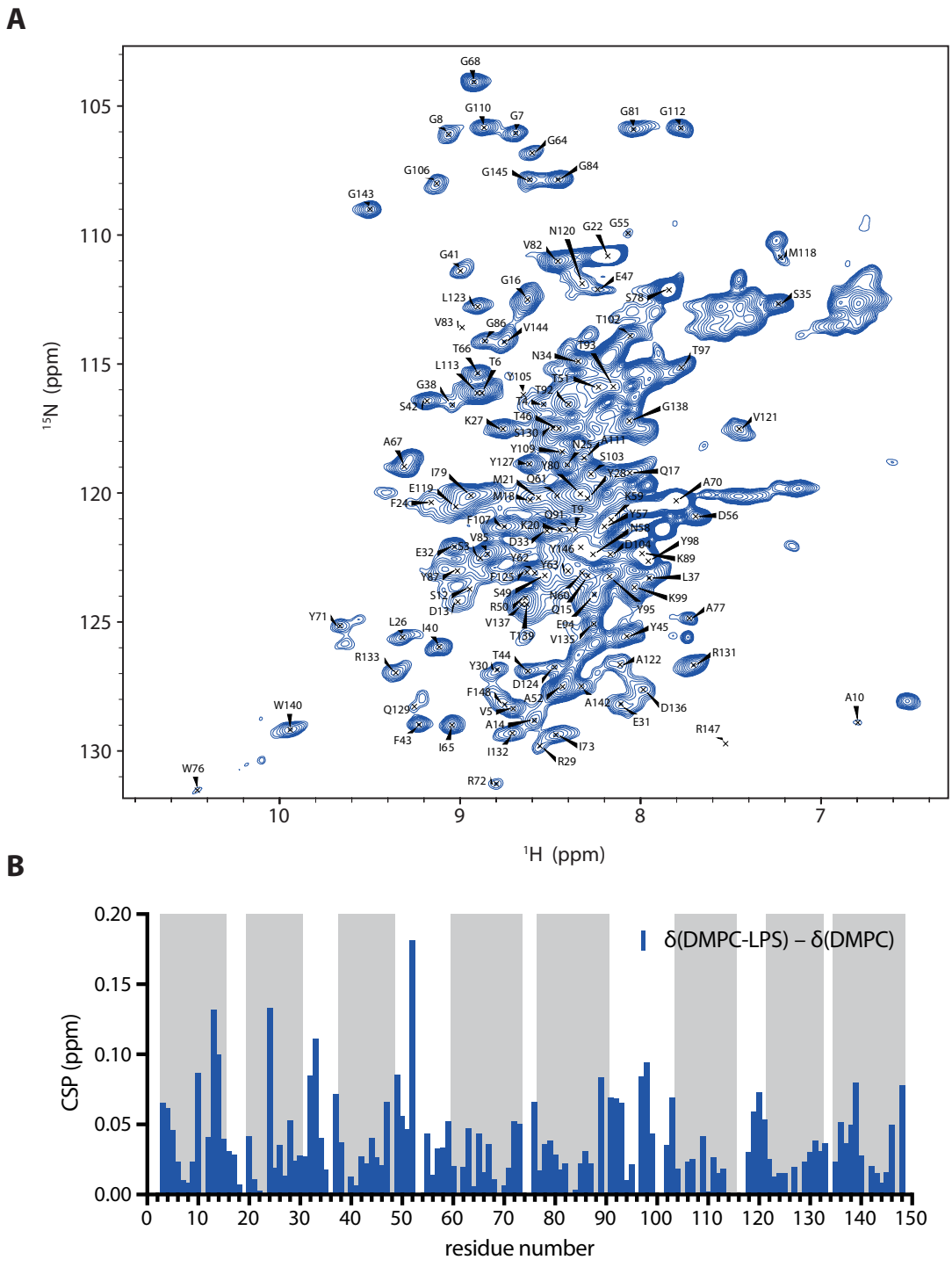

Figure 3-18 (*opposite*): NMR spectrum of OmpX in SapA-DMPC-LPS nanoparticles.

A) 2D [^{1}H,^{15}N]-SOFAST-TROSY spectrum of non-deuterated ^{15}N-labelled OmpX in SapA-DMPC-LPS nanoparticles. The spectrum was recorded at 318 K on a Bruker Avance AVIII 800 spectrometer (^{1}H frequency of 800 MHz) equipped with a 5 mm TXI HCN/z cryoprobe. The experiments were recorded with 3,078 scans, resulting in an experiment time of 36 h. B) Weighted chemical shift perturbations between OmpX in SapA-DMPC-LPS nanoparticles and OmpX in SapA-DMPC nanoparticles were calculated and plotted against the residue number. The secondary structure of OmpX is shown with grey bars.

3.3 Conclusions

This chapter demonstrated the successful incorporation of OmpX into SapA nanoparticles. The nanoparticles provide a similar lipid bilayer environment to conventional MSP nanodiscs. Incorporation yields were consistently high and allowed us to obtain high-quality [^{1}H,^{15}N] NMR spectra even in the absence of deuteration. Further, the good incorporation yields enabled a systematic investigation of the impact of lipid composition on OmpX structure. OmpX was incorporated into nanoparticles containing the lipids DMPC, DPPC, POPC, DMPG and POPG. By comparing the resulting NMR spectra, we concluded that aliphatic chain length and double bond content exert only a very moderate influence on the chemical environment of OmpX. In contrast, the negatively charged PG headgroups in DMPG and POPG significantly changed the chemical environment of the protein, especially for aromatic residues at the membrane-water interface and some of the charged residues in the loops. These spectroscopic studies confirmed the composition of the lipid bilayer as an important determinant of membrane protein dynamics and conformation and suggest that variations in lipid composition will affect protein function. A specific lipid environment might be necessary for a membrane protein to function, or the lipid environment may be able to modulate the function of a membrane protein through specific protein-lipid interactions possibly in the context of allostery. In view of the above-mentioned reasons, we attempted to incorporate LPS into the bilayer to better mimic the bacterial outer membrane and allow investigation of any interactions between OmpX and LPS. Our

preliminary data shows that the LPS did not go into the bilayer. We hypothesised that this was due to high solubility of LPS. Further experiments using shorter versions of LPS will have to be performed to delineate the interactions between OmpX and LPS. Nevertheless, SapA lipid nanoparticles provide an opportunity to investigate the effect of lipids. Variations in lipid composition might be important in localization and might change in different phases of the cell cycle. This study could open up a new research area investigating the effect of lipid modulation on protein function, where further spectroscopic studies would be paired with functional assay data.

4 INCORPORATION OF SEVEN-TRANSMEMBRANE PROTEINS INTO SAPA LIPID NANOPARTICLES

4.1 Introduction

4.1.1 Using Microbial rhodopsins as a model protein for incorporation

Chapter 3 showed that a β-barrel protein, OmpX, can be stabilised in SapA lipid nanoparticles and studied by NMR spectroscopy. To be a generalised membrane mimetic, it was hoped that SapA lipid nanoparticles could also be used to study α-helical transmembrane proteins by NMR spectroscopy. The microbial rhodopsins, *Anabaena* sensory rhodopsin (ASR) and *Natronomonas pharaonis* sensory rhodopsin II (pSRII), are suitable model systems for several reasons. Firstly, they are small enough for NMR and have been studied in detergent micelles by NMR in the past. Similar to the case for OmpX, this not only provides us with a good starting point in view of the construct and knowledge of protein production being available but also with regard to the NMR parameters being at hand for comparison. Secondly, ASR and pSRII can be expressed using the *E. coli* expression system with high yield. This is advantageous because isotope labelling, which is necessary for NMR studies, is well established in the *E. coli* expression system. Finally, microbial rhodopsins absorb visible light via their bound retinal chromophore which results in a sample with a visible colour and a

characteristic UV-visible light absorption profile. These aspects make it very easy to track the protein during experimental steps.

4.1.2 Microbial rhodopsins

Microbial rhodopsins are a group of light-sensitive membrane proteins that sense and respond to light. They are found in Archaea, Bacteria, and Eukaryota.[170] Microbial rhodopsins share a characteristic seven-transmembrane α-helical fold with a retinal chromophore covalently attached, which gives rise to the ability to sense light. The retinal isomerises as it absorbs a photon with wavelength 400–500 nm, initiating a conformational change in the microbial rhodopsin and triggering a down-stream signalling cascade. Microbial rhodopsins have a wide variety of functions. For example, bacteriorhodopsin is a light-driven proton pump,[171] halorhodopsin is an anion pump,[172] channelrhodopsin is an ion channel,[173] and sensory rhodopsin II is a negative phototaxis receptor.[174] Although microbial rhodopsins have no evolutionary link to GPCRs,[175] the overall seven-transmembrane helical architecture is similar, and they are therefore often considered as GPCR structural analogues or a model system for structural studies. We used two microbial rhodopsins in this chapter, ASR and pSRII.

4.1.3 Structure and function of ASR

ASR is a 30 kDa protein which covalently binds retinal at lysine 210, resulting in a strong absorbance at around 550 nm. ASR was the first microbial rhodopsin identified in bacteria that carries out a sensory function.[176] The distinct characteristic of ASR is its photochromism which does not exist in previously characterised microbial rhodopsins. The retinal chromophore in ASR exists in stable all-*trans* and 13-*cis* states and the two forms can be interconverted by light activation, at 550 nm to activate the all-*trans* state and at 537 nm for the 13-*cis* state.[177,178] All other microbial rhodopsins present a single stable all-*trans* state which is activated to 13-*cis* by light absorption and eventually relaxes back to the all-*trans* state. Given that ASR can sense different wavelengths of light, it has been proposed that the function of ASR is to optimise light harvesting according to the environment by modulating the gene expression level through its transducer ASRT.[178]

The structure of ASR has been solved by X-ray crystallography[179] and solid-state NMR in a lipid environment.[35] The oligomeric state of ASR observed in the two structures was different. A bacteriorhodopsin-like symmetric trimer was observed in the solid-

state NMR structure, in contrast to a dimer in the crystal structure. Additional paramagnetic relaxation enhancement data also supported a trimeric arrangement of ASR in both detergents and lipids.[180]

4.1.4 Structure and function of pSRII

pSRII is a 26 kDa protein that binds a retinal chromophore at lysine 205 which absorbs blue-green light at 498 nm. pSRII is responsible for phototaxis signalling. The signalling begins from blue light detected by pSRII leading to a conformational change in pSRII and its transducer protein (pHtrII). pHtrII initiates a His/Asp kinase signalling cascade, and the kinases regulate rotation of flagellum by phosphorylation, which eventually results in the archaeon moving away from the light.[174] pSRII is found expressed when the cell is in an environment that has sufficient oxygen supply and the respiratory activity is high, allowing the archaeon to migrate to the dark in order to avoid sunlight and potential photo-oxidative damage.[181] When the oxygen level drops, pSRII expression is suppressed and bacteriorhodopsin and halorhodopsin are synthesized to harvest orange light for energy (by ion pumping). In addition, the expression of SRI, having the opposite function to SRII, encourages the cell to move into a region containing orange light where the ion pumps can be maximally activated.[181]

The high stability and high expression yield of pSRII has allowed extensive structural studies including two crystal structures[182,183] and one solution NMR structure determined in our group.[30] The crystal structure of pSRII in complex with pHtrII was also solved, revealing a 2:2 stoichiometry.[184] The structure also shows that pHtrII is a membrane spanning protein with a long coiled-coil cytoplasmic domain. A number of crystal structures are also available of the protein in different light-activated states.[185]

4.1.5 Aim

The previous chapter established that SapA lipid nanoparticles can be used as a membrane mimetic system for NMR studies of the β-barrel protein OmpX. In order to confirm that the SapA system is a versatile tool that can be applied to membrane proteins with different folds, we wished to explore its applicability to α-helical transmembrane proteins. ASR and pSRII were consider to be perfect candidates because of several desirable characteristics. We aimed to incorporate these two microbial rhodopsins into SapA lipid nanoparticles and perform NMR experiments. pSRII has

been studied in our lab for a long time and the expression and purification of the protein as well as its characterisation by NMR are well-established.[30] Therefore, detergent solubilised pSRII could be produced using existing protocols ready for incorporation into SapA lipid nanoparticles. ASR, on the other hand, required optimisation of expression and purification. We hoped to find an optimal condition that produced a high quality detergent solubilized ASR sample for solution NMR. After this, ASR would be incorporated into SapA lipid nanoparticles for studies by NMR of the membrane protein in a lipid bilayer environment.

4.2 Results and discussion

4.2.1 Optimisation of ASR expression

For NMR structural studies, a large quantity of sample is usually required. In order to study ASR using solution NMR spectroscopy, we started by screening for optimal conditions for ASR expression in the *E. coli* expression system. This included screening different *E. coli* strains for optimal ASR expression yield, the flask type used for *E. coli* culture, the induction point, and the concentration of IPTG used for induction. Three BL21 derivatives were tested for ASR expression. Cells were lysed and the membrane fractions were solubilized with 2% LMNG. The amount of ASR in the soluble fractions was determined by UV-Vis absorbance at 549 nm. The result showed that BL21-RIL yielded about 1.4 mg per litre culture, more than double the yields of BL21-rosetta and BL21-tuner cells (Figure 4-1 A). During the expression trials, we also found that the yield was significantly affected by the types of flask used. The yield was again determined by the characteristic absorbance of ASR at 549 nm during the Ni-NTA elution step. The results showed that flasks with dimpled baffles yielded 45% more than those with long baffles (Figure 4-1 B). Next, we screened the best time point for induction (Figure 4-1 C) and the IPTG concentration used for induction (Figure 4-1 D). Five O.D. points were tested for induction and O.D. = 0.51 had the highest yield, while lower or higher O.D. yields were less than 80% of this. We also found that the IPTG concentration affected the ASR yield as 0.2 mM IPTG only yielded around 60% of that at 0.5 mM and 1mM. Therefore, at least 0.5 mM IPTG needed to be supplied for optimal ASR expression. Overall, we screened for the best expression strain, the best culture flask and induction conditions that should give us the optimal ASR production level. The next step was to optimise the purification protocol.

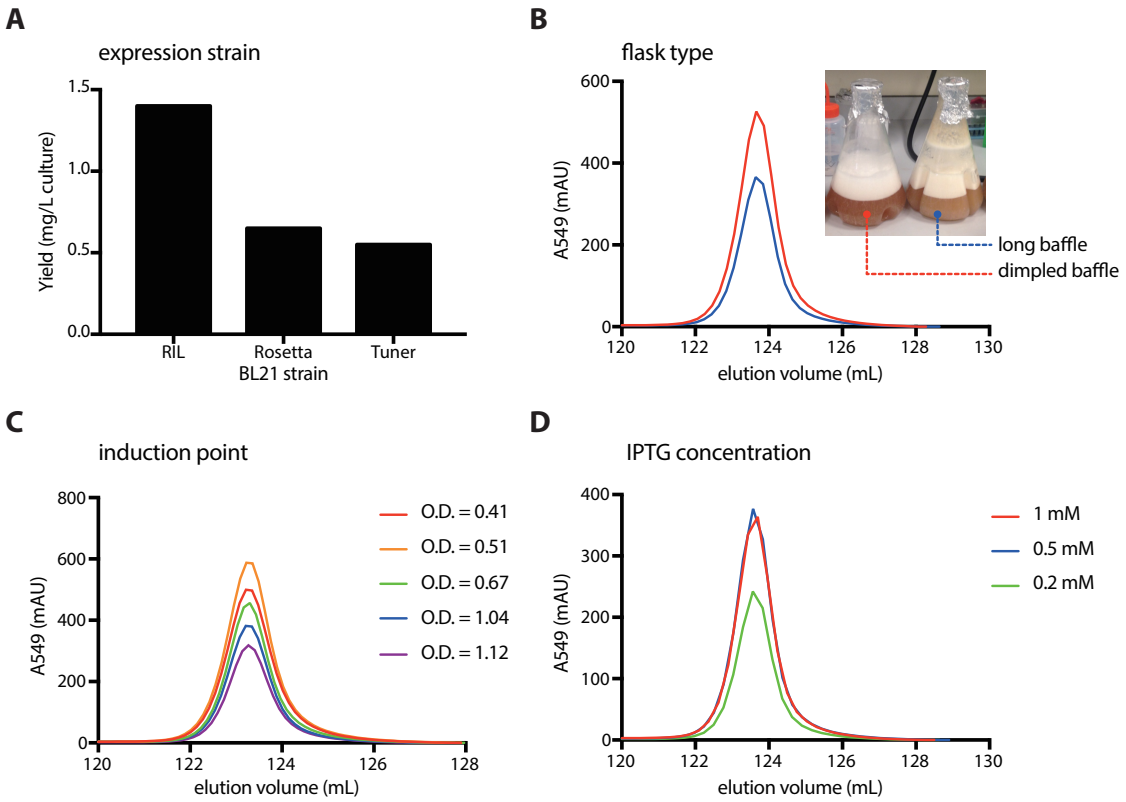

Figure 4-1: Optimisation of ASR expression for maximum yield.

A) Expression strain, B) flask type, C) induction point, and D) IPTG concentration were screened. Each condition was tested in 1 L culture. Ni-NTA purification was performed and UV-Vis absorbance at 549 nm was monitored to indicate correctly folded ASR.

4.2.2 Optimisation of ASR purification

After optimising the expression of ASR, we attempted to find the most suitable detergent for extracting ASR from the *E. coli* membrane. Six detergents were tested including 1.5% DDM, 3% DM, 2% OG, 2% LMNG, 2% C7-DHPC, 2% C6-DHPC. One benefit of working with ASR is that it has an observable purple colour enabling the amount of protein to be estimated immediately by eye. Six samples containing the same amount of cell pellet were solubilised separately at 4 ºC overnight. Soluble fractions were collected by ultracentrifugation (100,000 g, 90 min). OG and C7-DHPC samples showed the darkest purple colour indicating the highest extraction efficiency. DDM and LMNG extracted medium amounts of ASR, whereas DM and C6-DHPC showed low levels of extraction (Figure 4-2 A). The same trend was observed from the pellet in which less purple indicated better extraction. OG and C7-DHPC created pellets with the faintest purple colour, while DM and C6-DHPC left pellets that were dark purple.

Interestingly, we also observed some white material in the centre of each pellet which is likely to contain other endogenous proteins due to the lack of colour (Figure 4-2 B). OG and C7-DHPC showed the smallest amount of white material, suggesting that they not only solubilised ASR but also other *E.* coli endogenous proteins. This conclusion was supported by SDS-PAGE analysis (Figure 4-2 C). Samples solubilised by OG and C7-DHPC showed many other bands on the SDS-PAGE gel even after two steps of purification, Ni-NTA and size-exclusion chromatography. DDM and LMNG showed sufficient purity after Ni-NTA chromatography, but DDM seemed to promote the formation of higher oligomers. We hypothesised that short chain detergents such as OG and C7-DHPC have a strong ability to disrupt membranes and extract proteins. However, this implies that many other impurities would also be solubilised by these detergents. Other proteins that were in the same micelles as ASR would be very difficult to remove. Considering both yield and purity of the ASR product, LMNG showed the most promising result, solubilising sufficient amounts of ASR while remaining mild enough to produce a high purity sample.

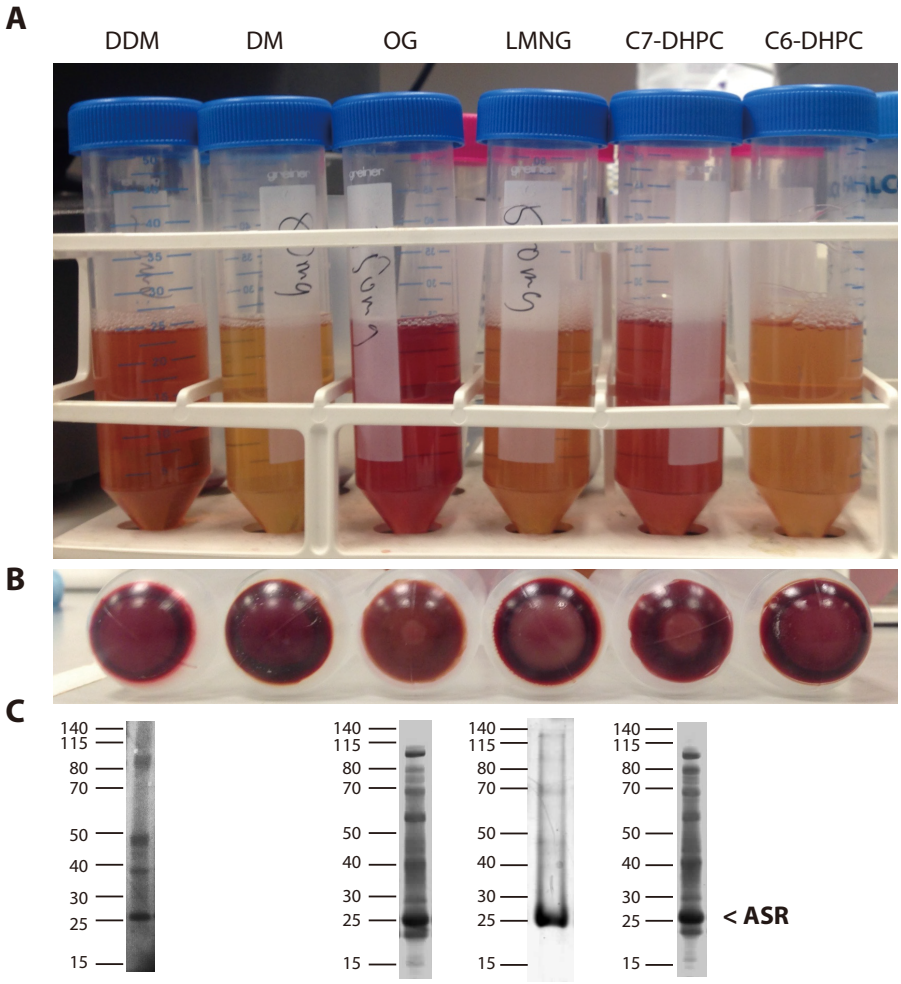

Figure 4-2 (*opposite*): Screening detergents for ASR extraction.

The membrane fraction from 6 L cell culture was resuspended and equally distributed into six samples. The samples were solubilised in 1.5% DDM, 3% DM, 2% OG, 2% LMNG, 2% C7-DHPC, and 2% C6-DHPC. The samples were centrifuged using ultracentrifuge to separate A) Soluble fractions and B) Insoluble fractions. The extraction efficiency can be judged directly from the colour of the soluble fractions. C) SDS-PAGE of samples from DDM and LMNG after Ni-NTA purification as well as samples from OG and C7-DHPC after Ni-NTA and size-exclusion purification.

The incubation temperature during ASR extraction also proved to be important. Higher temperature should in theory make the extraction more efficient by providing more energy. However, higher temperatures could also lead to the precipitation of unstable proteins. To explore the balance between these two effect, two temperatures were tested, 4 ºC and 25 ºC, during the LMNG solubilisation step. The result shows that 25 ºC solubilised 40% more ASR than 4 ºC as judged by Ni-NTA purification (Figure 4-3). In addition, the sample purity was not compromised, as confirmed by SDS-PAGE (Figure 4-3).

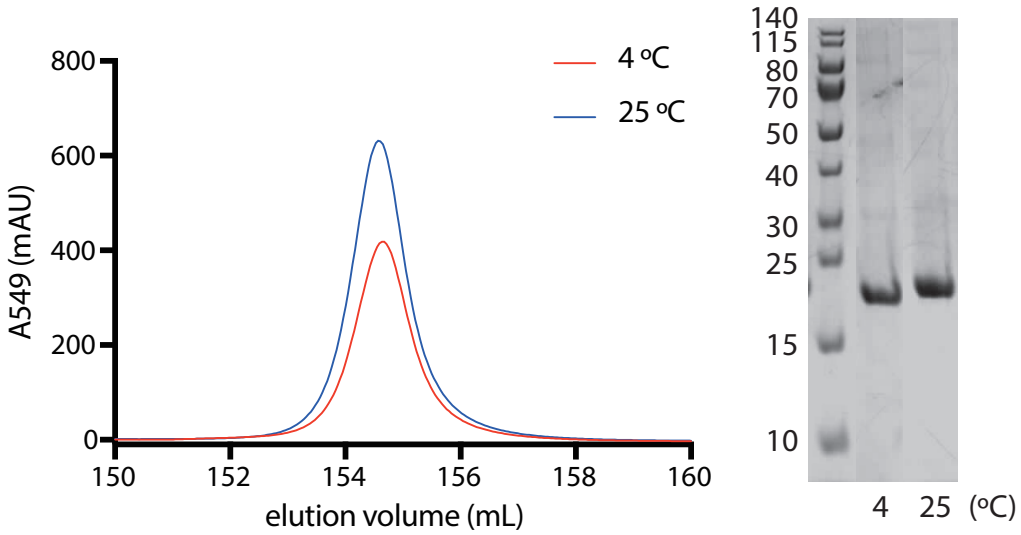

Figure 4-3: Screening the solubilisation temperature for optimal ASR extraction.

Cell pellets from 1 L culture containing ASR were solubilised using LMNG incubated at 4 ºC (red) and 25 ºC (blue) followed by cell lysis and Ni-NTA purification. ASR yields and sample purity were checked by the absorbance at 549 nm and SDS-PAGE.

This section shows the results of ASR extraction using six detergents. We found that LMNG had the most promising properties, and was able to extract a medium amount of ASR but produced a very high purity sample. Increasing the incubation temperature during solubilisation from 4 ºC to 25 ºC further improved the ASR yield by 40%.

4.2.3 Optimisation of ASR sample condition for NMR experiments

Having established a protocol to express and extract the maximum amount of ASR from *E. coli*, the next step was to find the best buffer condition that would optimise the quality of NMR spectra. A few criteria of the sample are preferred for solution NMR experiments, including small particle size, high stability, and low salt. Three detergents, LMNG, HEGA-10 and C7-DHPC, were tested to see which one would stabilise ASR the most. The starting material was LMNG-solubilised ASR produced as described in the previous section. For the HEGA-10 and C7-DHPC samples, on-column detergent exchange was performed using an Ni-NTA column. For each of the three detergent samples, we screened a range of salt concentrations and pH values by diluting the concentrated ASR sample 20 times into the desired buffer compositions. The stability of ASR was determined by quantifying the characteristic UV-vis absorbance of ASR at 549 nm, which should correlate with the proportion of correctly folded ASR. The absorbance at 549 nm was measured just after sample preparation as the starting point, then again after 65 h of incubation at 50 ºC. The ratio of the two measurements indicated the percentage of correctly folded ASR remaining in the sample. The results showed that LMNG could offer the most stabilising effect, with more than 80% of ASR remaining structured in low pH and high salt conditions. However, LMNG-solubilised ASR seemed to be very sensitive to the buffer condition as less than 20% ASR survived in a high pH and low salt condition (Figure 4-4 A). In contrast, the stability of ASR in HEGA-10 was affected to a lesser extent by the buffer condition: 30% to 70% of ASR remained structured in all conditions tested here. In addition, a clear trend that higher salt was more stabilising could be observed for HEGA-10 (Figure 4-4 B). C7-DHPC showed the least stabilising effect. Almost all the conditions gave less than 30% structured ASR with the exception of the conditions with 1 M salt which gave around 50%. Overall, ASR in LMNG with high NaCl concentrations showed the most promising results. However, as the NaCl concentration decreased, the stability significantly reduced. High salt concentration is generally not good for NMR measurements because it increases the pulse length, and hence reduces the sensitivity. In

HEGA-10, the stability of ASR was relatively unaffected by changes in salt concentration.

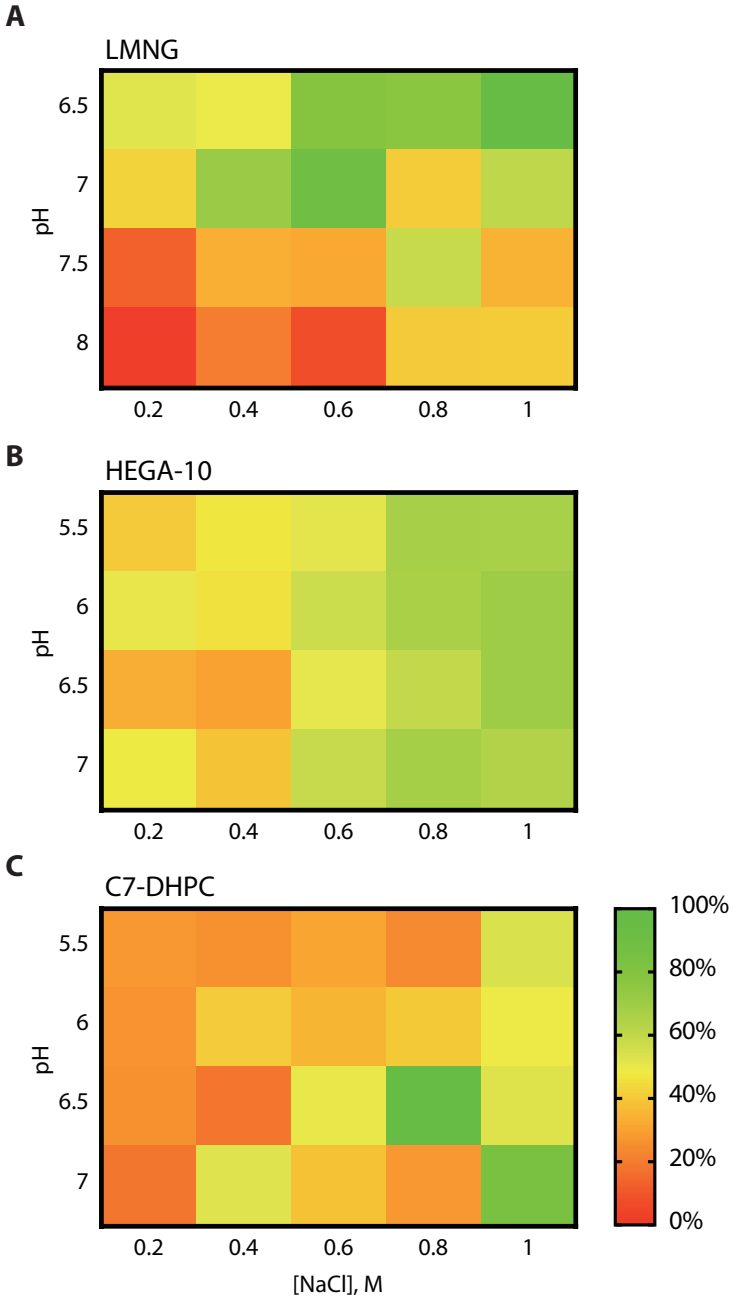

Figure 4-4: Screening for the optimal stability of ASR solubilised in three detergents.

ASR in A) 0.002% LMNG, B) 0.5% HEGA-10, and C) 0.1% C7-DHPC were mixed with buffer with different NaCl concentration and pH. The concentration of correctly folded ASR in each condition was measured using the UV-vis absorbance at 549 nm before and after 65 h incubation at 50 °C. The ratio are presented in a heat map format, showing the remaining percentage of correctly folded ASR.

The particle size is also a very important factor for NMR experiments. Larger particles should have a longer correlation time (τ_c) leading to faster transverse relaxation and hence broader lines leading to a reduced signal-to-noise ratio. Therefore, we assessed the particle size of ASR in LMNG and in HEGA-10, two promising candidates, using translational diffusion measurement by pulsed field gradient (PFG) ^{1}H NMR and dynamic light scattering (DLS). Larger particles diffuse slower leading to a smaller diffusion coefficient. The diffusion coefficients of ASR in HEGA-10 and LMNG were determined and plotted against temperature. The results (Figure 4-5) showed that ASR in HEGA-10 appeared to be much smaller than in LMNG. The diffusion coefficients of pSRII in C7-DHPC measured by Dr. Mark Bostock were included for comparison. The structure of pSRII in C7-DHPC has been solved by solution NMR previously in our lab,[30] therefore its diffusion coefficient was set to be a standard that we hoped would lead to high NMR spectral quality. ASR in HEGA-10 appeared to be slightly larger than pSRII in C7-DHPC[30] but was still in the same region, whereas ASR in LMNG appeared to be much larger (Figure 4-5 A, filled circles). The size difference was probably due to the properties of the detergents. Empty LMNG micelles should be much bigger than HEGA-10 micelles and C7-DHPC micelles because of the longer chain length (Figure 4-5 A, empty circles). However, we cannot exclude the possibility of ASR forming higher-order oligomers in LMNG micelles, which could also contribute to a larger apparent particle size. Diffusion coefficient measurements can be theoretically translated into effective molecular weight estimates based on the solvent viscosity and the assumption that the molecular assembly is a sphere of constant density. The standard set of assumptions is, however, not useful for membrane protein cases because the detergent molecules that surround the membrane protein mean the particle cannot be approximated as spherical and the density would not be the same as that of a pure protein. The presence of protein-free micelles in the solution would also make the estimation of solvent viscosity inaccurate. The observation of a larger ASR species in LMNG is also supported by DLS data in various salt concentrations which suggested a diameter of about 13 nm, whereas ASR in HEGA-10 appeared to be around 9 nm (Figure 4-5 B). Overall, ASR in HEGA-10 appeared to be significantly smaller than ASR in LMNG, and slightly larger than pSRII in C7-DHPC. Therefore, HEGA-10 was expected to be favourable for NMR experiments in terms of the particle size.

In summary, ASR in HEGA-10 was sufficiently stable and was able to tolerate low salt concentrations. More importantly, ASR in HEGA-10 also produced particles with a

much smaller apparent size than comparable preparations using LMNG. Combining these results, HEGA-10 was considered favourable for further investigation of ASR using NMR.

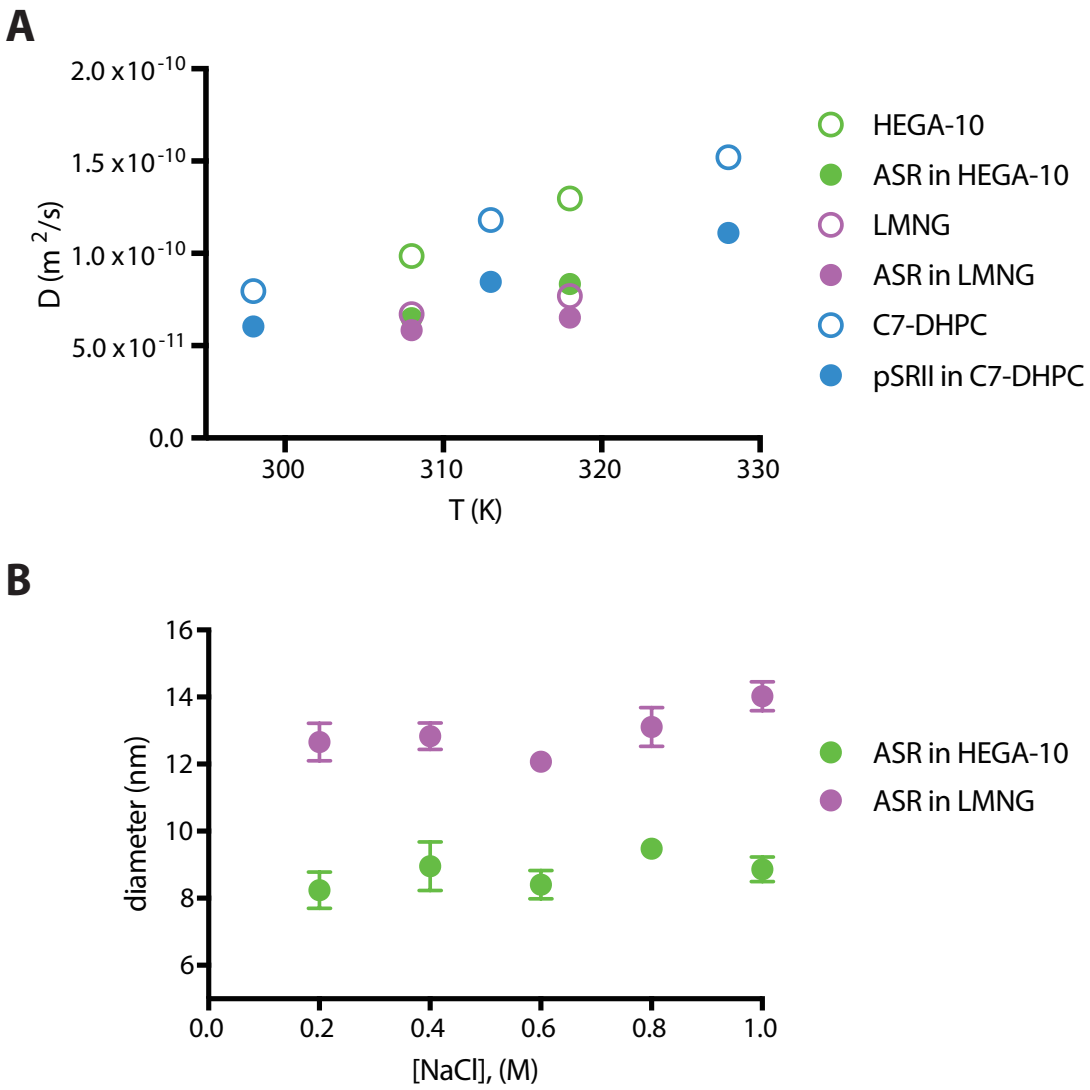

Figure 4-5: Assessment of particle size of ASR in LMNG and in HEGA-10.

A) Translational diffusion coefficient of empty detergent micelles (open circles) and ASR containing micelles (filled circles). Diffusion coefficients for empty C7-DHPC micelles and pSRII in C7-DHPC micelles, which yields good quality NMR spectra, are included for comparison. B) DLS measurements of ASR in HEGA-10 and LMNG with different salt concentrations.

4.2.4 NMR spectrum of ASR in HEGA-10

Based on the screening results discussed above, HEGA-10 showed the most favourable characteristics for NMR experiments. We decided to express ^{15}N-labelled ASR for 2D

[^{1}H, ^{15}N]-TROSY measurements. The spectrum for ASR in 1.5% DDM was recorded previously by Dr. Duncan Crick in our group (Figure 4-6).[186] The spectral quality was poor and only a few peaks could be observed, far fewer than the expected 235 backbone amide signals. These intense signals are from highly flexible regions of the protein, probably loops, and the N-terminal, or C-terminal regions. The rest of the signals were too broad to be observed due to the large particle size. One possible explanation was the formation of higher order oligomers as shown before by SDS-PAGE (Figure 4-2 C). The large particle size and inhomogeneous nature of the sample resulted in poor spectral quality and sensitivity.

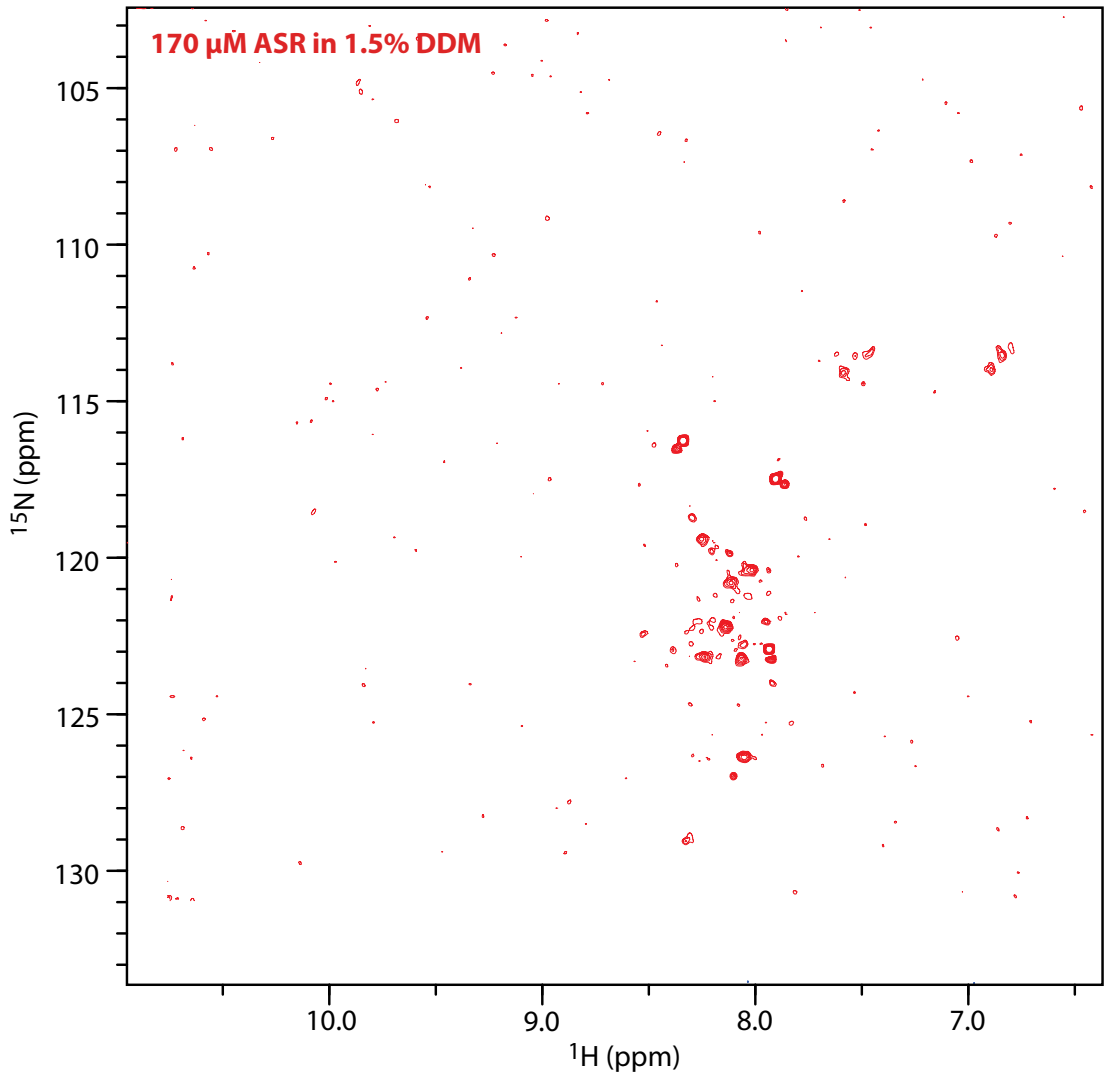

Figure 4-6: NMR spectrum of ASR in DDM.

2D [^{1}H, ^{15}N]-TROSY spectrum of ASR in 1.5% DDM. The spectrum was recorded at 323 K on an 800 MHz spectrometer (^{1}H frequency of 800 MHz) with 64 scans.

In comparison to the spectrum in DDM, ASR in HEGA-10 clearly showed an improved spectral quality (Figure 4-7 A). The sample contained 200 μM ASR solubilised in 20 mM sodium phosphate, pH 6.5, 200 mM NaCl, 0.5% HEGA-10, and the spectrum was recorded at 318 K using a conventional 5 mm diameter NMR tube. The number of resolved peaks increased significantly and around 200 peaks are now visible. The relatively high salt concentration, which was necessary to stabilise ASR, substantially reduced the NMR sensitivity. In order to increase the sensitivity, the same sample was concentrated further to 325 μM, 60% higher than the original, and a 3 mm NMR tube, which only requires 175 μL sample, was used. The use of a smaller diameter NMR tube substantially increases the salt tolerance and hence is of benefit when measuring high salt samples. We also increased the number of scans by 25% to improve the signal-to-noise ratio. Together, these new parameters significantly improved the spectral quality (Figure 4-7 B). Several new peaks became visible as shown in the selected regions.

In conclusion, we have found that ASR in HEGA-10 showed characteristics that were most suitable for NMR experiments. Indeed, the spectral quality was much better than for the spectrum of ASR in DDM recorded previously. The number of peaks was close to the expected maximum of 235 backbone amide signals. Although the spectrum looks very promising, the quality was not sufficient enough to allow the recording of three-dimensional NMR experiments for backbone assignment purposes. Deuteration of the protein would be required to improve the spectral quality to an extent that would allow resonance assignment to be possible.

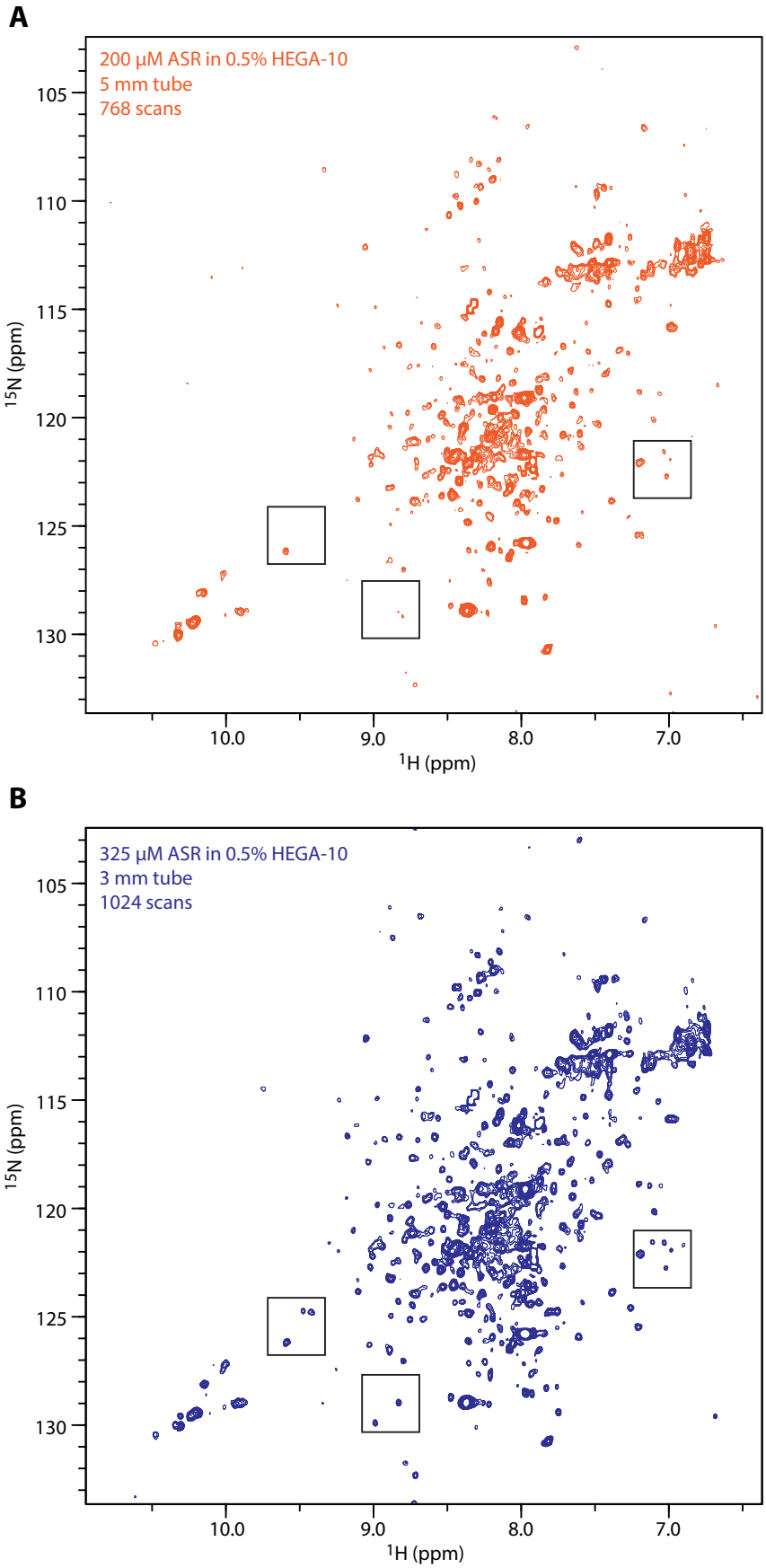
A
200 µM ASR in 0.5% HEGA-10
5 mm tube
768 scans
105
110
115
120
125
130
15N (ppm)
10.0
9.0
8.0
7.0
1H (ppm)
B
325 µM ASR in 0.5% HEGA-10
3 mm tube
1024 scans
105
110
115
120
125
130
15N (ppm)
10.0
9.0
8.0
7.0
1H (ppm)

Figure 4-7 (*opposite*): NMR spectra of ASR in HEGA-10.

2D [^{1}H, ^{15}N]-SOFAST-TROSY spectrum of ASR in 0.5% HEGA-10. The spectrum was recorded at 318 K on a 800 MHz spectrometer (^{1}H frequency of 800 MHz) A) The spectrum was recorded using a conventional 5 mm NMR tube with the ASR concentration of 200 μM with 768 scans, corresponding to 14 h recording time. B) The same sample was concentrated to 325 μM, and the spectrum was recorded using a 3 mm NMR tube with 1024 scans, corresponding to 18 h acquisition time. Three boxes indicate the same selected regions in two spectra for comparison.

4.2.5 Incorporation of ASR into SapA lipid nanoparticles

In order to study the effect of a lipid bilayer on the structure and function of ASR, we attempted to incorporate ASR into SapA-DMPC nanoparticles. The SapA:DMPC:ASR ratio used in the assembly mixture was 2:56:1 and LMNG was removed by 2 h incubation with 80% Amberlite beads. The resulting chromatogram showed inhomogeneous ASR-containing particles, as indicated by the UV absorbance at 549 nm (Figure 4-8). Several reasons have lead to this result. First, the mixing ratio was not optimised; too many ASR molecules per nanoparticle would promote ASR oligomer formation in one nanoparticle. Second, the detergent might not have been removed completely as an A280 peak at around 16.5 mL could be observed which was likely to be SapA-LMNG based on similarity to the SapA-DDM SEC profile in Figure 2-5 A. Therefore, the multiple peaks seen in the A549 trace may have corresponded to a mixture of ASR in LMNG, ASR in SapA-DMPC, ASR in SapA-LMNG, or ASR in SapA-DMPC/LMNG. At the time this experiment was performed, we had not established the 2,6-dimethylphenol assay to check the detergent concentration, as discussed in Chapter 2. A working protocol for removing LMNG was established after this experiment, as discussed in Chapter 5. Finally, it is possible that ASR was able to exchange between monomeric, dimeric, and trimeric states in the bilayer. We did not pursue the incorporation of ASR further, but instead focused on the incorporation of pSRII because its sample preparation and NMR experiments were well-characterised in our lab.

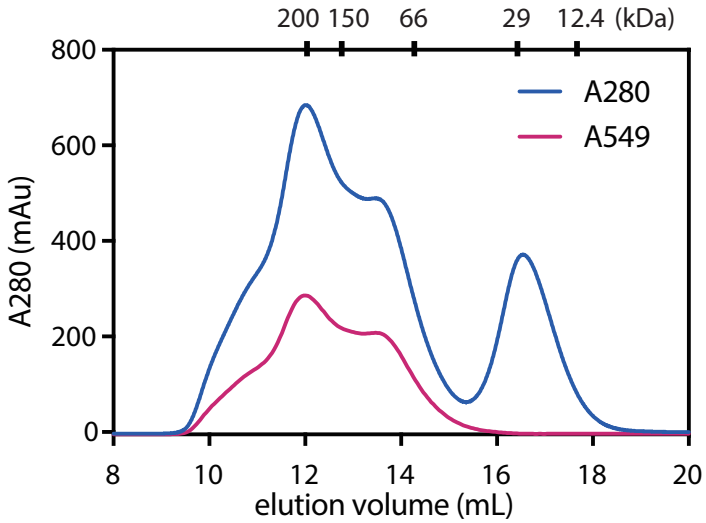

Figure 4-8: SEC of ASR in SapA-DMPC nanoparticles.

Absorbance at 280 nm (blue) and 549 nm (purple) are indicated. The molecular weight standards are shown on top of the graph.

4.2.6 Incorporation of pSRII into SapA lipid nanoparticles

pSRII was expressed and purified by following the previously reported protocol.[30] The final sample was prepared in DDM which was much more easily removed by Amberlite beads compared to LMNG as shown in Chapter 2. The incorporation protocol we used for pSRII was exactly the same as for OmpX described in Chapter 2. SapA, DMPC, and pSRII were mixed in a ratio of 10:50:1 with the addition of 0.2% DDM in pH 6 buffer. The assembly mixture was then incubated with 80% (w/v) Amberlite XAD2 detergent removal beads at 25 °C for 2 h. The sample was harvested and checked by SEC to confirm successful pSRII incorporation showing a single, homogeneous peak at 12.3 mL, corresponding to an apparent molecular weight of about 200 kDa (Figure 4-9 A). The presence of pSRII was assessed by the orange colour or the absorbance at 498 nm, the characteristic absorbance of the correctly folded pSRII (Figure 4-9 A). The UV spectrum of the sample was measured and overlaid with the spectrum for pSRII in DDM (Figure 4-9 B). The extra absorbance at 280 nm in SapA-DMPC nanoparticles originates from SapA scaffold proteins. The sample homogeneity was also confirmed by negative-stained electron microscopy images showing well-distributed particles with similar size (Figure 4-9 C).

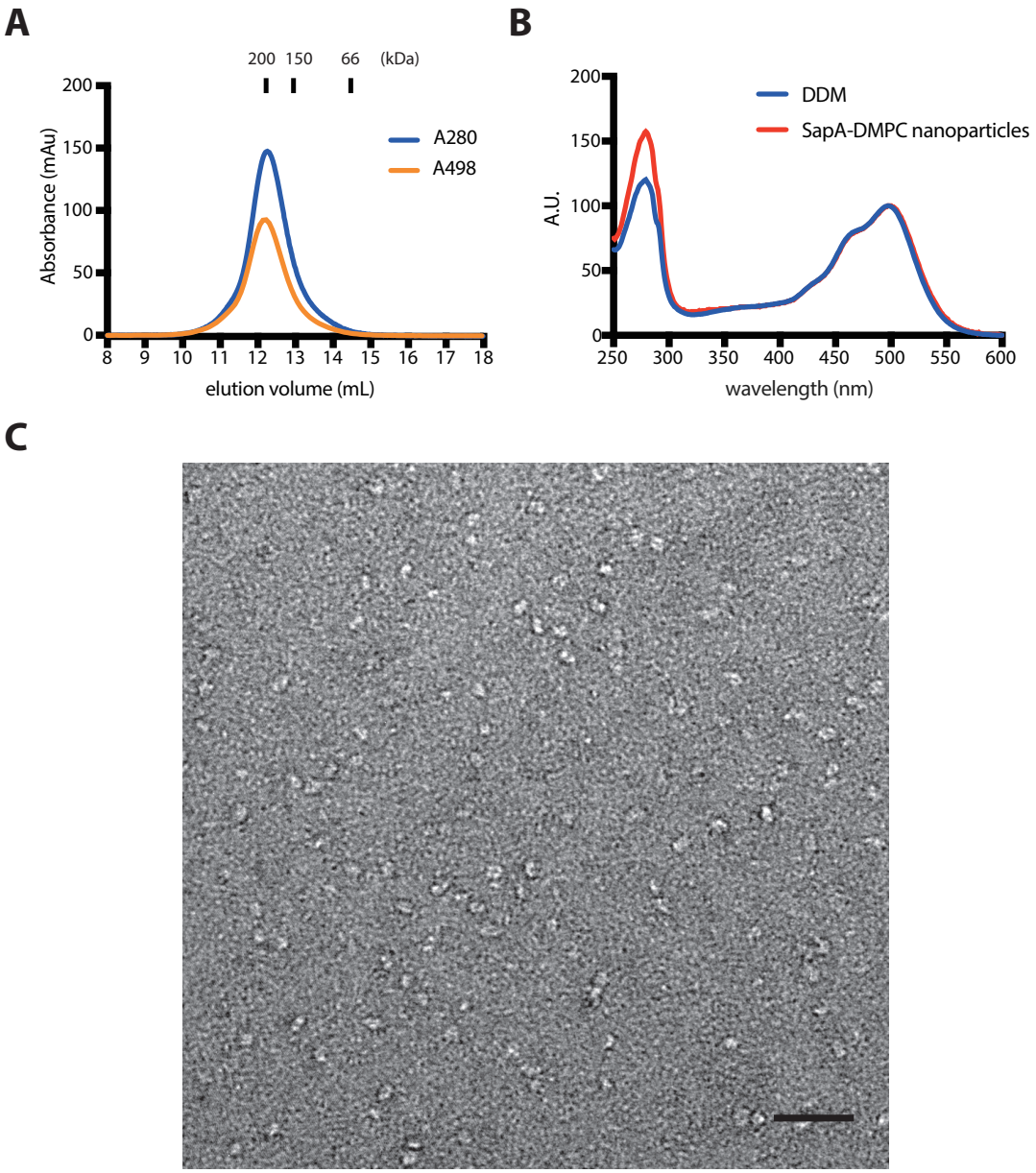

Figure 4-9: Characterisation of pSRII in SapA-DMPC nanoparticles.

A) SEC of pSRII in SapA-DMPC nanoparticles. Molecular weight standards are indicated on top of the graph. B) UV-Vis spectrum of pSRII in DDM (blue) and in SapA-DMPC nanoparticles (red). C) Negative-stain electron microscopy images of pSRII in SapA-DMPC nanoparticles. Scale bar, 50 nm.

Although the particle size was estimated to be around 200 kDa, this was significantly larger than we anticipated for a monomer of pSRII (26.4 kDa) in SapA-DMPC nanoparticles. Therefore, we decided to investigate the stoichiometry of the particle. The concentration of pSRII could be determined from the absorbance at 498 nm which shows 1.8 µM for this sample (Figure 4-10). The concentration of SapA in the sample

was determined by quantifying the band intensity on an SDS-PAGE gel. A series of SapA only samples with known concentration were run as standards together with the unknown sample on the same SDS-PAGE. The band intensities of the standard samples were plotted against the concentration and a linear regression was performed to obtain the correlation between the band intensity and the concentration (Figure 4-10). The SapA concentration in the pSRII sample was then back calculated using the regression formula (SapA band intensity = 2112 × [SapA] + 13501), showing 3.3 µM. Therefore, we concluded that the SapA:pSRII ratio was 2:1. Based on the 200 kDa particle size estimate and the SapA:pSRII ratio of 2:1, the nanoparticles were composed of two pSRII and four SapA, consistent with dimeric pSRII in $SapA_4$-DMPC nanoparticles. $SapA_4$-DMPC nanoparticles on their own displayed an effective molecular weight of about 170 kDa as shown in section 2.2.4, which supports of the proposed composition.

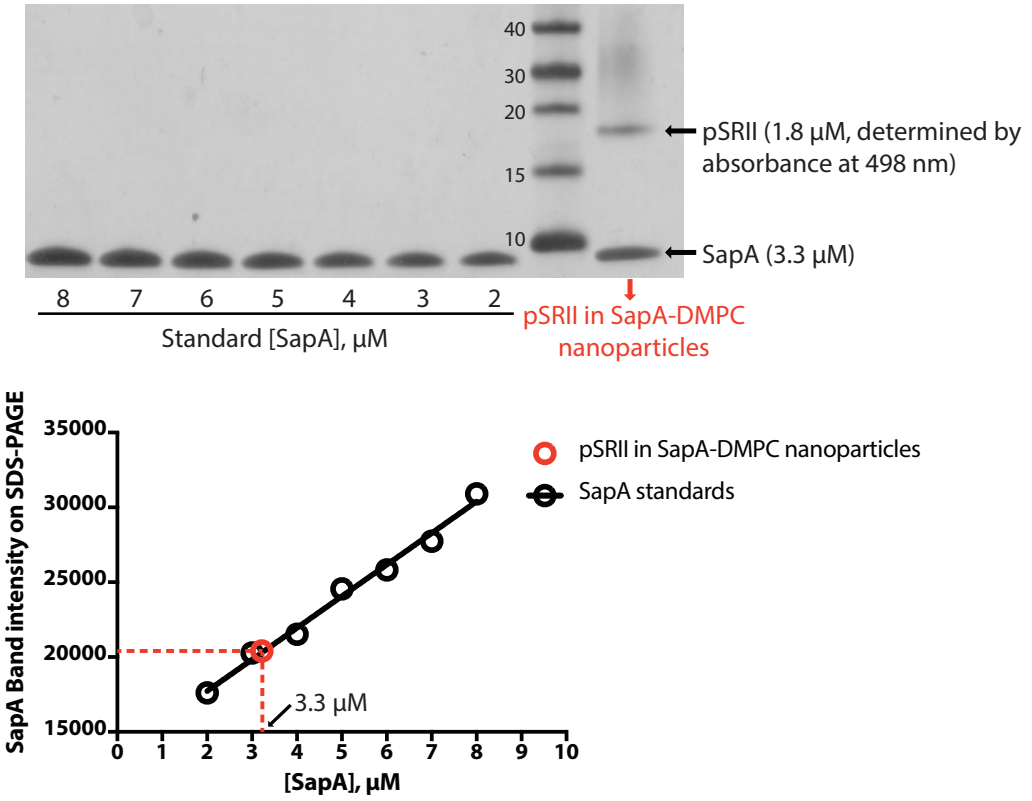

4.2.7 NMR spectrum of pSRII in SapA-DMPC nanoparticles

Despite the large particle size, we still attempted to obtain an NMR spectrum using ^{15}N-labelled pSRII in $SapA_4$-DMPC nanoparticles. The result showed that although the NMR spectral quality was worse compared to that of monomeric pSRII in C7-DHPC micelles, as expected due to the larger apparent molecular weight, a similar overall backbone fingerprint was observed (Figure 4-11). The strong signals in particular overlaid perfectly because they correspond to residues in the loop region and the N and C-termini, which are completely solvent exposed, and hence not affected by changing the membrane mimetic. In contrast, the well dispersed peaks shifted significantly, suggesting that the lipid bilayer changed the chemical environment of the hydrophobic part of the protein. Moreover, the tryptophan side-chain signals at around 10 ppm (^1H) also showed distinct chemical shifts. We have shown previously in Figure 3-11 using OmpX that tryptophan side-chains are very sensitive to the membrane mimetic used because they always position at the membrane-water interface.[164] Although the spectral quality was not good enough to perform 3D NMR experiments for backbone assignment, perdeuteration would be expected to further improve the spectral quality for more extensive solution NMR studies of pSRII in $SapA_4$-DMPC nanoparticles.

Figure 4-10 (*opposite*): Determination of the SapA:pSRII ratio for pSRII in SapA-DMPC nanoparticles.

Using the absorbance at 498 nm and the extinction coefficient of 48000 $M^{-1}cm^{-1}$, the concentration of pSRII in the sample was determined to be 1.8 μM. The concentration of SapA in the sample was determined by comparing the band intensity to SapA standards with known concentration via SDS-PAGE (upper panel). The band intensity of the SapA bands was quantified using ImageJ, plotted against the SapA concentration in black open circles, and fitted by linear regression (bottom panel). The SapA concentration in the pSRII in SapA-DMPC nanoparticles was calculated to be 3.3 μM using the fitted result. The results show the SapA:pSRII ratio is 2:1.

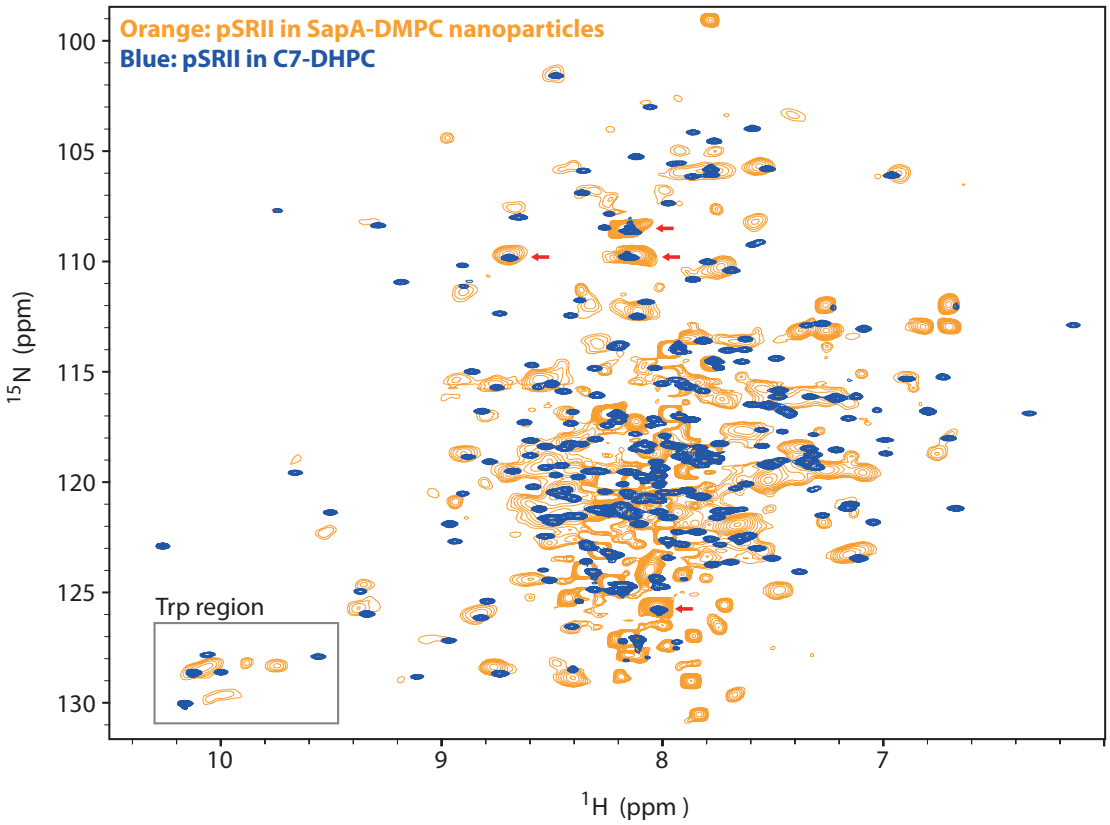

Figure 4-11: NMR spectra of pSRII in different membrane mimetics.

Overlay of 2D-[^{15}N, ^{1}H]-SOFAST-TROSY spectra of ^{15}N-labelled pSRII in C7-DHPC micelles (blue) and in SapA$_4$-DMPC nanoparticles (orange). Tryptophan region is indicated in grey box. Four representative strong signals from both spectra that overlaid perfectly are indicated by red arrows. The spectra were recorded at 800 MHz (^{1}H) and 318 K.

4.3 Conclusions

This section described the optimisation of ASR NMR sample production including protein expression, purification, and determination of the detergent that was most suitable for NMR experiments. HEGA-10 gave acceptable NMR spectral quality that was dramatically improved compared to spectra in DDM. Partial incorporation of ASR into SapA-DMPC nanoparticles was observed. The reason for the incomplete incorporation could potentially be an incorrect ratio used in the assembly mixture or incomplete LMNG removal. Despite these inconclusive results for ASR, successful incorporation of pSRII into SapA-DMPC nanoparticles was obtained, yielding a single homogeneous particle with an effective size of 200 kDa. The properties of the particle

were consistent with two pSRII molecules surrounded by four copies of SapA. The 2D-[^{15}N, ^{1}H] spectrum showed significant perturbation of the peak positions compared to those in C7-DHPC micelles, indicating the impact of the lipid environment on the protein's conformation. In conclusion, SapA lipid nanoparticles are a very versatile membrane mimetic that can accommodate a range of different seven-transmembrane proteins making them suitable for studies of GPCRs in a more native-like environment.

5 NMR STUDIES OF β_1-ADRENERGIC RECEPTOR IN LIPID BILAYER

5.1 Introduction

5.1.1 β_1-adrenergic receptors

β-adrenergic receptors (βAR) are class A GPCRs and can activate intracellular heterotrimeric G proteins upon binding to adrenaline or noradrenaline. There are three subtypes: β_1AR, β_2AR, and β_3AR and all recognise G_s G proteins in the activated state, which connect to adenylate cyclase, thus increasing the intracellular concentration of cAMP. β_1AR is the dominant βAR in normal heart tissue while β_2AR is the main regulatory receptor in vascular and non-vascular smooth muscle. Activation of the β_1AR leads to an increase in contractile force and the heart rate. On the other hand, activation of β_2AR results in relaxation of vascular and non-vascular smooth muscle. Despite such distinct functions within the βAR family, the receptors are highly similar both in structure and sequence between subtypes. For example, a sequence comparison of β_1AR and β_2AR shows 67% identity in the transmembrane region and the residues directly contacting the agonist in the ligand-binding pocket are the same. For drug development, it is important to modify a ligand into a more specific binder to the target, so that side effects during treatment can be reduced. β_1AR selective antagonists such as CGP 20712A bind to β_1AR 500-fold stronger than to β_2AR; the β_2AR selective antagonist, ICI 118551, is 550-fold and 661-fold selective over β_1AR and β_3AR, respectively.[187]

Understanding the molecular mechanisms of both targets is important for further development of drugs with high specificity. Knowledge of the structure and dynamics of β_1AR is still lacking compared to the extensively studied β_2AR, therefore we aimed to understand more detail about β_1AR.

5.1.2 Structural studies of β_1-adrenergic receptor

The human β_1AR, unlike β_2AR discussed in section 1.3.2, is more difficult to purify because of its instability in detergent.[188] The first crystal structure of β_1AR from turkey (*Meleagris gallopavo*) was solved using a modified construct. The modifications included truncation of the flexible N- and C- terminal regions and intracellular loop 3, the introduction of six thermostabilising mutations (R68S, M90V, Y227A, A282L, F327A, and F338M), and two other mutations to improve protein expression (C116L) and eliminate the palmitoylation site (C358A).[188] Since then, 18 crystal structures of thermostabilised β_1AR bound to different ligands have been solved.[188–193] Similar to observations made about β_2AR, the agonist bound form of β_1AR does not show the expected outward movement of TM6 (Figure 5-1). Only a local contraction by 2–3 Å of the binding pocket is observed in full agonist bound structures when compared to the antagonist bound state.[189] Unlike β_2AR, there are currently no crystal structures of β_1AR bound to an intracellular binding partner, G protein or G protein mimicking nanobody available.

Similar to the studies of β_2AR the landscape of conformations that are accessible to β_1AR is not visible in crystal structures. An NMR spectroscopy approach has been used to study thermostabilised β_1AR, by investigating ^{15}N labelled valine residues. The chemical shifts of residue V226 in TM5 of β_1AR were found to correlate with the efficacy of the surveyed ligands, indicating the presence of several conformations and the population in each state was modulated by the ligands.[194] A ^{13}C methyl methionine NMR study of β_1AR was performed and published by our group.[195] We observed similar behaviour giving evidence for extensive μs-to-ms timescale dynamics in the full agonist bound state.[195] Based on our data, agonists not only modulate the population of active-like conformations in the absence of an intracellular binding partner, i.e. a G protein mimicking nanobody, but also induce different conformations in the ternary agonist-β_1AR-nanobody complex. A model was proposed in which ligand efficacy

determines the quality of the interaction between β_1AR and the G protein leading to different signalling levels.[195]

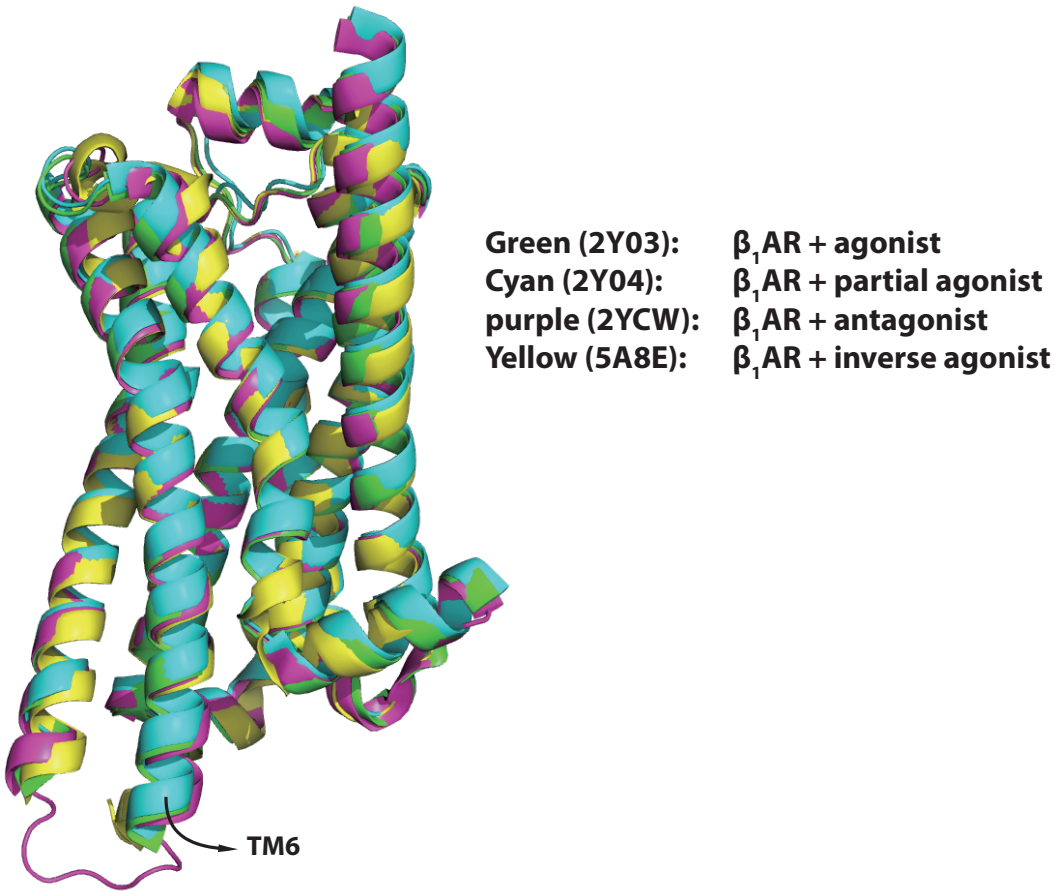

Figure 5-1: Crystal structures of β_1AR.

Overlay of crystal structure of agonist bound β_1AR (green) (PDB ID: 2Y03), partial agonist bound β_1AR (cyan) (PDB ID: 2Y04), antagonist bound β_1AR (purple) (PDB ID: 2YCW), and inverse agonist bound β_1AR (yellow) (PDB ID: 5A8E).

5.1.3 GPCR in lipid bilayer

Most of the previous GPCR studies were done using detergents as the membrane mimetic because these are easier to handle experimentally. Detergents are simply included in the buffer as additives and spontaneously form micelles to solubilise the membrane protein. However, studying GPCRs in a lipid environment has become more

and more popular recently due to technological advances and a realisation of the importance of lipids in GPCR activation.

A comparison between different membrane mimetics has been reported for β_2AR, revealing a much slower exchange rate between active and inactive states and a higher population of the active state when bound to full agonists in lipid bilayer nanodiscs compared to DDM micelles.[105] Another study showed that lipids with a PG head group significantly favoured agonist binding and encouraged β_2AR activation, whereas phosphatidylethanolamine favoured antagonist binding and stabilised the inactive form of β_2AR.[161] Two independent MD simulation works support the idea that anionic lipids stabilise the active-like state of β_2AR making it more likely to dock with a G protein.[196,197] A mechanism was proposed in which the lipid molecule binds to β_2AR through an electrostatic interaction between the anionic head group and $R^{3.50}$ of the DRY motif (superscripts refer to Ballesteros–Weinstein numbering[198]), resulting in transient stabilisation of an active-like conformation.[197] The effect of lipid composition on the structure and function of β_2AR is not limited to phospholipids. Two cholesterol molecules were observed in a crystal structure of β_2AR interacting with conserved residues.[199] This result lead to a prediction that 44% of human class A GPCRs would contain a cholesterol consensus motif.[199] NMR studies suggest that there are two classes of cholesterol interaction with one on nanosecond and one on microsecond timescales.[200] Specific binding of cholesterol near helices 5–7 appears to limit the conformational variability of β_2AR, as revealed by experimental data[201] and atomistic simulation.[202]

There are also several studies investigating the effect of lipids on GPCRs other than β_2AR. Three class A GPCRs, NTSR1, β_1AR, A_{2A}R, were found to bind PIP2, and this interaction selectively stabilises active states and enhances G_s selectivity.[160] Negatively charged POPG dramatically affects the NTSR1-catalysed GDP/GTP nucleotide exchange rates for G_q.[203] Cholesterol has been shown to affect the BLT2 conformational landscape.[204]

5.1.4 Cell-free expression system of membrane proteins

Most NMR studies of GPCRs have used the baculovirus-insect cell expression system to produce functional and selectively labelled GPCR.[66,194,195] However, the ability to introduce selective isotope labelling using this expression system is still limited because

of the high costs of the required media and isotope scrambling. Isotope scrambling occurs when one amino acid is the precursor for the synthesis of another. Ten out of the twenty genome-encoded amino acids, which locate at the end of the metabolic pathways (Ala, Arg, Asn, Cys, His, Ile, Lys, Met, Pro, and Trp) exhibit minimal isotope scrambling when they are added to growth media, but inter-conversion occurs for the remaining amino acids.[205] In this regard, the cell-free expression system has the advantage of very low levels of scrambling and requiring only a small amount of isotope labelled amino acids to be added making this system substantially cheaper. Cell-free systems provide a powerful new tool for NMR studies offering flexibility for a wide range of possible NMR labelling strategies.

The cell-free expression system is an *in-vitro* protein synthesis method that uses biological machinery to produce a protein of interest. Expression based on *E. coli* extracts is the most commonly used system[206] but extracts from other eukaryotic cells including wheat germ embryos[207,208] or rabbit reticulocytes[209] are also used. These reaction systems have been optimised for several years such that for some proteins they can consistently produce milligram quantities of protein per mL reaction volume. The most revolutionary advancement was the introduction of a dialysis implementation, also known as continuous-exchange cell-free expression. Dialysis mode vessels consist of two compartments, containing the reaction mixture (RM) and the feeding mixture (FM) separated by a dialysis membrane (Figure 5-2). RM, which is where the protein production happens, contains large molecules such as enzymes and nucleic acids. FM, on the other hand, holds small molecules such as precursors including amino acids, nucleotides, and other energy sources. This design can extend the reaction time to 12–24 h, because the FM continuously supplies fresh precursors into the RM and removed inhibitory breakdown products from the RM.

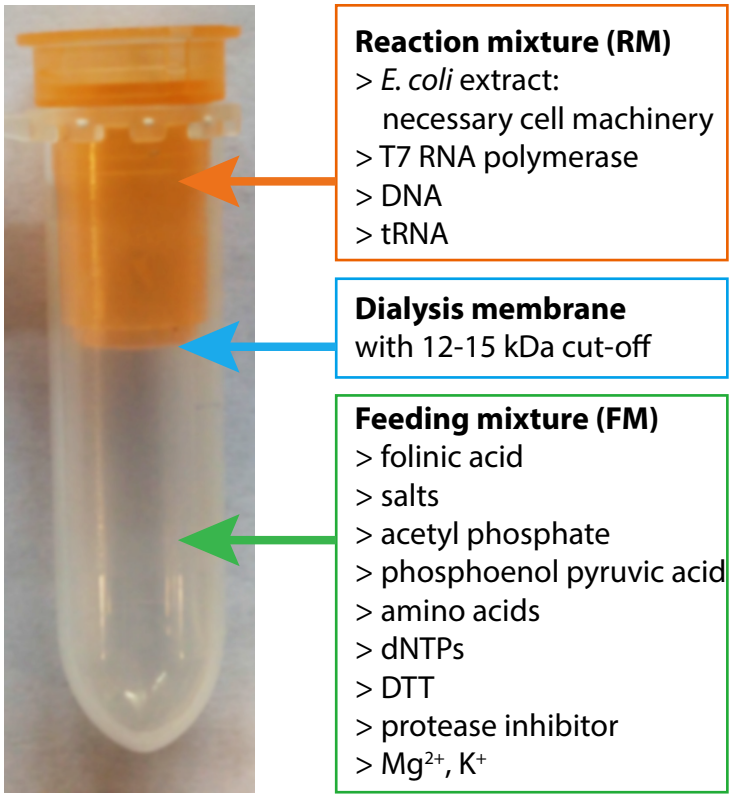

Figure 5-2: The design of a dialysis mode cell-free expression.

Reaction mixture (RM) with a sample volume of 100 µL is in the container at the top (orange). A dialysis membrane with 12–15 kDa cut-off is at the bottom of the container. This container is placed on top of a 2 mL tube where feeding mixture (FM) is. The components in RM and FM are indicated in the boxes.

Cell-free expression offers many advantages over other expression systems and is highly suitable for the expression of toxic proteins or where additives are required such as chaperones, detergents, cofactors and others during protein expression. These can be used without the need to consider potential problems related to transport into the cell. This approach is especially attractive for NMR studies because its low level of metabolic conversion (scrambling) enables selective isotope labelling strategies.[210,211] Cell-free expression combined with combinatorial triple-selective labelling strategies[212] has enabled the backbone resonance assignment of detergent-solubilized membrane proteins,[213] which is impossible via conventional triple resonance backbone assignment due to low NMR sensitivity.

Cell-free expression systems are highly suited for the production of membrane proteins, which in *E. coli* frequently express into inclusion bodies. The three main strategies for expressing membrane proteins using cell-free methodology are detergent-based cell-free

expression (D-CF), lipid-based cell-free expression (L-CF), and precipitate-based cell-free expression (P-CF).[206] D-CF conducts the cell-free reaction in the presence of protein-solubilising detergents and enables the direct translation of membrane proteins into detergent micelles, producing solubilised membrane proteins. Alternatively, artificial liposomes can also be added to cell-free reaction mixtures (L-CF), generating membrane protein embedded liposomes. Functional proteins can be obtained without refolding steps from D-CF and L-CF. In contrast, the reaction is carried out in the absence of protein solubilising compounds in P-CF mode, thus generating membrane proteins that precipitate. As a result, a refolding step that reconstitutes the membrane protein into a membrane mimetic is necessary to produce functional samples. Providing that a suitable refolding method is available, the P-CF method is a more attractive approach as expression yields are generally higher in the absence of inhibiting hydrophobic compounds such as detergents and the reaction product is typically rather pure when obtained as a precipitate. A number of GPCRs have been expressed as functional proteins in cell-free expression system for structural studies[209] but in most cases D-CF or L-CF were used. Although, no high resolution GPCR structures have been solved using cell-free as the expression system yet, two seven-transmembrane-helical protein structures have been published; an NMR structure of bacterial proteorhodopsin[214] and a crystal structure of *Acetabularia* rhodopsin II.[215] Overall, it has been shown that cell-free synthesis has become an important expression method that has the potential to play a crucial role for structural studies of GPCRs.

5.1.5 Aims

Although it has been shown that lipids can play an important role in modulating GPCR activity, information for a detailed molecular mechanism is still lacking. Previous studies of β_1AR in the detergent LMNG using solution NMR in our group have revealed a complex energy landscape of β_1AR activation.[195] Knowledge of β_1AR expression and purification, constructs of β_1AR designed for methionine selective labelling experiments, and the corresponding NMR spectra are all established in our laboratory giving us a good starting point to explore the effect of the lipid bilayer on β_1AR. Since Chapter 3 showed the suitability of SapA lipid nanoparticles for NMR studies and the promising ability of this system to study the impact of different lipid compositions, we hoped to employ SapA lipid nanoparticles to study the activation mechanism of β_1AR in lipid bilayer. Comparing the results for β_1AR in a lipid bilayer with our previous data

for β_1AR in LMNG would allow us to investigate if lipid molecules are important and are part of the mechanism that allosterically modulates β_1AR activity. Once we had established a working protocol for incorporating β_1AR into SapA lipid nanoparticles, we aimed to explore the effect of lipid compositions on the activation of β_1AR, in order to understand the fundamental mechanism of lipid modulation on GPCR activity.

The expression system used in our previous study was the baculovirus-insect cell system. However, producing selectively isotope labelled β_1AR by this method is rather costly. Therefore, the first aim was to explore the possibility of expressing functional β_1AR using the cell-free system because of its ability to economically isotope label proteins for NMR studies. First of all, we needed to establish the system and validate it by expressing a model protein, green fluorescence protein (GFP). Then the expression of β_1AR was tested using different modes of the cell-free expression system, P-CF, D-CF, L-CF.

5.2 Results and discussion

5.2.1 Optimisation of cell-free expression system

For condition screening and system optimisation, a GFP plasmid was used in the cell-free expression system. This is because the quantification of GFP is very straightforward by fluorescence spectroscopy. In addition, the characteristic fluorescence of GFP, excitation at 395 nm, emission at 509 nm, is unique, so the cell-free product can be measured without any need for prior purification. Hence GFP is utilized as a standard protein for determining the expression yield of a certain setup.

The most expensive component in the cell-free system was the purified T7 RNA polymerase (T7RNAP). We decided to prepare it in-house following previously established protocols.[206] The T7RNAP was overexpressed in BL21 (DE3) Rosetta cells. The T7RNAP product did not have to be very pure because the cells were the same as those used for preparing *E. coli* extract. This meant that any impurities in the T7RNAP preparation would also be present in the extract, therefore a single ion exchange purification was expected to provide T7RNAP with adequate purity. T7RNAP eluted at approximately 150 mM NaCl as shown in the chromatogram (Figure 5-3). Fractions from the elution were checked by SDS-PAGE. Large bands at around 100 kDa were observed at the expected molecular weight of T7RNAP. The yield was approximately 40 mg/L cell culture with low sample purity. Analytical scale cell-free expression used

to test the activity of T7RNAP in 5% glycerol and compared with a purchased sample of T7RNAP. The result showed that the T7RNAP activity was three times higher than that achieved using commercially available T7RNAP. However, T7RNAP in 50% glycerol had only 60% of the activity of the commercial enzyme. These results suggested that a high concentration of glycerol may inhibit T7RNAP activity in the cell-free expression reaction mixture. Nevertheless, 50% glycerol was used for long-term storage of home-made T7RNAP at -80 ˚C. The results also indicated that 33 µg/mL T7RNAP would suffice for successful production of GFP i.e. the yield from one litre of cell culture would provide enough for 300 mL of cell-free expression.

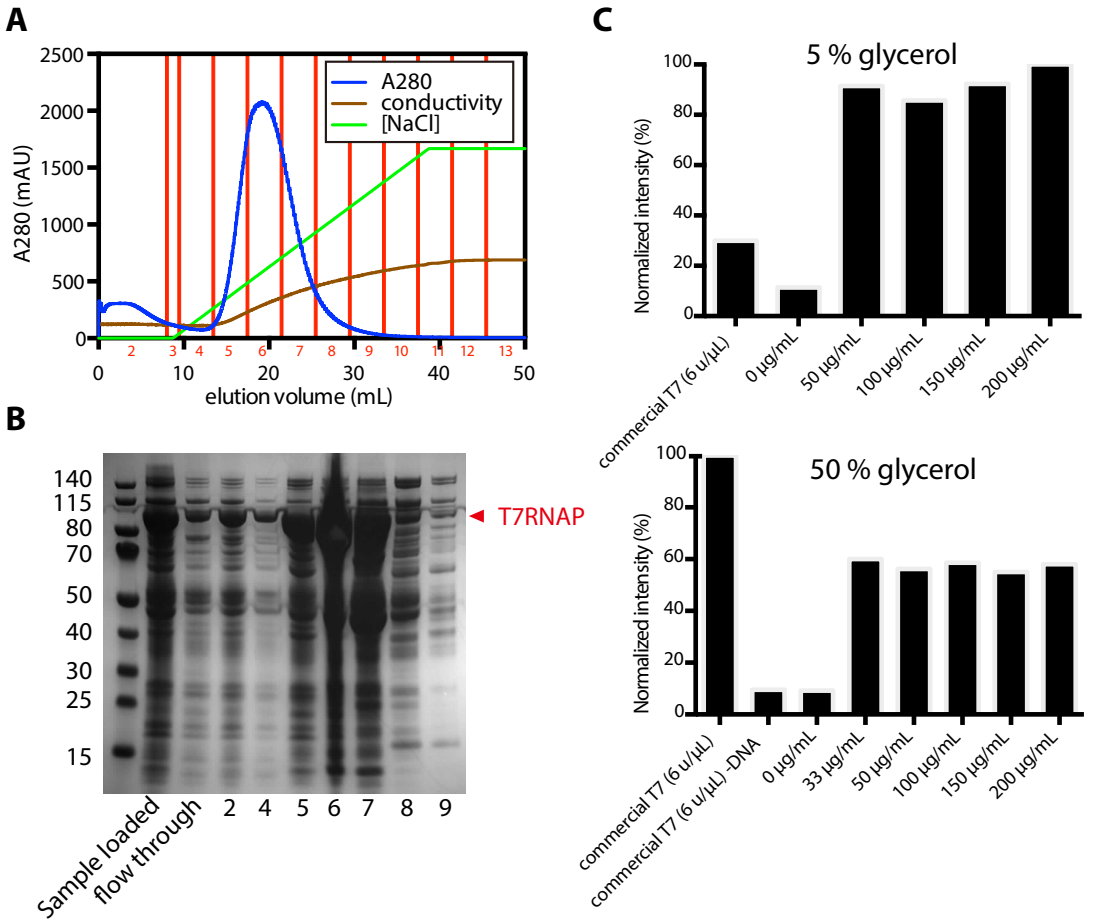

Figure 5-3: Purification and cell-free activity test of T7RNAP.

A) Anion exchange chromatogram of T7RNAP purification. T7RNAP was eluted at 150 mM NaCl. B) SDS-PAGE of fractions from the anion exchange purification. The molecular weight (kDa) of the protein standards is noted on the left. (C) Cell-free expression activity test of T7RNAP in 5% glycerol (upper panel) and 50% glycerol (bottom panel) using GFP as the standard. Fluorescence at 509 nm was measured and normalized by the highest intensity.

The concentration of Mg^{2+} concentration in cell-free expression reaction mixture is an important factor that should be optimised for every batch of the *E. coli* extract or T7RNAP in order to reach the highest protein yield. First we screened for the optimal Mg^{2+} concentration for commercial T7RNAP using concentrations of $Mg(OAc)_2$ from 4.9 mM to 22.9 mM (Figure 5-4). The fluorescence results showed the highest yields of GFP with 12.9 mM Mg^{2+} in the reaction mixture. The yield dropped to below 30% when a Mg^{2+} concentration higher than 16.9 mM was used. The same screening procedure was performed for T7RNAP prepared in-house, which showed an optimal Mg^{2+} concentration of 12 mM. Interestingly, the yield halved when the concentration was increased from 12 mM to 13 mM Mg^{2+}, which was the best value for the commercial T7RNAP. These results highlight the importance of optimising the Mg^{2+} concentration after any change in the composition of the cell-free system. According to this data, 12 mM Mg^{2+} should be used for the following cell-free expression with this specific batch of T7RNAP and *E. coli* extract prepared in-house.

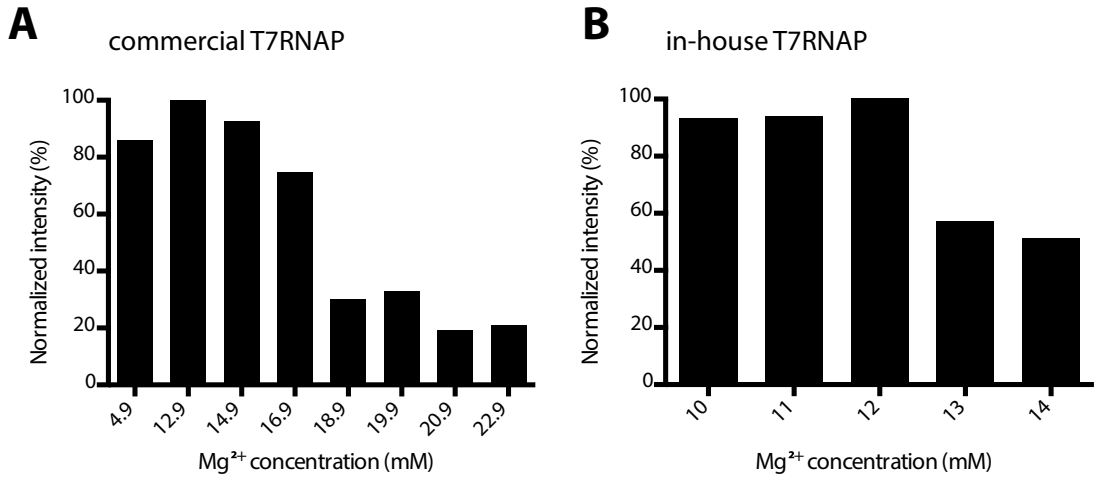

Figure 5-4: Mg^{2+} concentration optimisation for cell-free expression system.

A) Commercial T7RNAP and B) T7RNAP prepared in-house were tested with different Mg^{2+} concentration. The level of GFP expression was quantified by fluorescence intensity at 509 nm and normalised by the highest intensity.

5.2.2 Precipitate-based cell-free expression and refolding of β_1AR

With our *E. coli*-based cell-free expression system established and optimised, P-CF of β_1AR was carried out and the resulting precipitate was solubilised in 15 mM SDS. An anti-histidine western blot was used to identify whether the His_6-tagged β_1AR had been expressed. The result showed a clear band between 25 and 30 kDa (Figure 5-5 A). It is

common for helical membrane proteins to show a smaller molecular weight than expected (38 kDa) because the α-helices remain formed in 15 mM SDS as shown in far-UV CD experiments on this sample (Figure 5-5 B), which makes them more compact than the fully denatured form hence smaller according to the SDS-PAGE. The band was also characterised by peptide fingerprinting analysis using trypsin digestion and MALDI-TOF mass spectrometry (Figure 5-5 C). This approach was able to identify peptides that covered 13% of the β_1AR sequence. Such low coverage was expected for an integral membrane protein because trypsin digestion can only occur in solvent accessible hydrophilic loop regions. As a result, the identified peptides were all in the loop regions when they were mapped onto the β_1AR topology. Overall, our data confirmed that the full β_1AR sequence had been expressed correctly in P-CF.

Based on this successful preliminary result, we scaled up the expression in order to produce more protein for characterisation and refolding trials. The β_1AR precipitates were first solubilised in 15 mM SDS followed by Ni column purification to remove all other impurities. SDS-PAGE of the fractions showed that β_1AR was present in both wash and elution fractions indicating that there was not much non-specific binding (Figure 5-5 D,E). The higher MW bands were oligomeric β_1AR as confirmed by mass fingerprinting. These might have resulted from intermolecular disulphide bond formation. The overall yield of β_1AR by P-CF was approximately 1 mg per 1 mL reaction, as estimated by UV-Vis spectroscopy.

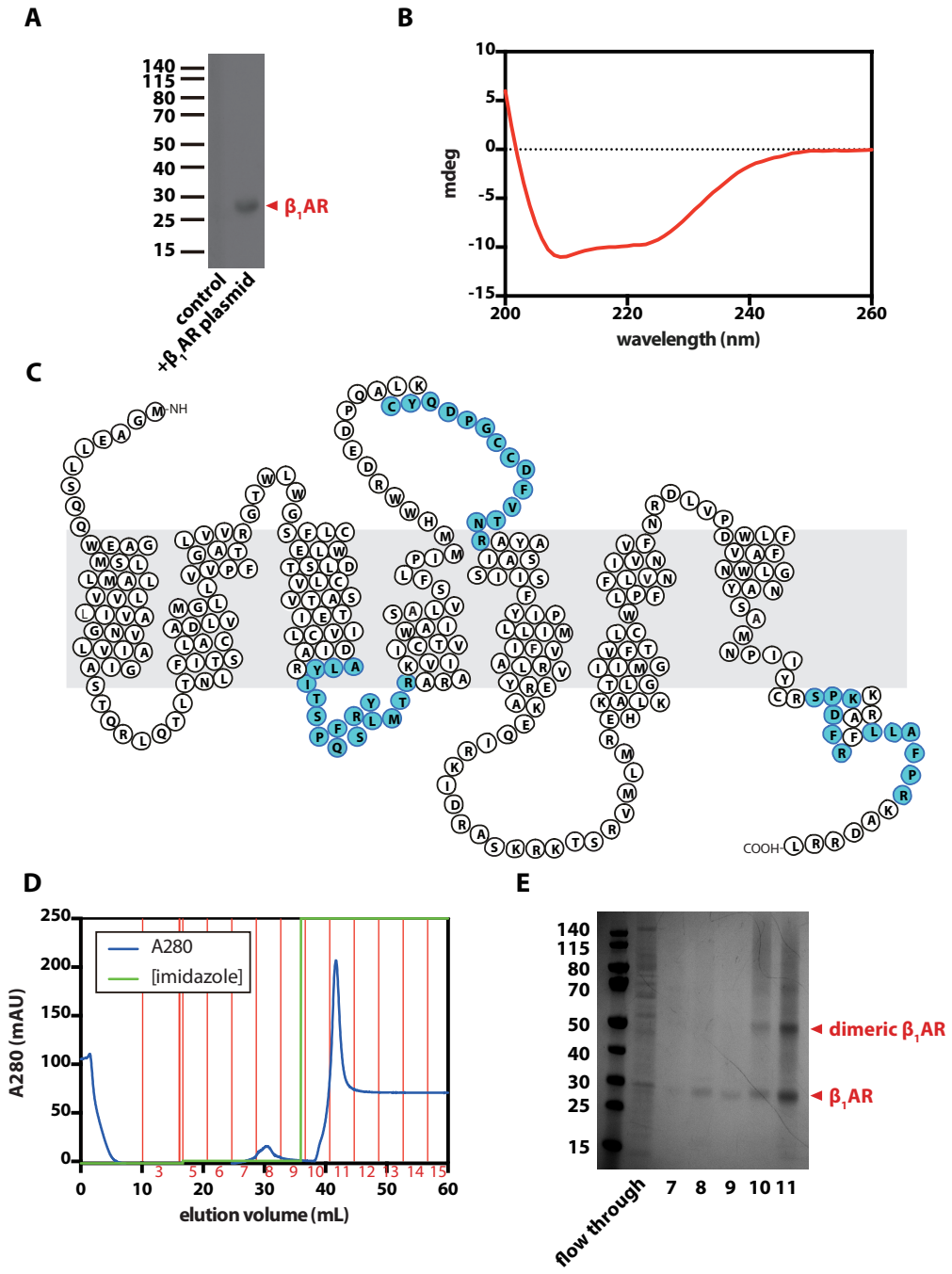

Figure 5-5: Precipitate-based cell-free expression and purification of β_1AR.

A) Anti-His western blot of analytical scale cell-free expression with and without β_1AR plasmid. The molecular weight in kDa is noted on the left and bands showing β_1AR are indicated on the right. B) Far-UV circular dichroism spectrum of β_1AR in 15 mM SDS. C) Peptide mass spectrometry fingerprinting of the β_1AR construct used in this work. Peptides that are recognised in MALDI-TOF mass spectrometry are mapped onto the β_1AR topology in blue. D) Purification of His-tagged β_1AR using a Ni-NTA column. E) SDS-PAGE of the fractions obtained from the Ni-NTA purification. Bands showing monomeric and dimeric β_1AR are indicated.

With the purified β_1AR product dissolved in SDS, we investigated the possibility of refolding it back into a functional state. The functionality of β_1AR can be determined by its binding to alprenolol, a β-blocker that binds to functional βAR.[216] We used a commercial alprenolol resin in a spin column, loaded the sample, eluted using alprenolol with a concentration of 0.8 mM, and checked the amount of β_1AR in each fraction using an anti-His western blot. A positive control of β_1AR expressed from baculovirus-insect cells showed clear bands in the elution fractions (Figure 5-6 A). In contrast, the negative control of β_1AR in SDS was not able to bind to the alprenolol resin, as we expected the protein to be in a non-native conformation in such a harsh detergent (Figure 5-6 B). Although this assay is not able to provide a quantitative measure of functional β_1AR, it should show qualitatively if the sample prepared is functional. With this validated functional assay, two refolding protocols were explored here: reconstitution of β_1AR into small isotropic bicelles composed of C7-DHPC and DMPC (q = 0.25) and on-column refolding in the presence of the detergent LMNG. Both refolding methods have been extensively used for other membrane proteins.[217,218] The functional assay showed that the bicelle sample did not bind to alprenolol resin, whereas LMNG on-column refolding showed that part of the β_1AR was successfully refolded and was present in the elution fractions (Figure 5-6 C,D). With this preliminary on-column refolding test showing positive results, the parameters of this protocol such as incubation time, incubation temperature, salt concentration and others needed to be optimised, to improve the refolding efficiency.

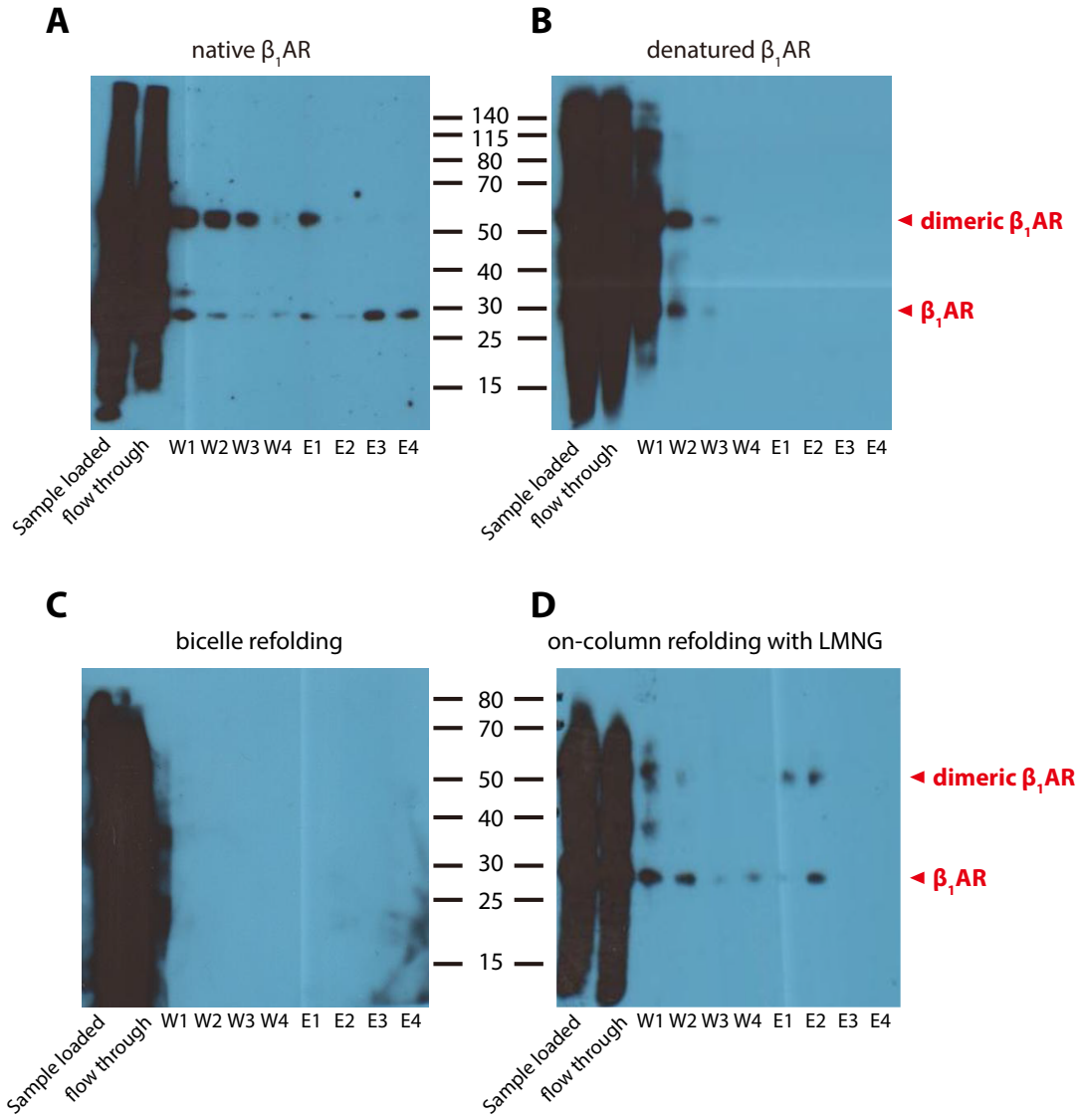

Figure 5-6: Anti-His western blot of the fractions from alprenolol spin column.

The assay was performed for A) β_1AR expressed in insect cells which is expected to be native and B) denatured β_1AR in 15 mM SDS as the positive and negative control, respectively. The fractions are noted at the bottom, W1-W4 are wash fractions and E1-E4 are elution fractions. Functional assay of β_1AR refolding trials by C) bicelle refolding using C7-DHPC and DMPC and D) on-column refolding with detergent LMNG.

5.2.3 Detergent-based cell-free expression of β_1AR

As the refolding of β_1AR was partially successful, an alternative D-CF was carried out to screen suitable detergents for solubilising β_1AR during the cell-free reaction, an approach similar to that used in a case study where the suitability of various detergents

was screened for D-CF GPCR production.[219] A similar procedure was conducted for β_1AR using five detergents DDM, LMNG, C6-DHPC, C7-DHPC and CHAPS. Equivalent amounts of each sample were loaded onto an SDS-PAGE gel and an anti-histidine western blot was performed to check the amount of β_1AR in the soluble fraction and in the precipitate. Despite the low quality of the western blot due to sample overload, it was clear that DDM, C6-DHPC, and CHAPS inhibited the protein production as the intensity of the band, which smeared across the whole lane, significantly decreased compared to the control. On the other hand, the yields from LMNG and C7-DHPC were more or less similar, and a small proportion of β_1AR was observed in the soluble fractions, which indicated that some β_1AR successfully translated into micelles during the cell-free expression. The solubilised β_1AR in LMNG and C7-DHPC were loaded onto the alprenolol spin column to check for sample functionality. The sample in C7-DHPC did not show alprenolol binding, whereas the LMNG sample looked promising. Different concentrations of LMNG in D-CF were screened to further optimise the amount of solubilised β_1AR. The results showed that the reactions were strongly inhibited when the LMNG concentration was higher than 200 μM. 10 μM and 20 μM seemed to solubilise similar amounts of β_1AR.

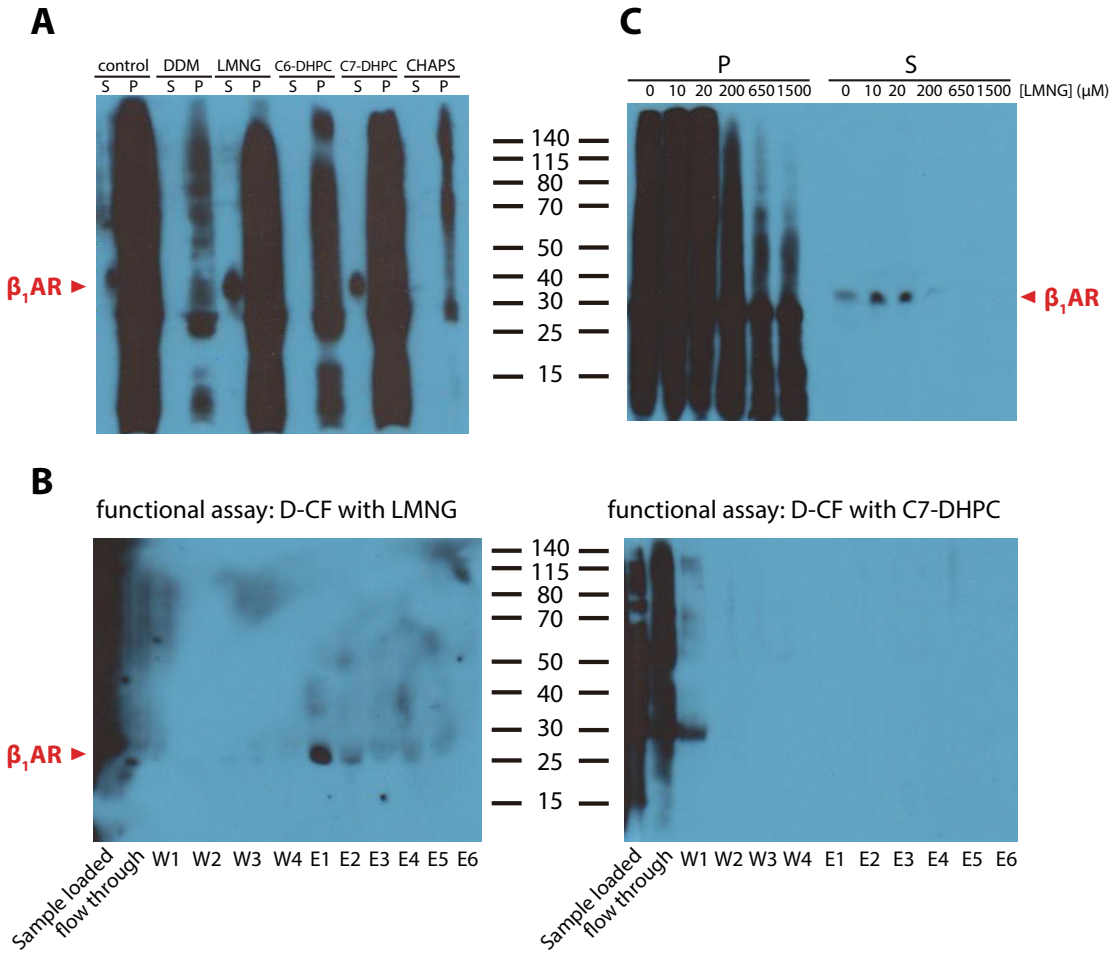

Figure 5-7: Anti-His western blot of β_1AR expressed in D-CF.

A) β_1AR was expressed in D-CF using different detergents. Detergents used for screening are shown in lane labels. Soluble and precipitate fractions are labelled as S and P, respectively. B) Functional assay of the soluble fractions of D-CF in LMNG (left) and C7-DHPC (right). C) LMNG concentration screening, ranging from 0 to 1500 μM, for β_1AR expression using D-CF.

5.2.4 Incorporation of β_1AR in DDM into SapA lipid nanoparticles

Despite our promising preliminary results for the cell-free expression of β_1AR, the yield of the overall functional receptor was still too low for NMR experiments. Therefore, we started using β_1AR samples that had been expressed in baculovirus-insect cells by another Ph.D. student, Andras Solt, in our lab. β_1AR was extracted and purified by Ni-NTA purification using DDM buffer. DDM is the preferred detergent for the purpose of incorporation into SapA lipid nanoparticles because it is easier to remove by detergent absorbent beads later on in the incorporation procedure. The purified DDM-solubilised

β_1AR was mixed with SapA and DMPC in a SapA:DMPC:β_1AR ratio of 10:250:1 at pH 7.4 (Table 5-1). Neutral pH was used because of the limited stability of β_1AR at lower pH values. The detergent removal step was then applied to this preparation by mixing with 80% w/v Amberlite XAD2 beads for 2 h at 25 ºC. Complete detergent removal was confirmed by the 2,6-dimethylphenol assay. Precipitates in the samples were pelleted and the supernatant was checked by SDS-PAGE (Figure 5-8 A). In the presence of SapA-DMPC (Figure 5-8 A lane 2), the β_1AR remained in solution indicating a successful incorporation (Figure 5-8 A). A negative control was performed with only DDM-solubilised β_1AR and Amberlite beads which showed no band on the SDS-PAGE gel. This was due to β_1AR precipitating when the DDM molecules were completely removed by the beads. β_1AR in the SapA-DMPC sample was then characterised by analytical size-exclusion chromatography (Figure 5-8 B). The chromatogram shows a homogeneous peak with a shoulder on the right, which corresponds to the empty SapA-DMPC nanoparticles. The resulting β_1AR in SapA-DMPC nanoparticles had an apparent molecular weight of about 160 kDa. The SDS-PAGE gel showed two faint bands at 13 kDa and 22 kDa, which we occasionally observed, corresponding to fragments of β_1AR from protease cleavage at ICL2.

Table 5-1: Composition of the β_1AR incorporation assembly mixture.

	Volume	Final concentration
SapA (3 mM)	20 µL	120 µM
DMPC (10 mM)	150 µL	3 mM
β_1AR (100 µM)	60 µL	12 µM
DDM (10%)	10 µL	0.2%
Buffer‡	260 µL	
Total volume	500 µL	

‡ The buffer used in the β_1AR incorporation is 50 mM Tris-HCl (pH 7.4), 150 mM NaCl.

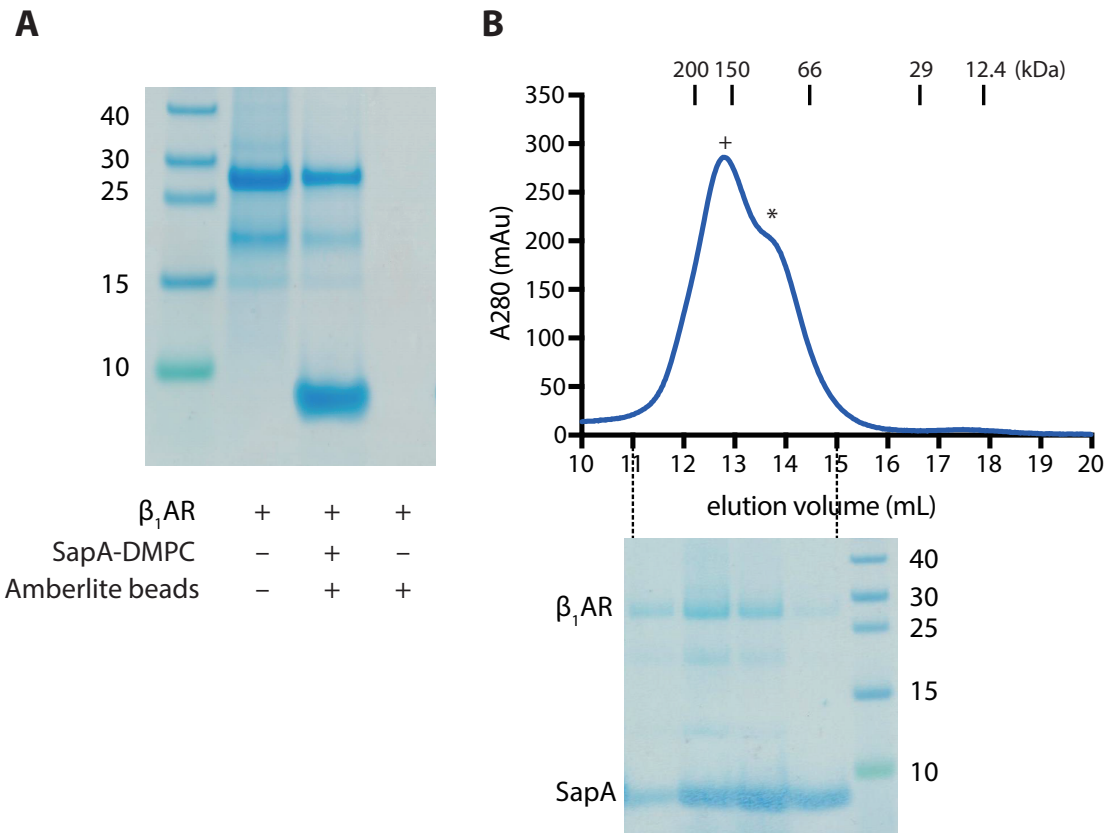

Figure 5-8: Incorporation of β1AR into SapA-DMPC nanoparticles.

A) SDS-PAGE of samples before and after the incorporation procedure. A negative control of β1AR incubated with Amberlite beads showing that β1AR crashed out of solution hence no bands on the SDS-PAGE. B) Analytical size-exclusion chromatography of β1AR in SapA-DMPC nanoparticles and the SDS-PAGE of the peak fractions. The peak indicated by + represents β1AR in SapA-DMPC nanoparticles; the peak indicated by * represents empty SapA-DMPC nanoparticles.

5.2.5 NMR spectra of β1AR in SapA-DMPC nanoparticles

The interaction between detergent-solubilised β1AR, the full agonist isoprenaline and the G-protein mimicking nanobody Nb80 was studied previously using NMR spectroscopy.[194,195] Due to the large molecular weight of the β1AR-detergent complex, a selective labelling strategy was necessary to produce interpretable NMR spectra. Following the previous study on β1AR conducted in our lab, [$^{13}C_{\varepsilon}$-methionine]-β1AR was used to investigate the activation process of β1AR in lipid bilayers by NMR. [$^{13}C_{\varepsilon}$-methionine]-β1AR was incorporated into SapA-DMPC nanoparticles and purified by

size-exclusion chromatography using the method described in the previous section (5.2.4). The construct used here had 12 methionine residues (M1, M44, M48, M90, M153, M178, M179, M223, M281, M283, M296, M338) shown in Figure 5-9, except M1 because it is not visible in the structure.

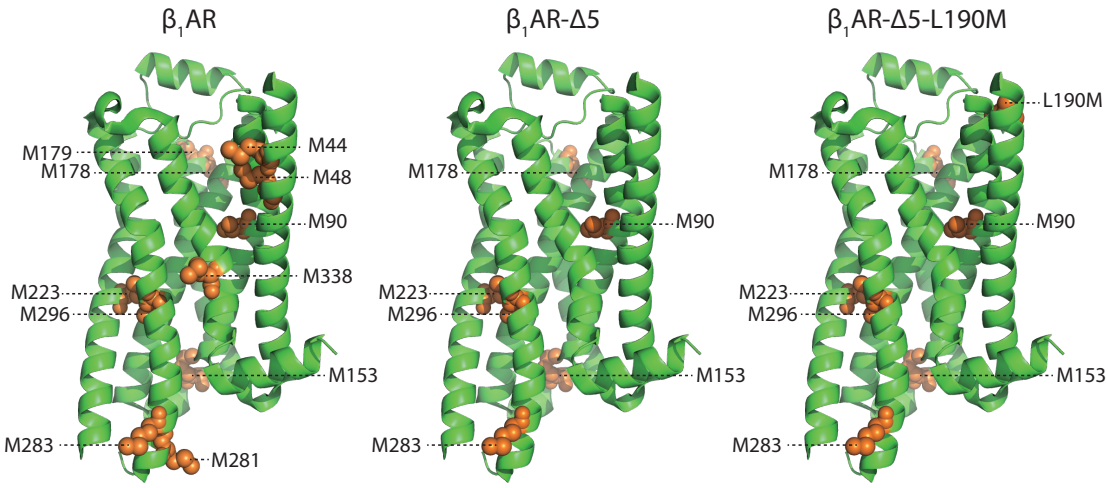

Figure 5-9: β_1AR constructs used in this study.

The original β_1AR construct contains 12 methionines. All methionines except M1, not resolved in the crystal structure, are mapped onto the crystal structure (PDB ID: 4BVN) shown in orange spheres. β_1AR-Δ5 with five methionine mutated (M44L, M48L, M179L, M281A, M338A) and β_1AR-Δ5-L190M with one introduced methionine, L190M, are indicated in the same way for comparison.

The ^{13}C HMQC spectrum of β_1AR in the apo state revealed 13 peaks for the 12 methionine residues (Figure 5-10 blue). These peaks possess varying intensities, indicating that different parts of the receptor have different dynamics. Several peaks showed chemical shift perturbation upon isoprenaline binding (Figure 5-10 green), indicating that the receptor changes conformation when bound to a full agonist. The substantial peak broadening observed for many of the signals also suggests that the receptor is able to exchange dynamically between several conformations on a µs-to-ms time scale. Addition of the G-protein mimicking Nb80 to form a fully active ternary complex induced further dramatic chemical shift perturbations. At the same time the recovery of peak intensities seems to indicate that the ternary complex samples fewer conformations, comparable to NMR observations for the β_2-adrenergic receptor.[67]

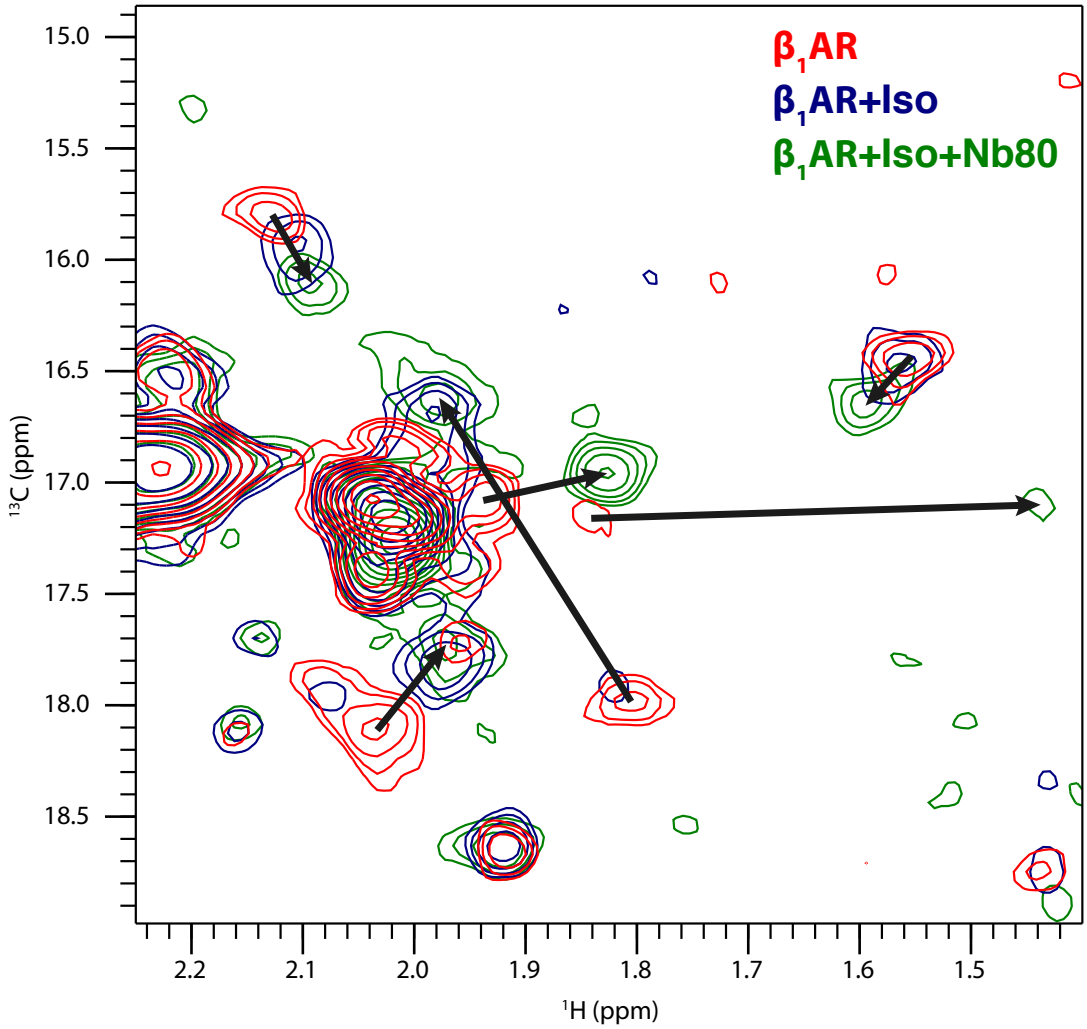

Figure 5-10: NMR spectra of β_1AR in SapA-DMPC nanoparticles.

Overlay of the 2D ^{13}C-SOFAST-HMQC spectra of [$^{13}C_\varepsilon$-methionine] β_1AR with a concentration of 40 µM in the apo state (red), the isoprenaline-bound state (blue), and the isoprenanline-Nb80 bound ternary complex (green). The spectra were recorded at 308 K on a Bruker Avance AVIII 800 spectrometer (^{1}H frequency of 800 MHz) equipped with a 5 mm TXI HCN/z cryoprobe. Spectra were recorded with 128 scans, resulting in an experiment time of 4 h.

While these results showed the successful incorporation of β_1AR into SapA-DMPC nanoparticles, individual resonance assignments will be required for further interpretation.

5.2.6 Optimisation of the incorporation protocol for β_1AR in LMNG

Although we have successfully incorporated β_1AR into SapA-DMPC nanoparticles and obtained NMR spectra of very good quality, we were not able to make further investigations without peak assignments. NMR peak assignments for β_1AR in LMNG were determined in our laboratory using a derivative β_1AR construct, in which five methionines are mutated to reduce the spectral complexity including M44L, M48L, M179L, M281A, M338A, hereafter called β_1AR-Δ5 (Figure 5-9). Therefore, our aim was to incorporate β_1AR-Δ5 into SapA-DMPC nanoparticles permitting the transfer of assignments from the LMNG spectra based on peak proximity. The main issue for β_1AR-Δ5 incorporation was that this construct is not stable in DDM as we observed protein precipitation after a few days at 4 ºC, leaving us with no choice but to use LMNG to solubilise β_1AR-Δ5. With LMNG, detergent removal was much more challenging using adsorbent beads as shown in Chapter 2. In order to be able to study β_1AR-Δ5 in SapA lipid nanoparticles, we had to establish an efficient protocol for removing LMNG first.

Together with a Part II student, Daniel Gentle, we started screening for the best condition to incorporate LMNG solubilised β_1AR into SapA-DMPC nanoparticles in order to find a procedure which removes LMNG completely but also keeps β_1AR in solution. The LMNG concentration was monitored by the 2,6-dimethylphenol assay and the β_1AR concentration was quantified by the band intensity in an SDS-PAGE gel prepared after the detergent removal step. The numbers were then normalised against the initial LMNG concentration and β_1AR concentration in the original LMNG solubilised β_1AR sample, respectively, showing the percentage of molecules left after treatment with Amberlite XAD2 beads. A successful incorporation was expected to show no LMNG left in the sample as well as β_1AR remaining in solution. We also carried out negative control experiments for all the conditions screened here, using the same parameters but in the absence of SapA-DMPC. The negative control for LMNG removal should show no LMNG and no β_1AR in solution because β_1AR should precipitate out of solution once all the LMNG molecules are completely removed by the beads.

We started by testing incubation times of four to five hours at 25 ºC (Figure 5-11, A) which were double the time required for DDM removal. The negative control showed that even though the beads were able to remove more than 70% LMNG, there was still a

detectable amount of β_1AR left in the sample, indicating the presence of residual LMNG micelles stabilising some β_1AR in solution. In the presence of SapA-DMPC, a significant amount of both LMNG and β_1AR was detected after the detergent removal process. Incomplete LMNG removal was observed regardless of changing for fresh beads half way through the incubation or doubling the amount of beads used, suggesting that this occurred because of the slow rate of removal but not due to reaching the capacity of the beads. In agreement with this, a 24 h incubation was able to remove all of the LMNG (Figure 5-11, B). The negative control showed 0% LMNG and 0% β_1AR left in the sample. In the presence of SapA-DMPC, LMNG was completely removed while β_1AR remained in solution showing that it was stabilised by the SapA-DMPC nanoparticles. This was evidence for successful β_1AR incorporation into SapA-DMPC nanoparticles.

Figure 5-11 (*opposite*): Optimisation of the LMNG removal for the β_1AR incorporation.

LMNG solubilised β_1AR with (right panel) or without (left panel) SapA-DMPC were incubated with 80% (w/v) Amberlite beads for a total A) 4 h or B) 24 h incubation time. The incubation temperature was 25 ºC unless indicated otherwise. Some conditions involved several steps meaning changing fresh Amberlite beads in between. LMNG concentration was determined by the 2,6-dimethylphenol assay. β_1AR concentration was determined by quantification of the corresponding band on SDS-PAGE. Both concentrations are normalised against the concentration of the original β_1AR sample, i.e. the percentage of LMNG or β_1AR left in the sample after the treatment. The data are presented in a heat map format showing 0% (purple) to 100% (yellow) in gradient. C) Investigation of the effect of incubation temperature (4 ºC or 25 ºC) on LMNG removal using the same experimental procedure. This experiment was performed using POPC/POPG (3:2) instead of DMPC.

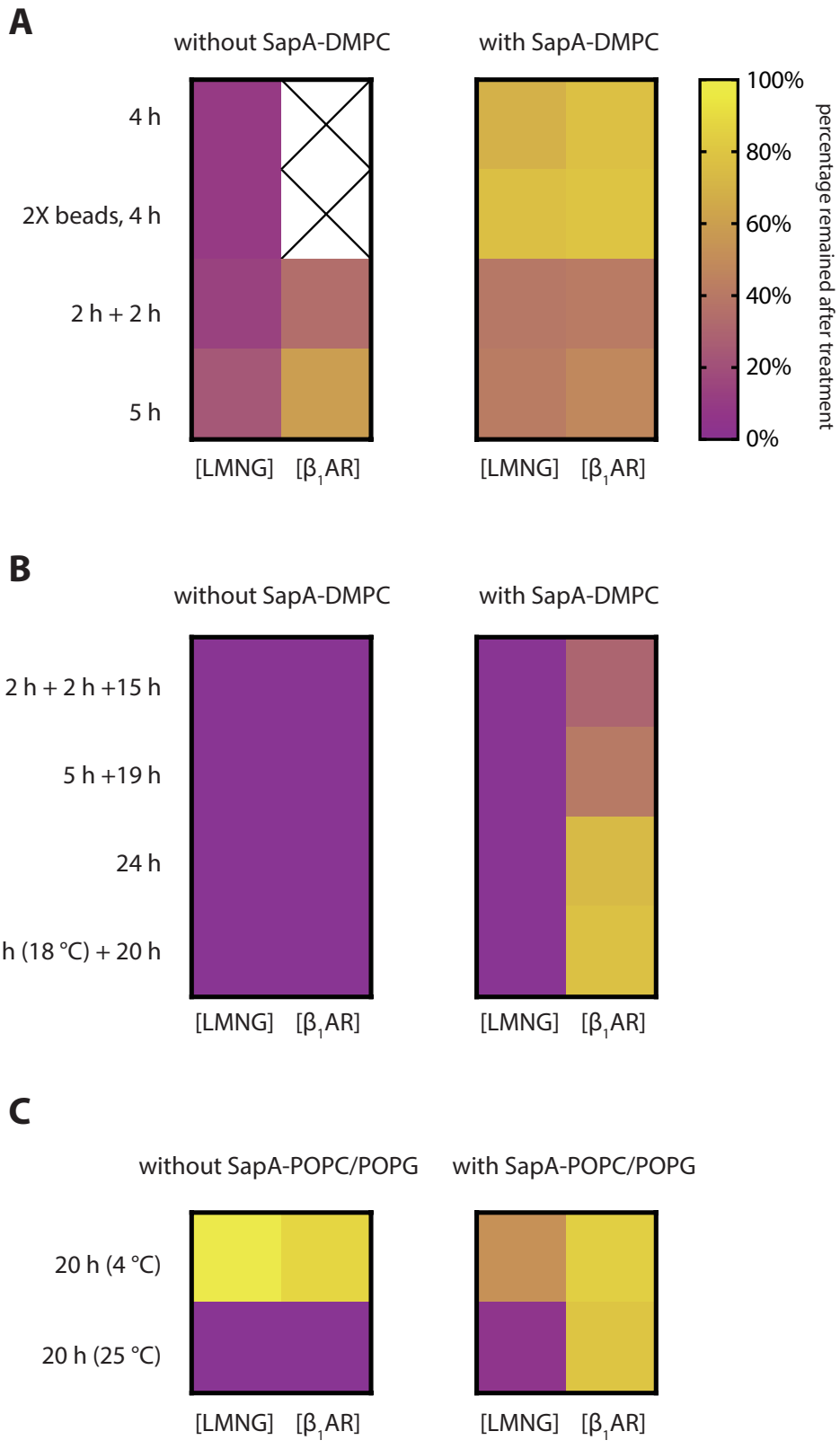
A
without SapA-DMPC
with SapA-DMPC
4 h
2X beads, 4 h
2 h + 2 h
5 h
[LMNG] [β1AR]
[LMNG] [β1AR]
100%
80%
60%
40%
20%
0%
percentage remained after treatment
B
without SapA-DMPC
with SapA-DMPC
2 h + 2 h +15 h
5 h +19 h
24 h
4 h (18 °C) + 20 h
[LMNG] [β1AR]
[LMNG] [β1AR]
C
without SapA-POPC/POPG
with SapA-POPC/POPG
20 h (4 °C)
20 h (25 °C)
[LMNG] [β1AR]
[LMNG] [β1AR]

In another set of experiments, we investigated the effect of temperature during incorporation of β_1AR into SapA-POPC/POPG (3:2) nanoparticles (Figure 5-11, C). It is generally believed that the incubation temperature in the detergent removal step must be near the phase-transition temperature of the lipids being used, which for POPC/POPG is around 0 ºC.[129] Therefore, the detergent removal for the assembly of MSP-POPC/POPG nanodiscs is often performed at 4 ºC in the reported literature.[105,135] However, we observed that barely any LMNG was removed at 4 ºC (almost 100% left shown in yellow). In contrast, at 25 ºC the process worked so well that no LMNG was left (purple) in the sample both with and without SapA-POPC/POPG. Our results also suggest that incorporation was achieved at 25 ºC as β_1AR remained in solution in the presence of SapA-POPC/POPG. We have shown previously that LMNG removal is very slow and we speculated that this is due to the very low CMC (0.001%) of LMNG. We hypothesised that a lower temperature would reduce the CMC resulting in little monomeric LMNG being present in solution where it could be absorbed by the beads. It is also possible that the low temperature reduced the exchange rate between LMNG monomers and LMNG micelles which became the rate-limiting step. These two factors are potential reasons for the extremely slow removal of LMNG.

This chapter has established a protocol for incorporating LMNG-solubilised β_1AR into SapA lipid nanoparticles. Incubation at 25 ºC for 24 h was necessary to completely remove LMNG, and β_1AR remained in solution after the incubation step indicating a successful incorporation. This allowed us to proceed with the incorporation of LMNG-solubilised β_1AR mutants for which we had NMR peak assignment information.

5.2.7 NMR peak assignment of β_1AR-Δ5-L190M in lipid bilayer

We used the protocol established in the previous section to incorporate β_1AR-Δ5-L190M into SapA-DMPC nanoparticles. This was a derivative construct based on β_1AR-Δ5 which has another introduced methionine on the extracellular loop 2 (Figure 5-9) for the purpose of monitoring agonist binding events. β_1AR-Δ5-L190M was solubilised in LMNG, therefore the incorporation procedure was performed for 24 h to ensure complete detergent removal. We also included an additional Ni-NTA purification step, which was not included previously, to remove empty SapA-DMPC nanoparticles (Figure 5-12 A). The flow-through fraction showed a SapA band

corresponding to empty SapA-DMPC nanoparticles. The elution fraction from the Ni-NTA purification step showed the presence of both β_1AR-Δ5-L190M and SapA, meaning SapA, without a His_6-tag, was in complex with the His_6-tagged β_1AR-Δ5-L190M. This result provided a strong indication that the incorporation step has proceeded successfully. The elution fraction was then analysed by analytical size-exclusion chromatography to check the particle size and the homogeneity (Figure 5-12 B). The chromatogram showed a single symmetrical peak at around 13.6 mL. The SDS-PAGE gel again confirmed the presence of SapA and β_1AR-Δ5-L190M. This data also confirmed that the shoulder peak indicated by * in the previous chromatogram (Figure 5-8 B) was indeed empty SapA-DMPC nanoparticles because the peak disappeared after the Ni-NTA separation step.

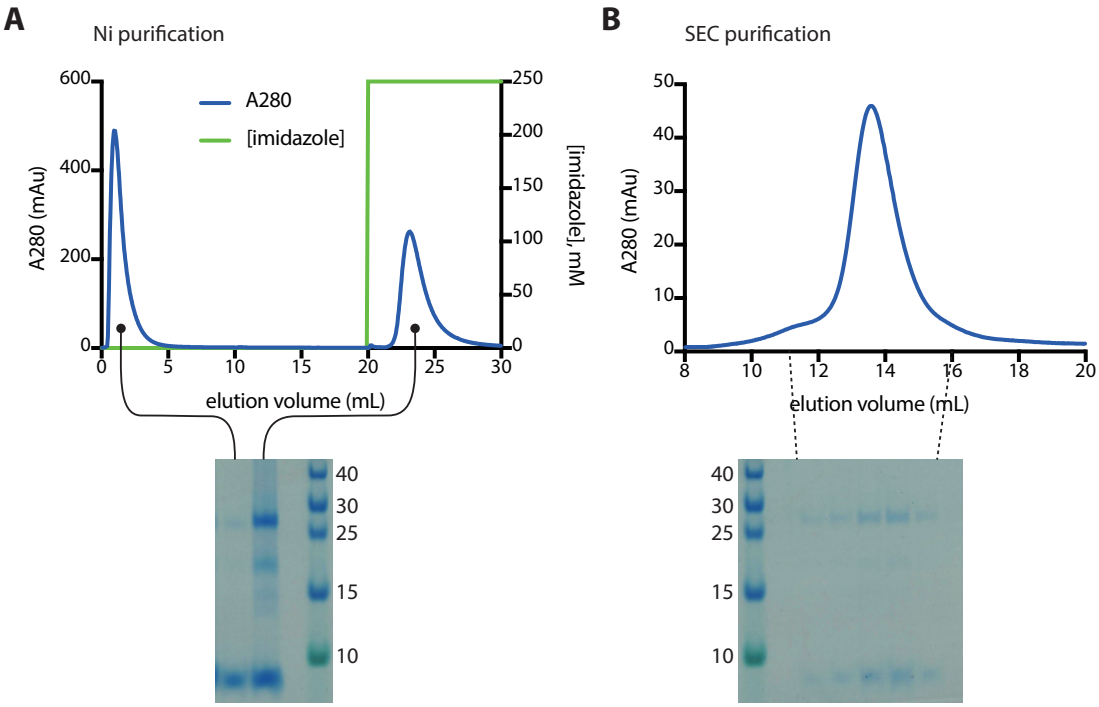

Figure 5-12: Purification of β_1AR-Δ5-L190M in SapA-DMPC nanoparticles.

A) Ni-NTA chromatogram of the assembly mixture shows the separation of empty SapA-DMPC nanoparticle from β_1AR-Δ5-L190M in SapA-DMPC nanoparticles. Flow-through and elution fractions were analysed using SDS-PAGE. B) SEC of the elution fractions from A). SDS-PAGE of the corresponding fractions is shown at the bottom.

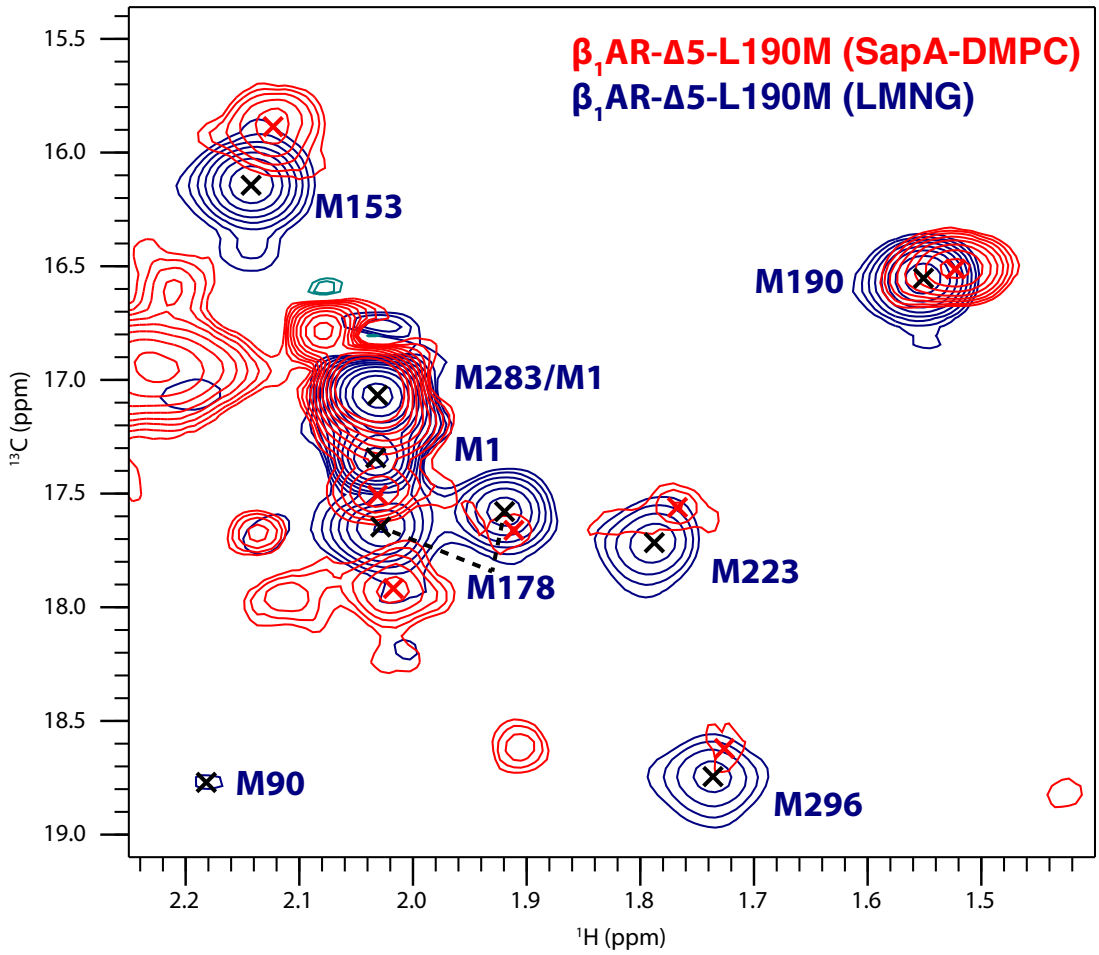

Figure 5-13: NMR peak assignments transfer for β1AR-Δ5-L190M.

Overlay of the 2D ^{13}C-SOFAST-HMQC spectra of [$^{13}C_{\varepsilon}$-methionine] apo β1AR-Δ5-L190M in SapA-DMPC nanoparticles (red) and in LMNG (blue). The peak assignments for β1AR-Δ5-L190M in LMNG that were obtained previously from mutagenesis are indicated. The spectra were recorded at 308 K on a Bruker Avance AVIII 800 spectrometer (^{1}H frequency of 800 MHz) equipped with a 5 mm TXI HCN/z cryoprobe. Spectra were recorded with 368 scans using a 60% non-uniform sampling (NUS) scheme, resulting in an experiment time of ~6 h.

A 2D ^{13}C-HMQC experiment was recorded for the sample and overlaid with the spectrum of the same construct in LMNG for which we already had the peak assignments (Figure 5-13). The peaks did not overlay perfectly in the two spectra which is what we would expect due to the different chemical environments provided by the membrane mimetic systems. The signal-to-noise ratio was worse in the SapA-DMPC spectrum because of the larger particle size and lower sample concentration. Nevertheless, the assignments were unambiguously transferred for M153, M190, M223,

and M296 based on peak proximity because these resonances were all isolated and well-resolved. However, the resonances for M283, M1, and M178 were in a crowded region and largely overlapped making the assignment transfer difficult. In addition, there was no observable peak near M90. All the peaks, except the most intense one, which is assigned to M283/M1 in the LMNG spectrum, shift significantly suggesting that the lipid bilayer indeed offers a distinct environment compared to detergent. M283 is located at a very dynamic and water-accessible loop region which should not be affected by different membrane mimetics used hence resulted in no significant perturbations.

Based on this spectrum, we were not able to assign a resonance for M178 because there are two peaks equally close to the M178 peak in the LMNG spectrum. M178 shows two peaks in the spectrum in LMNG micelles, a distinct behaviour, which indicates two conformations of M178 in the β_1AR apo state. This was an interesting finding and we hoped to obtain M178 assignments for the SapA-DMPC spectrum as well. Therefore, a β_1AR-Δ5-M178A construct was used to clarify the peak assignment for M178. Note that this construct did not contain M190 or M178 and thus the spectrum was expected to lack signals for M190 and M178. The same incorporation procedure and NMR experiment were performed. An overlay of the NMR spectra of β_1AR-Δ5-L190M and β_1AR-Δ5-M178A showed the disappearance of two peaks in addition to the disappearance of the resonance corresponding to M190 (Figure 5-14). Therefore, we assigned the remaining two peaks to M178. Although similar behaviour is observed, in that M178 shows two peaks as found in the LMNG spectrum, the intensity ratio between the two peaks is different (Figure 5-13). This suggests that the lipid bilayer has an effect on the equilibrium between these two conformations of M178. Here, we obtained assignments for five key residues that provide well-distributed reporters on β_1AR, M153 on the intracellular side, M223 and M296 in the membrane region, and M178 and M190 on the extracellular side. The next step was to investigate the conformational changes of β_1AR upon activation by monitoring the chemical shift of these assigned methionine residues.

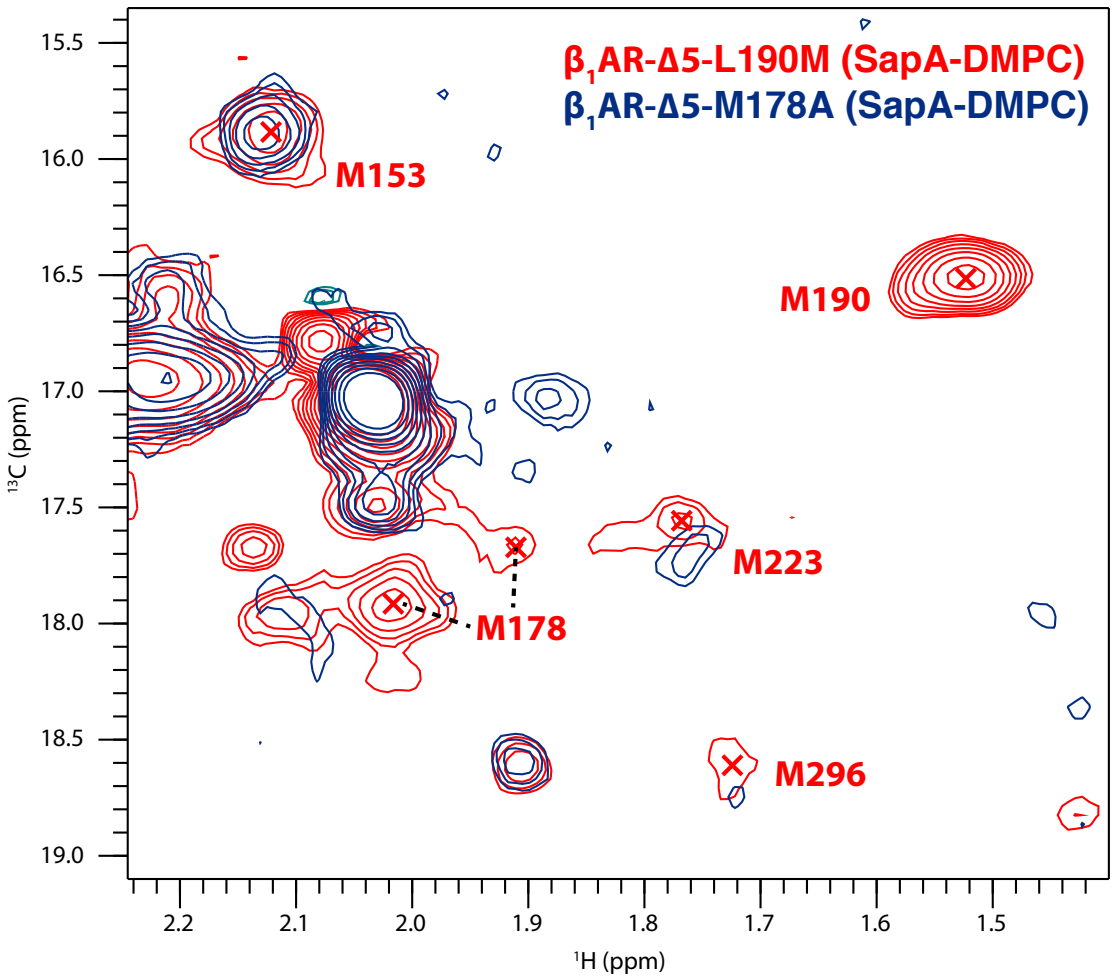

Figure 5-14: Identification of peaks for M178 in the spectrum of β_1AR-Δ5-L190M.

Overlay of the 2D ^{13}C-SOFAST-HMQC spectra of [$^{13}C_\varepsilon$-methionine] β_1AR-Δ5-L190M (red) and β_1AR-Δ5-M178A (blue) in SapA-DMPC nanoparticles. The peak assignments are indicated. Two peaks are assigned to M178 due to the disappearance in the M178A spectrum. The spectra were recorded at 308 K on a Bruker Avance AVIII 800 spectrometer (^{1}H frequency of 800 MHz) equipped with a 5 mm TXI HCN/z cryoprobe. Spectra were recorded with 368 scans using a 60% non-uniform sampling (NUS) scheme, resulting in an experiment time of ~6 h.

5.2.8 Activation of β_1AR in lipid bilayer

With the methionine peaks assigned, next we monitored the movement of these peaks upon sequential addition of the full agonist, isoprenaline, and the G protein mimicking nanobody, Nb6B9. This experiment was previously performed on β_1AR-Δ5-L190M in LMNG by Andras Solt (Figure 5-15 A). The isoprenaline bound spectrum (Figure 5-15 A, blue) showed no perturbations for M178 and M190, and only a subtle shift for M153.

M223 and M296, on the other hand, shifted significantly together with a decrease in intensity. A drop in intensity or peak broadening is an indication of a very dynamic state in which the receptor exchanges between multiple conformations at a rate comparable to the chemical shift difference between them. This result is consistent with the previous observation for β_2AR that the full agonist-bound state showed a dynamic characteristic, which is thought to be essential for G protein recognition.[105,135] In LMNG detergent in the spectrum of the ternary complex (Figure 5-15 A, green) in which the receptor is bound to isoprenaline and Nb6B9, both M223 and M296 showed a large peak shift indicating a large conformational change upon binding to Nb6B9. In addition, the intensities of both peaks were restored suggesting that β_1AR was in a more uniform environment compared to the isoprenaline bound state. M153 and one of the M178 peaks, which showed little perturbation upon binding isoprenaline, also showed significant peak shifts from the isoprenaline bound to the ternary complex state. This suggests that major conformational changes of M153 and M178 only happen in complex with an intracellular binding partner.

In order to investigate the effect of the lipid bilayer on the activation of β_1AR, the same set of experiments was performed for β_1AR-Δ5-L190M in SapA-DMPC nanoparticles (Figure 5-15 B). In the 2D ^{13}C-HMQC spectrum with isoprenaline bound (Figure 5-15 B, blue), M223 and M296 were not detectable, whereas very weak peaks were observed in the LMNG spectrum (Figure 5-15 A, blue). This is probably due to the very low sample concentration and larger particle size which degraded the sensitivity of the experiment so much that it could not pick up peaks with such low intensity. Although the signals from M223 and M296 were too weak to be observed, the disappearance of peaks suggests that the conformational exchange in the full agonist bound state as discussed above for the LMNG sample was preserved in the lipid bilayer. Interestingly, we observed signals from M153 and M178 shifting significantly when the receptor bound to full-agonist in the lipid bilayer; in addition, the second M178 resonance disappeared. This was a different behaviour to that in LMNG where either subtle shifts or no changes were observed, and the second M178 peak remained in the same position. This suggests that the conformational change induced by agonist binding probably needed the participation of the lipid bilayer. This data supports the generally believed GPCR activation model that binding the full-agonist on the extracellular side induces a conformational change on the intracellular side which then promotes G-protein binding.[48] Next, the G-protein mimicking nanobody Nb6B9 was added into the sample

for 2D ^{13}C-HMQC measurement of the ternary complex (Figure 5-15 A, green). A large chemical shift change as well as the restoration of peak intensities for M223 and M296 was observed, similar to our observations for the spectra recorded in LMNG micelles. The resonance for M153 remained at the same position as in the spectrum with isoprenaline bound, whereas M178 signals shifted further in the same direction. Overall, we observed the same pattern of intensity changes and the same direction of chemical shift changes following the sequential addition of the full agonist isoprenaline and the G protein mimicking nanobody Nb6B9 indicating that the general activation mechanism for β_1AR in LMNG micelles and in the DMPC bilayer is similar.

Figure 5-15 (*opposite*): Activation of β_1AR-Δ5-L190M in different membrane mimetics.

Overlay of the 2D ^{13}C-SOFAST-HMQC spectra of [$^{13}C_\varepsilon$-methionine] β_1AR-Δ5-L190M in A) LMNG and B) SapA-DMPC nanoparticles. Spectra of the apo state (red), the isoprenaline-bound state (blue), and the isoprenanline-Nb6b9 bound ternary complex (green) are overlaid. Peak assignments and the peak shifts are indicated. The spectra were recorded at 308 K on a Bruker Avance AVIII 800 spectrometer (^{1}H frequency of 800 MHz) equipped with a 5 mm TXI HCN/z cryoprobe. Spectra were recorded with 368 scans using 60% non-uniform sampling (NUS) scheme, resulting in an experiment time of ~6 h.

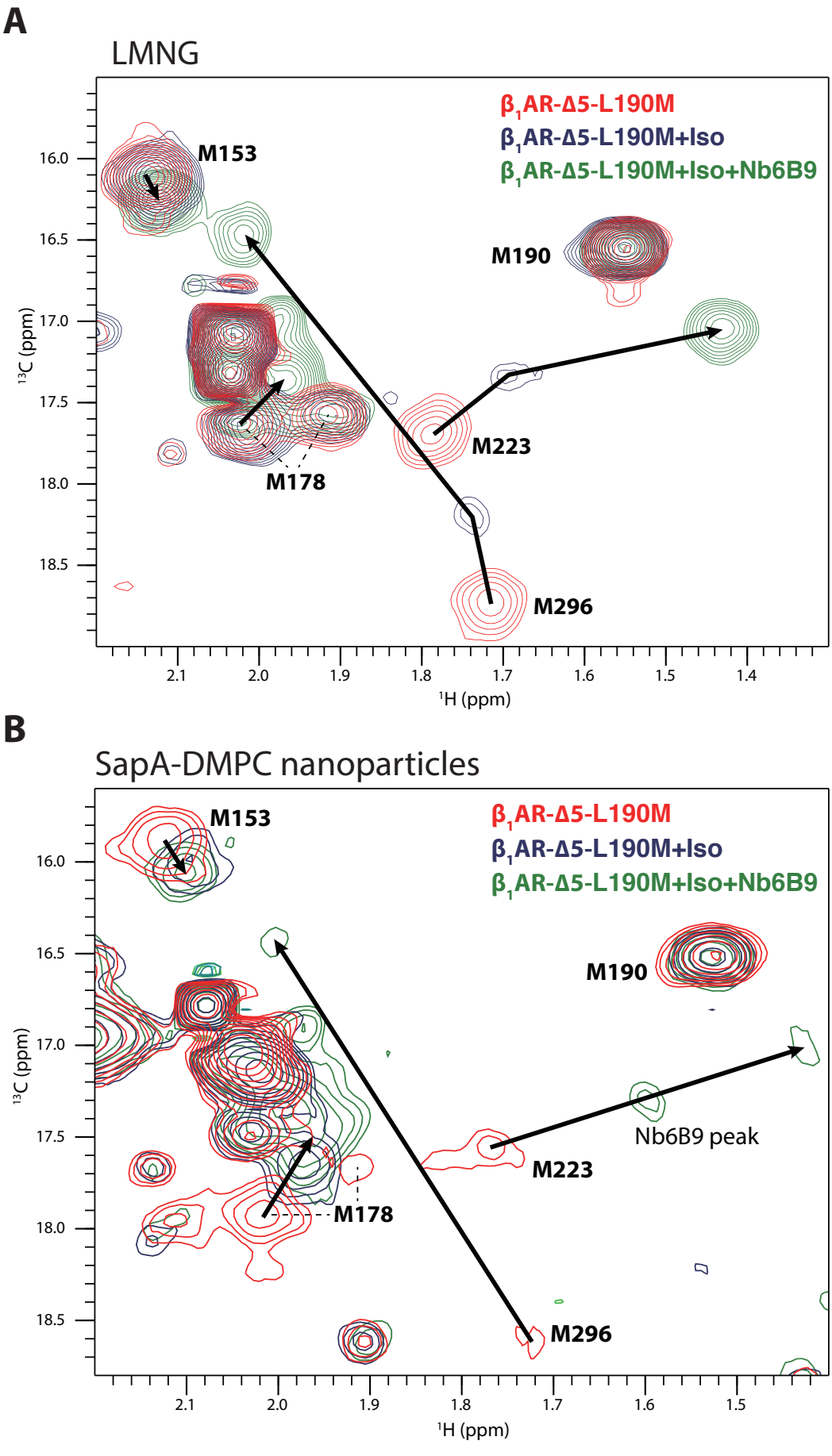
A
LMNG
β1AR-Δ5-L190M
β1AR-Δ5-L190M+Iso
β1AR-Δ5-L190M+Iso+Nb6B9
M153
M190
M223
M178
M296
13C (ppm)
1H (ppm)
B
SapA-DMPC nanoparticles
β1AR-Δ5-L190M
β1AR-Δ5-L190M+Iso
β1AR-Δ5-L190M+Iso+Nb6B9
M153
M190
Nb6B9 peak
M223
M178
M296
13C (ppm)
1H (ppm)

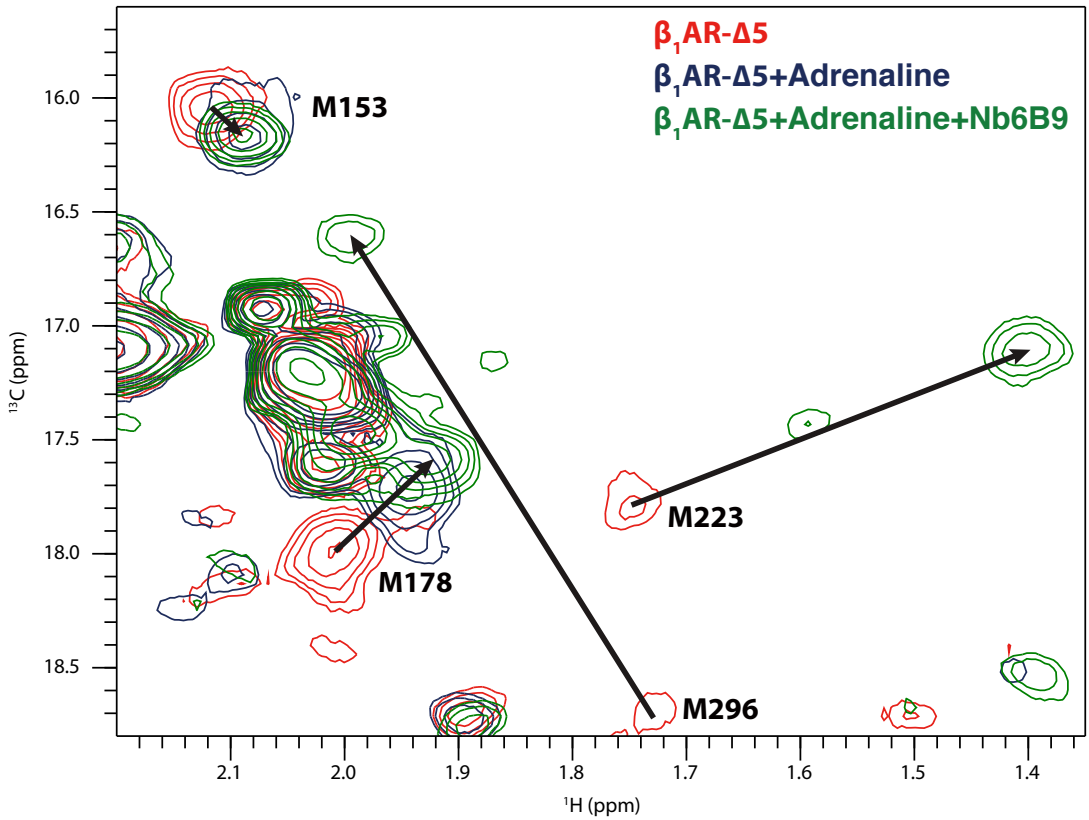

Figure 5-16: Adrenaline activation of β_1AR-Δ5 in SapA-DMPC nanoparticles.

2D ^{13}C-SOFAST-HMQC spectra of [$^{13}C_\varepsilon$-methionine] β_1AR-Δ5 in SapA-DMPC nanoparticles. Spectra of the apo state (red), the adrenaline-bound state (blue), and the adrenaline-Nb6b9 bound ternary complex (green) are overlaid. Peak assignments and the peak shifts are indicated. The spectra were recorded at 308 K on a Bruker Avance AVIII HD 950 spectrometer (^{1}H frequency of 950 MHz) equipped with a 5 mm TXI HCN/z cryoprobe. Spectra were recorded with 368 scans using 60% non-uniform sampling (NUS) scheme, resulting in an experiment time of ~6 h.

In another set of experiments, we looked at the activation of β_1AR-Δ5 in SapA-DMPC nanoparticles using the endogenous activating ligand, adrenaline (Figure 5-16). The signals from M223 and M296 still showed the same behaviour and the corresponding peaks in the adrenaline bound form were not observable. In the adrenaline-bound state, the signal from M153 perfectly overlaid the equivalent peak in the spectrum of the adrenaline-bound ternary complex. This result suggests that, in the absence of IBP, adrenaline can activate the receptor to a higher level than isoprenaline. In the adrenaline-bound state, the peak for M178 also shifted to a position closer to that found

in the ternary complex state. From these observations about the signals from M153 and M178 it can be concluded that, adrenaline induces a more active-like conformation than isoprenaline. Despite subtle conformational differences in the ligand bound state between adrenaline and isoprenaline, the overall activation mechanism appears to be the same, so these ligands cause very similar spectral changes.

5.3 Conclusions

This Chapter began by establishing a cell-free expression system in which all the components were optimised. Then it explored the possibility of expressing β_1AR using the cell-free expression system. The expression yield was high but most of the expressed protein precipitated, and only a small fraction of the precipitated β_1AR could be successfully refolded and shown to be functional. Including detergent molecules in the cell-free setup also produced a small amount of functional β_1AR, but unfortunately not enough for NMR studies. Therefore, we used β_1AR produced by the more conventional baculovirus-insect cell expression system for incorporation into SapA-DMPC nanoparticles. The incorporation proved to be successful and the appearance of the NMR spectra indicate that the activation mechanism was similar to that observed in LMNG micelles. However, M153 (IL2) on the intracellular side of β_1AR appeared to adopt a more active-like conformation when bound to the agonist isoprenaline in the nanoparticle system. Taken together, these results suggest that the lipid bilayer plays an important role in receptor activation and that interactions with specific lipids may participate in this process.

6 CONCLUSIONS

In this thesis, I established SapA lipid nanoparticles as an alternative membrane mimetic system for NMR studies of membrane proteins. Firstly, the molecular mechanism of SapA opening was explored. Both pH and detergents are important factors that facilitate the formation of SapA lipid nanoparticles. The size-flexibility of SapA and its ability to interact with a wide range of lipids were shown, and these properties make SapA lipid nanoparticles a promising membrane mimetic system. Next, we demonstrated that the chemical environment of OmpX, a β-barrel model protein, in SapA lipid nanoparticles is consistent with the MSP nanodiscs, indicating the same lipid bilayer environments. The SapA system allowed us to investigate the effect of lipid composition on the conformation of OmpX because of their high incorporation yield and high NMR spectral quality. A negatively charged lipid showed strong effects on the charged residues in the loop regions as well as aromatic residues which are usually found at the membrane-water interface. This experiment revealed that membrane proteins can be studied in various lipid compositions using the SapA system, advancing the research into how the structure and function of membrane proteins are regulated by lipids. To confirm the versatility of SapA lipid nanoparticles, a microbial rhodopsin pSRII that has seven transmembrane helical structure was incorporated, yielding a dimeric pSRII in $SapA_4$-DMPC nanoparticles. The NMR spectrum showed a marked pattern compared to the same protein in C7-DHPC detergent micelles, exhibiting a different conformation and oligomeric state in lipid bilayer. This result justified that SapA lipid nanoparticles are versatile and can accommodate a wide variety of membrane proteins with different sizes and structures for solution NMR studies, and yet the incorporation process is very straightforward. Finally, the agonist-bound β_1AR

in SapA-DMPC nanoparticles was shown to adopt a more active-like conformation compared to that in detergent, suggesting that lipids directly or indirectly participate in the activation process of GPCRs. NMR studies of biologically important membrane proteins in SapA lipid nanoparticles provide valuable structure and dynamics information that are necessary for understanding their functions. Overall, SapA phospholipid nanoparticles provide a promising membrane bilayer mimetic in which functionally important NMR studies can be conducted in the future.

7 METHODS

7.1 Protein expression and purification

7.1.1 Small-scale expression test

For test expression, a 1 mL LB culture supplemented with the corresponding antibiotics was inoculated with a single colony from the plate which was prepared from transformed *E. coli* cells. The cells were grown at the desired temperature for 4 h followed by addition of 1 mM IPTG. After 2 h of incubation, the cells were collected by centrifugation (20,000 g, 10 min) and the supernatant was discarded. 50 µL of BugBuster® (Merck) was mixed with the cells by pipetting up and down until the solution became clear. The resulting sample was checked by SDS-PAGE.

7.1.2 SapA

Saposin-A (SapA) was expressed and purified using the protocol reported previously.[128] The SapA plasmid was a kind gift from Dr. Janet Deane. The sequence of the construct is as following:

MGSLPCDICKDVVTAAGDMLKDNATEEEILVYLEKTCDWLPKPNMSASCKEIV
DSYLPVILDIIKGEMSRPGEVCSALNLCESLQ

SapA was expressed using *E. coli* SHuffle® T7 cells. Cells were grown at 30 ˚C in LB supplemented with 100 µg/mL ampicillin for approximately 5 h to reach OD_{600} of 0.8. Cells were then induced with 1 mM IPTG, and incubated overnight at 16 ˚C. The cells were harvested by centrifugation (5,000 g, 30 min). Cell pellets were resuspended in anion-exchange buffer (50 mM Tris-HCl, pH 7.4, 25 mM NaCl) with protease inhibitor cocktail (Sigma-Aldrich) and lysed by applying three runs on EmulsiFlex-C5 (Avestin).

Soluble proteins were separated by centrifugation (40,000 g, 30 min, 4 ˚C). The supernatant was incubated at 85 ˚C with gentle mixing for 15 min to denature other proteins. The solution should become cloudy after the heating step. Precipitated proteins were pelleted by centrifugation (40,000 g, 30 min, 4 ˚C) and discarded. The anion-exchange purification was performed using a 5 mL HiTrap QSepharose column (GE Healthcare) equilibrated with anion-exchange buffer. Elution used a 0–50% linear gradient of elution buffer (50 mM Tris-HCl, pH 7.4, 1 M NaCl). Fractions were checked by SDS-PAGE and those containing SapA were pooled and concentrated using Amicon Ultra-15 (3,000 MWCO). The sample was further purified by size-exclusion chromatography using a HiPrep 16/60 Sephacryl S-200 (GE Healthcare). The purity of the sample was checked by SDS-PAGE before concentrating to a final concentration of approximately 3 mM. The sample was aliquoted, flash frozen and stored in the -80 ˚C freezer.

7.1.3 OmpX

[U-^{15}N]-OmpX sample was kindly provided by my colleague, Yi Lei Tan. The sequence used in this study is as following:

MATSTVTGGYAQSDAQGQMNKMGGFNLKYRYEEDNSPLGVIGSFTYTEKSRT
ASSGDYNKNQYYGITAGPAYRINDWASIYGVVGVGYGKFQTTEYPTYKHDTS
DYGFSYGAGLQFNPMENVALDFSYEQSRIRSVDVGTWIAGVGYRF

The protocol she used was adapted from a previous study.[77] Briefly, transformed *E. coli* BL21 (DE3) cells were grown at 37 °C in M9 medium supplemented with 1g/L [U-99%^{15}N]-NH_4Cl. Protein expression was induced at an OD_{600} of 0.3 by the addition of 1 mM IPTG followed by 5 h incubation at 37 °C. Cells were collected by centrifugation (4,300 g, 20 min) and lysed using Emulsiflex. Inclusion body was prepared by centrifugation (4,300 g, 1 h) and resuspension with buffer (20 mM Tris-HCl, pH 8.0, 5 mM EDTA) three times. The protein was finally solubilised in 6 M GuHCl, 50 mM Tris/HCl pH 8.5, 100 mM NaCl, 5 mM EDTA for 2 h at 37 ºC. Sample in the supernatant was collected after the centrifugation (14,300 g, 20 min). Sample was purified using a Superdex S200 16/60 HR (GE Healthcare) equilibrated with buffer (20 mM Tris-HCl, pH 8.5, 5 mM EDTA, 8 M Urea). OmpX refolding was performed at room temperature by dropwise dilution of 5 mL 300 μM OmpX into 50 mL of refolding buffer (0.5% dodecylphosphocholine (DPC), 50 mM Tris-HCl, pH 8.5, 5 mM EDTA, 500 mM L-arginine followed by stirring at room temperature overnight. Refolded

protein was dialysed against 5 L of 20 mM Tris-HCl, pH 8.5, 100 mM NaCl, 5 mM EDTA. DPC with a final concentration of 0.1% was added before the second dialysis against 5 L of 20 mM sodium phosphate, pH 6.8, 100 mM NaCl, 5 mM EDTA. The protein sample was concentrated to 1mL using a Vivaspin concentrator (10,000 MWCO) and stored at 4 ºC.

7.1.4 β_1AR

β_1AR expression was performed by my colleague, Andras Solt. The sequence of the thermostabilised turkey β_1AR construct used in this study is as following:

MGAELLSQQWEAGMSLLMALVVLLIVAGNVLVIAAIGSTQRLQTLTNLFITSLA
CADLVMGLLVVPFGATLVVRGTWLWGSFLCELWTSLDVLCVTASIWTLCVIAI
DRYLAITSPFRYQSLMTRARAKVIICTVWAISALVSFLPIMMHWWRDEDPQALK
CYQDPGCCDFVTNRAYAIASSIISFYIPLLIMIFVYLRVYREAKEQIRKIDRASKR
KTSRVMAMREHKALKTLGIIMGVFTLCWLPFFLVNIVNVFNRDLVPKWLFVAF
NWLGYANSAMNPIIY CRSPDFRKAFKRLLAFPRKADRRLHHHHHHHH

For ^{13}C-methyl methionine labelled β_1AR expression, Sf9 cells, grown in serum free SF4 media were centrifuged (500 g, 10 min) and washed with sterile PBS, to reduce the carry-over of unlabelled methionine. The washed cells were diluted to a density of $3x10^6$ cells/mL into methionine deficient SF4 media at half the intended final culture volume. The culture was then infected with 4 mL/L of high density viral stock, and incubated for 5 h, before supplementing the culture with 250 mg/L of ^{13}C-methyl methionine and diluting to a final density of $1.5x10^6$ cells/mL. The initial reduction in culture volume ensures optimal aeration in the initial phase of the viral infection. Cells were grown at 27 ºC for 48 h and were harvested by centrifugation (3,500 g, 15 min).

The frozen insect cell pellet was thawed with solubilisation buffer (20 mM Tris-HCl pH 8.0, 350 mM NaCl, 3 mM imidazole, Complete Protease Inhibitor Cocktail (Roche), 1% DDM or 2% LMNG) and stirred for 1 h. The solubilised cells were briefly sonicated for 1.5 min and then clarified by centrifugation (175,000 g, 45 min). The supernatant was loaded onto a nickel affinity column equilibrated with the buffer (20 mM Tris-HCl pH 8.0, 350 mM NaCl, 3 mM imidazole, 0.06% DDM or 0.02% LMNG). The protein was eluted with the same buffer supplemented with 250 mM imidazole. The sample purity of the elution was checked by SDS-PAGE. The fractions contained β_1AR were pooled and concentrated. A buffer exchange step was included to remove imidazole

using either dilute-concentrate or desalting chromatography. The final sample was in 10 mM Tris-HCl pH 8.0, 150 mM NaCl, 0.06% DDM or 0.02% LMNG.

7.1.5 T7 RNA polymerase

pAR1219 plasmid containing the T7 RNA polymerase (T7RNAP) sequence was used to transform competent BL21 (Rosetta) cells. Cells were incubated at 37 ℃ with 200 rpm shaking, and induced by addition of 1 mM isopropyl β-D-1-thiogalactopyranoside (IPTG) at OD_{600} of 0.8. Cells were incubated for 5 hours before harvesting by centrifugation (4,500 g, 15 min, 4 ℃). Cell lysis was done by passing through an Emulsiex-C5 High Pressure Homogeniser (Avestin) four times. Cell debris were removed by centrifugation (20,000 g, 30 min, 4 ℃). There is no tag in T7RNAP plasmid, therefore ammonium sulfate precipitation was used to purify T7RNAP. Protein purification started by addition of 200 mM ammonium sulfate and 1% polyethylenimine (PEI) in the final concentration to precipitate unwanted protein and DNA. After removing the pellet by centrifugation (39,000 g, 15 min, 4 ℃), 140 mL of saturated ammonium sulfate was added to precipitate T7RNAP. The pellet was collected by centrifugation (12,000 g, 10 min, 4 ℃) and dissolved in 20 mM sodium phosphate (pH 7.7), 1 mM EDTA, 1 mM DTT, 5% glycerol and 100 mM NaCl. Anion exchange purification was carried out using a Hitrap Q HP (1 mL) with a gradient from 50 mM NaCl to 500 mM NaCl in 30 column volumes (CV). Sample quality was confirmed by SDS-PAGE. T7RNAP was concentrated to approximately 4 mg/mL, dialyzed into 50% glycerol, dispensed into aliquots, flash-frozen, and stored at -80 ℃.

7.1.6 pSRII

The sequence of the pSRII in this study is as following:

MVGLTTLFWLGAIGMLVGTLAFAWAGRDAGSGERRYYVTLVGISGIAAVAYA
VMALGVGWVPVAERTVFVPRYIDWILTTPLIVYFLGLLAGLDSREFGIVITLNTV
VMLAGFAGAMVPGIERYALFGMGAVAFIGLVYYLVGPMTESASQRSSGIKSLY
VRLRNLTVVLWAIYPFIWLLGPPGVALLTPTVDVALIVYLDLVTKVGFGFIALD
AAATLRAEHGESLAGVDTDTPAVADLEHHHHHH

The *E. coli* expression strain BL21 Tuner (DE3) Cells were transformed using the pET-28b(+) vector containing the pSRII gene and grown in LB medium at 37 °C. The expression was induced at an OD_{600} of 1.0 by the addition of 1 mM IPTG. All-*trans* retinal was also added at this point to a final concentration of 10 μM. The culture was

incubated at 25 ºC for 10 h with the addition of 10 μM all-*trans* retinal every 2 h. Cells were collected by centrifugation (4,000 g, 20 min, 4 ºC). The cell pellet was resuspended in buffer (50 mM Tris-HCl, pH 8, 5 mM $MgCl_2$) with protease inhibitor cocktail (Sigma-Aldrich) and lysed using an Emulsiex-C5 High Pressure Homogeniser (Avestin). Crude membranes were collected by ultracentrifugation (100,000g, 90 min, 4 °C) and resuspended in solubilisation buffer (50 mM MES, pH 6.5, 300 mM NaCl, 5 mM Imidazole, 1.5% DDM). The mixture was incubated overnight in the cold room. Insoluble material was removed by ultracentrifugation (100,000g, 1 h, 4 °C). Solubilized pSRII was mixed with Ni-NTA affinity beads (Novagen) for 2 h in the cold room. The beads were washed with 25 column volumes of the same buffer containing 0.06% DDM and then two additional washing steps with the same buffer containing 25 mM and 50 mM Imidazole. The protein was eluted in 50 mM Tris-HCl, pH 7.0, 300 mM NaCl, 0.1% DDM, 150 mM imidazole. The imidazole was removed by multiple dilute-concentrate steps using an Amicon Ultra-15 (50,000 MWCO). The final sample was checked by SDS-PAGE.

7.1.7 ASR

The sequence of the ASR used in this study is as following:

MNLESLLHWIYVAGMTIGALHFWSLSRNPRGVPQYEYLVAMFIPIWSGLAYMA
MAIDQGKVEAAGQIAHYARYIDWMVTTPLLLLSLSWTAMQFIKKDWTLIGFL
MSTQIVVITSGLIADLSERDWVRYLWYICGVCAFLIILWGIWNPLRAKTRTQSSE
LANLYDKLVTYFTVLWIGYPIVWIIGPSGFGWINQTIDTFLFCLLPFFSKVGFSFL
DLHGLRNLNDSRQHHHHHH

Optimisation of the protocol for expressing and purifying ASR is explored in section 4.2.1 and 4.2.2, respectively. The final optimised protocol is described here. BL21-RIL competent cells were transformed with pKJ606 plasmid containing the ASR sequence. Cells were grown in LB culture supplemented with chloramphenicol and ampicillin at 37 ºC until OD_{600} of 0.4. Cells were induced by addition of 1 mM IPTG and 10 μM all-*trans* retinal (Merck) and incubated for 22 h at 30 ºC. Cells were collected by centrifugation (4,500 g, 20 min, 4ºC). The cell pellet from one litre culture is resuspended with 25 mL lysis buffer (20 mM NaPi, pH 6.5, 500 mM NaCl, 0.002% LMNG) with protease inhibitor cocktail (Sigma-Aldrich). Cells were lysed by three passes through an Emulsiex-C5 High Pressure Homogeniser (Avestin). The lysate was centrifuged (100,000 g, 90 min, 4 ºC) and the supernatant was discarded. The pellet was

resuspended and homogenised in buffer (50 mM MES, pH 6.5, 300 mM NaCl, 2% LMNG) and mixed using a rotating wheel overnight at room temperature. The solubilised sample was collected by centrifugation (100,000 g, 60 min, 4 ºC) and loaded onto a 5 mL Ni-NTA column which was equilibrated with buffer (20 mM NaPi, pH 6.5, 500 mM NaCl, 0.002% LMNG). The column was washed with the same buffer with 50 mM and 100 mM imidazole before elution with 500 mM imidazole.

For elution into HEGA-10 or C7-DHPC, the column was washed with 10 CV of buffer (20 mM NaPi, pH 6.5, 500 mM NaCl) containing no detergents. Then the column was washed with 5 CV of the buffer with desired detergent (20 mM NaPi, pH 6.5, 500 mM NaCl, 0.5% HEGA-10/ 0.1% C7-DHPC) followed by a washing step with the same buffer with 50 mM and 100 mM imidazole and the elution step with 500 mM imidazole. Imidazole was removed by multiple dilute-concentrate using an Amicon Ultra-15 (50,000 MWCO). The ASR concentration was calculated from the UV-Vis absorbance at 549 nm (A_{549}) using the extinction coefficient at 549 nm (ε_{549}) of 48,000 $M^{-1}cm^{-1}$. The purity of the ASR sample was estimated by measuring the ratio of A_{549} and A_{280} assuming 100% being $\varepsilon_{549}/\varepsilon_{280}$, where A_{280} is the absorbance at 280 nm and ε_{280} is the extinction coefficients at 280 nm of 88,000 $M^{-1}cm^{-1}$. The samples were also checked by SDS-PAGE.

7.1.8 ^{15}N-labelled protein production for NMR experiments

^{15}N labelled proteins used in this study were produced in the same way as described in the section above except for using the M9 minimal medium instead of LB medium. M9 minimal medium for expressing ^{15}N labelled proteins composed of 47.7 mM Na_2HPO_4, 22 mM KH_2PO_4, 8.6 mM NaCl, 2 μM $FeCl_3$, 4 μM $ZnSO_4$, 1 μM $MnCl_2$, 0.7 μM H_3BO_3, 0.7 μM $CuSO_4$, 5 μM $MgSO_4$, 100 μM $CaCl_2$, 0.5% (w/v) Glucose, and 0.1% (w/v) $^{15}NH_4Cl$. All the components are sterilised by either autoclaving or filtering through 0.2 μm filter (Millipore)

7.2 Protein characterisation

7.2.1 SDS-PAGE

Polyacrylamide gel electrophoresis was performed using 12% handcasting Bis-Tris gels. The gels were prepared using the established protocol and casted in the empty gel cassette (Invitrogen). Gels were run in NuPAGE™ MES running buffer (Invitrogen) for

35 min at 200 mV. If the sample contains SapA, the gel was run only for 28 min to make sure the small proteins remain visible on the gel. PageRuler™ prestained protein ladder (Thermo Scientific) were used and gels were stained in Instant Blue™ coomassie stain (Expedeon).

7.2.2 Western blot

The western blots showed in this study were all detecting His tag on the protein using SuperSignal® West HisProbe™Kit (Thermo Scientific). The gel was first transferred onto PVDF membrane in buffer (25 mM Tris, pH 8.3, 192 mM Glycine, 20% Methanol) using the transfer apparatus (Invitrogen) for 1 h at 175 mA. The membrane was blocked with 25 mg/mL BSA in TBST (25 mM Tris, pH 7.6, 150 mM NaCl, 0.05% Tween-20) for 1 h at room temperature. The membrane was washed twice with 15 mL TBST for 10 min each before incubating with 10 mL HisProbe-HRP Working Solution for 1 h. The membrane was washed again four times with 15 mL TBST for 10 min each. Finally, the blot was incubated with 7.5 mL SuperSignal West Pico Substrate Working Solution for 5 min before film development.

7.2.3 Analytical size-exclusion and molecular weight calibration

The analytical size-exclusion chromatography was done using an S200 Increase 10/300 column (GE Healthcare) in the cold room. Calibration was done using the Gel filtration Molecular Weight Calibration Kit (Sigma, #MWGF200). The standard protein mixture containing 2 mg/mL Cytochrome c, 3 mg/mL Carbonic anhydrase, 10 mg/mL Albumin, 5 mg/mL Alcohol dehydrogenase, and 4 mg/mL β-amylase was dissolved in 1 mL of 50 mM Tris-HCl, pH 8, 150 mM KCl. The elution volume of each protein standard was obtained from the resulting chromatogram (Figure 7-1, A). The known molecular weights were plotted against the elution volumes and fitted with an logarithmic curve (Figure 7-1, B).

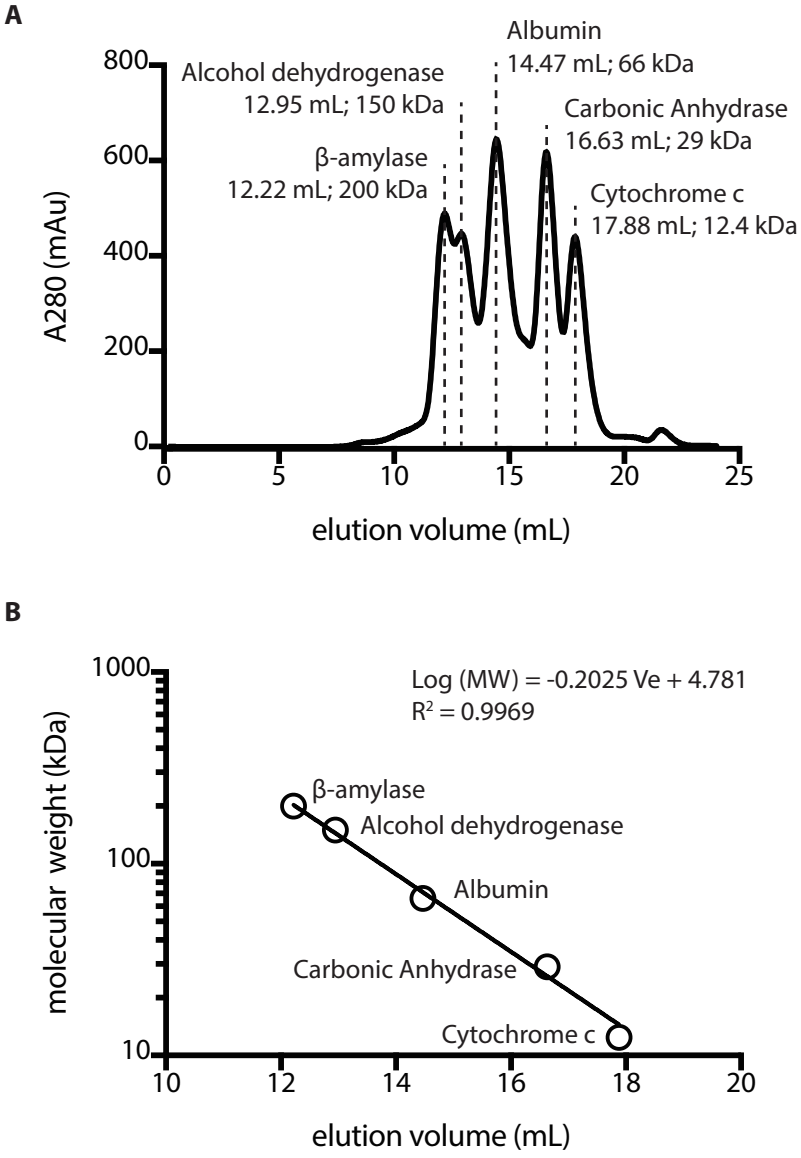

Figure 7-1: Molecular weight calibration of the SEC column.

A) SEC chromatogram of molecular weight standards. The elution volume and the molecular weight of each peak are indicated. B) Molecular weights of the protein standards are plotted against the elution volumes and fitted with logarithmic curve. The resulting formula and the fitting quality are shown.

For SEC runs, samples were always centrifuged (21,130 g, 5 min) prior to loading in order to remove precipitate. Sample with a volume of 500 µL was injected into the column that was equilibrated with the desired buffer. The flow rate was 0.6 mL/min and the fractions were collected every 1 mL. Absorbance at 280 nm was always monitored. In the case of bacterial rhodopsin, additional absorbance wavelengths were monitored, 549 nm for ASR and 498 nm for pSRII.

7.2.4 DLS measurements

DLS measurements were performed to check the particle size of ASR in 0.5% HEGA-10 or in 0.002% LMNG. Each sample contained 70 µL of ASR sample with a concentration of 0.625 mg/mL in 20 mM NaPi, pH 6.5. Since the purpose of the DLS measurements was to investigate the effect of NaCl concentration on the particle size in section 4.2.3, the NaCl concentration was adjusted according to the value screened. The measurements were carried out on Zetasizer Nano S (Malvern Panalytical). Five separate measurements with 17 scans each were performed for every sample.

7.2.5 UV-Vis spectroscopy-Nanodrop

We used UV-Vis spectroscopy to quantify the corrected folded ASR in the sample. For the purpose of screening conditions for ASR in section 4.2.3, UV-Vis spectra were recorded using a Nanodrop ND-1000 spectrometer (Thermo Scientific) to reduce total experimental time because of a large number of samples. Samples were centrifuged at 22,000 g for 30 s at 20 ºC before each measurement. Triplicate measurements were recorded. To assess the stability of ASR, the absorbance at 549 nm (A_{549}) was used as a quantification of correctly folded ASR. The percentage of ASR remaining in the sample after incubation was calculated by the ratio of A_{549} after and before the incubation.

7.2.6 UV-Vis spectroscopy

To obtain an UV-Vis spectrum with higher spectral quality and sensitivity, samples were recorded using a UV-Vis spectrophotometer UV-1800 (SHIMADZU). A sample with a volume of 100 µL was transferred to an absorption cuvette (Hellma). Three scans from 250 nm to 600 nm with a sampling interval of 1 nm were recorded and averaged to produce the final spectrum.

7.2.7 Intrinsic fluorescence spectroscopy

Intrinsic fluorescence was measured using a LS 55 fluorescence spectrophotometer (PerkinElmer). A sample with 100 µL volume was transferred to a fluorescence cuvette (Hellma). The spectrum was recorded from 300 nm to 450 nm with the excitation wavelength of 280 nm. The excitation and emission bandwidth was 5 nm and 10 nm, respectively. Scanning speed was 100 nm/min.

7.2.8 Far-UV Circular dichroism

Far-UV circular dichroism (CD) measurements were carried out using an Aviv model 410 CD spectrophotometer at 298 K to monitor the secondary structure of β1AR in SDS. Each measurement contained 300 μL of protein solution with a concentration of 0.1 mg/mL using a 1 mm quartz cell (Hellma). The far-UV CD spectra were collected between 200 and 260 nm with a bandwidth of 1 nm.

7.2.9 Negative-stained electron microscopy

For the EM grid preparation, sample with a concentration of 10 μg/mL were applied to a glow discharged carbon-coated copper grid (400 mesh) (EMresolution) for 30 s. Washing was done with three drops of water before staining with 2% (w/v) uranyl acetate for 30 s. The grids were blotted dry and stored at room temperature. Negative-stain image data were collected with a FEI Tecnai F20 field emission gun transmission electron microscope at an accelerating voltage of 200 kV fitted with either a 1K × 1K or a 4K × 4K CCD camera at the Wolfson Electron Microscopy Suite, University of Cambridge.

7.3 Detergent/lipid quantification

7.3.1 2,6-dimethylphenol assay

A 2,6-dimethylphenol assay was employed to determine the concentration of sugar-based detergents including DDM and LMNG. The protocol was adapted from previous reports.[130,131] Briefly, a 5 μL sample was first diluted with 320 μL water in an eppendorf tube. Then, 25 μL of 20% 2,6-dimethylphenol in absolute ethanol was added under the fume hood, followed by 650 μL concentrated sulfuric acid. The tube was mixed by inverting a few times. The sample became warm because of the strong exothermic reaction. Samples were incubated at room temperature for 1 h. The absorbance at 510 nm was measured.

7.3.2 Molybdate assay

To quantify the phospholipid concentration, we used a molybdate assay described previously[131] to determine the phosphate concentration in the sample. The reagents needed in this assay were prepared in advance including 10% magnesium in 95% ethanol, 10% ascorbic acid in water, ammonium molybdate solution, which was

prepared by dissolving 0.42 g ammonium molybdate tetrahydrate and 2.86 mL sulfuric acid in 100 mL water. A 5 μL sample was mixed with 30 μL of 10% magnesium nitrate followed by ashing over a Bunsen burner. The resulting powder was dissolved in 350 μL of 0.5 N HCl, and 300 μL of the sample was transferred to a 1.5 mL eppendorf tube and boiled for 15 min. After the tube had cooled down, 700 μL of the ascorbic acid/ molybdate solution, 100 μL of 10% ascorbic acid in water and 600 μL of ammonium molybdate solution, was added and incubated at 45 ºC for 25 min. This produced phosphomolybdate complex with blue colour and the absorbance at 825 nm (A_{825}) was measured. In order to quantify the concentration of DMPC in an unknown sample, a standard curve was produced first. Triplicate DMPC samples with the concentration in the range of 0–5 mM were prepared and treated with the molybdate assay described above. The A_{825} of each sample was plotted against the DMPC concentration and fitted by linear regression (Figure 7-2). The fitting result describes the relationship between A_{825} and the concentration of DMPC. Sample of interest was treated by molybdate assay and the concentration of DMPC was back calculated from A_{825} using the formula obtained from the standard curve.

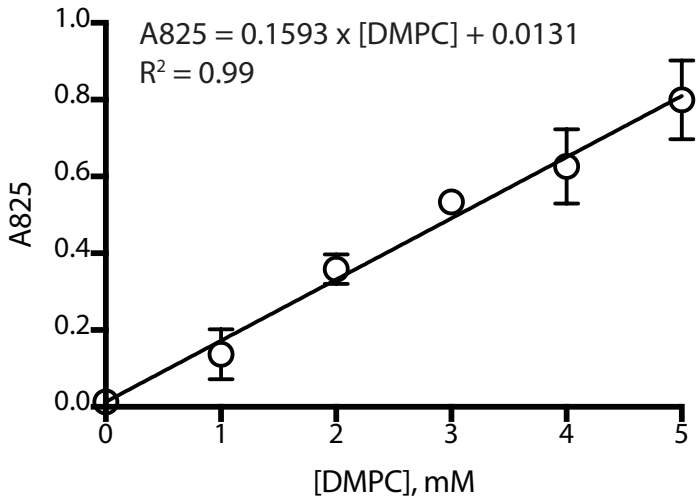

Figure 7-2: The standard curve for DMPC quantification by molybdate assay.

Triplicate DMPC samples with known concentration ranging from 0 mM to 5 mM were prepared and treated by the molybdate assay. The absorbance at 825 nm of each sample was plotted against DMPC concentration. A linear fit was performed, and the resulting formula and the fitting quality are shown. The relationship between A_{825} and the concentration of DMPC was used to determine DMPC concentration in the samples of interest.

7.4 Incorporation of membrane proteins into SapA lipid nanoparticles

7.4.1 Incorporation of OmpX into SapA lipid nanoparticles

The incorporation of OmpX into SapA lipid nanoparticles was done at pH 6 with the SapA:lipid:OmpX ratio of 10:50:1 with a final OmpX concentration of 12 μM. The assembly mixture was prepared starting from mixing OmpX solubilised in 0.5% DPC and lipid followed by the addition of DDM with a final concentration of 0.2%. SapA was then included in the mixture. A clear solution should be observed at this point. After the buffer (50 mM sodium acetate, pH 6, 150 mM NaCl) was added, the assembly mixture was incubated at room temperature for 10 min. Detergent removal was done by addition of 80% w/v washed Amberlite XAD2 beads (Sigma-Aldrich), 500 μL mixture with 400 mg beads in a 1.5 mL Eppendorf tube, and was performed at 25 ºC for 2 h with gentle shaking. Beads were removed by centrifugation (2,000 g, 10 min). The sample was centrifuged to remove precipitate (21,130 g, 5 min) before analysing by SEC using a Superdex 200 Increase 10/300 (GE Healthcare) equilibrated with the buffer used in the assembly mixture. Large-scale preparation for NMR experiments were performed using the same setup in multiple Eppendorf tubes and a concentration step using an Amicon Ultra-15 (3,000 MWCO) was added before SEC. The SEC fractions corresponding to OmpX in SapA lipid nanoparticles were pooled and concentrated again to a volume of 400 μL. The OmpX concentration in the final NMR samples were in general around 200 μM. The concentration was estimated by the absorbance at 280 nm and the contribution from SapA was taken into account.

7.4.2 Incorporation of β_1AR into SapA lipid nanoparticles

The incorporation of β_1AR into SapA lipid nanoparticles was done in a similar way to the OmpX case. β_1AR solubilised in 0.6% DDM was mixed with SapA and DMPC with the SapA:DMPC:β_1AR ratio of 10:150:1 with the final β_1AR concentration of 12 μM. Additional 0.2% DDM was included to encourage the opening of SapA. Buffer (50 mM Tris-HCl, pH 7.4, 150 mM) was added into the assembly mixture and incubated at room temperature for 10 min. DDM removal was achieved by addition of 80% w/v Amberlite XAD2 beads (Sigma-Aldrich) and incubated at 25 ºC for 2 h with gentle shaking. Beads were removed by centrifugation (2,000 g, 10 min). The sample was analysed by analytical SEC using a Superdex 200 Increase 10/300 (GE Healthcare).

The incorporation of other β_1AR mutants including Δ5, Δ5-L190M was achieved using the same ratio and the same buffer. The only difference is that these mutants are purified in LMNG because they are not stable in DDM. Therefore, the incubation time in the detergent removal step was 24 h instead of 2 h. Other parameters such as the amount of beads and the incubation temperature are the same. The assembly mixture was purified using a 5 mL Ni-NTA column to separate the empty nanoparticles followed by the SEC. The successful incorporation was confirmed by the presence of a SapA band on the SDS-PAGE after the purification. For the preparation of NMR samples, only the Ni-NTA purification was performed to reduce the sample loss in multiple purification steps. The elution fractions from Ni-NTA purification were pooled and concentrated using Amicon Ultra-15 (3,000 MWCO). Three runs of 10 times dilute-concentration were performed to remove imidazole in the sample. The concentration of β_1AR in the final NMR sample was in general about 40 μM, estimated by the UV absorbance at 280 nm.

7.5 Cell-free expression

7.5.1 *E. coli* extract preparation

E. coli extract was prepared from BL21 (DE3) Rosetta cells using a fermenter. Sterilized 20 L 2x YTPG medium (22 mM KH_2PO_4, 52 mM K_2HPO_4, 86 mM NaCl, 110 mM glucose, 10 g/L yeast extract, 16 g/L tryptone) in a fermenter was inoculated with 200 mL starting culture. Fermentation was carried out at 37 ˚C, pH 7, 8 L/min air flow, 600–800 rpm shaking. OD_{600} was monitored every 20 min. Cells were harvested at OD_{600} = 3.5 by centrifugation (4,000 g, 15 min, 4 ˚C). The pellet was re-suspended in extract buffer (10 mM Tris, 14 mM magnesium acetate, 60 mM potassium acetate, pH 8.2). Cells were lysed using an Emulsiflex (Avestin) and cell debris were removed by centrifugation (12,000 g, 30 min, 4 ˚C). Supernatant was incubated (2 h, 300 rpm, 30 ˚C). The sample was dialyzed in extract buffer with 1 mL/L β-mercaptoethanol in the cold room overnight. The final product was divided into 1 mL aliquots, flash frozen in liquid nitrogen, and stored at -80 ˚C. The whole process should be done on ice or in the cold room. All the equipment including centrifuge bottles, beakers, cylinders was cleaned by RNAseZap and DEPC water and pre-chilled before use.

7.5.2 Expression system setup

The S30-based cell-free expression system was set up based on a previous protocol.[206] In short, the components in the reaction mixture are 0.04 mg/mL PK, 0.5 mg/mL TRNA, 6 units/μL T7RNAP, 0.3 units/μL RNAguard, 0.015 μg/mL DNA, 35% S30 extract. In addition, the reaction mixture and feeding mixture both have 0.05% NaN_3, 2% PEG 8000, 150 mM KOAc, 12 mM $Mg(OAc)_2$ (concentration was optimized), 0.1 M HEPES buffer, 1 x complete protease inhibitor cocktail (Roche), 0.1 mg/mL folinic acid, 2 mM DTT, 1 x NTP mix, 20 mM PEP, 20 mM Acp, 0.5 mM Amino acid mix, 1 mM RCWMDE (amino acid mixture). For analytical scale, 2 mL eppendorf tubes were used for the feeding mixture compartment and Slide-A-Lyzer™ MINI device (Thermo Scientific) with 12–15 kDa molecular weight cutoff membrane was used for the reaction mixture compartment. For preparative scale (1 mL), dialysis tubing and 50 mL centrifuge tubes were used for the reaction mixture and feeding mixture, respectively. The reaction was carried out at 30 ˚C, with shaking at 300 rpm for 24 h.

7.5.3 GFP fluorescence measurements

The yield of GFP was quantified by fluorescence measurement using an Infinite® 200 PRO (Tecan) fluorometer with a plate reader format. The excitation wavelength was set to 395 nm, the characteristic excitation wavelength of GFP, and a full spectrum was recorded from 475 nm to 625 nm. The emission intensity at 509 nm, where GFP fluorescence is the highest, was used as a quantification of GFP.

7.5.4 Bicelle refolding

Purified β_1AR from the P-CF reaction was originally solubilised in 15 mM SDS, 50 mM sodium phosphate (pH 8). In order to reduce the SDS concentration, β_1AR was dialysed overnight using a 30-fold excess of the same buffer without SDS. Subsequently the SDS concentration was kept at around 2 mM using overnight dialysis against a 30-fold excess of the same buffer with 2 mM SDS containing the redox-shuffling system GSH/GSSG (reduced and oxidized glutathione, Carl Roth, Karlsruhe, Germany). To concentrate the β_1AR, 30% (w/v) PEG 20,000 (Sigma Aldrich, Deisenhofen, Germany) was added to the dialysis buffer, until the β_1AR concentration of 1 mg/ml was reached. For the bicelle preparation, 104 mM C7-DHPC and 26 mM DMPC (q = 0.25) (Avanti Polar Lipids, Alabaster, USA) were dispersed in 1 mL 50 mM sodium phosphate (pH 8). Three 20 min heat/cooling cycles were performed between 42 °C and 4 °C, respectively.

The β_1AR was added to the prepared bicelle and three additional heat/cooling cycles were applied. To remove residual SDS, the bicelle/β_1AR sample was dialyzed overnight using buffer without SDS.

7.5.5 On-column refolding

Purified β_1AR from the P-CF reaction was loaded onto a Histrap 5 mL column (GE Healthcare). The column was washed with 5 CV of binding buffer (50 mM sodium phosphate, 15 mM SDS, pH 8) followed by 5 CV of the same buffer without SDS to reduce the SDS concentration. Buffer exchange was carried out with 5 CV of refolding buffer (20 mM Tris, 350 mM NaCl, pH 8) followed by 5 CV of refolding buffer with 0.02% LMNG. Elution buffer (20 mM Tris, 350 mM NaCl, 250 mM imidazole, pH 8) was used to elute the protein. The sample was then concentrated and checked by SDS-PAGE.

7.6 NMR experiments

7.6.1 NMR sample preparation

Protein samples for NMR experiments were concentrated to around 400 µL and mixed with 10% D_2O required for the lock. The sample was transferred to a 5 mm NMR tube (Wilmad). In some cases, a 3 mm NMR tube was used which only needs 160 µL sample.

7.6.2 Translational diffusion measurements

Pulsed Field Gradient NMR measurements were carried out on a Bruker DRX-500MHz spectrometer (Bruker). Experimental temperature and conditions are indicated in the results sections. The translational diffusion of molecules can be measured by spatially labelling molecules using a pulsed field gradient. This allows the position of the molecules in the NMR tube to be encoded. The molecules diffuse during a set period of time before applying the second gradient. The farther the molecule moves from its original position the weaker the signal. A peak that represents the particle of interest is used for determination of the translational diffusion coefficient. For example, the amide region of protein samples or choline proton signal for DMPC containing particles.

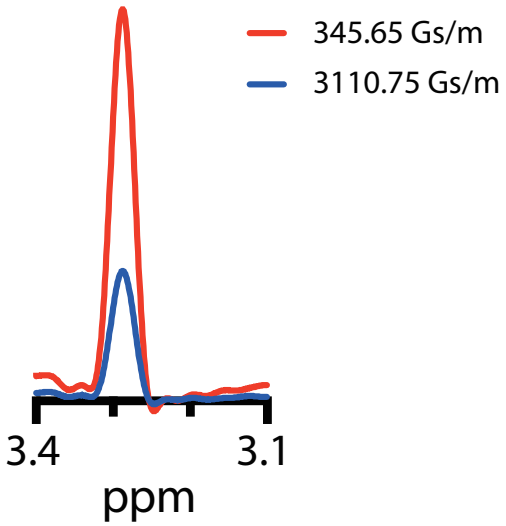

Figure 7-3: Diffusion measurement using the choline proton signal.

Diffusion measurements were performed using PFG NMR. Two experiments with different gradient strength, 345.65 Gs/m (red) and 3110.75 Gs/m (blue), were applied to the sample. A representative peak was used to measure the intensity ratio between two experiments. In this example, a choline signal originated from DMPC was used for measuring the diffusion coefficient of SapA-DMPC nanoparticles.

The signal intensity is described by

$$I = I_0 e^{-D\gamma^2 g^2 \delta^2 \left(\Delta - \frac{\delta}{3}\right)},$$

where I is the observed signal intensity, I_0 is the original signal intensity without gradient, D is the diffusion coefficient, γ is the gyromagnetic ratio (26752.21 $s^{-1}Gs^{-1}$), g is the gradient strength (346.65 Gs/m and 3110.75 Gs/m), δ is the length of the gradient (2 ms), and Δ is the diffusion time (500 ms). With the signal intensities measured from the NMR spectra and the known experimental parameters, the diffusion coefficient can be derived from this formula.

7.6.3 SOFAST-TROSY experiments

NMR experiments were all recorded on a Bruker Avance AVIII 800 spectrometer (^{1}H frequency of 800 MHz) equipped with a 5 mm TXI HCN/z cryoprobe. All the spectra were processed with Azara (W. Boucher, unpublished) or NMRPipe[220] and analysed with SPARKY software (Goddard and Kneller).

Spectra for OmpX with a concentration of 200 μM in pH 6 buffer (50 mM sodium acetate, pH 6, 150 mM NaCl), were recorded at 318 K using a [^{1}H, ^{15}N]-SOFAST-TROSY experiment. The direct (^{1}H) dimension was acquired with 10,000 Hz spectral width and 1024 points, whereas 2,778 Hz spectral width and 128 points was used for the indirect dimension (^{15}N). Spectra were recorded with 3,078 scans, resulting in an experiment time of 36 h.

Spectra for ASR in buffer (20 mM NaPi, pH 6.5, 200 mM NaCl, 0.5% HEGA-10) were recorded at 318 K. The experiment was performed using a 5 mm NMR tube with 500 μL ASR with a protein concentration of 200 μM. To improve the sensitivity, the same sample was further concentrated to 325 μM and a volume of 250 μL and the NMR experiments recorded for the same experiment time. Both experiments were carried out with 1,000 scans and 100 complex points, giving an acquisition time of 17 h.

7.6.4 SOFAST-HMQC

In the β_1AR experiments, 50 μM ^{13}C methyl-methionine labelled β_1AR in pH 7.4 buffer (50 mM Tris-HCl, pH 7.4, 150 mM NaCl) was used, and 1 mM isoprenaline and 50 μM Nb80 were added sequentially into the sample to record NMR spectra. All the spectra were recorded at 308 K using a SOFAST ^{1}H, ^{13}C HMQC experiment[221] with gradient coherence-order selection[222] and non-uniform sampling (NUS) in the ^{13}C dimension. The direct (^{1}H) dimension was acquired with 10,000 Hz spectral width and 1024 points. A 60% Poisson-Gap sampling schedule was used on the indirect dimension (^{13}C) acquisition,[223] with 4,000 Hz spectral width. Spectra were recorded with 368 scans, giving an acquisition time of 6 h. Multiple 6 h experiments were recorded and added in order to obtain spectra with higher signal-to-noise ratio. Spectra were reconstructed using the iterative hard thresholding (IHT) compressed sensing (CS) implementation[224] in the Cambridge CS package, an in-house program written by Dr. Mark Bostock. Data were analysed using CCPN Analysis v2.[225]

7.6.5 Weighted chemical shift perturbation

Weighted chemical shift perturbations of the backbone amide resonances were defined as:

$$\Delta\delta_{\mathrm{H,N}} = \sqrt{(\Delta\delta_{\mathrm{H}})^2 + 0.13 \times (\Delta\delta_{\mathrm{N}})^2}$$

where $\Delta\delta_{\mathrm{H}}$ and $\Delta\delta_{\mathrm{N}}$ are the observed chemical shift differences along the proton and nitrogen dimensions, respectively, with respect to the original spectrum.

8 REFERENCES

(1) Goodman, S. R. *Medical Cell Biology*; Elsevier, 2008.

(2) Almén, M.; Nordström, K. J. V.; Fredriksson, R.; Schiöth, H. B. Mapping the Human Membrane Proteome: A Majority of the Human Membrane Proteins Can Be Classified According to Function and Evolutionary Origin. *BMC Biol.* **2009**, *7* (1), 50.

(3) Lodish, H.; Berk, A.; Zipursky, S. L.; Matsudaira, P.; Baltimore, D.; Darnell, J. *Molecular Cell Biology. 4th Edition*; W.H.Freeman & Co Ltd, 2000.

(4) Xiong, J. *Essential Bioinformatics*; Cambridge University Press, 2006.

(5) Lomize, A. L.; Pogozheva, I. D.; Lomize, M. A.; Mosberg, H. I. Positioning of Proteins in Membranes: A Computational Approach. *Protein Sci.* **2006**, *15* (6), 1318–1333.

(6) Engelman, D. M.; Henderson, R.; McLachlan, A. D.; Wallace, B. A. Path of the Polypeptide in Bacteriorhodopsin. *Proc. Natl. Acad. Sci.* **1980**, *77* (4), 2023–2027.

(7) Eilers, M.; Shekar, S. C.; Shieh, T.; Smith, S. O.; Fleming, P. J. Internal Packing of Helical Membrane Proteins. *Proc. Natl. Acad. Sci. U. S. A.* **2000**, *97* (11), 5796–5801.

(8) Kyte, J.; Doolittle, R. F. A Simple Method for Displaying the Hydropathic Character of a Protein. *J. Mol. Biol.* **1982**, *157* (1), 105–132.

(9) Cuthbertson, J. M.; Doyle, D. A.; Sansom, M. S. P. Transmembrane Helix Prediction: A Comparative Evaluation and Analysis. *Protein Eng. Des. Sel.* **2005**, *18* (6), 295–308.

(10) Fairman, J. W.; Noinaj, N.; Buchanan, S. K. The Structural Biology of β-Barrel Membrane Proteins: A Summary of Recent Reports. *Curr. Opin. Struct. Biol.* **2011**, *21* (4), 523–531.

(11) Slusky, J. S. Outer Membrane Protein Design. *Curr. Opin. Struct. Biol.* **2017**, *45*, 45–52.

(12) Endo, T.; Yamano, K. Transport of Proteins across or into the Mitochondrial Outer Membrane. *Biochim. Biophys. Acta - Mol. Cell Res.* **2010**, *1803* (6), 706–714.

(13) Noinaj, N.; Guillier, M.; Barnard, T. J.; Buchanan, S. K. TonB-Dependent Transporters: Regulation, Structure, and Function. *Annu. Rev. Microbiol.* **2010**, *64* (1), 43–60.

(14) Konovalova, A.; Kahne, D. E.; Silhavy, T. J. Outer Membrane Biogenesis. *Annu. Rev. Microbiol.* **2017**, *71* (1), 539–556.

(15) Berman, H. M.; Westbrook, J.; Feng, Z.; Gilliland, G.; Bhat, T. N.; Weissig, H.; Shindyalov, I. N.; Bourne, P. E. The Protein Data Bank. *Nucleic Acids Res.* **2000**, *28* (1), 235–242.

(16) Krogh, A.; Larsson, B.; von Heijne, G.; Sonnhammer, E. L. Predicting Transmembrane Protein Topology with a Hidden Markov Model: Application to Complete Genomes. *J. Mol. Biol.* **2001**, *305* (3), 567–580.

(17) Parker, J. L.; Newstead, S. Membrane Protein Crystallisation: Current Trends and Future Perspectives. In *Advances in Experimental Medicine and Biology*; 2016; Vol. 922, pp 61–72.

(18) Rasmussen, S. G. F.; Choi, H.-J.; Rosenbaum, D. M.; Kobilka, T. S.; Thian, F. S.; Edwards, P. C.; Burghammer, M.; Ratnala, V. R. P.; Sanishvili, R.; Fischetti, R. F.; et al. Crystal Structure of the Human B2 Adrenergic G-Protein-Coupled Receptor. *Nature* **2007**, *450* (7168), 383–387.

(19) Zou, Y.; Weis, W. I.; Kobilka, B. K. N-Terminal T4 Lysozyme Fusion Facilitates Crystallization of a G Protein Coupled Receptor. *PLoS One* **2012**, *7* (10).

(20) Warne, T.; Serrano-Vega, M. J.; Tate, C. G.; Schertler, G. F. X. Development and Crystallization of a Minimal Thermostabilised G Protein-Coupled Receptor. *Protein Expr. Purif.* **2009**, *65* (2), 204–213.

(21) Ishchenko, A.; Abola, E. E.; Cherezov, V. Crystallization of Membrane Proteins: An Overview. In *Methods in Molecular Biology*; 2017; Vol. 1607, pp 117–141.

(22) Deisenhofer, J.; Epp, O.; Miki, K.; Huber, R.; Michel, H. Structure of the Protein Subunits in the Photosynthetic Reaction Centre of *Rhodopseudomonas Viridis* at 3 Å Resolution. *Nature* **1985**, *318* (6047), 618–624.

(23) Landau, E. M.; Rosenbusch, J. P. Lipidic Cubic Phases: A Novel Concept for the Crystallization of Membrane Proteins. *Proc. Natl. Acad. Sci.* **1996**, *93* (25), 14532–14535.

(24) Wadsten, P.; Wöhri, A. B.; Snijder, A.; Katona, G.; Gardiner, A. T.; Cogdell, R. J.; Neutze, R.; Engström, S. Lipidic Sponge Phase Crystallization of Membrane Proteins. *J. Mol. Biol.* **2006**, *364* (1), 44–53.

(25) Rouhani, S.; Cartailler, J. P.; Facciotti, M. T.; Walian, P.; Needleman, R.; Lanyi, J. K.; Glaeser, R. M.; Luecke, H. Crystal Structure of the D85S Mutant of Bacteriorhodopsin: Model of an O-like Photocycle Intermediate. *J. Mol. Biol.* **2001**, *313* (3), 615–628.

(26) Liang, B.; Tamm, L. K. NMR as a Tool to Investigate the Structure, Dynamics and Function of Membrane Proteins. *Nat. Struct. Mol. Biol.* **2016**, *23* (6), 468–474.

(27) Pervushin, K.; Riek, R.; Wider, G.; Wüthrich, K. Attenuated T2 Relaxation by Mutual Cancellation of Dipole-Dipole Coupling and Chemical Shift Anisotropy Indicates an Avenue to NMR Structures of Very Large Biological Macromolecules in Solution. *Proc. Natl. Acad. Sci. U. S. A.* **1997**, *94* (23), 12366–12371.

(28) Takeuchi, K.; Arthanari, H.; Wagner, G. Perspective: Revisiting the Field Dependence of TROSY Sensitivity. *J. Biomol. NMR* **2016**, *66* (4), 221–225.

(29) Arora, A.; Abildgaard, F.; Bushweller, J. H.; Tamm, L. K. Structure of Outer Membrane Protein A Transmembrane Domain by NMR Spectroscopy. *Nat. Struct. Biol.* **2001**, *8* (4), 334–338.

(30) Gautier, A.; Mott, H. R.; Bostock, M. J.; Kirkpatrick, J. P.; Nietlispach, D. Structure Determination of the Seven-Helix Transmembrane Receptor Sensory Rhodopsin II by Solution NMR Spectroscopy. *Nat. Struct. Mol. Biol.* **2010**, *17* (6), 768–774.

(31) Liang, B.; Bushweller, J. H.; Tamm, L. K. Site-Directed Parallel Spin-Labeling and Paramagnetic Relaxation Enhancement in Structure Determination of Membrane Proteins by Solution NMR Spectroscopy. *J. Am. Chem. Soc.* **2006**, *128* (13), 4389–4397.

(32) Cierpicki, T.; Liang, B.; Tamm, L. K.; Bushweller, J. H. Increasing the Accuracy of Solution NMR Structures of Membrane Proteins by Application of Residual Dipolar Couplings. High-Resolution Structure of Outer Membrane Protein A. *J. Am. Chem. Soc.* **2006**, *128* (21), 6947–6951.

(33) Crick, D. J.; Wang, J. X.; Graham, B.; Swarbrick, J. D.; Mott, H. R.; Nietlispach, D. Integral Membrane Protein Structure Determination Using Pseudocontact Shifts. *J. Biomol. NMR* **2015**, *61* (3–4), 197–207.

(34) Castellani, F.; Van Rossum, B.; Diehl, A.; Schubert, M.; Rehbein, K.; Oschklnat, H. Structure of a Protein Determined by Solid-State Magic-Angle-Spinning NMR Spectroscopy. *Nature* **2002**, *420* (6911), 98–102.

(35) Wang, S.; Munro, R. A.; Shi, L.; Kawamura, I.; Okitsu, T.; Wada, A.; Kim, S.-Y.; Jung, K.-H.; Brown, L. S.; Ladizhansky, V. Solid-State NMR Spectroscopy Structure Determination of a Lipid-Embedded Heptahelical Membrane Protein. *Nat. Methods* **2013**, *10* (10), 1007–1012.

(36) Shahid, S. A.; Bardiaux, B.; Franks, W. T.; Krabben, L.; Habeck, M.; Van Rossum, B. J.; Linke, D. Membrane-Protein Structure Determination by Solid-State NMR Spectroscopy of Microcrystals. *Nat. Methods* **2012**, *9* (12), 1212–1217.

(37) Retel, J. S.; Nieuwkoop, A. J.; Hiller, M.; Higman, V. A.; Barbet-Massin, E.; Stanek, J.; Andreas, L. B.; Franks, W. T.; Van Rossum, B. J.; Vinothkumar, K. R.; et al. Structure of Outer Membrane Protein G in Lipid Bilayers. *Nat. Commun.* **2017**, *8* (1).

(38) Dubochet, J.; Adrian, M.; Lepault, J.; McDowall, A. W. Cryo-Electron Microscopy Of Vitrified Biological Specimens. *Trends Biochem. Sci.* **1985**, *10* (4), 143–146.

(39) Frank, J.; Goldfarb, W.; Eisenberg, D.; Baker, T. S. Reconstruction of Glutamine Synthetase Using Computer Averaging. *Ultramicroscopy* **1978**, *3* (C), 283–290.

(40) Faruqi, A. R.; Henderson, R. Electronic Detectors for Electron Microscopy. *Curr. Opin. Struct. Biol.* **2007**, *17* (5), 549–555.

(41) Liao, M.; Cao, E.; Julius, D.; Cheng, Y. Structure of the TRPV1 Ion Channel Determined by Electron Cryo-Microscopy. *Nature* **2013**, *504* (7478), 107–112.

(42) Bai, X.; Yan, C.; Yang, G.; Lu, P.; Ma, D.; Sun, L.; Zhou, R.; Scheres, S. H. W.; Shi, Y. An Atomic Structure of Human γ-Secretase. *Nature* **2015**, *525* (7568), 212–217.

(43) Hite, R. K.; Yuan, P.; Li, Z.; Hsuing, Y.; Walz, T.; MacKinnon, R. Cryo-Electron Microscopy Structure of the Slo2.2 Na+-Activated K+channel. *Nature* **2015**, *527* (7577), 198–203.

(44) Liang, Y.-L.; Khoshouei, M.; Radjainia, M.; Zhang, Y.; Glukhova, A.; Tarrasch, J.; Thal, D. M.; Furness, S. G. B.; Christopoulos, G.; Coudrat, T.; et al. Phase-Plate Cryo-EM Structure of a Class B GPCR–G-Protein Complex. *Nature* **2017**, *546* (7656), 118–123.

(45) Kang, Y.; Kuybeda, O.; de Waal, P. W.; Mukherjee, S.; Van Eps, N.; Dutka, P.; Zhou, X. E.; Bartesaghi, A.; Erramilli, S.; Morizumi, T.; et al. Cryo-EM Structure of Human Rhodopsin Bound to an Inhibitory G Protein. *Nature* **2018**, *558* (7711), 553–558.

(46) Draper-Joyce, C. J.; Khoshouei, M.; Thal, D. M.; Liang, Y.-L.; Nguyen, A. T. N.; Furness, S. G. B.; Venugopal, H.; Baltos, J.-A.; Plitzko, J. M.; Danev, R.; et al. Structure of the Adenosine-Bound Human Adenosine A1 Receptor–Gi Complex. *Nature* **2018**, *558* (7711), 559–563.

(47) García-Nafría, J.; Nehmé, R.; Edwards, P. C.; Tate, C. G. Cryo-EM Structure of the Serotonin 5-HT1B Receptor Coupled to Heterotrimeric Go. *Nature* **2018**, *558* (7711), 620–623.

(48) Hilger, D.; Masureel, M.; Kobilka, B. K. Structure and Dynamics of GPCR Signaling Complexes. *Nat. Struct. Mol. Biol.* **2018**, *25* (1), 4–12.

(49) Bjarnadóttir, T. K.; Gloriam, D. E.; Hellstrand, S. H.; Kristiansson, H.; Fredriksson, R.; Schiöth, H. B. Comprehensive Repertoire and Phylogenetic Analysis of the G Protein-Coupled Receptors in Human and Mouse. *Genomics* **2006**, *88* (3), 263–273.

(50) Kolakowski, L. F. GCRDb: A G-Protein-Coupled Receptor Database. *Receptors Channels* **1994**, *2* (1), 1–7.

(51) Hollenstein, K.; de Graaf, C.; Bortolato, A.; Wang, M.-W.; Marshall, F. H.; Stevens, R. C. Insights into the Structure of Class B GPCRs. *Trends Pharmacol. Sci.* **2014**, *35* (1), 12–22.

(52) Schulte, G.; Bryja, V. The Frizzled Family of Unconventional G-Protein-Coupled Receptors. *Trends Pharmacol. Sci.* **2007**, *28* (10), 518–525.

(53) Brauner-Osborne, H.; Wellendorph, P.; Jensen, A. Structure, Pharmacology and Therapeutic Prospects of Family C G-Protein Coupled Receptors. *Curr. Drug Targets* **2007**, *8* (1), 169–184.

(54) Hauser, A. S.; Chavali, S.; Masuho, I.; Jahn, L. J.; Martemyanov, K. A.; Gloriam, D. E.; Babu, M. M. Pharmacogenomics of GPCR Drug Targets. *Cell* **2018**.

(55) Black, J. W. Drugs from Emasculated Hormones: The Principles of Synoptic Antagonisms. *Biosci. Rep.* **1988**, *9* (3), 886–894.

(56) Downes, G. B.; Gautam, N. The G Protein Subunit Gene Families. *Genomics* **1999**, *62* (3), 544–552.

(57) Cherezov, V.; Rosenbaum, D. M.; Hanson, M. A.; Rasmussen, S. G. F.; Thian, F. S.; Kobilka, T. S.; Choi, H.-J.; Kuhn, P.; Weis, W. I.; Kobilka, B. K.; et al. High-Resolution Crystal Structure of an Engineered Human Beta2-Adrenergic G Protein-Coupled Receptor. *Science* **2007**, *318* (5854), 1258–1265.

(58) Wacker, D.; Fenalti, G.; Brown, M. A.; Katritch, V.; Abagyan, R.; Cherezov, V.; Stevens, R. C. Conserved Binding Mode of Human Beta2 Adrenergic Receptor Inverse Agonists and Antagonist Revealed by X-Ray Crystallography. *J. Am. Chem. Soc.* **2010**, *132* (33), 11443–11445.

(59) Rosenbaum, D. M.; Zhang, C.; Lyons, J. A.; Holl, R.; Aragao, D.; Arlow, D. H.; Rasmussen, S. G. F.; Choi, H.-J.; DeVree, B. T.; Sunahara, R. K.; et al. Structure and Function of an Irreversible Agonist-B2 Adrenoceptor Complex. *Nature* **2011**, *469* (7329), 236–240.

(60) Altenbach, C.; Kusnetzow, A. K.; Ernst, O. P.; Hofmann, K. P.; Hubbell, W. L. High-Resolution Distance Mapping in Rhodopsin Reveals the Pattern of Helix Movement Due to Activation. *Proc. Natl. Acad. Sci.* **2008**, *105* (21), 7439–7444.

(61) Hubbell, W. L.; Altenbach, C.; Hubbell, C. M.; Khorana, H. G. Rhodopsin Structure, Dynamics, and Activation: A Perspective from Crystallography, Site-

Directed Spin Labeling, Sulfhydryl Reactivity, and Disulfide Cross-Linking. In *Advances in Protein Chemistry*; 2003; Vol. 63, pp 243–290.

(62) Rasmussen, S. G. F.; Choi, H.-J.; Fung, J. J.; Pardon, E.; Casarosa, P.; Chae, P. S.; DeVree, B. T.; Rosenbaum, D. M.; Thian, F. S.; Kobilka, T. S.; et al. Structure of a Nanobody-Stabilized Active State of the B2 Adrenoceptor. *Nature* **2011**, *469* (7329), 175–180.

(63) Rasmussen, S. G. F.; DeVree, B. T.; Zou, Y.; Kruse, A. C.; Chung, K. Y.; Kobilka, T. S.; Thian, F. S.; Chae, P. S.; Pardon, E.; Calinski, D.; et al. Crystal Structure of the B2 Adrenergic Receptor–Gs Protein Complex. *Nature* **2011**, *477* (7366), 549–555.

(64) Mittermaier, A. K.; Kay, L. E. Observing Biological Dynamics at Atomic Resolution Using NMR. *Trends Biochem. Sci.* **2009**, *34* (12), 601–611.

(65) Kerfah, R.; Plevin, M. J.; Sounier, R.; Gans, P.; Boisbouvier, J. Methyl-Specific Isotopic Labeling: A Molecular Tool Box for Solution NMR Studies of Large Proteins. *Curr. Opin. Struct. Biol.* **2015**, *32*, 113–122.

(66) Kofuku, Y.; Ueda, T.; Okude, J.; Shiraishi, Y.; Kondo, K.; Maeda, M.; Tsujishita, H.; Shimada, I. Efficacy of the β_2-Adrenergic Receptor Is Determined by Conformational Equilibrium in the Transmembrane Region. *Nat. Commun.* **2012**, *3* (1), 1045.

(67) Nygaard, R.; Zou, Y.; Dror, R. O. O.; Mildorf, T. J. J.; Arlow, D. H. H.; Manglik, A.; Pan, A. C. C.; Liu, C. W. W.; Fung, J. J. J.; Bokoch, M. P. P.; et al. The Dynamic Process of B2-Adrenergic Receptor Activation. *Cell* **2013**, *152* (3), 532–542.

(68) Manglik, A.; Kim, T. H.; Masureel, M.; Altenbach, C.; Yang, Z.; Hilger, D.; Lerch, M. T.; Kobilka, T. S.; Thian, F. S.; Hubbell, W. L.; et al. Structural Insights into the Dynamic Process of B2-Adrenergic Receptor Signaling. *Cell* **2015**, *161* (5), 1101–1111.

(69) Bokoch, M. P.; Zou, Y.; Rasmussen, S. G. F.; Liu, C. W.; Nygaard, R.; Rosenbaum, D. M.; Fung, J. J.; Choi, H.; Thian, F. S.; Kobilka, T. S.; et al. Ligand-Specific Regulation of the Extracellular Surface of a G-Protein-Coupled Receptor. *Nature* **2010**, *463* (7277), 108–112.

(70) Cross, T. A.; Murray, D. T.; Watts, A. Helical Membrane Protein Conformations and Their Environment. *European Biophysics Journal*. 2013, pp 731–755.

(71) Privé, G. G. Detergents for the Stabilization and Crystallization of Membrane Proteins. *Methods* **2007**, *41* (4), 388–397.

(72) Moraes, I.; Evans, G.; Sanchez-Weatherby, J.; Newstead, S.; Stewart, P. D. S. Membrane Protein Structure Determination - the next Generation. *Biochim. Biophys. Acta* **2013**, *1838* (1), 78–87.

(73) Ding, Y.; Fujimoto, L. M.; Yao, Y.; Plano, G. V.; Marassi, F. M. Influence of the Lipid Membrane Environment on Structure and Activity of the Outer Membrane Protein Ail from Yersinia Pestis. *Biochim. Biophys. Acta* **2015**, *1848* (2), 712–720.

(74) Zhang, M.; Huang, R.; Im, S. C.; Waskell, L.; Ramamoorthy, A. Effects of Membrane Mimetics on Cytochrome P450-Cytochrome B5 Interactions Characterized by NMR Spectroscopy. *J. Biol. Chem.* **2015**, *290* (20), 12705–12718.

(75) Laganowsky, A.; Reading, E.; Allison, T. M.; Ulmschneider, M. B.; Degiacomi, M. T.; Baldwin, A. J.; Robinson, C. V. Membrane Proteins Bind Lipids Selectively to Modulate Their Structure and Function. *Nature* **2014**, *510* (7503), 172–175.

(76) Frey, L.; Lakomek, N. A.; Riek, R.; Bibow, S. Micelles, Bicelles, and Nanodiscs: Comparing the Impact of Membrane Mimetics on Membrane Protein Backbone Dynamics. *Angew. Chemie - Int. Ed.* **2017**, *56* (1), 380–383.

(77) Hagn, F.; Etzkorn, M.; Raschle, T.; Wagner, G. Optimized Phospholipid Bilayer Nanodiscs Facilitate High-Resolution Structure Determination of Membrane Proteins. *J. Am. Chem. Soc.* **2013**, *135* (5), 1919–1925.

(78) Warschawski, D. E.; Arnold, A. A.; Beaugrand, M.; Gravel, A.; Chartrand, É.; Marcotte, I. Choosing Membrane Mimetics for NMR Structural Studies of Transmembrane Proteins. *Biochim. Biophys. Acta - Biomembr.* **2011**, *1808* (8), 1957–1974.

(79) Popot, J.-L.; Althoff, T.; Bagnard, D.; Banères, J.-L.; Bazzacco, P.; Billon-Denis, E.; Catoire, L. J.; Champeil, P.; Charvolin, D.; Cocco, M. J.; et al. Amphipols From A to Z*. *Annu. Rev. Biophys.* **2011**, *40* (1), 379–408.

(80) Bon, C. Le; Pia, E. A. Della; Giusti, F.; Lloret, N.; Zoonens, M.; Martinez, K. L.; Popot, J. L. Synthesis of an Oligonucleotide-Derivatized Amphipol and Its Use to Trap and Immobilize Membrane Proteins. *Nucleic Acids Res.* **2014**, *42* (10).

(81) Tribet, C.; Audebert, R.; Popot, J.-L. Amphipols: Polymers That Keep Membrane Proteins Soluble in Aqueous Solutions. *Proc. Natl. Acad. Sci.* **1996**, *93* (26), 15047–15050.

(82) Piai, A.; Fu, Q.; Dev, J.; Chou, J. J. Optimal Bicelle Size q for Solution NMR Studies of the Protein Transmembrane Partition. *Chem. - A Eur. J.* **2017**, *23* (6), 1361–1367.

(83) Laguerre, A.; Löhr, F.; Henrich, E.; Hoffmann, B.; Abdul-Manan, N.; Connolly, P. J.; Perozo, E.; Moore, J. M.; Bernhard, F.; Dötsch, V. From Nanodiscs to Isotropic Bicelles: A Procedure for Solution Nuclear Magnetic Resonance Studies of Detergent-Sensitive Integral Membrane Proteins. *Structure* **2016**, *24* (10), 1830–1841.

(84) Poulos, S.; Morgan, J. L. W.; Zimmer, J.; Faham, S. Bicelles Coming of Age: An Empirical Approach to Bicelle Crystallization. *Methods Enzymol.* **2015**, *557*, 393–416.

(85) Pollock, N. L.; Lee, S. C.; Patel, J. H.; Gulamhussein, A. A.; Rothnie, A. J. Structure and Function of Membrane Proteins Encapsulated in a Polymer-Bound Lipid Bilayer. *Biochim. Biophys. Acta - Biomembr.* **2018**, *1860* (4), 809–817.

(86) Dörr, J. M.; Scheidelaar, S.; Koorengevel, M. C.; Dominguez, J. J.; Schäfer, M.; van Walree, C. A.; Killian, J. A. The Styrene–Maleic Acid Copolymer: A Versatile Tool in Membrane Research. *Eur. Biophys. J.* **2016**, *45* (1), 3–21.

(87) Broecker, J.; Eger, B. T.; Ernst, O. P. Crystallogenesis of Membrane Proteins Mediated by Polymer-Bounded Lipid Nanodiscs. *Structure* **2017**, *25* (2), 384–392.

(88) Sun, C.; Benlekbir, S.; Venkatakrishnan, P.; Wang, Y.; Hong, S.; Hosler, J.; Tajkhorshid, E.; Rubinstein, J. L.; Gennis, R. B. Structure of the Alternative Complex III in a Supercomplex with Cytochrome Oxidase. *Nature* **2018**, *557* (7703), 123–126.

(89) Parmar, M.; Rawson, S.; Scarff, C. A.; Goldman, A.; Dafforn, T. R.; Muench, S. P.; Postis, V. L. G. Using a SMALP Platform to Determine a Sub-Nm Single Particle Cryo-EM Membrane Protein Structure. *Biochim. Biophys. Acta - Biomembr.* **2018**, *1860* (2), 378–383.

(90) Bersch, B.; Dörr, J. M.; Hessel, A.; Killian, J. A.; Schanda, P. Proton-Detected Solid-State NMR Spectroscopy of a Zinc Diffusion Facilitator Protein in Native Nanodiscs. *Angew. Chemie - Int. Ed.* **2017**, *56* (9), 2508–2512.

(91) Banerjee, S.; Sen, K.; Pal, T. K.; Guha, S. K. Poly(Styrene-Co-Maleic Acid)-Based PH-Sensitive Liposomes Mediate Cytosolic Delivery of Drugs for Enhanced Cancer Chemotherapy. *Int. J. Pharm.* **2012**, *436* (1–2), 786–797.

(92) Puthenveetil, R.; Nguyen, K.; Vinogradova, O. Nanodiscs and Solution NMR: Preparation, Application and Challenges. *Nanotechnol. Rev.* **2017**, *6* (1), 111–125.

(93) Yasuhara, K.; Arakida, J.; Ravula, T.; Ramadugu, S. K.; Sahoo, B.; Kikuchi, J. I.; Ramamoorthy, A. Spontaneous Lipid Nanodisc Fomation by Amphiphilic Polymethacrylate Copolymers. *J. Am. Chem. Soc.* **2017**, *139* (51), 18657–18663.

(94) Ravula, T.; Hardin, N. Z.; Ramadugu, S. K.; Cox, S. J.; Ramamoorthy, A. Formation of PH-Resistant Monodispersed Polymer–Lipid Nanodiscs. *Angew. Chemie - Int. Ed.* **2018**, *57* (5), 1342–1345.

(95) Oluwole, A. O.; Danielczak, B.; Meister, A.; Babalola, J. O.; Vargas, C.; Keller, S. Solubilization of Membrane Proteins into Functional Lipid-Bilayer Nanodiscs Using a Diisobutylene/Maleic Acid Copolymer. *Angew. Chemie - Int. Ed.* **2017**, *56* (7), 1919–1924.

(96) Fiori, M. C.; Jiang, Y.; Altenberg, G. A.; Liang, H. Polymer-Encased Nanodiscs with Improved Buffer Compatibility. *Sci. Rep.* **2017**, *7* (1).

(97) Bayburt, T. H.; Grinkova, Y. V.; Sligar, S. G. Self-Assembly of Discoidal Phospholipid Bilayer Nanoparticles with Membrane Scaffold Proteins. *Nano Lett.* **2002**, *2* (8), 853–856.

(98) Denisov, I. G.; Sligar, S. G. Nanodiscs in Membrane Biochemistry and Biophysics. *Chem. Rev.* **2017**, *117* (6), 4669–4713.

(99) Denisov, I. G.; Grinkova, Y. V.; Lazarides, A. A.; Sligar, S. G. Directed Self-Assembly of Monodisperse Phospholipid Bilayer Nanodiscs with Controlled Size. *J. Am. Chem. Soc.* **2004**, *126* (11), 3477–3487.

(100) McLean, M. A.; Gregory, M. C.; Sligar, S. G. Nanodiscs: A Controlled Bilayer Surface for the Study of Membrane Proteins. *Annu. Rev. Biophys.* **2018**, *47* (1), 107–124.

(101) Raschle, T.; Hiller, S.; Yu, T.-Y.; Rice, A. J.; Walz, T.; Wagner, G. Structural and Functional Characterization of the Integral Membrane Protein VDAC-1 in Lipid Bilayer Nanodiscs. *J. Am. Chem. Soc.* **2009**, *131* (49), 17777–17779.

(102) Etzkorn, M.; Raschle, T.; Hagn, F.; Gelev, V.; Rice, A. J.; Walz, T.; Wagner, G. Cell-Free Expressed Bacteriorhodopsin in Different Soluble Membrane Mimetics: Biophysical Properties and NMR Accessibility. *Structure* **2013**, *21* (3), 394–401.

(103) Imai, S.; Osawa, M.; Mita, K.; Toyonaga, S.; Machiyama, A.; Ueda, T.; Takeuchi, K.; Oiki, S.; Shimada, I. Functional Equilibrium of the KcsA Structure Revealed by NMR. *J. Biol. Chem.* **2012**, *287* (47), 39634–39641.

(104) Minato, Y.; Suzuki, S.; Hara, T.; Kofuku, Y.; Kasuya, G.; Fujiwara, Y.; Igarashi, S.; Suzuki, E.-I.; Nureki, O.; Hattori, M.; et al. Conductance of P2X4 Purinergic Receptor Is Determined by Conformational Equilibrium in the Transmembrane Region. *Proc. Natl. Acad. Sci. U. S. A.* **2016**, *113* (17), 4741–4746.

(105) Kofuku, Y.; Ueda, T.; Okude, J.; Shiraishi, Y.; Kondo, K.; Mizumura, T.; Suzuki, S.; Shimada, I. Functional Dynamics of Deuterated β 2 -Adrenergic Receptor in Lipid Bilayers Revealed by NMR Spectroscopy. *Angew. Chemie Int. Ed.* **2014**, *53* (49), 13376–13379.

(106) Chromy, B. A.; Arroyo, E.; Blanchette, C. D.; Bench, G.; Benner, H.; Cappuccio, J. A.; Coleman, M. A.; Henderson, P. T.; Hinz, A. K.; Kuhn, E. A.; et al. Different Apolipoproteins Impact Nanolipoprotein Particle Formation. *J. Am. Chem. Soc.* **2007**, *129* (46), 14348–14354.

(107) Zhang, M.; Huang, R.; Ackermann, R.; Im, S. C.; Waskell, L.; Schwendeman, A.; Ramamoorthy, A. Reconstitution of the Cytb5-CytP450 Complex in Nanodiscs for Structural Studies Using NMR Spectroscopy. *Angew. Chemie - Int. Ed.* **2016**, *55* (14), 4497–4499.

(108) Park, S. H.; Berkamp, S.; Cook, G. A.; Chan, M. K.; Viadiu, H.; Opella, S. J. Nanodiscs versus Macrodiscs for NMR of Membrane Proteins. *Biochemistry* **2011**, *50* (42), 8983–8985.

(109) Frauenfeld, J.; Löving, R.; Armache, J. P.; Sonnen, A. F. P.; Guettou, F.; Moberg, P.; Zhu, L.; Jegerschöld, C.; Flayhan, A.; Briggs, J. A. G.; et al. A Saposin-Lipoprotein Nanoparticle System for Membrane Proteins. *Nat. Methods* **2016**, *13* (4), 345–351.

(110) Lyons, J. A.; Bøggild, A.; Nissen, P.; Frauenfeld, J. Saposin-Lipoprotein Scaffolds for Structure Determination of Membrane Transporters. In *Methods in Enzymology*; Elsevier Inc., 2017; Vol. 594, pp 85–99.

(111) Flayhan, A.; Mertens, H. D. T.; Ural-Blimke, Y.; Martinez Molledo, M.; Svergun, D. I.; Löw, C. Saposin Lipid Nanoparticles: A Highly Versatile and Modular Tool for Membrane Protein Research. *Structure* **2018**, *26* (2), 345–355.e5.

(112) Kolter, T.; Sandhoff, K. Lysosomal Degradation of Membrane Lipids. *FEBS Lett.* **2010**, *584* (9), 1700–1712.

(113) Schuette, C. G.; Pierstorff, B.; Huettler, S.; Sandhoff, K. Sphingolipid Activator Proteins: Proteins with Complex Functions in Lipid Degradation and Skin Biogenesis. *Glycobiology* **2001**, *11* (6), 81R–90R.

(114) O'Brien, J. S.; Kretz, K. a; Dewji, N.; Wenger, D. a; Esch, F.; Fluharty, a L. Coding of Two Sphingolipid Activator Proteins (SAP-1 and SAP-2) by Same Genetic Locus. *Science* **1988**, *241* (4869), 1098–1101.

(115) Bruhn, H. A Short Guided Tour through Functional and Structural Features of Saposin-like Proteins. *Biochem. J.* **2005**, *389* (2), 249–257.

(116) Xu, Y.-H.; Barnes, S.; Sun, Y.; Grabowski, G. A. Multi-System Disorders of Glycosphingolipid and Ganglioside Metabolism. *J. Lipid Res.* **2010**, *51* (7), 1643–1675.

(117) Kolter, T.; Sandhoff, K. Principles of Lysosomal Membrane Digestion: Stimulation of Sphingolipid Degradation by Sphingolipid Activator Proteins and Anionic Lysosomal Lipids. *Annu. Rev. Cell Dev. Biol.* **2005**, *21* (1), 81–103.

(118) Matsuda, J. A Mutation in the Saposin A Domain of the Sphingolipid Activator Protein (Prosaposin) Gene Results in a Late-Onset, Chronic Form of Globoid Cell Leukodystrophy in the Mouse. *Hum. Mol. Genet.* **2001**, *10* (11), 1191–1199.

(119) Spiegel, R.; Bach, G.; Sury, V.; Mengistu, G.; Meidan, B.; Shalev, S.; Shneor, Y.; Mandel, H.; Zeigler, M. A Mutation in the Saposin A Coding Region of the Prosaposin Gene in an Infant Presenting as Krabbe Disease: First Report of Saposin A Deficiency in Humans. *Mol. Genet. Metab.* **2005**, *84* (2), 160–166.

(120) Tamargo, R. J.; Velayati, A.; Goldin, E.; Sidransky, E. The Role of Saposin C in Gaucher Disease. *Mol. Genet. Metab.* **2012**, *106* (3), 257–263.

(121) Hill, C. H.; Cook, G. M.; Spratley, S. J.; Fawke, S.; Graham, S. C.; Deane, J. E. The Mechanism of Glycosphingolipid Degradation Revealed by a GALC-SapA Complex Structure. *Nat. Commun.* **2018**, *9* (1), 151.

(122) Zhou, Y.-F.; Metcalf, M. C.; Garman, S. C.; Edmunds, T.; Qiu, H.; Wei, R. R. Human Acid Sphingomyelinase Structures Provide Insight to Molecular Basis of Niemann-Pick Disease. *Nat. Commun.* **2016**, *7*, 13082.

(123) Gorelik, A.; Illes, K.; Heinz, L. X.; Superti-Furga, G.; Nagar, B. Crystal Structure of Mammalian Acid Sphingomyelinase. *Nat. Commun.* **2016**, *7*, 12196.

(124) Xiong, Z.-J.; Huang, J.; Poda, G.; Pomès, R.; Privé, G. G. Structure of Human Acid Sphingomyelinase Reveals the Role of the Saposin Domain in Activating Substrate Hydrolysis. *J. Mol. Biol.* **2016**, *428* (15), 3026–3042.

(125) Ahn, V. E.; Leyko, P.; Alattia, J.-R.; Chen, L.; Privé, G. G. Crystal Structures of Saposins A and C. *Protein Sci.* **2006**, *15* (8), 1849–1857.

(126) Popovic, K.; Holyoake, J.; Pomes, R.; Prive, G. G. Structure of Saposin A Lipoprotein Discs. *Proc. Natl. Acad. Sci.* **2012**, *109* (8), 2908–2912.

(127) Li, J.; Richards, M. R.; Bagal, D.; Campuzano, I. D. G.; Kitova, E. N.; Xiong, Z. J.; Privé, G. G.; Klassen, J. S. Characterizing the Size and Composition of Saposin A Lipoprotein Picodiscs. *Anal. Chem.* **2016**, *88* (19), 9524–9531.

(128) Hill, C. H.; Read, R. J.; Deane, J. E. Structure of Human Saposin A at Lysosomal PH. *Acta Crystallogr. Sect. Struct. Biol. Commun.* **2015**, *71*, 895–900.

(129) Hagn, F.; Nasr, M. L.; Wagner, G. Assembly of Phospholipid Nanodiscs of Controlled Size for Structural Studies of Membrane Proteins by NMR. *Nat. Protoc.* **2018**, *13* (1), 79–98.

(130) Prince, C.; Jia, Z. Measurement of Detergent Concentration Using 2,6-Dimethylphenol in Membrane-Protein Crystallization. *Acta Crystallogr. Sect. D Biol. Crystallogr.* **2012**, *68* (12), 1694–1696.

(131) Prince, C.; Jia, Z. Quantification of Detergent Using Colorimetric Methods in Membrane Protein Crystallography. In *Methods in Enzymology*; Elsevier Inc., 2015; Vol. 557, pp 95–116.

(132) Nielsen, S. S. Phenol-Sulfuric Acid Method for Total Carbohydrates. In *Food Analysis*; Springer, Boston, MA, 2010; pp 47–53.

(133) Hopper, J. T. S.; Yu, Y. T.-C.; Li, D.; Raymond, A.; Bostock, M.; Liko, I.; Mikhailov, V.; Laganowsky, A.; Benesch, J. L. P.; Caffrey, M.; et al. Detergent-Free Mass Spectrometry of Membrane Protein Complexes. *Nat. Methods* **2013**, *10* (12), 1206–1208.

(134) Bibow, S.; Polyhach, Y.; Eichmann, C.; Chi, C. N.; Kowal, J.; Albiez, S.; McLeod, R. A.; Stahlberg, H.; Jeschke, G.; Güntert, P.; et al. Solution Structure of Discoidal High-Density Lipoprotein Particles with a Shortened Apolipoprotein A-I. *Nat. Struct. Mol. Biol.* **2017**, *24* (2), 187–193.

(135) Okude, J.; Ueda, T.; Kofuku, Y.; Sato, M.; Nobuyama, N.; Kondo, K.; Shiraishi, Y.; Mizumura, T.; Onishi, K.; Natsume, M.; et al. Identification of a Conformational Equilibrium That Determines the Efficacy and Functional Selectivity of the μ-Opioid Receptor. *Angew. Chemie Int. Ed.* **2015**, *54* (52), 15771–15776.

(136) Yu, T. Y.; Raschle, T.; Hiller, S.; Wagner, G. Solution NMR Spectroscopic Characterization of Human VDAC-2 in Detergent Micelles and Lipid Bilayer Nanodiscs. *Biochim. Biophys. Acta - Biomembr.* **2012**, *1818* (6), 1562–1569.

(137) Glück, J. M.; Wittlich, M.; Feuerstein, S.; Hoffmann, S.; Willbold, D.; Koenig, B. W. Integral Membrane Proteins in Nanodiscs Can Be Studied by Solution NMR Spectroscopy. *J. Am. Chem. Soc.* **2009**, *131* (34), 12060–12061.

(138) Shenkarev, Z. O.; Lyukmanova, E. N.; Paramonov, A. S.; Shingarova, L. N.; Chupin, V. V.; Kirpichnikov, M. P.; Blommers, M. J. J.; Arseniev, A. S. Lipid−Protein Nanodiscs as Reference Medium in Detergent Screening for High-Resolution NMR Studies of Integral Membrane Proteins. *J. Am. Chem. Soc.* **2010**, *132* (16), 5628–5629.

(139) Yao, Y.; Nisan, D.; Fujimoto, L. M.; Antignani, A.; Barnes, A.; Tjandra, N.; Youle, R. J.; Marassi, F. M. Characterization of the Membrane-Inserted C-Terminus of Cytoprotective BCL-XL. *Protein Expr. Purif.* **2016**, *122*, 56–63.

(140) Yao, Y.; Fujimoto, L. M.; Hirshman, N.; Bobkov, A. A.; Antignani, A.; Youle, R. J.; Marassi, F. M. Conformation of BCL-XL upon Membrane Integration. *J. Mol. Biol.* **2015**, *427* (13), 2262–2270.

(141) Kucharska, I.; Edrington, T. C.; Liang, B.; Tamm, L. K. Optimizing Nanodiscs and Bicelles for Solution NMR Studies of Two β-Barrel Membrane Proteins. *J. Biomol. NMR* **2015**, *61* (3–4), 261–274.

(142) Nasr, M. L.; Baptista, D.; Strauss, M.; Sun, Z. Y. J.; Grigoriu, S.; Huser, S.; Plückthun, A.; Hagn, F.; Walz, T.; Hogle, J. M.; et al. Covalently Circularized Nanodiscs for Studying Membrane Proteins and Viral Entry. *Nat. Methods* **2016**, *14* (1), 49–52.

(143) Bayburt, T. H.; Sligar, S. G. Membrane Protein Assembly into Nanodiscs. *FEBS Lett.* **2010**, *584* (9), 1721–1727.

(144) Strahl, H.; Errington, J. Bacterial Membranes: Structure, Domains, and Function. *Annu. Rev. Microbiol.* **2017**, *71* (1), 519–538.

(145) Rollauer, S. E.; Sooreshjani, M. A.; Noinaj, N.; Buchanan, S. K. Outer Membrane Protein Biogenesis in Gram-Negative Bacteria. *Philos. Trans. R. Soc. Lond. B. Biol. Sci.* **2015**, *370* (1679).

(146) Koebnik, R.; Locher, K. P.; Van Gelder, P. Structure and Function of Bacterial Outer Membrane Proteins: Barrels in a Nutshell. *Mol. Microbiol.* **2000**, *37* (2), 239–253.

(147) Vogt, J.; Schulz, G. E. The Structure of the Outer Membrane Protein OmpX from Escherichia Coli Reveals Possible Mechanisms of Virulence. *Structure* **1999**, *7* (10), 1301–1309.

(148) Fernández, C.; Hilty, C.; Wider, G.; Güntert, P.; Wüthrich, K. NMR Structure of the Integral Membrane Protein OmpX. *J. Mol. Biol.* **2004**, *336* (5), 1211–1221.

(149) Fernández, C.; Adeishvili, K.; Wüthrich, K. Transverse Relaxation-Optimized NMR Spectroscopy with the Outer Membrane Protein OmpX in Dihexanoyl Phosphatidylcholine Micelles. *Proc. Natl. Acad. Sci. U. S. A.* **2001**, *98* (5), 2358–2363.

(150) Hagn, F.; Wagner, G. Structure Refinement and Membrane Positioning of Selectively Labeled OmpX in Phospholipid Nanodiscs. *J. Biomol. NMR* **2015**, *61* (3–4), 249–260.

(151) Lee, D.; Hilty, C.; Wider, G.; Wüthrich, K. Effective Rotational Correlation Times of Proteins from NMR Relaxation Interference. *J. Magn. Reson.* **2006**, *178* (1), 72–76.

(152) Piknová, B.; Pérochon, E.; Tocanne, J. F. Hydrophobic Mismatch and Long-Range Protein/Lipid Interactions in Bacteriorhodopsin/Phosphatidylcholine Vesicles. *Eur. J. Biochem.* **1993**, *218* (2), 385–396.

(153) Kurrle, A.; Sackmann, E.; Rieber, P. Reconstitution of Transferrin Receptor in Mixed Lipid Vesicles. An Example of the Role of Elastic and Electrostatic Forces for Protein/Lipid Assembly. *Biochemistry* **1990**, *29* (36), 8274–8282.

(154) Nezil, F. A.; Bloom, M. Combined Influence of Cholesterol and Synthetic Amphiphillic Peptides upon Bilayer Thickness in Model Membranes. *Biophys. J.* **1992**, *61* (5), 1176–1183.

(155) Lewis, B. A.; Engelman, D. M. Bacteriorhodopsin Remains Dispersed in Fluid Phospholipid Bilayers over a Wide Range of Bilayer Thicknesses. *J. Mol. Biol.* **1983**, *166* (2), 203–210.

(156) Lomize, M. A.; Pogozheva, I. D.; Joo, H.; Mosberg, H. I.; Lomize, A. L. OPM Database and PPM Web Server: Resources for Positioning of Proteins in Membranes. *Nucleic Acids Res.* **2012**, *40* (D1).

(157) Pogozheva, I. D.; Tristram-Nagle, S.; Mosberg, H. I.; Lomize, A. L. Structural Adaptations of Proteins to Different Biological Membranes. *Biochim. Biophys. Acta - Biomembr.* **2013**, *1828* (11), 2592–2608.

(158) Martinez-Seara, H.; Róg, T.; Pasenkiewicz-Gierula, M.; Vattulainen, I.; Karttunen, M.; Reigada, R. Effect of Double Bond Position on Lipid Bilayer Properties: Insight through Atomistic Simulations. *J. Phys. Chem. B* **2007**, *111* (38), 11162–11168.

(159) Hansen, S. B.; Tao, X.; MacKinnon, R. Structural Basis of PIP2 Activation of the Classical Inward Rectifier K+ Channel Kir2.2. *Nature* **2011**, *477* (7365), 495–498.

(160) Yen, H.-Y.; Hoi, K. K.; Liko, I.; Hedger, G.; Horrell, M. R.; Song, W.; Wu, D.; Heine, P.; Warne, T.; Lee, Y.; et al. PtdIns(4,5)P2 Stabilizes Active States of GPCRs and Enhances Selectivity of G-Protein Coupling. *Nature* **2018**, *559* (7714), 423–427.

(161) Dawaliby, R.; Trubbia, C.; Delporte, C.; Masureel, M.; Van Antwerpen, P.; Kobilka, B. K.; Govaerts, C. Allosteric Regulation of G Protein–Coupled Receptor Activity by Phospholipids. *Nat. Chem. Biol.* **2016**, *12* (1), 35–39.

(162) Pöyry, S.; Vattulainen, I. Role of Charged Lipids in Membrane Structures — Insight given by Simulations. *Biochim. Biophys. Acta - Biomembr.* **2016**, *1858* (10), 2322–2333.

(163) Killian, J. A.; von Heijne, G. How Proteins Adapt to a Membrane–Water Interface. *Trends Biochem. Sci.* **2000**, *25* (9), 429–434.

(164) Ridder, A. N. J. A.; Morein, S.; Stam, J. G.; Kühn, A.; De Kruijff, B.; Killian, J. A. Analysis of the Role of Interfacial Tryptophan Residues in Controlling the Topology of Membrane Proteins. *Biochemistry* **2000**.

(165) Schiffer, M.; Chang, C. H.; Stevens, F. J. The Functions of Tryptophan Residues in Membrane Proteins. *Protein Eng. Des. Sel.* **1992**.

(166) Delcour, A. H. Outer Membrane Permeability and Antibiotic Resistance. *Biochim. Biophys. Acta* **2009**.

(167) Zhang, G.; Meredith, T. C.; Kahne, D. On the Essentiality of Lipopolysaccharide to Gram-Negative Bacteria. *Current Opinion in Microbiology*. 2013.

(168) Edrington, T. C.; Kintz, E.; Goldberg, J. B.; Tamm, L. K. Structural Basis for the Interaction of Lipopolysaccharide with Outer Membrane Protein H (OprH) from Pseudomonas Aeruginosa. *J. Biol. Chem.* **2011**, *286* (45), 39211–39223.

(169) Kucharska, I.; Liang, B.; Ursini, N.; Tamm, L. K. Molecular Interactions of Lipopolysaccharide with an Outer Membrane Protein from Pseudomonas Aeruginosa Probed by Solution NMR. *Biochemistry* **2016**, *55* (36), 5061–5072.

(170) Boeuf, D.; Audic, S.; Brillet-Guéguen, L.; Caron, C.; Jeanthon, C. MicRhoDE: A Curated Database for the Analysis of Microbial Rhodopsin Diversity and Evolution. *Database* **2015**, *2015*, bav080.

(171) Voet, D.; Voet, J. G. *Biochemistry 4e*; Wiley, 2010.

(172) Schobert, B.; Lanyi, J. K. Halorhodopsin Is a Light-Driven Chloride Pump. *J. Biol. Chem.* **1982**, *257* (17), 10306–10313.

(173) Nagel, G.; Ollig, D.; Fuhrmann, M.; Kateriya, S.; Musti, A. M.; Bamberg, E.; Hegemann, P. Channelrhodopsin-1: A Light-Gated Proton Channel in Green Algae. *Science* **2002**, *296* (5577), 2395–2398.

(174) Spudich, J. L.; Luecke, H. Sensory Rhodopsin II: Functional Insights from Structure. *Curr. Opin. Struct. Biol.* **2002**, *12* (4), 540–546.

(175) Strotmann, R.; Schröck, K.; Böselt, I.; Stäubert, C.; Russ, A.; Schöneberg, T. Evolution of GPCR: Change and Continuity. *Mol. Cell. Endocrinol.* **2011**, *331* (2), 170–178.

(176) Jung, K. H.; Trivedi, V. D.; Spudich, J. L. Demonstration of a Sensory Rhodopsin in Eubacteria. *Mol. Microbiol.* **2003**, *47* (6), 1513–1522.

(177) Sineshchekov, O. A.; Trivedi, V. D.; Sasaki, J.; Spudich, J. L. Photochromicity of Anabaena Sensory Rhodopsin, an Atypical Microbial Receptor with a Cis -Retinal Light-Adapted Form. *J. Biol. Chem.* **2005**, *280* (15), 14663–14668.

(178) Kawanabe, A.; Kandori, H. Photoreactions and Structural Changes of Anabaena Sensory Rhodopsin. *Sensors* **2009**, *9* (12), 9741–9804.

(179) Vogeley, L.; Sineshchekov, O. A.; Trivedi, V. D.; Sasaki, J.; Spudich, J. L.; Luecke, H. Anabaena Sensory Rhodopsin: A Photochromic Color Sensor at 2.0 A. *Science* **2004**, *306* (5700), 1390–1393.

(180) Wang, S.; Munro, R. A.; Kim, S. Y.; Jung, K.-H.; Brown, L. S.; Ladizhansky, V. Paramagnetic Relaxation Enhancement Reveals Oligomerization Interface of a Membrane Protein. *J. Am. Chem. Soc.* **2012**, *134* (41), 16995–16998.

(181) Hoff, W. D.; Jung, K. H.; Spudich, J. L. Molecular Mechanism of Photosignaling by Archaeal Sensory Rhodopsins. *Annu. Rev. Biophys. Biomol. Struct.* **1997**, *26* (1), 223–258.

(182) Luecke, H.; Schobert, B.; Lanyi, J. K.; Spudich, E. N.; Spudich, J. L. Crystal Structure of Sensory Rhodopsin II at 2.4 Angstroms: Insights into Color Tuning and Transducer Interaction. *Science* **2001**, *293* (5534), 1499–1503.

(183) Royant, A.; Nollert, P.; Edman, K.; Neutze, R.; Landau, E. M.; Pebay-Peyroula, E.; Navarro, J. X-Ray Structure of Sensory Rhodopsin II at 2.1-A Resolution. *Proc. Natl. Acad. Sci.* **2001**, *98* (18), 10131–10136.

(184) Gordeliy, V. I.; Labahn, J.; Moukhametzianov, R.; Efremov, R.; Granzin, J.; Schlesinger, R.; Büldt, G.; Savopol, T.; Scheidig, A. J.; Klare, J. P.; et al. Molecular Basis of Transmembrane Signalling by Sensory Rhodopsin II-Transducer Complex. *Nature* **2002**, *419* (6906), 484–487.

(185) Gushchin, I.; Reshetnyak, A.; Borshchevskiy, V.; Ishchenko, A.; Round, E.; Grudinin, S.; Engelhard, M.; Bldt, G.; Gordeliy, V. Active State of Sensory Rhodopsin II: Structural Determinants for Signal Transfer and Proton Pumping. *J. Mol. Biol.* **2011**, *412* (4), 591–600.

(186) Crick, D. Solution NMR Studies of Seven-Transmembrane Helix Proteins, University of Cambridge, 2014.

(187) Baker, J. G. The Selectivity of β-Adrenoceptor Agonists at Human B1-, B2- and B3-Adrenoceptors. *Br. J. Pharmacol.* **2010**, *160* (5), 1048–1061.

(188) Warne, T.; Serrano-Vega, M. J.; Baker, J. G.; Moukhametzianov, R.; Edwards, P. C.; Henderson, R.; Leslie, A. G. W.; Tate, C. G.; Schertler, G. F. X. Structure of a B1-Adrenergic G-Protein-Coupled Receptor. *Nature* **2008**, *454* (7203), 486–491.

(189) Warne, T.; Moukhametzianov, R.; Baker, J. G.; Nehmé, R.; Edwards, P. C.; Leslie, A. G. W.; Schertler, G. F. X.; Tate, C. G. The Structural Basis for Agonist and Partial Agonist Action on a B1-Adrenergic Receptor. *Nature* **2011**, *469* (7329), 241–245.

(190) Moukhametzianov, R.; Warne, T.; Edwards, P. C.; Serrano-Vega, M. J.; Leslie, A. G. W.; Tate, C. G.; Schertler, G. F. X. Two Distinct Conformations of Helix 6 Observed in Antagonist-Bound Structures of a Beta1-Adrenergic Receptor. *Proc. Natl. Acad. Sci. U. S. A.* **2011**, *108* (20), 8228–8232.

(191) Warne, T.; Edwards, P. C.; Leslie, A. G. W.; Tate, C. G. Crystal Structures of a Stabilized B1-Adrenoceptor Bound to the Biased Agonists Bucindolol and Carvedilol. *Structure* **2012**, *20* (5), 841–849.

(192) Christopher, J. A.; Brown, J.; Doré, A. S.; Errey, J. C.; Koglin, M.; Marshall, F. H.; Myszka, D. G.; Rich, R. L.; Tate, C. G.; Tehan, B.; et al. Biophysical Fragment Screening of the B1-Adrenergic Receptor: Identification of High Affinity Arylpiperazine Leads Using Structure-Based Drug Design. *J. Med. Chem.* **2013**, *56* (9), 3446–3455.

(193) Miller-Gallacher, J. L.; Nehmé, R.; Warne, T.; Edwards, P. C.; Schertler, G. F. X.; Leslie, A. G. W.; Tate, C. G. The 2.1 Å Resolution Structure of Cyanopindolol-Bound B1-Adrenoceptor Identifies an Intramembrane Na+ Ion That Stabilises the Ligand-Free Receptor. *PLoS One* **2014**, *9* (3), e92727.

(194) Isogai, S.; Deupi, X.; Opitz, C.; Heydenreich, F. M.; Tsai, C.-J.; Brueckner, F.; Schertler, G. F. X.; Veprintsev, D. B.; Grzesiek, S. Backbone NMR Reveals Allosteric Signal Transduction Networks in the B1-Adrenergic Receptor. *Nature* **2016**, *530* (7589), 237–241.

(195) Solt, A. S.; Bostock, M. J.; Shrestha, B.; Kumar, P.; Warne, T.; Tate, C. G.; Nietlispach, D. Insight into Partial Agonism by Observing Multiple Equilibria for

Ligand-Bound and Gs-Mimetic Nanobody-Bound B1-Adrenergic Receptor. *Nat. Commun.* **2017**, *8* (1), 1795.

(196) Bruzzese, A.; Gil, C.; Dalton, J. A. R.; Giraldo, J. Structural Insights into Positive and Negative Allosteric Regulation of a G Protein-Coupled Receptor through Protein-Lipid Interactions. *Sci. Rep.* **2018**, *8* (1), 4456.

(197) Neale, C.; Herce, H. D.; Pomès, R.; García, A. E. Can Specific Protein-Lipid Interactions Stabilize an Active State of the Beta 2 Adrenergic Receptor? *Biophys. J.* **2015**, *109* (8), 1652–1662.

(198) Ballesteros, J. A.; Weinstein, H. [19] Integrated Methods for the Construction of Three-Dimensional Models and Computational Probing of Structure-Function Relations in G Protein-Coupled Receptors. In *Methods in Neurosciences*; 1995; Vol. 25, pp 366–428.

(199) Hanson, M. A.; Cherezov, V.; Griffith, M. T.; Roth, C. B.; Jaakola, V.-P.; Chien, E. Y. T.; Velasquez, J.; Kuhn, P.; Stevens, R. C. A Specific Cholesterol Binding Site Is Established by the 2.8 Å Structure of the Human B2-Adrenergic Receptor. *Structure* **2008**, *16* (6), 897–905.

(200) Gater, D. L.; Saurel, O.; Iordanov, I.; Liu, W.; Cherezov, V.; Milon, A. Two Classes of Cholesterol Binding Sites for the β_2AR Revealed by Thermostability and NMR. *Biophys. J.* **2014**, *107* (10), 2305–2312.

(201) Zocher, M.; Zhang, C.; Rasmussen, S. G. F.; Kobilka, B. K.; Muller, D. J. Cholesterol Increases Kinetic, Energetic, and Mechanical Stability of the Human 2-Adrenergic Receptor. *Proc. Natl. Acad. Sci.* **2012**, *109* (50), E3463–E3472.

(202) Manna, M.; Niemelä, M.; Tynkkynen, J.; Javanainen, M.; Kulig, W.; Müller, D. J.; Rog, T.; Vattulainen, I. Mechanism of Allosteric Regulation of B2- Adrenergic Receptor by Cholesterol. *Elife* **2016**, *5*, 1–21.

(203) Inagaki, S.; Ghirlando, R.; White, J. F.; Gvozdenovic-Jeremic, J.; Northup, J. K.; Grisshammer, R. Modulation of the Interaction between Neurotensin Receptor NTS1 and Gq Protein by Lipid. *J. Mol. Biol.* **2012**, *417* (1–2), 95–111.

(204) Casiraghi, M.; Damian, M.; Lescop, E.; Point, E.; Moncoq, K.; Morellet, N.; Levy, D.; Marie, J.; Guittet, E.; Banères, J. L.; et al. Functional Modulation of a G Protein-Coupled Receptor Conformational Landscape in a Lipid Bilayer. *J. Am. Chem. Soc.* **2016**, *138* (35), 11170–11175.

(205) Verardi, R.; Traaseth, N. J.; Masterson, L. R.; Vostrikov, V. V.; Veglia, G. Isotope Labeling for Solution and Solid-State NMR Spectroscopy of Membrane Proteins. In *Advances in experimental medicine and biology*; Atreya, H. S., Ed.; Springer Netherlands: Dordrecht, 2012; Vol. 992, pp 35–62.

(206) Schwarz, D.; Junge, F.; Durst, F.; Frölich, N.; Schneider, B.; Reckel, S.; Sobhanifar, S.; Dötsch, V.; Bernhard, F. Preparative Scale Expression of Membrane Proteins in Escherichia Coli-Based Continuous Exchange Cell-Free Systems. *Nat. Protoc.* **2007**, *2* (11), 2945–2957.

(207) Endo, Y.; Sawasaki, T. Cell-Free Expression Systems for Eukaryotic Protein Production. *Curr. Opin. Biotechnol.* **2006**, *17* (4), 373–380.

(208) Morita, E. H.; Sawasaki, T.; Tanaka, R.; Endo, Y.; Kohno, T. A Wheat Germ Cell-Free System Is a Novel Way to Screen Protein Folding and Function. *Protein Sci.* **2003**, *12* (6), 1216–1221.

(209) Milić, D.; Veprintsev, D. B. Large-Scale Production and Protein Engineering of G Protein-Coupled Receptors for Structural Studies. *Front. Pharmacol.* **2015**, *6* (MAR), 66.

(210) Sobhanifar, S.; Reckel, S.; Junge, F.; Schwarz, D.; Kai, L.; Karbyshev, M.; Löhr, F.; Bernhard, F.; Dötsch, V. Cell-Free Expression and Stable Isotope Labelling Strategies for Membrane Proteins. *J. Biomol. NMR* **2010**, *46* (1), 33–43.

(211) Staunton, D.; Schlinkert, R.; Zanetti, G.; Colebrook, S. A.; Campbell, I. D. Cell-Free Expression and Selective Isotope Labelling in Protein NMR. *Magn. Reson. Chem.* **2006**, *44 Spec No*, S2-9.

(212) Löhr, F.; Reckel, S.; Karbyshev, M.; Connolly, P. J.; Abdul-Manan, N.; Bernhard, F.; Moore, J. M.; Dötsch, V. Combinatorial Triple-Selective Labeling as a Tool to Assist Membrane Protein Backbone Resonance Assignment. *J. Biomol. NMR* **2012**, *52* (3), 197–210.

(213) Maslennikov, I.; Klammt, C.; Hwang, E.; Kefala, G.; Okamura, M.; Esquivies, L.; Mörs, K.; Glaubitz, C.; Kwiatkowski, W.; Jeon, Y. H.; et al. Membrane Domain Structures of Three Classes of Histidine Kinase Receptors by Cell-Free Expression and Rapid NMR Analysis. *Proc. Natl. Acad. Sci. U. S. A.* **2010**, *107* (24), 10902–10907.

(214) Reckel, S.; Gottstein, D.; Stehle, J.; Löhr, F.; Verhoefen, M.-K.; Takeda, M.; Silvers, R.; Kainosho, M.; Glaubitz, C.; Wachtveitl, J.; et al. Solution NMR Structure of Proteorhodopsin. *Angew. Chemie Int. Ed.* **2011**, *50* (50), 11942–11946.

(215) Wada, T.; Shimono, K.; Kikukawa, T.; Hato, M.; Shinya, N.; Kim, S. Y.; Kimura-Someya, T.; Shirouzu, M.; Tamogami, J.; Miyauchi, S.; et al. Crystal Structure of the Eukaryotic Light-Driven Proton-Pumping Rhodopsin, Acetabularia Rhodopsin II, from Marine Alga. *J. Mol. Biol.* **2011**, *411* (5), 986–998.

(216) Warne, T.; Chirnside, J.; Schertler, G. F. X. Expression and Purification of Truncated, Non-Glycosylated Turkey Beta-Adrenergic Receptors for Crystallization. *Biochim. Biophys. Acta - Biomembr.* **2003**, *1610* (1), 133–140.

(217) Oganesyan, N.; Kim, S. H.; Kim, R. On-Column Protein Refolding for Crystallization. *J. Struct. Funct. Genomics* **2005**, *6* (2–3), 177–182.

(218) Dürr, U. H. N.; Gildenberg, M.; Ramamoorthy, A. The Magic of Bicelles Lights Up Membrane Protein Structure. *Chem. Rev.* **2012**, *112* (11), 6054–6074.

(219) Junge, F.; Luh, L. M.; Proverbio, D.; Schäfer, B.; Abele, R.; Beyermann, M.; Dötsch, V.; Bernhard, F. Modulation of G-Protein Coupled Receptor Sample Quality by Modified Cell-Free Expression Protocols: A Case Study of the Human Endothelin A Receptor. *J. Struct. Biol.* **2010**, *172* (1), 94–106.

(220) Delaglio, F.; Grzesiek, S.; Vuister, G.; Zhu, G.; Pfeifer, J.; Bax, A. NMRPipe: A Multidimensional Spectral Processing System Based on UNIX Pipes. *J. Biomol. NMR* **1995**, *6* (3), 277–293.

(221) Schanda, P.; Kupče, Ē.; Brutscher, B. SOFAST-HMQC Experiments for Recording Two-Dimensional Deteronuclear Correlation Spectra of Proteins within a Few Seconds. *J. Biomol. NMR* **2005**, *33* (4), 199–211.

(222) Davis, A. L.; Keeler, J.; Laue, E. D.; Moskau, D. Experiments for Recording Pure-Absorption Heteronuclear Correlation Spectra Using Pulsed Field Gradients. *J. Magn. Reson.* **1992**, *98* (1), 207–216.

(223) Hyberts, S. G.; Takeuchi, K.; Wagner, G. Poisson-Gap Sampling and Forward Maximum Entropy Reconstruction for Enhancing the Resolution and Sensitivity of Protein NMR Data. *J. Am. Chem. Soc.* **2010**, *132* (7), 2145–2147.

(224) Bostock, M. J.; Holland, D. J.; Nietlispach, D. Compressed Sensing Reconstruction of Undersampled 3D NOESY Spectra: Application to Large Membrane Proteins. *J. Biomol. NMR* **2012**, *54* (1), 15–32.

(225) Vranken, W. F.; Boucher, W.; Stevens, T. J.; Fogh, R. H.; Pajon, A.; Llinas, M.; Ulrich, E. L.; Markley, J. L.; Ionides, J.; Laue, E. D. The CCPN Data Model for NMR Spectroscopy: Development of a Software Pipeline. *Proteins Struct. Funct. Bioinforma.* **2005**, *59* (4), 687–696.